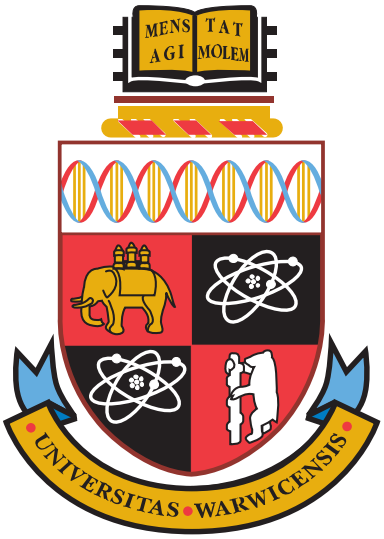


# Extreme Nanowires: Structural and Functional Properties of Filled Single Walled Carbon Nanotubes

by

**Charlotte Anna Slade**

**Thesis**

Submitted to the University of Warwick

for the degree of

**Doctor of Philosophy**

**Physics**

October 2020

# Contents

# List of Tables

# List of Figures

# Acknowledgments

I would like to acknowledge several amazing people, without whom I would not have been able to complete this chapter of my life.

I would like to thank Dr Jeremy Sloan, for his knowledge, support, and unending belief in me. Without his creativity and enthusiasm for "the next big experiment", this thesis would not have been what it is.

Secondly, Dr Ana Sanchez, whose openness brought out the social butterfly in us all. Her generosity - with her time, her knowledge, her food - got me through more than she'll ever know.

Dr Jonathon J. P. Peters, not only for his excellent IT & programming skills, but also his unrelenting patience and guidance. He made us all feel included, kept us social, and entertained many a ridiculous conversation - I'll be forever appreciative of that.

James Gott, amongst many things, for showing me that there is always a worse worst case scenario, and muddling through the realities of PhD life with me anyway. Also for giving me someone with whom to discuss the highs and lows of growing up in Lincolnshire on a daily basis.

Thank you to Steve Hindmarsh and Steve York; your endless patience and technical wizardry truly keep the Microscopy suite running.

Without funding from University of Warwick Physics Department this project, and thesis, would never have existed.

To my family, I could not have asked for a more loving or supportive group of people. Without them, I would not be the person I am today, nor would I have been able to get here. I am truly proud to be their daughter, and sister.

Finally, my amazing partner, Jack, who - no matter the late hour; the working weekend; the illness; or the exam, presentation, and “this experiment’s not working” stress - somehow always managed to put a smile on my face. I’m not quite sure how I would have navigated it all without you: thank you for helping me to grow into a remotely well-adjusted person.

# Declarations

I declare that this thesis contains an account of my research work carried out at the Department of Physics, University of Warwick, between October 2016 and September 2020 under the supervision of Dr J. Sloan and Prof A. M. Sanchez. The research reported here has not been previously submitted, wholly or in part, at this or any other academic institution for admission to a higher degree.

Parts of this thesis have been published by the author between October 2016 and September 2020:

- The experimental data in Sections 4.2.2, and 4.2.3 on the structures of encapsulated SnSe inside SWCNTs has been published as:

  C. A. Slade, A. M. Sanchez, & J. Sloan, Unprecedented New Crystalline Forms of SnSe in Narrow to Medium Diameter Carbon Nanotubes, *NanoLett.* **19**, 2979 – 84 (2019).

  C. A. Slade, A. M. Sanchez, & J. Sloan, "AR-TEM and STEM Studies of Encapsulated PCMs in Narrow to Medium Diameter SWCNTs", International Microscopy Congress, September 2019, International Convention Centre, Sydney, AUS, Conference Presentation.

  C. A. Slade, A. M. Sanchez, & J. Sloan, "AR-TEM and STEM Studies of Encapsulated PCMs in Narrow to Medium Diameter SWCNTs", Electron Mi-

croscopy and Analysis Group Conference, 6 July 2018, University of Warwick, UK, Conference Presentation.

C. A. Slade, S. Marks, A. M. Sanchez, & J. Sloan, "HR-TEM and STEM Studies of Encapsulated SnSe in Narrow to Medium Diameter SWCNTs", Psi-K Conference, September 2018, Unviersity of Warwick, UK, Poster.

C. A. Slade, S. Marks, A. M. Sanchez, & J. Sloan, "HR-TEM and STEM Studies of Encapsulated SnSe in Narrow to Medium Diameter SWCNTs", Microscience Microscopy Congress, July 2017, Manchester Central, UK, Poster.

- The experimental data in Chapter 3 will be disseminated as three separate articles, and submitted for publishing. This work has also been presented as:

  C. A. Slade, A. M. Sanchez, & J. Sloan, "AR-TEM and STEM Studies of Encapsulated PCMs in Narrow to Medium Diameter SWCNTs", Microscience Microscopy Congress, 4 July 2019, Manchester Central, UK, Conference Presentation

All the work presented here was completed by myself, except for the following:

- Acquisition of the XRD data presented in Section 3.5 was aided by D. Walker, University of Warwick
- Full training and support in the acquisition of initial DSC/TGA measurements from D. Hammond, University of Warwick
- Research in Chapter 5 on CNT sample growth and Raman analysis, which was conducted by J. Viner & D. Smith at the University of Southampton

- AIRSS and AIMD modelling and simulations for $Sb_2Te_3$@SWCNT bundles (Fig. 3.8) was carried out by A. Vasylenko, University of Cambridge
- Select transmission electron microscopy images and electron diffraction patterns were acquired by J. Sloan, University of Warwick, and have been accordingly attributed in Chapter 5

# Abstract

The development of technology continues to grow and progress at an increasing rate. With the desire for increasing capability and applications, one key area is making smaller, more powerful devices. This has seen the growth of nancomposites, and components at the nanoscale. With this reduced size comes additional considerations for quality control and visualising these materials, which is beyond the resolving limitations of optical microscopy. The research presented in this thesis is primarily based around the experimental synthesis, imaging, and characterisation of Extreme Nanowires by electron microscopy - particularly High Resolution Transmission Electron Microscopy, Scanning Transmission Electron Microscopy, and Scanning Electron Microscopy. Further characterisation techniques, such as Differential Scanning Calorimetry, Thermogravimetric Analysis, and X-Ray Diffraction - have also been reported and provide an insight into the thermal, conduction, and phase change properties of the synthesised nanocomposites.

Firstly, this research investigates the structures that form when two different phase change materials - $Sb_2Te_3$ and SnSe - are nano-confined inside SWCNTs with diameters of less than $\sim 2$ nm, and how this may affect their phase change behaviour in relation to the bulk. This includes cataloguing, and producing structural models for, the encapsulated nanowires via high resolution (scanning) transmission electron microscopy imaging. Many of the structures have not been observed or published before for these materials, and have no analogue to the bulk structure. In the case of SnSe, this catalogue of nanostructures includes linear chain, zig-zag, 2x1, 2x2, and a novel form that has never been seen before for SnSe but is possibly isometric with that seen for free-standing MoS nanowires. Samples are shown to contain a

consistently high filling fraction of SWCNTs with the desired phase change material ($> 95$ % for $Sb_2Te_3$, and $> 40$ % for SnSe) - as confirmed by transmission electron microscopy and energy dispersive x-ray analysis.

Next, this research investigates the amorphous-crystalline transformation, and how electron beam irradiation and heat treament affect the phase of the encapsulated structure. This is primarily conducted via selected area electron diffraction studies of the nano-confined materials. In particular, nano-confined $Sb_2Te_3$ has been observed to undergo a reversible amorphous-crystalline phase transition when exposed to beam irradiation and *in situ* heating. Examination of this transition has shown it to be cyclable under a beam dose of $< 25\ \mathrm{pA \cdot cm^{-2}}$ and a maximum temperature not exceeding 800°C. This phase transition has also been shown to be induced by heating alone, and by laser irradiation. Room temperature and temperature-dependent powder X-ray diffraction studies support the reported electron microscopy and diffraction results. The temperature-induced behaviour for nano-confined $Sb_2Te_3$ and SnSe also been tracked and evidenced by combined differential scanning calorimetry and thermogravimetric analysis measurements. Here, we report evidence of an unprecented suppression in melt point of nano-confined $Sb_2Te_3$ in comparison with the bulk ($\sim 80$°C), which persists through heat cycling of the material.

Finally, collaborative work with J. Viner and D. Smith from the University of Southampton in growing SWCNTs across slits in etched silicon nitride are presented. This work follows the development of the substrate and synthesis process - to reproducibly grow defect-free single walled carbon nanotubes - through to the successful filling and analysis of these suspended carbon nanotubes. The quality of the grown samples has been repeatedly confirmed. Latter experiments branched into the filling of these grown carbon nanotubes, with a view to characterising them via Raman spectroscopy and Rayleigh scattering. Intial selected area electron diffraction results of the successful filling of these thin bundles of single walled carbon nanotubes with $Sb_2Te_3$ are presented alongside the complementary data for bundles of $Sb_2Te_3$@SWCNTs grown here at Warwick.

# Nomenclature

The next list describes several abbreviations and symbols that will be later used within the body of the document.

### Abbreviations

1D One-Dimensional

2D Two-Dimensional

3D Three-Dimensional

ABF Annular Bright Field

AC Aberration-Correction (Corrected)

ADF Annular Dark Field

AIMD *ab initio* Molecular Dynamics

AIRSS *ab initio* Random Structure Searching

ARM Atomic Resolution Microscope

BF Bright Field

CL(1) Condenser Lens (Aperture 1)

CNT(s) Carbon NanoTube(s)

CSVT Close Space Vapour Transport

DFT Density Functional Theory

DSC Differential Scanning Calorimetry

DWCNT Double Walled Carbon NanoTube

ED Electron Diffraction

EDX/EDS Energy Dispersive X-ray Spectroscopy

EELS Electron Energy Loss Spectroscopy

EM Electron Microscope (Microscopy)

FFT Fast Fourier Transform

FIB Focused Ion Beam

HAADF High Angle Annular Dark Field

HDR-ED High Dynamic Range - Electron Diffraction

HR-TEM High Resolution Transmission Electron Microscope (Microscopy)

MD Molecular Dynamics

MEMS MicroElectroMechanical System

MWCNT Multi-Walled Carbon NanoTube

nC nano-Confined

PCM Phase Change Material

RDF Radial Distribution Function

SADP Selected Area electron Diffraction Pattern

SAED Selected Area Electron Diffraction

SEM Scanning Electron Microscope (Microscopy)

STEM Scanning Transmission Electron Microscope (Microscopy)

SWCNT Single-Walled Carbon NanoTube

TEM Transmission Electron Microscope

TGA ThermoGravimetric Analysis

UHV Ultra-High Vacuum

VPT Vapour Phase Transport (Transported)

XRD X-Ray Diffraction

## Crystallographic Notations

$\alpha, \beta, \gamma$ Lattice Angles

$\phi_n$ Diameter of SWCNT Diffraction Ring "n"

$\theta_{obj}$ Semiangle of Collection of the Objective Lens

hkl Miller Indices

uvw Real Space Indices

(n,m) Chiral Indices

$\theta_c$ Chiral Angle

$\theta$ Angle of Incidence

[uvw] Direction in the Basis of the Real Lattice Vector

$<$ uvw $>$ Set of all directions equivalent to [hkl]

(hkl) Plane Orthogonal to the Reciprocal Lattice Vector

{hkl} Set of all planes equivalent to (hkl)

$\mathbf{s_{uvw}}$ Lattice Vector

$\mathbf{g_{hkl}}$ Reciprocal Lattice Vector

$d_{hkl}$ Interplanar Spacing in Crystals

$R_{vdW,C}$ van der Waals Radius of Carbon

$d_{SWCNT}$ Diameter of SWCNT

a,b,c Lattice Constants

$d = d_{hkl}$ Interplanar Lattice Spacing

## Number Sets

$\mathbb{C}$ Complex Numbers

$\mathbb{R}$ Real Numbers

$\mathbb{Z}$ Integer Numbers

## Other Symbols

$\Delta E$ Change in Energy of Electrons

$\Delta I$ Variation in Lens Current

$\Delta V$ Fluctuation in Accelerating Voltage

$\Delta z_c$ Defocus Spread

$\kappa$ Chromatic Parameter

$\lambda$ Wavelength

$\chi(\theta)$ Total Geometrical Wave Aberration Function

$\Delta G$ Change in Gibbs Free Energy of a System

$\omega, \bar{\omega}$ Complex Angles

$\phi_c$ Contact Angle

$\psi_{ep}(\omega)$ Complex Exiting Electron Plane Wave

$C_1$ Defocus of the Lens

$C_3/C_S$ Constant of Proportionality of Spherical Aberration

$C_C$ Chromatic Aberration Coefficient

$E_0$ Incident Energy of Electrons

$r_{chromatic}$ Radius of Image Formed due to Chromatic Aberration

$r_{min}$ Minimum Resolvable Separation

$r_{spherical}$ Radius of Deviation of Beam due to Spherical Aberration

$t(\omega)$ Complex Phase Contrast Transfer Function

$T_m^{\infty}$ Melting Temperature of the Bulk

$T_m^{nC}$ Melting Temperature of Nano-Confined Material

$T_m(x)$ Melting Temperature of Particle of Given Diameter

$T_r$ Temperature of Recrystallisation

$T_s$ Temperature at the Sample

$V_c$ Critical Voltage

| | |
|---|---|
| $\Delta G_{ac}$ | Change in Gibbs Free Energy between Amorphous and Crystalline Phases (per unit volume) |
| $\rho$ | Density |
| $\rho_s$ | Density of Solid |
| $\sigma$ | Electron scattering cross-section |
| $\sigma_{ac}$ | Surface Energy of Amorphous-Crystalline Interface |
| $\sigma_{sl}$ | Surface Energy of Solid-Liquid Interface |
| $l_j$ | Spin Orbital Quantum Number |
| $n$ | Principal Quantum Number |
| A,B,C | Antoine Coefficients |
| d | Spacing between diffracting planes |
| $H_f$ | Latent Heat of Fusion (Bulk, per gram of material) |
| $I_0$ | Lens Current |
| J | Thermionic Emission Current Density |
| P | Pressure |
| T | Temperature |
| $V_0$ | Accelerating Voltage |
| x | Diameter of Particle |

## Physical Constants

| | |
|---|---|
| $\lambda_e$ | Relativistic Wavelength of Electron |
| $m_e$ | Mass of electron |
| $m_o$ | Rest Mass of Electron |
| $p_e$ | Momentum of electron |
| h | Planck's Constant |

# Chapter 1

# Introduction

## 1.1 Introduction

The field of electronics has undergone significant advancement over the last decade, with developments being made in optical data storage [1, 2], micro-thermoelectric devices [3–7], photovoltaics [8–11], and batteries [12, 13], both academically and commercially. The desire for increasing the capability and applications of electronics has seen the growth of nancomposites, and components at the nanoscale [14–16]. However, whilst they are powerful, devices on this scale push beyond the resolving limitations of optical microscopy. Therefore, we must turn to Electron Microscopy (EM) to analyse these nanostructures. Although this allows these materials to be visualised at the atomic level, it also introduces its own issues and considerations, such as the effect that irradiation under the electron beam will have on the material. This thesis investigates the structures that phase change materials (PCMs) form, when they are nano-confined (nC) inside single walled carbon nanotubes (SWCNTs), and how this affects the properties in relation to the bulk. A particular focus, beyond cataloguing the encapsulated crystals, has been made on their temperature-dependency and tracking the characteristic phase changes via *in situ* electron diffraction. Therefore, to fully appreciate the impact that nano-confinement has on these PCMs, we must first understand the background and literature behind SWCNTs, bulk PCMs, and encapsulated nanowires.

## 1.2 Single Walled Carbon Nanotubes

Since the discovery of SWCNTs in 1993, there have been numerous strides in the progression of their size, purity, and improving large scale growth processes [17–21]. A variety of methods for the synthesis of SWCNTs have been developed. Many of these have proven to be appropriate for efficient and reliable large scale production, including carbon arc, laser ablation, and chemical vapour deposition techniques. A common identifier for CNTs is by the method of fabrication and the catalysts that these processes employ. For example, the "HiPCO$^{TM}$" process utilises a high pressure carbon monoxide gaseous catalyst, whilst "CoMoCAT$^{TM}$" employs a supported catalyst containing cobalt and molybdenum [21–26].

Numerous studies have been carried out on the unique thermal, electrical, and mechanical properties of SWCNTs [2, 3, 6, 12, 27, 28]. SWCNTs can be either metallic or semi-conducting, and are structurally robust up to temperatures of 1400 K in vacuum [16], whilst having highly specific surface areas and diameters. They are also stable under electron beam irradiation, provided the beam dose conditions are moderate and below the 86 keV threshold for knock-on damage - the dominant mechanism for beam-induced damaged to SWCNTs, as discussed in Section 2.2.5 [6, 25, 29, 30]. Furthermore, the electronic properties of the nanotubes can be modulated by the presence of a magnetic field, such that increasing the magnetic flux results in the oscillation of the energy-band structure of the SWCNT from metal to semiconductor [31]. In combination, these properties make SWCNTs suitable for a wide range of uses across diverse areas of study, such as energy applications, structural materials, and microelectronics [3, 27, 32, 33].

In the context of this research, these properties - and the structural conformation and internal van der Waals surface - make SWCNTs particularly suitable as confining structures for investigations into the properties and structural transformation of encapsulated materials. Therefore, combining the versatile properties of SWCNTs as confining components and the fact that nano-confinement increases the stability of the encapsulated structures, it is unsurprising the interest that this area of materials science has amassed.

Due to the underlying graphene lattice structure of the walls of the SWCNTS, accessible diameters are highly specific. These diameters are defined by the chiral indices (n,m), which assigns values to the hexagonal constituents of the graphene lattice from an arbitrary starting point, as depicted in Fig. 1.1 (a). The chiral indices are confined to taking integer values, with the additional constraint that ($0 \leq |m| \leq n$) [19, 20]. Therefore, the diameter of a given SWCNT ($d_{SWCNT}$) is defined by the

relation,

$$d_{SWCNT} = \frac{a}{\pi}\sqrt{n^2 + m^2 + nm}, \tag{1.1}$$

where a = 2.46 Å for a SWCNT, due to the carbon-carbon bond lengths in the underlying graphene lattice [19, 26, 34].

In turn, this identifies the conformation associated with a SWCNT of a given diameter [26, 34], since each combination of (n,m) values has a characteristic angle through which the lattice is rolled to attain the SWCNT. This angle is known as the chiral angle $\theta_c$ (Fig. 1.1 (a)), and is defined by the relation,

$$\sin(\theta_c) = \frac{\sqrt{3}m}{2\sqrt{n^2 + m^2 + nm}}. \tag{1.2}$$

The relationship between the rolling of monolayer graphene and the resulting conformation of the SWCNT is depicted in Fig. 1.1 (a) and (I). In turn, the conductive properties of SWCNTs are linked to the chiral indices of the honeycomb lattice of the SWCNTs, such that,

$$(n - m) = 3i \left\{ \begin{array}{l} i = \mathbb{Z}, \text{ metal.} \\ i \neq \mathbb{Z}, \text{ semicond.} \end{array} \right\}, \tag{1.3}$$

which is how we are able to access both metallic and semi-conducting applications for the SWCNTs (Fig. 1.1 (a)), where $\mathbb{Z}$ is mathematically defined as the ring of integers, and includes zero.

Once these relations have been taken into account, the final incorporation of the van der Waals radius of carbon ($R_{vdW,C}$ = 1.77 Å) gives the interior and exterior diameters of the SWCNT, with a specific chirality [35]. The van der Waals forces between nanotubes acts in a similar way to the binding of graphene monolayers. In multi-wall carbon nanotubes (MWCNTS), this is $\sim$ 16 kPa, which is the shear stress that can overcome the bundling of these nanotubes. However, for SWCNTs, it is on the order of $\sim$ 100 MPa, such that ultrasonication or similar is required to effectively separate them [36].

The three general chirality types of SWCNTs present as having differing atomic distributions at their walls in high resolution transmission electron microscopy (HR-TEM) imaging, as shown in Fig. 1.1 (b-d). The zig-zag, chiral, and armchair SWCNTs have distinct allowed chiral indice combinations - (n,0), (n,m), and (n,n), respectively (Fig. 1.1) [19, 20, 37]. Due to the relationship between the chiral indices (n,m) and the chiral angle ($\theta_c$), as given in Eq. 1.2 and depicted in Fig. 1.1,

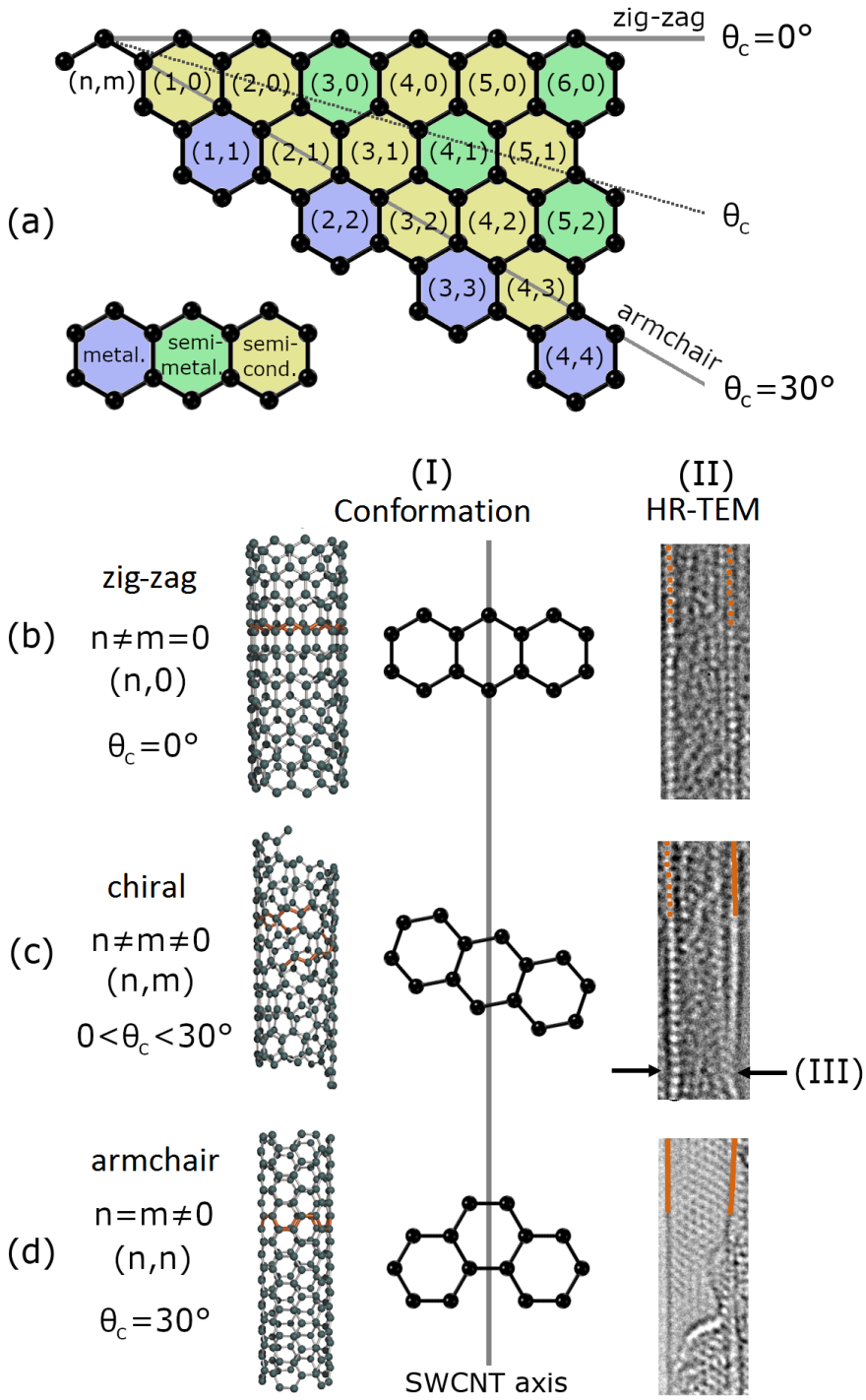


Figure 1.1: The effect of the chirality and conformation of a SWCNT on the appearance in HR-TEM imaging. (a) How the conformation (n,m) and conductive properties of the resulting SWCNT depends upon the angle (chiral angle, $\theta_c$) and circumference of the rolled graphene layer. The three general chirality types - (b) zig-zag, (c) chiral, (d) armchair. (I) The arrangement of the hexagonal lattice with respect to the SWCNT axis results in varying atomic spacings at the SWCNT walls, which (II) appear as lines or distinct dots in HR-TEM imaging. (III) A spontaneous constriction in the wall of an unfilled chiral SWCNT.

each chirality type therefore has a different orientation of the underlying honeycomb lattice of carbon atoms with respect to SWCNT axis - where $\theta_c$ is orthogonal to the SWCNT axis, as depicted in Fig. 1.1 (a). Therefore, the atom spacings at the walls of the SWCNT - when viewed in the 2D projection of HR-TEM imaging - appear differently, as illustrated in Fig. 1.1 (II). For zig-zag SWCNTs, the atom columns at the walls are sufficiently spaced so as to be distinguishable from one another, which gives the appearance of dotted chains at both walls in HR-TEM imaging, as depicted in Fig. 1.1 (b-II). In contrast, the atomic columns at armchair SWCNTs walls are so close together that they cannot be resolved, with both walls appearing as continuous lines in HR-TEM images, as shown in Fig. 1.1 (d-II). Due to the angle of the lattice in the chiral SWCNT, one wall appears as a line, whilst the other has clear atomic dots. This can be seen in the right and left walls, respectively, of the chiral SWCNT depicted in Fig. 1.1 (c-II). This distinction between the appearance of the SWCNT walls allows for potential conformations to be identified from atomic resolution images, by taking into account the diameter and the wall appearance.
When used in conjunction with electron diffraction the precise (n,m) conformation of the SWCNT can be established from the specific reflections [38, 39]. In order for this to be achieved to a high level of accuracy, the SWCNT of interest should be analysed over the maximum length possible for the imaging conditions. This is due to the occurence of spontaneous shrinking and twisting of SWCNTs, which can cause the diameter of the SWCNT to appear as wider or narrower over short lengths. This phenomenon occurs even when they are unfilled [40], as indicated in Fig. 1.1 (III) where a clear constriction can be seen in the diameter of a chiral SWCNT with respect to that of the rest of its shown length. Additionally, if a chiral SWCNT (Fig. 1.1 (c)) is tilted, then atom spacings will only be resolved on one wall of the SWCNT in HR-TEM imaging - much akin to the grooves on a screw.
This research into SWCNTs utilises two different types of SWCNTs in order to access a wider range of diameters and chiralities. SWCNTs from SWeNT are the thinner of the two, with tubes typically having diameters in the range $(0.7 - 1.3)$ nm, and with a batch of SWCNTs having an average diameter of $\sim 1.0$ nm, as quoted by the suppliers of the SWeNT SWCNTs [41]. In contrast, NanoIntegris (NI) SWCNTs have diameters spanning the $(1.2 - 1.7)$ nm range, with a mean diameter of 1.4 nm [42]. Both types of SWCNT have lengths in the 100 nm $- 4$ $\mu$m range, with a mean length of 1.0 $\mu$m. Further specifications and additions are discussed in Section 2.1, as well as the incorporation of as-supplied batches of high-purity (6,5) SWCNTs.
Whilst the size of SWCNTs makes them highly interesting subjects for both research and technological applications, this does necessitate the careful inspection of safety

considerations for working with SWCNTs from an experimental standpoint. Section 2.1 will further handle the particular relevance of this to the research presented in this thesis. These include possible carcinogenic and genotoxic effects. Several studies have been carried out on the long- and short-term effects of the inhalation of a variety of SWCNTs and MWCNTs on animals and their associated effects on cells [32, 43–47]. Despite this, there are very few definitive results on the effects, reversibility and implications of exposure to CNTs, especially over prolonged time periods. Therefore, caution must be exercised by anyone working with SWCNTs, including advisement to and responsibility for the well-being of potential bystanders.

## 1.3 Phase Change Materials

"Phase Change Materials" (PCMs) is the moniker given to materials that possess the ability to absorb, or release, large amounts of latent heat when undergoing a state or phase transition [48, 49]. Such properties are highly exploitable, and have been extensively researched and documented for the bulk forms [50–54]. Furthermore, these materials can possess significantly modified attributes either side of the phase transitions [55–57]. Generally, this transition will have a temperature-dependency, and will involve a change in the physical state of the material [58–61].

Due to this characteristic phase transition behaviour, applications for PCMs span a wide range of markets and scientific disciplines, from biotechnology and medicine [62, 63] to textiles and construction [64–71] to energy harvesting and storage and quantum computing [72–79].

At present, the largest commercial market for PCM use is in building materials and construction [66]. However, research into PCMs is largely driven by the growing technological demand for improved high-density, non-volatile memory and energy storage [49]. Indeed, the observation that the phase transition can be induced by beam irradiation and laser pulsing in some PCMs - reviewed and illustrated quite nicely by Raoux et. al [74] - has only heightened interest in this area of scientific and commercial research [51, 53, 54, 80]. The reliability and specificity of the latent heat properties of these materials make them natural energy storage devices: a direct parallel can be drawn between the storage and release of electric energy in rechargeable batteries, and the behaviour of PCMs in relation to thermal energy [68].

PCMs can, rudimentarily speaking, be placed into one of two over-arching classifications - organics and inorganics [81]. The former are noted for being - for the most

part - chemically stable, predictable, non-toxic, and non-corrosive, with excellent melting and freezing properties [70, 82]. However they can also be flammable and very expensive [75, 83]. Organic PCMs include alcohols, lipids, glycols, and hydrocarbons (with the melt point being linked to the length of the hydrocarbon chains) [84, 85], which can be further sub-categorised into paraffins and non-paraffins. Meanwhile, the inorganic PCMs tend to be cheaper, more readily available, and possess higher thermal conductivities and densities, whilst also being easier to work with [70, 73]. These properties form the basis behind why inorganic PCMs are the primary focus of the work presented in this thesis. This group of materials can be broadly classified as being salt hydrates, and includes the extensively studied GeSbTe (GST) system [49, 51, 52, 54, 61], $Sb_2X_3$ chalcogenides (X=Te,Se) [1, 86, 87], and binary systems such as GeTe, SnTe, and SnSe [9, 88–91]. However, whilst inorganic PCMs possess comprehensively documented properties and sharp melt points, care must be taken during heating, as they are more susceptible to phase separation and incongruent melting than organics - both during growth and temperature cycling [48, 92].

The requirements of the system - such as working temperature, conductive behaviour, tensile strength - and application for which it shall be used dictate the precise chosen PCM [66, 85]. High purity PCMs have narrow melting ranges, and distinct characteristic properties [83]. In isolation, these can be used in highly specific applications. However, an increasing interest is also being taken in the layering of such PCMs, and the effects of combining their properties. In particular, promising results have been observed in the field of technological applications, such as PCMs for rapid phase change memory and data and energy storage [10, 80, 93–98]. An insightful and in-depth review of applications for GST-PCMs in non-volatile memory, neuromorphic computing, and spatial light modulation technologies - amongst others - has been written by Guo et. al [54].

In the context of the key PCMs studied in this thesis, the properties of SnSe and $Sb_2Te_3$ have already been extensively catalogued. In its bulk form, SnSe is known to be a narrow band-gap semiconductor, and has proven applications as a low-cost photovoltaic, and in memory-switching devices [9, 91, 99, 100]. $Sb_2Te_3$ possesses similarly well-documented properties for applications in technology and devices in its bulk form [10, 86, 95, 101, 102]. Therefore, with the progression of technological advancement to smaller and smaller physical scales, the future of research into such PCMs appears to lie at the nanoscale [79, 103–107]. In particular, this raises interesting questions as to how this alters the range of structures accessible for a material, but also whether the associated properties for these PCMs persist or change [73, 74].

## 1.4 Encapsulated Nanowires

Encapsulated Nanowires - sometimes referred to as "Extreme Nanowires" [108] - have garnered significant interest, particularly in relation to the use of quasi-one-dimensional carbon nanotubes (CNTs) as confining components [109, 110]. The unique properties of SWCNTs - as introduced in Section 1.2 - make them not only worthy of study in their own right, but also particularly suitable for investigations into the properties and structure transformation of nano-Confined Phase Change Materials (nC-PCMs), in addition to the encapsulation of materials in general. This is due both to the properties of the CNTs, and the scale of the resulting nano-confined structures. The van der Waals forces at the internal surfaces of the SWCNTs act to constrain the encapsulated material. These confined surfaces can have cross-sections down to 1 $nm^2$. This results in structures that can often vary significantly from that of the bulk form of the material [34, 56, 110–112].

Extreme nanowires and encapsulated materials as small as one to three atoms in cross section are being formed by a variety of single elements including S, Ag, Au, As and Te and, increasingly, from binary systems including CsI, HgTe, KI, SnTe and now SnSe [90, 113–124]. SnSe is of particular interest as it belongs to the group of so-called "Phase Change Materials", alongside $Sb_2Te_3$. Such materials have highly exploitable latent heat properties, and can possess significantly modified attributes either side of a temperature-dependent phase transition, which have been extensively documented in their bulk forms. Therefore, the encapsulation of these two materials in particular raises interesting questions as to the alteration or persistence of such properties, and how this relates to the potentially novel structures that form as a result of nano-confinement. The procedures and fundamentals towards answering these questions is what forms the grounding of this thesis.

In all observed and recorded cases for encapsulated materials so far, profound effects are noted in both fundamental changes in crystal growth and phase formation. Polymerization of distinct molecules has been observed in the case of S, P and As [116–118, 125], whilst Te forms continuous chains or coils [60]. Furthermore, unprecedented new crystalline single, zig-zag and double zig-zag chain forms have been reported for semiconductors including SnTe [119, 120] and SnSe [124, 126].

Even between these dramatic low dimensional forms and more conventionally observed 'bulk'-like nanowire structures of the same materials, there exists a critical size domain in which new crystalline forms are possible. Such systems exhibit novel

coordination and novel symmetry, which can produce profound changes in physical properties. This is true for Extreme Nanowires formed at or below this critical size. For the ultimate scale (i.e. single atomic chain) these include novel metallicity in sulphur [116]; $P_4$ and $As_4$ polymerisation [117, 118]; Peierls instabilities and distortions - distortion of the periodic lattice, specifically of a 1D crystal, arising from the oscillation of atomic positions - in Te [60, 127, 128]; and enhancement of the Seebeck coefficient in SnTe when the nanowire is modelled in isolation [119].
When the atomic thickness reaches 2-3 atoms, novel symmetries emerge [108, 114, 115] which give rise to Raman measurable optical phonons and optical spectra that cannot be reproduced in the bulk structure [121]. Enhancements to the semiconducting band gap - as observed in HgTe, which is a semimetal in its bulk form but semiconducting with a bandgap of at least 1.2 eV in its low-dimensional form - [89, 114, 126], and improvements to thermoelectric characteristics are also anticipated by theory [7, 15, 60, 119, 123, 129]. However these properties need to be separated from, or incorporated with, the properties of the embedding carbon nanotubes. Given the highly selective nature of each structure, with respect to the diameter range of the encapsulating SWCNT, it is possible to obtain a specific form by filtering out the desired chiralities, paying close attention to the conducting form of the host nanotubes [24, 130].
The size, and form, of the nano-confined structures is dictated by $d_{SWCNT}$ [34]. As stated in Section 1.2, the calculation of the diameter of SWCNTs that can accommodate the identified filling structure must also take into account the van der Waals radius of carbon ($R_{vdW,C} = 1.77$ Å) [35]. By combining atomic imaging and compositional analysis, it is possible to accurately model, and simulate images of, the nano-confined crystals inside SWCNTs [131, 132]. Furthermore, the spontaneous shrinking and twisting of SWCNTs can be observed in HR-TEM imaging, and occurs even when they are unfilled [40]. Therefore, it is unsurprising that the structures that form can also cause deformations to the CNTs, such as in the case of a 2x1 nano-confined structure. Such contortions can be similarly tracked, and exploited, for 3D-like modelling and structural-reconstruction. In addition, this can be induced by *in situ* beam irradiation [56].
The growth of nanowires on such a small physical scale presents unique challenges for high performance electron microscopy and spectroscopy, as these must perform at a sensitivity level of a single atom. To date, the lack of universally-suitable and simple methods for efficiently and non-destructively characterising extreme nanowires is a key limiting factor in the rate of progression of this area of materials physics and engineering [133]. It is important to understand these limitations,

as the research presented in this thesis is based around the experimental synthesis, imaging, and characterisation of Extreme Nanowires by electron microscopy - particularly High Resolution Transmission Electron Microscopy (HR-TEM), Scanning Transmission Electron Microscopy (STEM), and Scanning Electron Microscopy (SEM). Additional work by collaborators on the study of encapsulated nanowires - inside both SWCNTs and Boron Nitride nanotubes - with THz, vibrational, and Raman spectroscopy provides complementary results [115, 134–136]. For instance, the Resonance Raman studies on HgTe@SWCNTs, conducted by Smith et. al using a customised optical configuration, depicted the necessity of resonant enhancement for the successful observation of Raman scattering from these 1D systems [133]. Further characterisation techniques, such as Differential Scanning Calorimetry (DSC), Thermogravimetric Analysis (TGA), and X-Ray Diffraction (XRD) - can also provide an insight into the thermal conduction and phase properties of the nanocomposites [71, 72, 92, 117, 118, 125, 137, 138].

Due to the small physical scale of these encapsulated nanowires, we must also consider how the radiation imparted by such analysis techniques might affect these structures [29, 139, 140]. Whilst such considerations differ significantly to those required for, say, biological and organic specimens, the sub-nanometer scale of some of these encapsulated structures present their own issues [141, 142]. Prolonged exposure of the encapsulated nanowires to the electron beam has been shown to have adverse effects on certain nano-confined fillings [56, 60, 120], such as the dissociation of nano-confined SnSe to clusters (see Section 2.2.5). Considerations for, and exploitation of, the irradiation effects on the materials are further discussed in the context of existing and interesting literature in the relevant introductory and methodological portions of this thesis.

Further to this, an observable depression in the melting temperature of certain materials when the size of the structures is compressed has long been established, such as a depression of 600 K for gold nanoparticles [143]. Indeed, even water has shown to possess extreme phase transition temperatures once confined [144]. Similar studies into diameter-dependence of the electronic, galvanomagnetic and thermoelectric properties of individual $Sb_2Te_3$ nanowires, with diameters in the range of (20 - 100) nm, have already been conducted by Zuev et al., at varying temperature [129]. However, not much rigorous experimentation has been conducted on materials once down to the scale of those is this research, confined or otherwise. Such investigation could, in the most fundamental instance, provide insight into the thermal durability of the nanowires.

The continuing research into encapsulated nanowires and 1D materials is largely

driven by the growing technological demand for improved high-density memory storage and electronic components [79, 88, 111, 112, 145–147]. A particular focus is now being made on investigations into the variation of the structure of the encapsulated material as a function of the diameter of the confining nanotube, and how this can affect the properties of the resultant materials. Initial studies into the induced phase change behaviour of the nC-PCMs are encouraging [56], which is complementary to observations of local atomic ordering in metallic glasses [148]. Further investigations into the properties of such nanocomposites, such as the photoconductivity of thin films, shows promise for device applications [15, 149, 150].
Therefore, the encapsulation of SnSe and $Sb_2Te_3$, amongst others, offers a distinct contrast to the previously employed coventional crystalline filling materials as they are PCMs [48, 151]. The properties of bulk SnSe have already been extensively catalogued, with current applications ranging from photovoltaics, to energy harvesting, to memory-switching devices [9, 91, 99, 100]. $Sb_2Te_3$ possesses similarly well-documented properties for applications in technology and devices [10, 86, 95, 101, 102]. Therefore, the nano-confinement of such compounds offers another dimension to not only the investigation of how encapsulation alters the range of structures accessible for a material, but also into how the associated properties change or develop [73, 79].

## 1.5 Thesis Outline

The research presented in this thesis is primarily based around the experimental synthesis, imaging, and characterisation of Extreme Nanowires by electron microscopy - particularly High Resolution Transmission Electron Microscopy (HR-TEM), Scanning Transmission Electron Microscopy (STEM), and Scanning Electron Microscopy (SEM). Additional work by collaborators has commenced on the study of these materials using vibrational spectroscopy and Raman spectroscopy. Further characterisation techniques, such as Differential Scanning Calorimetry (DSC), Thermogravimetric Analysis (TGA), and X-Ray Diffraction (XRD) - can also provide an insight into the thermal, conduction, and phase properties of the nanocomposites.
This thesis investigates the structures that form when different phase change materials are nano-confined, and how this may affect the phase change behaviour in relation to the bulk. This includes cataloguing the encapsulated nanowires via electron microscopy imaging, tracking the phase changes via *in situ* electron diffraction and characterising the temperature-dependency of such transitions. Whilst HR-(S)TEM

formed the primary analytical procedure, a range of techniques and systems were used to characterise the samples. These are outlined in detail in Chapter 2. Samples were deemed to have been successfully grown if both the stoichiometry was congruent with that of the bulk source material, and the filling fraction of SWCNTs with the desired PCM was relatively high ($> 40$ %). These results were then deemed reproducible if observed in at least three further samples using the same growth parameters - although the actual number of identical grown samples typically far exceeded that.

Chapter 3 presents the result of the nano-confinement of $Sb_2Te_3$ in diameters in the range $(0.7 - 2.1)$ nm. The nanocomposites are primarily characterised by high resolution electron microscopy imaging techniques, in combination with EDX compositional analysis. This culminates in the formation of a catalogue of modelled structures alongside atomic scale imaging. Later sections then go on to investigate the amorphous-crystalline characteristics, and how electron beam irradiation and heat treament affects the phase of the encapsulated structure. This is evidenced via *in situ* electron diffraction, which is supported by variable temperature powder X-ray diffraction investigations. Complementary differential scanning calorimetry (DSC) and thermogravimetric analysis (TGA) - heat flow through and mass loss in a sample, respectively - show an unprecendented depression in the melt point of the nano-confined $Sb_2Te_3$ material, when compared with the bulk.

Chapter 4 presents similar analysis for encapsulated SnSe. The comprised catalogue for observed and modelled nano-confined SnSe structures includes four new forms that has never been reported for SnSe before [124]. Diffraction analysis, and the observed response to beam irradiation and heat treatment, of the sample are presented. These prove complementary to DSC/TGA investigations on the material.

Chapter 5 presents SEM, TEM, and EDX studies of attempts, by J. Viner and D. Smith from the University of Southampton, to grow SWCNTs across slits in etched silicon nitride. Once the quality of the grown samples, and confirmation of their true SWCNT nature, had been repeatedly confirmed, later experiments branched into the filling of these grown CNTs, with a view to characterising them via Raman spectroscopy and Rayleigh scattering. Intial SADP results of the successful filling of these thin bundles of SWCNTs with $Sb_2Te_3$ are presented.

# Chapter 2

# Methods

## 2.1 Sample Growth

### 2.1.1 Carbon Nanotube Preparation & Handling

Handling of, and experimentation with, CNTs must be practiced under explicit safety considerations, taking into account the possible carcinogenicity and genotoxicity of CNTs, as initially outlined in Section 1.2. There have been several studies on the long and short term effects of inhalation of a variety of single and multi-walled carbon nanotubes on animals and effects on cells [32, 43–47]. However, there are very few definitive results on the effects, reversibility and long-term implications of exposure to CNTs, especially over prolonged exposure. Therefore, caution must be exercised by anyone working with CNTs, including advisement and responsibility for the well-being of potential bystanders.

Several grades of ultra-high purity SWCNTs were utilised in this research, which provided access to $d_{SWCNT}$ values in the range $\sim (0.7 - 2.1)$ nm, with few outliers (Sections 3.2 and 4.2). This, relatively wide, range was achieved through the use of nanotubes from multiple sources (Fig. 2.1). The $\sim (0.7 - 1.1)$ nm diameter range was covered by the SWeNT SWCNTs, which cite as being comprised $>$ 90 % carbon ($<$ 10 % contaminants from growth), with $\geq$ 77 % carbon as SWCNTs (Fig. 2.1 (a-I)). SWCNTs with diameters $\sim (1.3 - 2.1)$ nm were supplied by NanoIntegris (NI), with $>$ 95 % carbon and $<$ 3.5 % catalyst impurity (Fig. 2.1 (b-I)). High-purity (6,5) chirality SWCNTs (Section 1.2) - commercially identified as CHASM (SGi65) SWCNTs - boasted a 40 % minimum population of single-chirality CNTs, with a population average diameter of $\sim$0.8 nm, and $\geq$ 95 % carbon as carbon nanotubes (Fig. 2.1 (c-I)). The CHASM SWCNTs were primarily employed in the latter stages of this project.

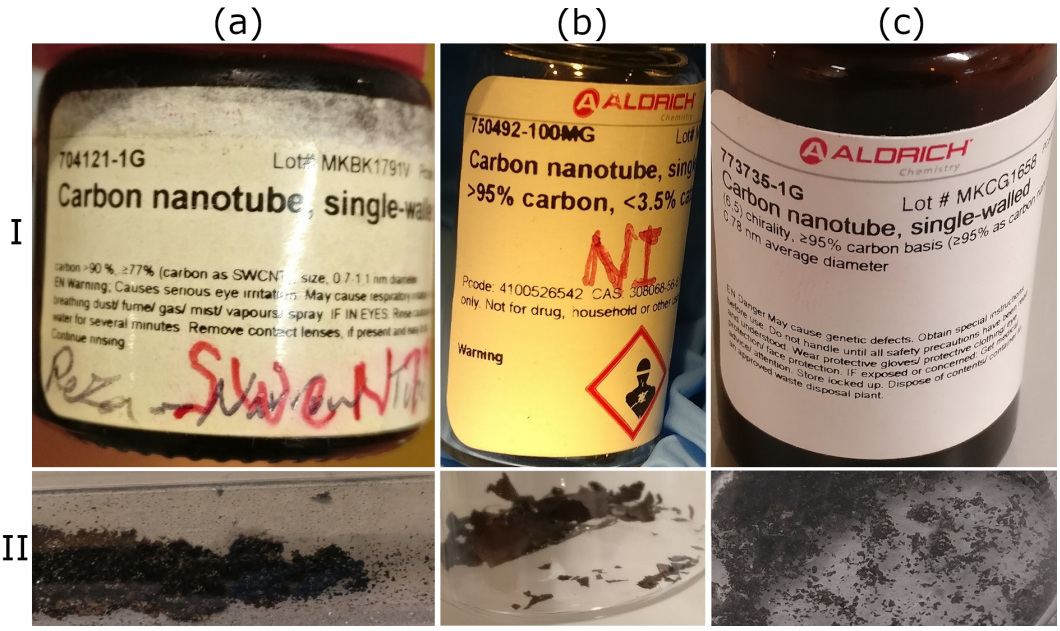


Figure 2.1: The different types of SWCNTs utilised in this research, as sourced from the supplier (Sigma Aldrich). The (a) SWeNT, (b) NI, and (c) CHASM SWCNTs were supplied in (I) sealed glass containers - with basic compositional details noted on the labels - as (II) powder or flakes.

CoMoCAT$^{TM}$ SWCNTs [25, 26] - originally supplied by SWeNT$^{TM}$ in USA - are now produced under the trademark CHASM$^{TM}$ in Canada using the same synthetic protocol. In the UK, Sigma Aldrich - which now trades under the brandname "Merck" - supplied first the SWeNT SWCNTs, and now the CHASM SWCNTs. The HiPCO$^{TM}$ NI SWCNTs were also sourced from Sigma Aldrich in the UK [25]. As depicted in Fig. 2.1 (II), the SWeNT (a) and CHASM (c) nanotubes were supplied in their powdered forms, whilst those from NI (b) were in sheets of "bucky paper" [26].

To ensure that the nanotubes were well-distributed and with minimal capped ends, it was necessary to pre-process them prior to filling. This comprised three main steps: sonication, cleaning, and gentle oxidation. The first step involves the dispersion of the as-supplied SWCNTs in chloroform via ultrasonication. This was achieved using a Cole-Parmer 750 W Homogenizer, pulsing repeatedly at 20 % power, 2 s on, 2 s off, for no longer than 10 min. This combination of pulsing and short time period limited damage to the SWCNTs, whilst ensuring maximum dispersion. This step is necessary since the van der Waals force (binding energy) between SWCNTs is on the order of $\sim$ 100 MPa, which can only be overcome by ultrasonication, or a similar, as outlined in Section 1.2 [36].

The solution is then vacuum filtered through a hydrophillic 47 mm diameter nitrocellulose membrane from Millipore, with a pore size of 0.22 $\mu$m. The solution is 99 % filtered after a few seconds, and is washed down with chloroform. The resultant dry film is then peeled of the membrane and placed in a silica boat for oxidation. It is important that the dispersant is chloroform, since ethanol, or similar, breaks down the nitrocellulose membrane. This decreases the filtration rate, sometimes to zero, and causes the SWCNTs to become fused with the warped membrane.
By gently oxidating the SWCNTs at 400°C in air in a tube furnace for up to 30 mins, the closed caps on the end of the SWCNTs are opened. Whilst the CNTs are thermally stable to $\sim$ 1100°C, they have an oxidation threshold of $\sim$ 400°C in air [20, 24]. Therefore, it is important to oxidate the nanotubes at a low temperature for as short a time as possible, so as to avoid significant mass loss. This is the final step to prepare the SWCNTs for filling.
The powdered form of SWCNTs is much more efficiently processed for growth, since they are already well-dispersed - so require little or no sonication and filtration - and oxidate much more rapidly. Therefore, they require less time in the furnace, and far less processing overall. They are also far more suited to growth procedures where the SWCNTs and the filling material are combined. However, they are almost impossible to use for methods that require separation of the materials (Section 2.1.2), due to the high susceptibility of CNTs to static electricity. Therefore, the powdered nanotubes are also much more difficult to handle than the sheet form and far more likely to be aerolised. Thus, they pose a much higher risk to users.

### 2.1.2 Filling Procedures

There are two main methods for filling SWCNTs and producing encapsulated nanowires. This is particularly for SWCNTs and nano-confined materials of the dimensions that this research is concerned with. The first is capillary - or melt infiltration - filling [152–154]. This protocol requires the filling material and the pre-treated SWCNTs to be ground together thoroughly using an agate pestle and mortar, as the aim is to fill the SWCNTs from the melt of the desired material. Conventionally, a temperature of 100°C above the ambient melt temperature of the filling material is used. The infiltration and filling of the SWCNT cavity by the liquid material is driven, and dictated, by capillarity on the nanoscale [155, 156]. This theory is underpinned by nanofluidics and Laplace pressure assisted infiltration [157, 158]. On the nanoscale, the penetration of a liquid into a pore can occur provided that the Laplace pressure on the liquid droplet and the miniscus pressure in the capillary

are balanced, and that

$$r_d < -\frac{r_p}{\cos(\phi_c)}, \tag{2.1}$$

where $r_d$ and $r_p$ are the radii of the liquid droplet and the pore, respectively, and $\phi_c$ is the contact angle subtended by the miniscus of the liquid with the surface of the cavity [127]. For non-wetting liquids $\phi_c > 90°$ [158, 159]. This relation, and the macroscopic description for the increase of liquid penetration depth with the square root of time hold well for nanoscale pores larger than $\sim 5$ nm [127, 157]. However, once down to sub-5 nm cavity dimensions, particularly in the case of CNTs, significant deviations arise when trying to quantify penetration criteria and depths of the liquids [157, 160–162]. The theory and experimental realities of this protocol are discussed at length in work published by P. De Jongh and T. Eggenhuisen [154].

The second procedure is sublimation filling. Encapsulation is achieved via Vapour Phase Transport (VPT) of sublimed material along a temperature gradient (Fig. 2.2), and subsequent deposition inside SWCNTs. Therefore, a growth temperature above the ambient melt temperature of the bulk filling material is customarily utilised for sublimation filling [153, 163]. This method exploits the fact that the vapor pressure of a substance destabilises when it is exposed to high vacuum conditions. Therefore, the substance is more likely to undergo a direct transition, that neglects an intermediary liquid phase, than it would be at standard atmospheric pressure. Additionally, there is an increase in mobility and penetration of the filling material due to the use of the gas phase, which often results in samples with higher filling fraction yields, and lower contamination. The use of a high vacuum also reduces the possibility of incongruency in the system, and dissociation of the constituent material. Although, for some substances there exist no known conditions under which congruent sublimation occurs.

Due to the differing properties of each material some are inherently better, or only, suited to one filling protocol over the other. In some instances this can be divined from existing literature and analysis of published phase diagrams [9, 49, 146, 164–168], as previously stated. Other materials required comprehensive testing of the respective growth procedures in the lab before a method could be adequately applied. In all cases, rigourous experimentation is necessary to achieve the desired stoichiometry combined with a reasonable to high filling fraction - as determined by an observed combination of the number, and length, of SWCNTs filled with nano-confined material in ADF-STEM imaging. Occasionally, materials are encountered which do not culminate in adequate outcomes or samples, or proffer unrealistic timescales due to repeated failures. Whilst these samples do not present the initially desired result,

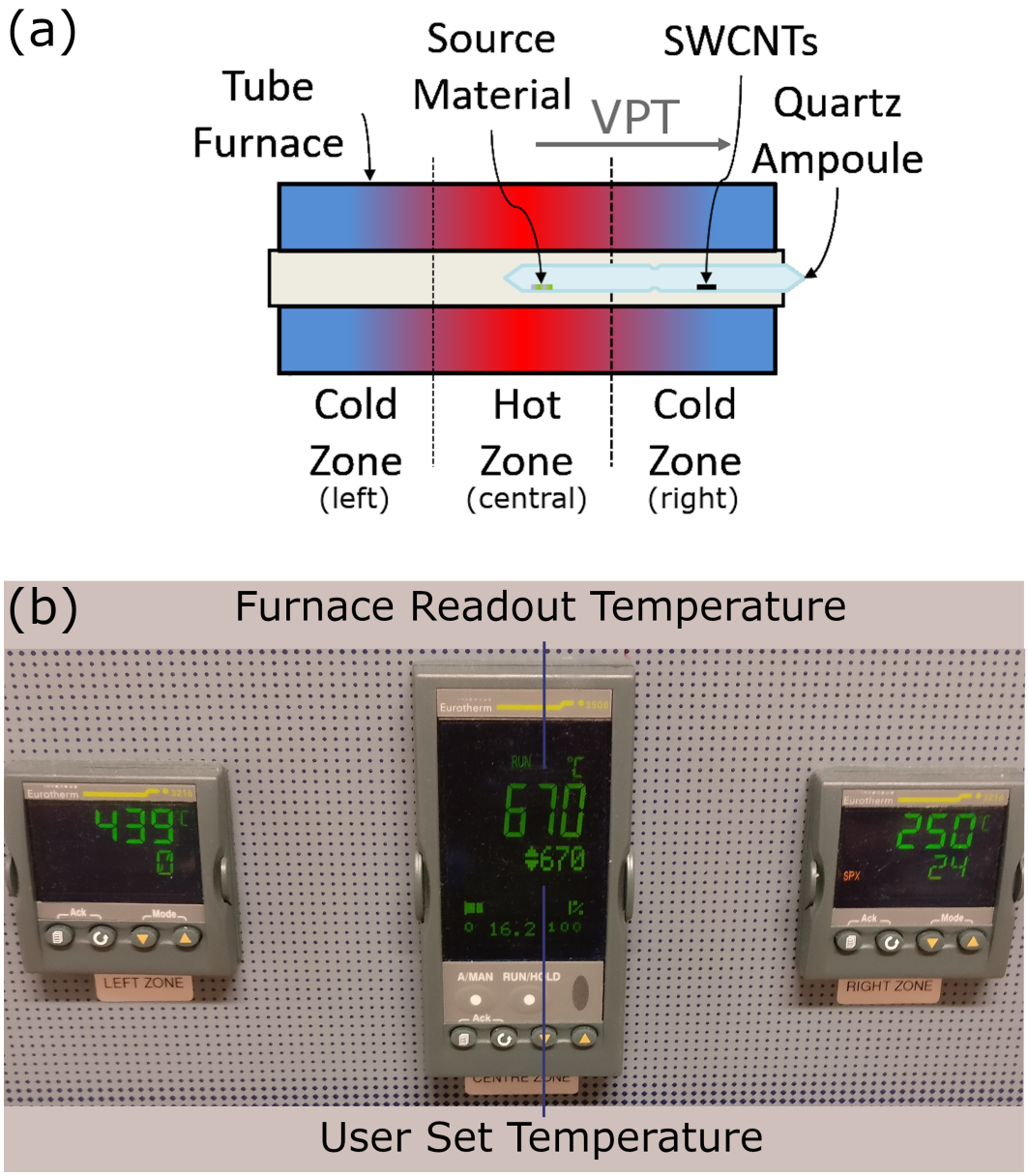


Figure 2.2: Schematic of procedural set-up used to fill the SWCNTs with the desired material by the sublimation method. (a) Diagram of the sample placement and temperature gradient inside a three-zone furnace for the growth of encapsulated nanowires via the sublimation procedure. (b) Representative "actual" (readout) and user set point temperatures for each zone (cool-left, hot-central, cool-right) on the three-zone furnace.

some interesting conclusions can be drawn from such occurrences, some examples of which have been presented in this thesis (Chapters 3 and 5).
Analysis of the phase diagrams for the filling materials gave good points of reference for what could be expected from the growth procedures. However investigations into their Antoine equations - experimentally obtained relations between the temperature and vapour pressure of a material, which will be discussed further in Section 2.1.3 - provided more accurate temperature ranges for the vacuum pressures used in this research [169]. In some cases, this analysis resulted in the use of growth temperatures outside those normally used in these methods, and resulted in samples with high filling fractions and the desired stoichiometries - such as those to be discussed in Chapter 4 for SnSe.
Due to the difference in approaches to the phase and temperature considerations of the two filling procedures, each requires a distinct ampoule design for growth (Fig. 2.3). The ampoules are primarily defined by the absence, or presence, of a constriction - or "neck" - in centre of the tube. The melt method utilises a single chamber ampoule (Fig. 2.3 (a)), as the material is ground together and encapsulation occurs at the material source. Conversely, the sublimation method requires a double chamber ampoule, with a neck separating the filling material - to be sublimed - and the SWCNTs (Fig. 2.3 (b)). This constriction not only focuses the vapour transported material, but also inhibits the SWCNTs from entering the first chamber. Furthermore, the single ampoules tend to be narrower than those utilised in the sublimation method, since we want to repress any instance of the vapour phase occuring in the melt procedure. Each chamber of the ampoules is $\sim$100 mm long. Both ampoules have an outer diameter of $\sim$15 mm, and an inner diameter of $\sim$10 mm. The neck is approximately 40 % narrower than the ampoule chamber.
In either procedure, the samples are annealed at the designated growth temperature for $\sim$ 72 h, to ensure the highest filling ratio possible [24]. To further reinforce this, a surplus of filling material is used over the SWCNTs. However, this does also cause an excess of external bulk material, which is indicated in the post-growth samples in Fig. 2.3. This remnant bulk material from the growth of the encapsulated nanowires generally forms large crystalline clusters on the walls of the ampoule and the outside of the SWCNTs. Therefore, additional processing steps must be carried out to purify the samples - as described in Section 2.1.5.
Once the source material has been placed at the desired position inside the respective ampoule, the ampoule is then evacuated to $\sim 10^{-6}$ mbar and sealed. The sealed sample is placed in the centre of a furnace. For melt filling, a single-zone furnace is sufficient to be able to control the growth and optimise the filling proportion of

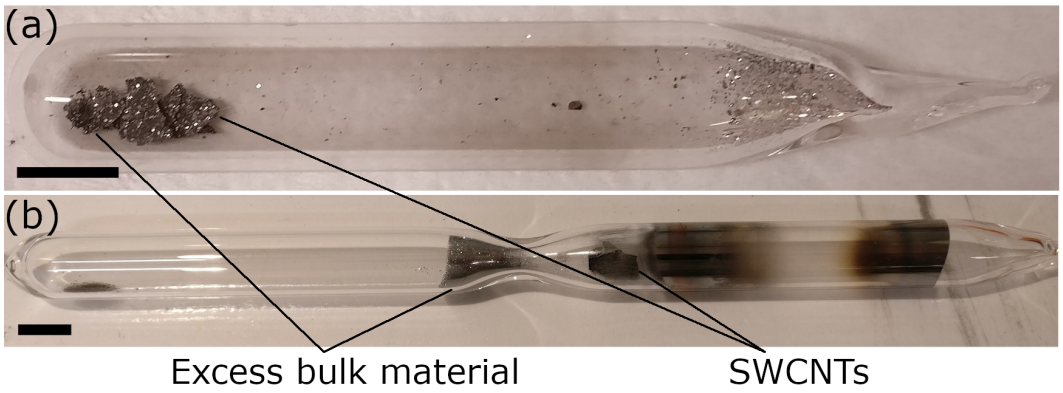


Figure 2.3: Ampoule specifications for the different growth procedures employed in this research. The (a) melt procedure utilises a single compartment ampoule, whilst the (b) ampoule for the sublimation method has two compartments. Excess deposition of bulk ("remnant") material is indicated. Scale bars are 10 mm.

the resultant nanocomposite. However, in the case of sublimation filling, it is more critical to control and monitor the temperature of the deposition zone - the right cold zone in Fig. 2.2 (a). Therefore, a three-zone furnace is far more appropriate. This not only ensures an optimum filling fraction, but also establishes a greater precedent for reproducibility.

To this end, it was also necessary to establish the discrepancy between the working, readout and set temperatures on the growth furnaces - the latter two of which are indicated in Fig. 2.2 (b). The temperature profiles for the furnaces used were checked using a combination of temperature gauges. These investigations for the three-zone furnace (Table 2.1) demonstrated the furnace to be calibrated correctly to the ambient temperature of the cavity, but was consistently $(16 \pm 1)$°C lower than the temperature of the sample, as measured by a contact thermometer (TechnoTerm 9400).

However, in the case of the single zone furnace, the ambient temperature of the centre of the furnace was shown to deviate slightly from the set temperature. This deviation scaled with the set temperature; at 100°C there was an observed deviation of $\sim 1$°C, which rose to $\sim 10$°C by 700°C. In addition, the temperature along the length of the furnace followed a parabolic curve, with a rapid drop off observed outside of the central hot zone (Fig. 2.4).

A similar phenomenon is observed in the three-zone furnace, if the two outer zones are set to a sufficiently low temperature. However, in the case of the three-zone furnace, this temperature gradient can be controlled and monitored by altering the set temperatures of the "cool" outer zones (Fig. 2.2 and Table 2.2). Thus allowing

for consistent and precise sample growth.

Furthermore, by sealing the ends of the furnace, we can limit air flow, ensure temperature stability, and force differential gradients. This is demonstrated in the four sets of temperature values given in Table 2.2, where "readout" and "set" refer to the indicated furnace values in Fig. 2.2 (b). If we look at (I) and (II) in Table 2.2, we see that the only difference between these two runs is the sealing of the left hand end of the tube. This small adjustment results in the "cool" left zone having a 150°C higher working temperature, and a temperature profile that is significantly skewed with respect ot the parabolic curve given in Fig. 2.4. As the outer zones are set at or below room temperature ($\sim 24$°C) in both cases - so the heating elements in these zones are essentially turned off - this temperature increase can be attributed to a decrease in the loss of heat out through the left end of the tube furnace, from the "hot" central zone. In contrast, only a minimal increase is also seen in the "cool" right zone, whose end remains open.

The readout values for the "cool" zones in (I) and (II) - and the right zone in (IV) - demonstrate how, when the heating elements in the outer zones are neglected, these zones still experience an elevation in working temperature due to heating in the central zone. The flow of heat through the three-zone furnace mirrors the temperature profile for the single-zone furnace given in Fig. 2.4 under these conditions.

However, if the "cool" zones are set to the same temperature as the middle zone - as in Table 2.2 (III) - we see that the readout values are consistent with the set point values to within $\pm 1$°C, even if the ends of the furnace are sealed. This demonstrates that the furnace is able to efficiently scale back the power to the heating elements, in order to stabilise and maintain a constant elevated "set" temperature. This is similarly illustrated in the left and central zone values in (IV), where both ends of

| Furnace Readout (°C) | Thermocouple (°C) | TechnoTerm 9400 (°C) |
|---|---|---|
| 480 | 478 | 495 |
| 500 | 499 | 516 |
| 525 | 525 | 541 |
| 550 | 551 | 567 |
| 575 | 575 | 580 |

Table 2.1: A calibration and temperature check conducted for the growth furnace. Two different temperature gauges were utilised. The thermocouple measured the ambient temperature, whilst the contact thermometer (TechnoTerm 9400) measured the temperature of the sample (ampoule). The thermocouple agreed with the read out from the furnace, whereas the contact thermometer placed the sample temperature at consistently $\sim 15$°C higher.

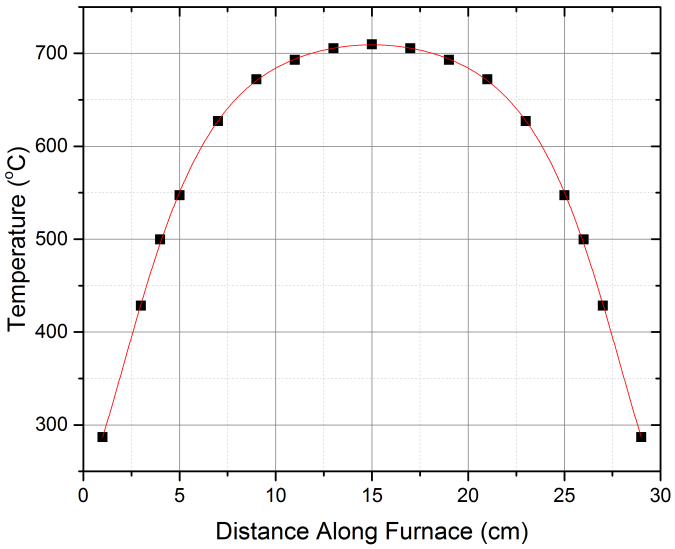


Figure 2.4: Temperature profile for the single zone furnace, when set to 700°C on the controls. The left and right openings (ends) of the furnace are at "0" and "30" centimetres, respectively.

| | Type | "Cool" Left Zone (°C) | "Hot" Central Zone (°C) | "Cool" Right Zone (°C) |
|---|---|---|---|---|
| I | Readout | 282 | 670 | 274 |
| | Set | 0 | 670 | 24 |
| II | Readout* | 439 | 670 | 281 |
| | Set* | 0 | 670 | 24 |
| III | Readout* | 671 | 670 | 670 |
| | Set* | 670 | 670 | 670 |
| IV | Readout | 598 | 700 | 271 |
| | Set | 600 | 700 | 100 |

Table 2.2: Indicative zone temperature readouts for the three-zone furnace and their corresponding set temperatures. * denotes where the far left end of the furnace has been sealed.

| Material | Structure | Space Group | $T_m$ (°C) |
|---|---|---|---|
| I | Orthorhombic | Cmca | 114 |
| AgCl | Cubic | $Fm\bar{3}m$ | 455 |
| $Sb_2S_3$ | Orthorhombic | Pbnm | 550 |
| $Sb_2Se_3$ | Orthorhombic | Pnma | 611 |
| $Sb_2Te_3$ | Rhombohedral | $R\bar{3}m$ | 629 |
| SnSe | Orthorhombic | Pnma | 861 |

Table 2.3: Basic melting temperatures ($T_m$) for the materials investigated over the course of this research, ranked by melting temperature and alongside their symmetry relations [182].

the tube furnace are open. The values in Table 2.2 (III) also illustrate how a flat temperature profile can be maintained across the three-zones.

### 2.1.3 Antoine Equations & Vapour Phase Investigations

When deciding upon a filling material, several aspects must be taken into account. An initial consideration is the upper limit for the sublimation temperature of the filling material imposed by the SWCNTs: $\sim$ 1100°C, as outlined in Section 1.2 and 2.1.1. Beyond this temperature, the nanotubes will begin to degrade, which can cause defects to form, or result in the destruction of the SWCNTs entirely [24]. Not only this, but even a temperature of 1000°C would make thermal analysis and temperature-dependence investigations much more difficult, due to the limiting constraints of many analytical systems. Therefore, only materials with designated growth temperatures below this threshold are appropriate for encapsulation inside SWCNTs (Table 2.3). Once it has been established that the standard melt temperature ($T_m$) of a material satisfies this constraint, then it is acceptable to continue with further investigation into its phase and temperature characteristics.
All of the materials investigated in this research have melt temperatures far below 1100°C, as outlined in Table 2.3. However, further investigation into the temperature and phase behaviour was carried out prior to growth, in order to try and ensure the quality and stoichiometry of the resultant sample. This included reviewing accepted phase diagrams [99, 166, 170–174], melt and sublimation vapor pressures [165, 175–177], and Antoine equations for each material [169, 178–181]. Whilst these published results are all experimentally obtained, Antoine equations, in particular, can vary significantly depending upon the specific conditions used. They take the general form of

$$\log_{10}(\mathrm{P}) = \mathrm{A} - \frac{\mathrm{B}}{\mathrm{T} + \mathrm{C}}, \tag{2.2}$$

where P is the vapour pressure, T is the temperature, and A, B & C are experimentally determined coefficients. The units for P and T are defined by the experimental parameters of the documented research, and so are explicitly linked to the values of the coefficients (Table 2.4). However, the parameters can be adjusted to provide alternative P and T units by using the relations

$$\mathrm{A}(\mathrm{P[Pa]}) = \mathrm{A}(\mathrm{P[bar]}) + \log_{10}(10^5), \tag{2.3}$$

and

$$\mathrm{C}(\mathrm{T[K]}) = \mathrm{C}(\mathrm{T[^\circ C]}) - 273.15, \tag{2.4}$$

to convert the coefficients from, in this instance,

$$(\mathrm{P}, \mathrm{T}) = (\mathrm{bar}, ^\circ \mathrm{C}) \ \rightarrow \ (\mathrm{Pa}, \mathrm{K}). \tag{2.5}$$

The conversion of coefficient "A" comes from the equivalency of 1 bar to $10^5$ Pa. The coefficient "B" requires no adjustment. These calculations have been conducted for the coefficients in Table 2.4 where the published Antoine equations were given in non-SI units.

Due to the dependency of these values on external factors, the equations are only valid within given temperature ranges. Therefore, these relations provide an insight into the sublimation behaviour of the bulk materials, under certain conditions. Given the variability of the reaction of a material to temperature when its dimensions are constricted [34, 82, 143, 183], these equations cannot be extrapolated or interpolated beyond the given experimental parameters and limits. However, for the bulk materials, the data can be highly reproducible, with different groups obtaining similar pressure threshold values and relations [169, 175].

Whilst this provides a solid basis when identifying possible growth temperatures for the encapsulated nanowires, further investigation of the literature helps to establish a fuller picture of the behviour of the materials, and how various external factors will affect the growth. For example, an investigation by Vigil-Galán et. al [10] into the effect of Close Space Vapour Transport (CSVT) deposition - a vapour phase method which often incorporates sputtering and heated substrates - at different temperatures on the composition of the resultant grown layers found distinctly different phases to arise from each temperature.

Furthermore, in the case of $Sb_2Te_3$, Zhu et. al have reported that nanoscale crystalli-

| Chem. | T (K) | A | B | C | Ref |
|---|---|---|---|---|---|
| AgCl | 1185 - 1837 | 9.95 | 8776 | -62.718 | [175] |
| $Sb_2S_3$ | 692 - 823 | 13.96 | 10490 | - | [165] |
| $Sb_2Se_3$ | 676 - 877 | 12.75 | 9566 | - | [178] |
| $Sb_2Te_3$ | 703 - 868 | 13.80 | 10936 | - | [165] |
| | 1062 - 1283 | 10.33 | 7719 | - | [181] |
| SnSe | 773 - 898 | 12.32 | 10495 | - | [179] |
| (*) | 933 - 973 | 13.03 | 9760 | - | [180] |

Table 2.4: Published coefficients and temperature ranges for sublimation-vapour pressure Antoine equations for materials in this research. In the instance that a published relation has given pressure in non-SI units, coefficients have been converted to universally provide pressure in Pa.

sation and nucleation phenomena resulted in the observed melting of the material at 580°C - which is 50°C lower than its standard bulk $T_m$ (Table 2.3) [184]. They then further reported that, when in an amorphous film form, it has been observed to undergo significant melting and complex recrystallisation under prolonged ($\sim$ 7 mins) exposure to an electron beam, with extensive and persistent alterations to the long-range structure occurring after $\sim$ 20 mins [184]. This phenomenon will be discussed further in the context of electron beam irradiation in Section 2.2.5, and in terms of its relevance to the results presented in this thesis in Section 3.3.2.

Further to this, for some materials the vapour phase equations are not enough to define the sublimation behaviour of the material, which can be highly complex. In the case of $Sb_2Se_3$, the speciation of the source material is observed in specific temperature ranges, resulting in combinations of products with differing stoichiometries to that of the source material [178].

In contrast, investigations into the vapour pressures of SnSe [179] established that the material melts [166], and sublimes, congruently from a stoichiometric source material,[151] up to a specific pressure and temperature [173, 174, 180]. This increases the ease of reproducibility of the research presented in this thesis, and is experimentally confirmed in Section 4.2 and 4.4. The temperature-pressure phase range for SnSe is bounded at low temperatures and high pressures by the formation of $SnSe_2$. This boundary line is described by the Antoine equation

$$\log_{10}(\mathrm{P[Pa]}) = 13.03 - \frac{9760}{\mathrm{T[K]}}, \tag{2.6}$$

which is given in Table 2.4(*), and was originally published by Sharma and Chang with P in units of bar [180].

However, once nano-confined, the vapour pressures of the materials are expected to

be distinctly altered. Primarily, this will present as an observed melt depression, when compared with the bulk. This phenomenon can be characterised by the Gibbs-Thomson effect [185], which is a more specialised arrangement of the Gibbs equation and assumes that the pressure remains constant in the thermodynamic system. In its most fundamental form, this relation describes the variations in vapour pressure across a curved surface, or interface [186]. More specifically, it is used to predict the change in melting point, $\Delta T_m(x)$, for an isolated particle, $T_m(x)$, with diameter x in comparison with the bulk (a crystal of infinite dimension), $T_m^\infty$. The Gibbs-Thomson effect is defined by

$$\Delta T_m(x) = T_m^\infty - T_m(x) = \frac{4\sigma_{sl} T_m^\infty}{H_f \rho_s x}, \tag{2.7}$$

where $\rho_s$ is the density of the solid, $H_f$ is the (latent) heat of fusion per gram of bulk material, and $\sigma_{sl}$ is the surface energy of the solid-liquid interface. The addition of the latter term accommodates the presence of a positive energy at the solid-liquid interface, This thereby increases the required energy for particles with high curvature to form, which would be expected to display a correlative elevated vapour pressure.

The relation can be readily adapted for the confinement of liquids inside pores with the addition of a cosine term, which makes an adjustment for the cylindrical confining geometry of the system, such that

$$\Delta T_m(x) = T_m^\infty - T_m(x) = \frac{4\sigma_{sl} T_m^\infty}{H_f \rho_s x} \cos(\phi_c), \tag{2.8}$$

where $\phi_c$ is the contact angle subtended by the liquid with the cavity interior surface (Section 2.1.2) [125]. For the classical Gibbs-Thomson (constant pressure) and Kelvin (constant temperature) cases, this is commonly assumed to take values of 0° and 180°, respectively [187]. These equations allow for predictions of the melting point depression to be made, on the assumption that evaporation occurs along a hemispherical interface at the liquid surface - such as that made by a droplet of liquid on a flat surface. In contrast, condensation inside cylindrical pores is believed to initially occur as monolayers with cylindrical geometry. This phenomenon will be further discussed in terms of the observation of a significant melt depression in nano-confined $Sb_2Te_3$ compared with the bulk in Section 3.4.

### 2.1.4 Considerations for Environment-Sensitive Materials

For some substances, it is necessary to ensure that they are not exposed to a standard, ambient atmosphere. For example aluminium is sensitive to oxygen, and will


Figure 2.5: Packaging and experimental considerations for light sensitive materials. (a) Silver chloride is supplied in opaque, reflective packaging to minimise risk of light exposure. (b) When not in a red-lamp environment, the sample must be wholly encased in light-blocking material. In this case, the entire double ampoule is encased in foil for the sublimation growth stage, and during any portion of the preparation that is not conducted in a dark room.

quickly react and degrade in its presence. Therefore, it is supplied in a container that has been sealed under an inert atmosphere, most commonly argon or nitrogen. These conditions must be maintained whilst handling the material. This is achieved through the use of a glovebox. All of the components are placed inside the glovebox and are then assembled inside the ampoule as outlined in Section 2.1.2. The end of the ampoule is then sealed with parafilm to avoid exposure to air and contamination prior to sealing. Once the ampoule has been evacuated and sealed, the growth stage can be carried out as outlined in Section 2.1.2, with few further considerations.
In the case of light sensitive materials, special arrangements must be made at every stage of the growth procedure to ensure that the material for encapsulation is not exposed to ultraviolet light - this includes natural light and standard lightbulbs. These materials are commonly supplied in opaque, reflective packaging, as shown in Fig. 2.5 (a). This is true for silver chloride (Fig. 2.5), which has a tendency to dissociate photolytically. This process results in a sample comprised of almost pure Ag solid, surrounded by $Cl_2$ gas, upon illumination with UV frequencies, or incautious heating. Therefore, a red lamp in an isolated dark room was utilised to compose the ampoule. This was carried out in conjunction with a portable glove bag, filled with nitrogen, to limit risk of contamination. When not in a red-lamp environment, the sample must be wholly encased in light-blocking material. Therefore, once the growth configuration had been constructed inside the ampoule, it was encased in aluminium foil, as shown in Fig. 2.5 (b). The sample was then sealed under light safe conditions, re-encased in foil, and placed in the furnace. Once encapsulated, the material is stabilised by the confining environment provided by the SWCNT, the dimensions of which are far smaller than the wavelength of UV light (100 nm) [24, 130, 146, 149, 188, 189].

### 2.1.5 Processing & Separating

Once grown, it is necessary to process the as-filled samples in order to prepare them for analysis. This is a vital step in ensuring the purity and quality of the sample prior to characterisation; the as-grown samples may contain rogue damaged SWCNTs, stray contaminants, or large populations of extraneous bulk material. The last is a particular issue that arises with samples that have been grown from the melt, since the SWCNTs must be ground with the filling material. The presence of external crystals can often be identified via a visual inspection of the samples, although the presence or absence of extraneous material at the nano- or micro-scale should be verified by SEM or TEM.

The removal of extraneous external material on the X@SWCNTs - where X = $Sb_2Te_3$, SnSe, etc. - samples can be accomplished via "exfoliation". This is achieved by a similar method to the sample growth (Section 2.1). The prepared sample is placed in a single quartz ampoule, which is then evacuated to $10^{-6}$ mbar and sealed. The ampoule is subsequently heated to a temperature that is sufficiently below the melt temperature of the filling material, and annealed. The extraneous material then sublimes, and deposits on the walls of the ampoule, without impeding or affecting the filling material. For example, in the case of $Sb_2Te_3$@SWCNTs, an appropriate temperature for this procedure would be 600°C, with the sample being annealed for 5 hours. This has been tested and verified experimentally (Section 3.4). The sublimation exfoliation method was developed with J. Sloan.

Throughout the course of this research, other methods and processes have been developed for the successful exfoliation of samples. The first of these is through the use of thermogravimetric analysis. When used in combination with differential scanning calorimetry, it not only provides information on the rates of mass loss, but also the heat flow characteristics for a sample, respectively (Sections 2.5 and 3.4, respectively). The results and key transitional temperatures from this method influence the second process - which utilises *in situ* heating whilst undergoing TEM analysis. This method of exfoliation is achieved by employing a DENS Solutions Wildfire single tilt heating holder. Whilst we have found this process to be highly effective - as outline in Sections 2.2.6, 3.2, and 3.3) - it is not very efficient or practical for sample sizes beyond those used in TEM, since it requires the dispersion and deposition of the sample onto microelectromechanical system (MEMS) chips.

Each process has its own particular parameters and limitations, the key one being the mass of the sample that can be exfoliated. In the case of *ex situ* furnace exfoliation, it is dictated by the size of the ampoule, so is in essence limited to the mass of the sample initially grown. However, there is no way of knowing the efficiency of the process without further post-exfoliation analysis on the sample. For DSC/TGA, the volume of the pan - name given to the sample holder in DSC/TGA - is the key limitation, which is up to $\sim$ 100 mg for powdered PCMs@SWCNTs. The mass loss can be tracked to high precision, but an element of estimation and trial and error is required to ensure loss of filling material does not occur, whilst removing all extraneous material. Finally, although *in situ* exfoliation offers the best opportunities for tracking the progress and efficiency of the process, it can only be conducted on as many filled SWCNTs as are dispersible onto the heating MEMS chip. Furthermore, the entirety of the exfoliated sample then needs to be removed from the chip, for example by washing or nano-tweezers, which usually results in some material loss

or chip damage.

Whilst the removal of extraneous material from the PCM@SWCNT samples does not directly impact our ability to analyse them using EM, it does enable more efficient analysis to be conducted. However, there are additional processing steps that are required for electron microscopy, due to the sample size requirements of the systems, which is outlined in detail in Section 2.2.1 and 2.2.2. More specifically, the filled SWCNTs must be dispersed onto substrates for analysis. The form of dispersed sample depends upon the requirements of the analytical technique that is to be used. If we want to image discrete filled SWCNTs, then the PCM@SWCNTs should be monodisperse. On the other hand, if the electron diffraction protocol - discussed in detail in Section 2.2.4 - is to be used, then thin bundles containing tens to a hundreds of PCMs@SWCNTs are required. The processing can be adjusted to influence the degree to which the SWCNTs are monodisperse.

Dispersion of the PCM@SWCNTs is achieved by dispersing a nominal volume of processed sample in chloroform (Fig. 2.6). This mixture undergoes ultrasonication, using a Cole-Parmer 750 W Homogenizer, pulsing repeatedly at 20 % power, 2 s on, 2 s off, for up to 30 min. Ultrasonication in this way not only disperses the bundles, but can also purify the sample. Pulsing of the relatively intense vibration is sufficient to break down damaged SWCNTs whilst leaving defect-free SWCNTs intact. Whilst the precise ratio of PCM@SWCNTs to chloroform is not critical, it is important that the solution not be oversaturated, as this will decrease separation of the SWCNTs and lead to large bundles that are difficult to analyse. An example of an oversaturated solution, after several weeks of resting, is given in Fig. 2.6 (a). The suspension is then immediately drop cast onto lacey carbon on copper TEM grids (Section 2.2.2) or MEMS chips (Section 2.2.6) using a micro-pipette. This step has to be done as quickly as possible, due to the rapid reagglomeration of the SWCNT bundles that can occur. This can be seen to be already beginning to occur in the dispersion in Fig. 2.6 (b), where the image was taken $< 5$ s after cessation of ultrasonication. The usually clear chloroform has turned a light grey - indicative of a well-dispersed suspension of SWCNTs - but micron sized bundles can be seen to be forming at the centre of the solution. After several weeks, the bundles are much larger and have almost completely reagglomerated - as can be seen in Fig. 2.6 (c).

Additional ultrasonication time is required to effectively disperse the filled SWCNTs in comparison with empty SWCNTs (Section 2.1.1), due to the increased density and diversity in the sample population. Similarly, the suspension persists for far longer for the unfilled SWCNTs solution than that of the filled samples. Once dispersed, the substrate is left to dry in air. Due to the rapid evaporation of most

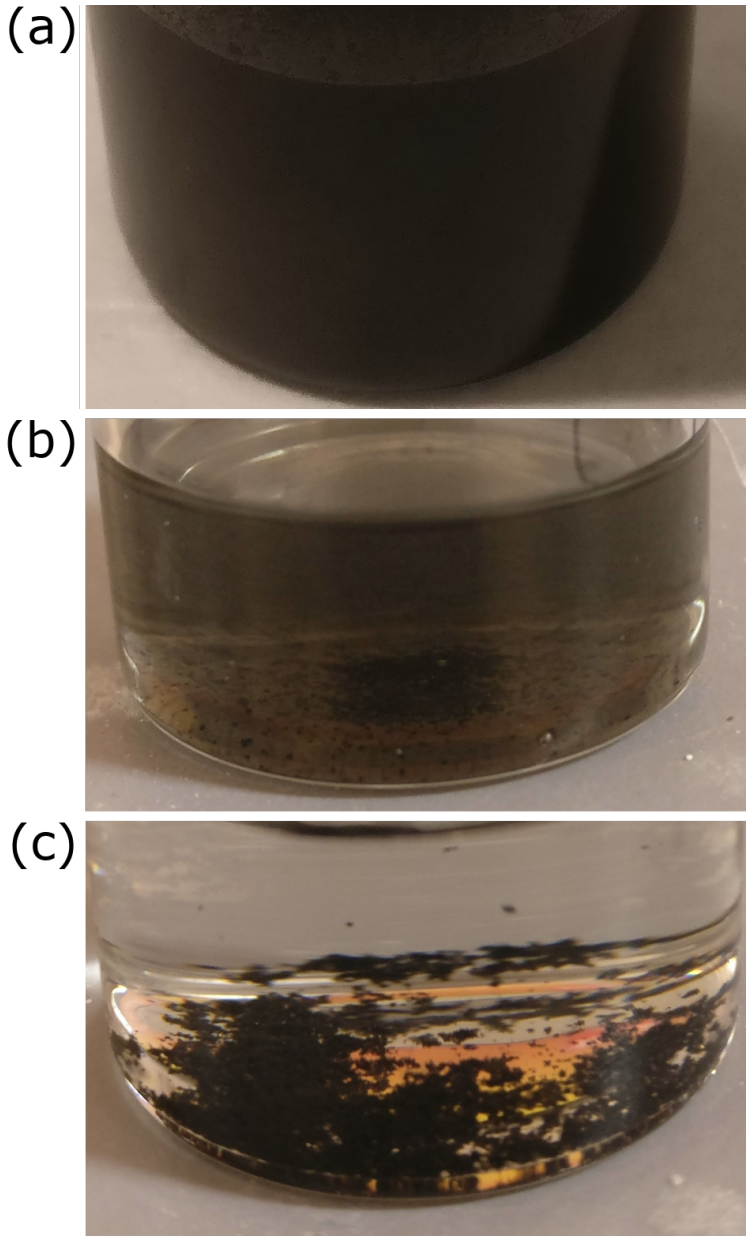


Figure 2.6: Various dispersions of SWCNTs in solvents. (a) An oversaturated dispersion of unfilled SWCNTs in chloroform after several weeks. (b) $Sb_2Te_3$@SWCNTs dispersion in chloroform immediately after ultrasonication at 20 % power for 5 mins. (c) $Sb_2Te_3$@SWCNTs dispersion in chloroform after several weeks.

solvents under atmospheric conditions, a hot lamp (a desk lamp with a standard 60 W incandescent bulb) is rarely necessary. Sample vials are wrapped in parafilm for storage, in order to limit liquid volume loss by evaporation.
Further to this, as introduced in Section 1.2, there lies considerable interest into the separation of SWCNTs according to their specific conformation (diameter) via ultracentrifugation. These investigations are ongoing, and form part of the research conducted by J.Sloan, M. Burdanova, K. Bal, E. Hu, R. Kashtiban, and J. Lloyd-Hughes as part of ESPRC project EP/R019428/1 (Chapter 6).
Research carried out by several groups into chemical treatment and oxidation methods for cleaning SWCNTs and X@SWCNT composites show varying degrees of success, often with undeniable caveats [153, 190–192]. It is often the case that effective and complete removal of contaminants results in the destruction of significant portions of the SWCNTs themselves. Oxidation of MWCNTs reduced the sample by 99 % [193]. *In situ* cleaning of CNTs using oxygen radicals by M. Petkov has been shown to effectively remove organic contaimnants - that contribute to hydrocarbon contamination under the beam - and chemical residue, without damaging the nanotubes [194]. The use of acids or surfactants has been observed to irreparably damage or functionalise the SWCNTs [195]. Therefore, even if the sample isn't destroyed, the properties of the SWCNTs may be altered or impaired.

## 2.2 Electron Microscopy

### 2.2.1 Scanning Electron Microscopy

A significant initial step in analysing the grown samples is verifying their quality. A quick surface method to achieve this is via Scanning Electron Microscopy (SEM). This provides information on the composition and surface of the sample on the micron scale, particularly when used in combination with Energy Dispersive X-ray spectroscopy (EDX) - which is discussed in detail in Section 2.4.
Standard imaging in the SEM gathers secondary electrons that come off the sample, to form images of the surface of the specimen (Fig. 2.7) [196, 197]. Also shown is a representation of the radii and depths from the surface of the sample for three key emissions for material characterisation in the SEM, including Secondary Electrons (SE), Back Scattered Electrons (BSE), and X-rays for EDX analysis. Additional emissions, not pictured, are Auger electrons and Cathodoluminescence (CL) [198]. The depth probing and information provided by these signals are outlined in Table 2.5, which is complementary to Fig. 2.7 [199]. The mechanisms and techniques

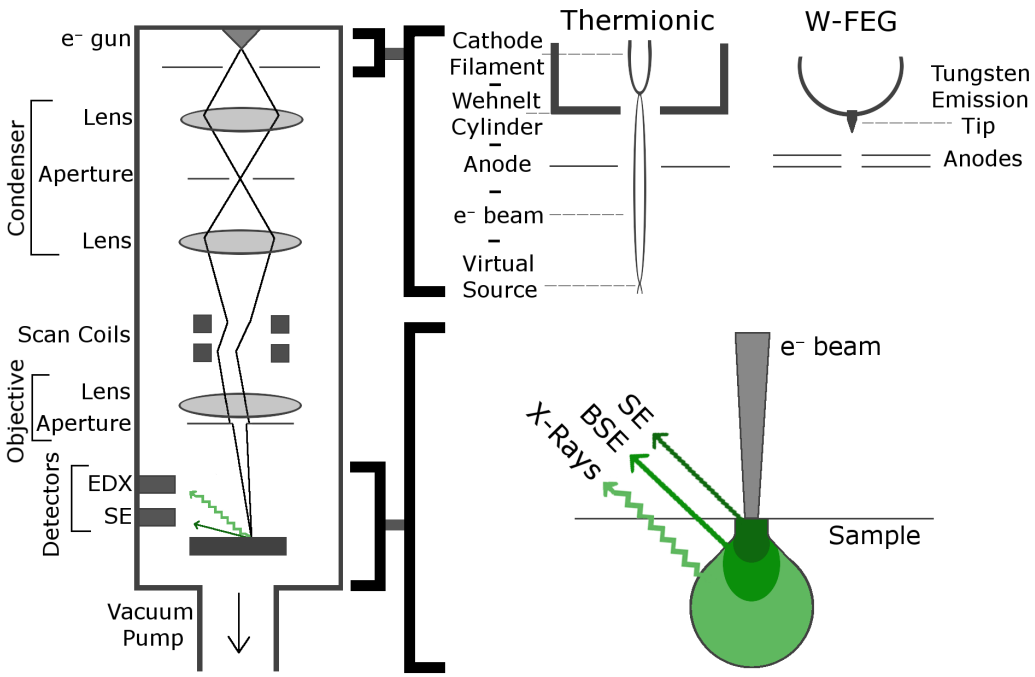


Figure 2.7: Schematic representation of a standard SEM configuration. Two possible electron gun configurations are depicted: the thermionic gun and the tungsten cold Field Emission Gun (W-FEG). The radii and depths from the sample surface of key emissions for material characterisation are also depicted [196, 197].

provided in Table 2.5 are by no means exhaustive, but they do include the key emissions of relevance to the work presented in this thesis.

Two different electron source configurations are also depicted in Fig. 2.7. The thermionic gun comprises a cathode filament source (usually tungsten or $LaB_6$) focused by a Wehnelt cylinder. The Field Emission Gun (FEG) employs an electron emitter that is either a cold-cathode - as shown in Fig. 2.7 "W-FEG", which comprises a single crystal tungsten tip ($< 310 >$ or $< 111 >$ orientation) - or warm field (Schottky) emitter. The former can achieve high beam coherence with an energy spread of $< 0.5$ eV, and can reach a brightness on the order of $10^9$ $Acm^{-2}sr^{-1}$ [196]. The tungsten cold-FEG has a much smaller beam spread, but also a much lower current. Whilst these (depicted in Fig. 2.7) are the two primary gun configurations for common SEMs, and TEMs, the high resolution TEM system at Warwick (ARM-200F) employs a Schottky gun. The principle of the Schottky gun configuration will be detailed in Section 2.2.2.

In reference to the research outlined in this thesis, SEM was primarily used to check the concentration of dispersed samples on TEM grids prior to analysis using the

| Emission/ Scattering | Depth | Technique & Information |
|---|---|---|
| Auger Electrons | $\leq 5$ nm | Surface atomic composition |
| Secondary Electrons | $\sim$5 nm | Topographical info |
| Back-Scattered Electrons | $\sim$400 nm | Z & phase differences |
| Characteristic X-rays | $\sim 3$ $\mu$m | EDX - thickness composition |
| Continuum X-rays | $\sim$ $\mu$m | - |
| Secondary Fluorescence | $\sim$ $\mu$m | CL - electrical info |
| Elastic & Rutherford Scattering | Transmitted | HR-imaging & diffraction |
| Inelastic Scattering | Transmitted | EELS - composition & bond states |
| Incoherent Elastic Scattering | Transmitted | (High Angle) Annular Dark Field |
| Unscattered & Small-Angle Scattered | Transmitted | Phase Contrast & Bright Field |

Table 2.5: Scattering and emissions from a sample for materials characterisation via EM, and complementary techniques. These are ranked by sample depth and categorised by emission type and analytical technique [29, 197, 198]. The precise values will vary according to the material and energy of the incident source.

ARM - detailed in Sections 2.2.2 and 2.2.3. This provided a rudimentary identification as to whether the SWCNT and chloroform dispersion required further dilution and/or sonication - the process of which is outlined in Sections 2.1 and 2.1.5. However, SEM was also helpful for observing and comparing platelet and large scale formations in a range of bulk crystals.

Imaging of the SWCNT bundles was conducted at accelerating voltages of $\leq 10$ kV. Imaging of individualised SWCNTs was typically carried out at 1 kV, as the lower accelerating voltage results in a shallower interaction depth in the sample. Therefore, the individualised SWCNTs have a higher contrast in imaging, with respect to the surrounding bulk material, than at higher accelerating voltages. This was particularly useful for the characterisation of SWCNTs grown across slits in $Si_3N_4$ chips (detailed in Chapter 5). Whilst this meant that the emission of secondary electrons was distinctly limited - impacting the resolution, signal to noise and contrast quality - the lower energy helped to limit potential damage to the samples from, for example, radiation and charging effects. Furthermore, low voltage operation decreases the penetration of electrons, which can help to increase the relative signal from the nanostructures with respect to surrounding material and supports [200]. However, for EDX investigations, higher beam energies (up to 20 kV) were often necessary to access the full spectrum of elements and their emissions. This is discussed further in Section 2.4.

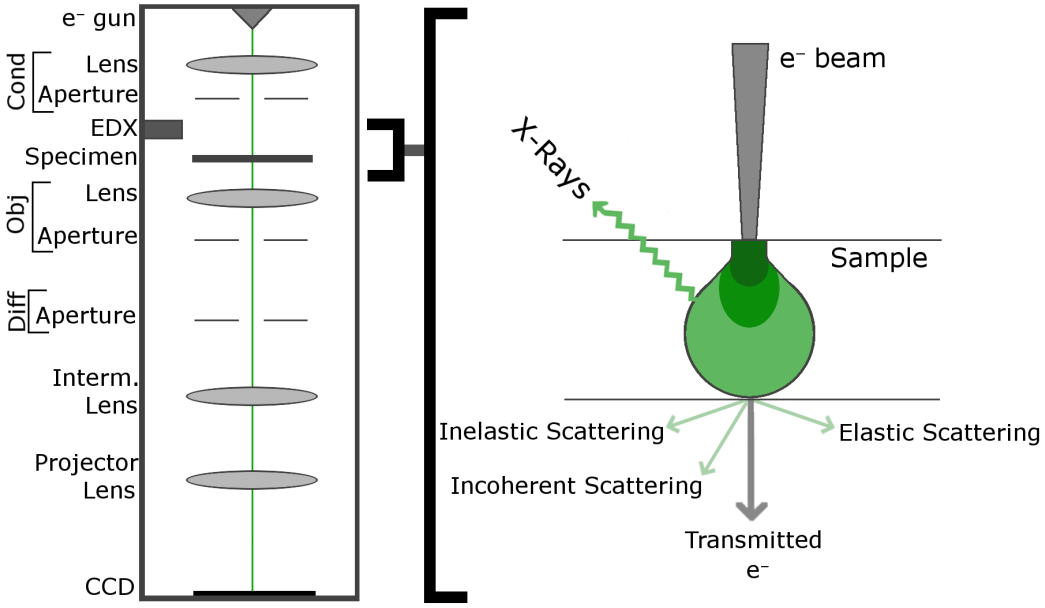


Figure 2.8: Schematic representation of a HR-TEM system, including sample interactions and scattering.

### 2.2.2 Transmission Electron Microscopy

Transmission Electron Microscopy (TEM), in contrast with SEM, collects transmitted electrons. These electrons can be used to build up a high resolution image of the full sample. For Phase contrast TEM imaging this includes electrons that have been elastically scattered and those that pass directly through the sample (Table 2.5 and Fig. 2.8). The information provided depends upon the interactions that the transmitted electrons have undergone on their way through the specimen. A brief overview of this information is outlined in Table 2.5, which is complementary to Fig. 2.8.

Imaging conditions are initially set by the selected apertures and lenses in the TEM column (Fig. 2.8). The different imaging modes in (S)TEM are achieved through the use of a series of apertures, lenses, and beam alignment coils [199, 201] - which enable or inhibit the paths of transmitted electrons to the detector depending upon the information that we want to access (Fig. 2.9 and Table 2.5). The differences between TEM and STEM imaging modes begin before the beam has interacted with the sample (Fig. 2.8): TEM uses parallel beam conditions from the source to the sample, whilst STEM imaging requires a convergent beam - as shown in Fig. 2.9 (a) [202].

A variety of information can be obtained from the samples using the different beam

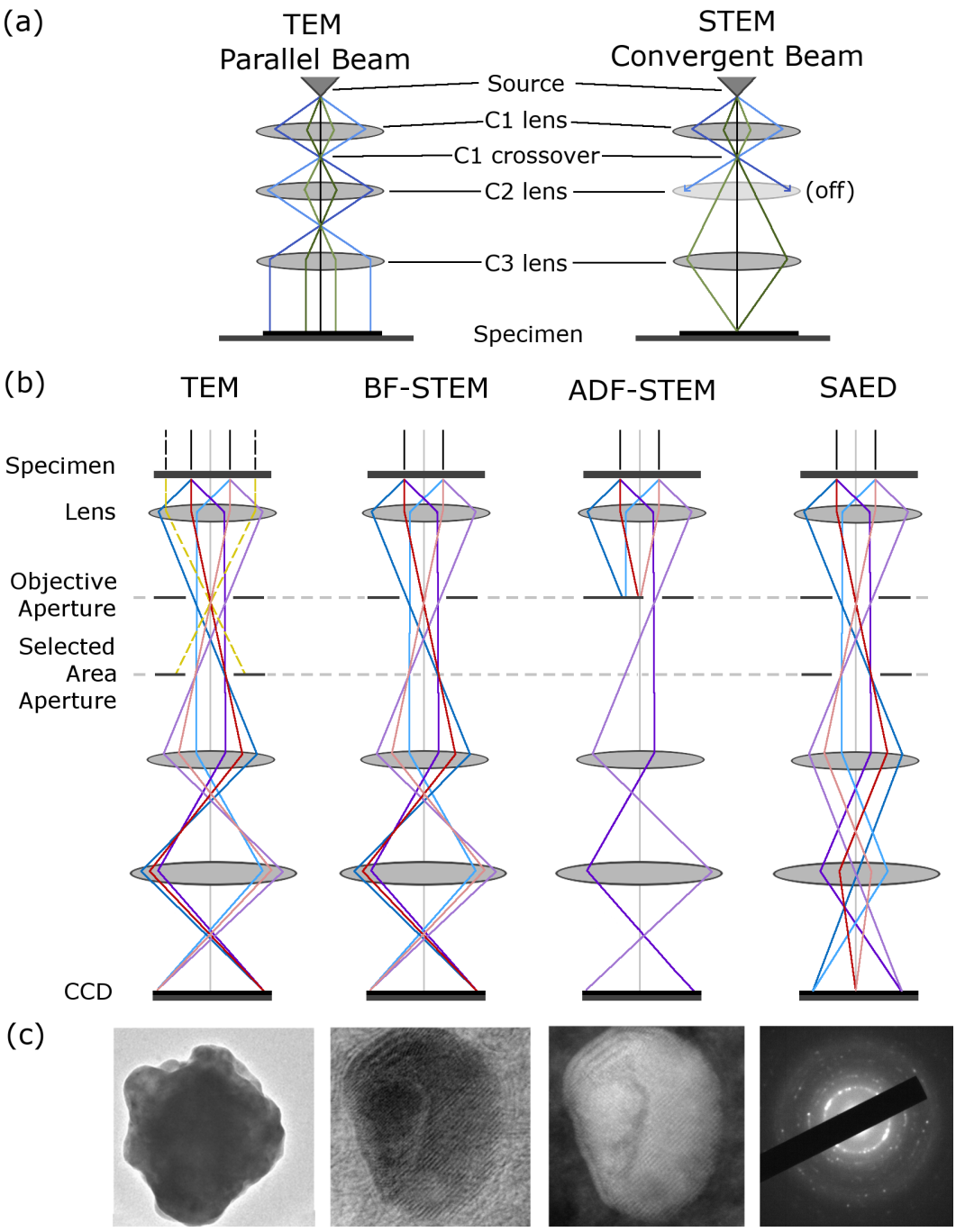


Figure 2.9: Schematic representation of beam configurations and images for the different analytical modes in a HR-TEM. (a) Overview of the parallel and convergent beam conditions from the electron source to the sample in TEM and STEM imaging, respectively. (b) Beam configurations for TEM, Bright Field (BF) and Annular Dark Field (ADF) STEM, and Selected Area Electron Diffraction (SAED) analysis. (c) Example images of a polycrystalline bulk $Sb_2Te_3$ microstructure taken in the respective mode.

configurations (Fig. 2.9 (a-b)). Examples of experimental images obtained for each mode are depicted in Fig. 2.9 (c). Therefore, depending upon the operational mode (collected transmitted electrons), we can qualitatively or quantitatively characterise the sample based upon the resultant image. Variations in contrast in HR-TEM imaging are the result of distinct interactions of the electron beam with the sample. This contrast can either be amplitude contrast - arising from thickness and mass variations in the sample - or phase contrast. Amplitude contrast introduces an atomic number (Z) dependency in the resultant image due to increased scattering from heavier elements and in thicker samples. This is a key source of contrast in HR-TEM imaging. However, the inclusion of phase contrast causes this to be non-quantitative [30].

Phase contrast in imaging derives from the impact of the atomic structure on the phase of the electron wave. The exact magnitude of this effect is dependent on the electrostatic potential of the crystal, the wavelength of the electron, and the acceleration voltage applied to the electron beam. Furthermore, phase contrast imaging can reach resolutions of $< 0.1$ nm, if the beam is properly abberation-corrected - which is described in detail in Section 2.2.3. Therefore, phase contrast is a key underpinning effect for HR-TEM imaging, since it (the incoming electron wave) provides direct information from the atomic structures within the sample without causing intensity variation in the image [202]. This is particularly helpful in very thin and atomically light samples, which offer low amplitude contrast. In the context of this research, it is particularly useful for visualising the SWCNTs in the bundles.

Whilst standard TEM imaging utilises the full range of transmitted electrons, Bright Field Scanning Transmission Electron Microscopy (BF-STEM) relies on direct, unscattered (brighter contrast) and small-angle ($\theta < 30$ mrad) scattered (darker contrast) electrons to build up an image (Fig. 2.9 (b-c)) [203]. Therefore, the main contrast mechanism in BF-imaging is coherent phase contrast. Phase contrast is built up from the inference between the relative phases of the trasmitted electrons [196]. However, diffracted beams can also contribute to the image, since the atoms diffract electrons as they pass through the material, as well as scatter them. As can be seen in the BF-STEM image in Fig. 2.9 (c), the crystal appears darker compared to the amorphous film that it is suspended on due to increased scattering in that region. The same is true of thicker materials, which will appear darker contrast due to increased scattering of the electrons as they pass through the material. However, the atomic columns of the crystal and the amorphous nature of the film can be clearly resolved in the BF-STEM image in Fig. 2.9 due to the reduced contribution from amplitude contrast with respect to standard TEM imaging. Amplitude

contrast is a scattering contrast that is dependent upon the scattering coefficient of each atom [204]. Therefore, the type and density of the specific atom will have a large impact on the amplitude contrast [196]. This difference can be most clearly noticed when directly comparing the TEM and BF-STEM images.

Conversely, Annular Dark-Field Scanning Transmission Electron Microscopy (ADF-STEM) excludes unscattered and low-angle scattered electrons from its images (Fig. 2.9 (b)). It also differs from traditional TEM dark-field as it collects only scattered electrons ($30 < \theta < 200$ mrad) through the use of an annular detector, as opposed to isolating them from the main beam with an objective aperture. This results in an inversion in contrast - where areas of vacuum and no scattering appear darkest - and a substantial dependence on the atomic number (Z) of the scattering atom (Fig. 2.9 (c)). Therefore, ADF can also be called Z-contrast imaging, due to the dependence of the scattering atom's nucleus (Rutherford scattering) on the image intensities.

High Angle ADF (HAADF) builds up a dark-field STEM image by collecting incoherently scattered electrons at very high angles ($120 < \theta < 450$ mrad). Therefore, the technique also has a significant dependence on the atomic number of the scattering atom, as there is a direct correlation between Z and the number of electrons scattered at high angles; the electrostatic interactions with the electron beam are more pronounced. The resultant contrast of the composed image is approximately proportional to the square of the atomic number ($I \propto Z^{1.7}$) [196, 199, 202].

Selected Area Electron Diffraction (SAED) in TEM originates corresponds to the scattering, and diffraction, of the electron beam as it travels through a specimen (Table 2.5). The diffracted beams, which are brought to a focus in the back focal plane in the standard TEM configuration, can be brought into plane of imaging by placing an aperture in the image plane of the objective lens [202]. This aperture defines the area from which signal is collected from the specimen. Therefore it is known as the "selected area aperture" (Fig. 2.9 (b)) [196]. Electrons can only contribute to the diffraction pattern formed on the screen by the next intermediate lens if their trajectories fall within the area of this aperture. Therefore, the observable area of the sample is actually significantly smaller than the size of the aperture, due to the magnification of the objective lens.

Diffraction from a crystalline sample forms a complex pattern of reflections, due to the compound interference from the repeating crystal lattice, as the periodic structure of the crystal acts as a diffraction grating (Fig. 2.9 (c)) [196, 204]. The geometrical arrangement of these reflections describe the fundamental features of the material: the crystallinity, lattice parameters, and symmetry. The intensity of

the reflection, meanwhile, provides limited data on the lattice content, which is discussed in detail in Section 2.2.4. A beam stop - which can be seen in the diffraction pattern in Fig. 2.9 (c) - is often used to prevent the central beam of highest intensity from destroying the pixels in the CCD. Acquired images were viewed and collated in DigitalMicrograph$^{TM}$. This software is widely used for evaluating (S)TEM images and SADPs.

Whilst the different imaging modes enable us to form images based upon the properties of the transmitted electrons, the extent of the information that can be drawn from EM analysis of a specimen fundamentally depends upon the key properties of the TEM system and of the sample. In terms of the instrumentation, the principal parameters concerned are the energy spread of the beam, and the resolving power of the TEM. Further to these, considerations for the thickness, and composition and stability of the sample must be accounted for [202].

The JEOL 2100 TEM system at Warwick employs a $LaB_6$ electron source (as detailed in Section 2.2.1), with the data being captured by an unshuttered Gatan Orius SC600 Camera. The ARM-200F HR-TEM system at Warwick University utilises a Schottky type FEG, and records data using an unshuttered Gatan Orius SC1000 CCD camera. In contrast with the cold-FEG depicted in Fig. 2.7 in Section 2.2.1, a Schottky FEG is a warm field emitter. Since the tip is warmed, the emission is more stable over time and requires a smaller extraction voltage than the cold-FEG. Whilst there is an associated (slight) increase in the energy spread of the electron beam from a warm field emitter, the total emission from the Schottky emitter is higher than that of the cold-FEG [196]. These properties lend themselves well to aberration-corrected (S)TEM, as will be detailed in Section 2.2.3.

Furthermore, extra care and time must be taken to properly align the system in order to attain atomic resolution in imaging. This is due to the variety of aberrations that arise when using the intricate system outlined above. Correcting for these aberrations is an involved process of compounded adjustments, as the total aberration function comprises a series of individual, complex perturbations, each of which have a characteristic effect on the resultant image and beam shape [196]. These are dicussed in more detail in Section 2.2.3. The ability to correct such aberrations in the objective lens not only dictates the size of the electron probe, but also the fundamental image resolution that can be attained [30].

| Symbol | Aberration | Wave Aberration $\Re()$ |
|---|---|---|
| $A_0$ | Beam/Image Shift | $A_0\bar{\omega}$ |
| $C_1$ | Defocus | $\frac{1}{2}C_1\omega\bar{\omega}$ |
| $A_1$ | Two-Fold Astigmatism | $\frac{1}{2}A_1\bar{\omega}^2$ |
| $B_2$ | Second Order Axial Coma | $B_2\omega^2\bar{\omega}$ |
| $A_2$ | Three-Fold Astigmatism | $\frac{1}{3}A_2\bar{\omega}^3$ |
| $C_3$ | Third Order Spherical Aberration | $\frac{1}{4}C_3(\omega\bar{\omega})^2$ |
| $S_3$ | Third Order Star Aberration | $S_3\omega^3\bar{\omega}$ |
| $A_3$ | Four-Fold Astigmatism | $\frac{1}{4}A_3\bar{\omega}^4$ |
| $B_4$ | Fourth Order Axial Coma | $B_4\omega^3\bar{\omega}^2$ |
| $D_4$ | Fourth Order Three-Lobe Aberration | $D_4\omega^4\bar{\omega}$ |
| $A_4$ | Five-Fold Astigmatism | $\frac{1}{5}A_4\bar{\omega}^5$ |
| $C_5$ | Fifth Order Spherical Aberration | $\frac{1}{6}C_5(\omega\bar{\omega})^3$ |
| $S_5$ | Fifth Order Star Aberration | $S_5\omega^4\bar{\omega}^2$ |
| $R_5$ | Fifth Order Rosette Aberration | $R_5\omega^5\bar{\omega}$ |
| $A_5$ | Five-Fold Astigmatism | $\frac{1}{6}A_5\bar{\omega}^6$ |

Table 2.6: Aberrations up to the fifth order and their contribution to the total wave aberration, as adapted from *Aberration-Correction Imaging in Transmission Electron Microscopy* [205].

### 2.2.3 Aberration-Correction

Whilst standard TEM instrumentation has stringent and specific requirements that must be met in order to effectively analyse and characterise a sample, extra care and time must be taken if one wishes to attain atomic resolution in imaging. This is due to the variety of aberrations that arise when using the intricate optics system outlined in Section 2.2.2. Whilst each component introduces their own factors to consider, a key limitation in high-resolution (S)TEM imaging is the aberrations introduced by the lenses - which are outlined up to fourth order in Table 2.6. The total aberration function comprises a series of individual, complex perturbations, each of which have a characteristic effect on the resultant image and beam shape [196]. Correcting for these aberrations, in order to get an ideal beam shape that does not limit the area of view, is conducted under computer-aided feedback control (Fig. 2.10).

If we first consider a perfect lens with no physical flaws, then we would expect that a point source on one side of such a lens would be focused to single image point on the other. The position of this point focus is defined as being in the "Gaussian image (focus) plane". In reality, this is never the case for the round electron lenses. Indeed, no matter how "perfect" a lens is produced, we will always see the introduction of aberrations. These can be split into two overarching classes: incoherent aberrations

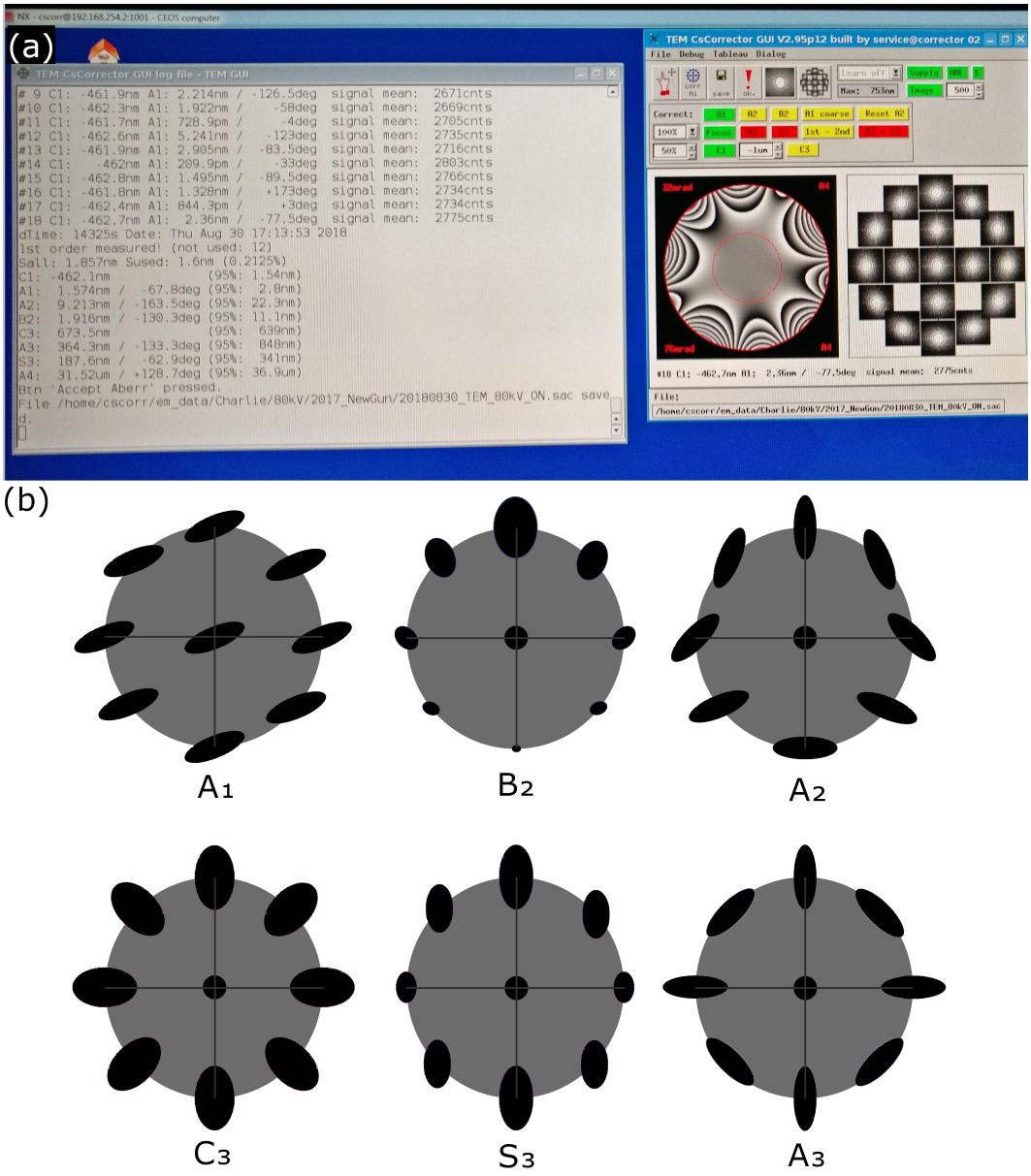


Figure 2.10: The resultant phase plate in TEM mode after aberration correction and contributions of the aberrations to the Zamlin tableau. (a) The CEOS corrector utilises a Zemlin tilt tableau to measure the aberrations present in an amorphous material. This is used to calculate the uniform phase plate. The log file for the values of the $C_1$, $A_1$, $A_2$, $B_2$, $C_3$, $A_3$, $S_3$, and $A_4$ aberrations is output with every tilt tableau compilation. (b) The impact of different aberrations on the appearance of the Zemlin tableau, adpated from [205].

- which distort the wavefront through the compounding of different contributions - and coherent, or geometric, aberrations - which are coherent distortions to the wavefront caused by the geometry of the electromagnetic field of the lens [196].
The key contributor to the limitation of resolution due to incoherent aberrations is chromatic aberration - where rays with different wavelengths (energies) are focused to different points. It is principally defined in TEM by the energy spread of the electron beam [202]. Whilst the energy resolution of the TEM system can be improved through the use of monochromators, the electron source is not monochromatic. Therefore, the electrons emerge from the gun with a range of energies, and so are then focused differently by the objective lens as they pass through. Electrons that have lost more energy ($\Delta$E) when transmitted through the specimen are bent through larger angles than those with energies closer to the initial beam energy ($E_0$). The ratio between these two energies is known as the chromatic parameter

$$\kappa = \frac{\Delta E}{E_0}. \tag{2.9}$$

The effect of chromatic aberration is more pronounced for thicker samples, since there is an increased proportion of inelastically scattered electrons. The image formed from a point at the specimen - due to chromatic aberration of the transmitted electrons - can be defined as a disc of radius

$$r_{\text{chromatic}} = C_C \kappa \theta_{\text{obj}}, \tag{2.10}$$

where $C_C$ is the chromatic aberration coefficent and $\theta_{\text{obj}}$ is the semiangle of collection of the objective lens from a point source at the specimen. Therefore, the point at which the focused beam is at its minimum diameter - referred to as the "disc of least confusion" - will not be in the Gaussian image plane, but rather at some distance, $\Delta$z, closer to the objective lens. This distance is known as the defocus spread and can be defined under the chromatic aberration effect and the attributes of the system by the relation

$$\Delta z_C = C_C \left( \frac{\Delta E}{V_0} + \frac{2\Delta I}{I_0} + \frac{\Delta V}{V_0} \right), \tag{2.11}$$

where $\Delta$V is the fluctuation in the accelerating voltage $V_0$, and $\Delta$I is the variation in the lens current $I_0$ [202]. The effects of chromatic aberration can be limited by filtering the electron beam in the gun, and the electrons after they have been transmitted through the sample, or by correcting the optics themselves. The first can be accomplished through the use of a monochromator, whilst the latter are more demanding and require a precise energy filter and field to correct the electron

trajectories [196].

Geometric aberrations are far easier to calculate and correct for, since they do not introduce the same incoherence to the distortion of the wavefront. Of these aberrations, spherical aberration has the primary impact on the resolution of the system. Whilst the magnitude of the effect of chromatic aberration is dependent upon the energy of the incoming electrons, spherical aberration causes electrons with trajectories at higher angles ($\theta$) from the centre to be brought to a focus before the Gaussian image plane [202]. The transverse deviation of the path of the ray from the point of focus of the unaberrated beam in the Gaussian image plane is given by a disc of radius

$$\mathrm{r_{spherical}} = \mathrm{C_S}\ \theta^3, \tag{2.12}$$

where $\mathrm{C_S}$ is the constant of proportionality of the spherical aberration. Since this spherical aberration has a cubed dependence on the ray angle, it is described as being a third-order aberration and is often denoted by "$\mathrm{C_3}$" (Table 2.6) [202]. Similarly to chromatic aberration (Eq. 2.11), this introduces a longitudinal shift in the focus of the objective lens in (S)TEM - the defocus of the lens. Since the sample area under illumination in TEM is very small, the effect of the location of the source on the object plane can generally be considered negligible [196, 205]. Therefore, the total geometrical wave aberration function - under this (isoplanatic) approximation [205] - can be defined by

$$\chi(\theta) = \frac{1}{2}\theta^2\mathrm{C_1} + \frac{1}{4}\theta^4\mathrm{C_3}, \tag{2.13}$$

where $\mathrm{C_1}$ is the defocus of the lens (Table 2.6) [30]. The defocus ($\mathrm{C_1}$) and third order spherical aberration ($\mathrm{C_3}$) are independent of the chromatic parameter (Eq. 2.9) [205]. This wave abberation function is a key impacting factor in HR-TEM phase contrast imaging, as it dictates how the exiting (from the sample) electron plane wave ($\psi_{\mathrm{ep}}(\theta)$) will be affected by the objective lens. The resultant wave at the image plane is given by

$$\psi(\theta) = \mathcal{F}^{-1}[\psi_{\mathrm{ep}}(\omega)\mathrm{t}(\omega)], \tag{2.14}$$

where $\psi_{\mathrm{ep}}(\omega)$ and $\mathrm{t}(\omega)$ define the exit-plane wave and phase contrast transfer function in complex components, respectively. The complex angles are defined by $\omega = \theta_\mathrm{x} - \mathrm{i}\theta_\mathrm{y}$ and $\bar{\omega} = \theta_\mathrm{x} + \mathrm{i}\theta_\mathrm{y}$, such that $\theta^2 = \omega\bar{\omega}$ [202]. The phase contrast function is primarily dependent on the complex abberation function of the lens ($\chi(\omega)$) through which the wave is passing, such that

$$\mathrm{t}(\omega) = \mathrm{e}^{-\frac{2\mathrm{i}\pi}{\lambda_\mathrm{e}}\chi(\omega)}, \tag{2.15}$$

where $\omega$ defines the complex angle of the electron trajectory in the aperture plane, and $\lambda_e$ is the relativistic wavelength of the electron.
If we combine these aberrations with the Rayleigh criterion for the minimum resolvable separation ($r_{min}$) then we obtain the relation

$$r_{min} = 0.91[C_3\lambda_e^3]^{0.25}, \tag{2.16}$$

where $\lambda_e$ is the wavelength of the electron [30, 206]. Therefore, the value of $C_3$ is the key limiting factor to the resolution of the system, and must be corrected for if a system is to achieve a resolution of $< 1$ Å. In the absence of the correcting elements in HR-TEM systems, the excitation, lens geometry and position of the object relative to the lens typically result in a $C_3$ value on the order of several millimeters [196]. However, even after correction, $C_3$ takes a non-zero value (as shown in Fig. 2.10 (a)).
Once the spherical aberration has been optimally corrected for, other aberrations - such as astigmatism and coma - have a more noticeable impact upon the ultimate resolution of the system. In order to reach the full potential of the TEM, the aberration function given in Eq. 2.13 must be expanded to include these. These additional aberrations are defined in complex components up to the fifth order in Table 2.6 [205]. Whilst the distinct aberrations contributing to the total axial (aperture) aberration function ($\chi$) can be easily listed up to the seventh order - as illustrated in Chapter 7 of *Aberration-Correction Imaging in Transmission Electron Microscopy* by R. Erni [205] - by the fifth order the aberrations become vanishingly small and are lost in the electromechanical noise of even the most advanced machines [196]. However, only aberrations up to the third order are corrected for by the CEOS Corrector and Zemlin tableau on the ARM-200F system - as depicted in Fig. 2.10. An illustration of how aberrations up to the seventh order appear spatially is given in Chapter 7 of the Erni's book [205].
The correction elements on the ARM-200F are controlled by the CEOS corrector, which utilises the Zemlin tilt tableau method to measure the aberrations present in a beam passing through an amorphous material. This is used to calculate the uniform phase plate and suggest which aberration should be corrected for next - as depicted in Fig. 2.10 (a). Multipole lenses in the column are used to correct the beam shape and counteract the effects of the aberrations (Fig. 2.10 (b)) by applying an equal and opposite correction [196]. In STEM imaging mode, the coma and astigmatism (Table 2.6) can be fine-tuned using the Ronchigram of an amorphous sample. The Ronchigram is formed from a projection image of the amorphous sam-

ple at moderate underfocus, and can act as an aberration map. Only the centre of the Ronchigram image is accurate to the spatial information of the sample. This is then surrounded by distorted features, known as "rings of infinite magnification", due to the geometrical aberrations of the system. The precise distortion and appearance of the Ronchigram gives an indication of which aberrations still require correction in order to be able to achieve optimum resolution [196].
The log file for the values of the different aberrations is output with every tilt tableau compilation (Fig. 2.10 (a)). Since the given aberrations are linked in such a way (Eq. 2.13) then adjusting one - even marginally - has an implicit effect on the value of the others. So, whilst the software runs the calculations and suggests corrections, it is down to the user which aberration should be addressed. This is typically done based on the deviation of each aberration coefficient from the optimal value, and how significantly it will affect both the ultimate resolution and the values of the other aberrations were an adjustment to be made. The effect that the lower order aberrations have upon the appearance of the tilt tableau is illustrated in Fig. 2.10 (b).

### 2.2.4 Electron Diffraction

Electron diffraction in TEM corresponds to the scattering, and diffraction, of the electron beam as it travels through a specimen. The diffracted beams, which are brought to a focus in the back focal plane in the standard TEM configuration, can be brought into plane of imaging by placing an aperture in the image plane of the objective lens (Fig. 2.9 in Section 2.2.2) [202]. This aperture defines the area from which signal is collected from the specimen. Therefore, it is known as the "selected area aperture" [196]. Electrons can only contribute to the diffraction pattern formed on the screen by the next intermediate lens if their trajectories fall within the area of this aperture. Therefore, the observable area of the sample is actually significantly smaller than the size of the aperture, due to the magnification of the objective lens. Diffraction from a crystalline sample forms a complex pattern of reflections, due to the compound interference from the repeating crystal lattice (Fig. 2.11). Information can then be extracted from the geometrical arrangement of the reflections. The arrangement describes the fundamental features of the material: the crystallinity, lattice parameters, and symmetry. The intensity of the reflection, meanwhile, provides some insight into the lattice content. This is underpinned simply by Bragg's law,

$$\mathrm{n}\lambda = 2\mathrm{d}\cdot\sin(\theta) \tag{2.17}$$

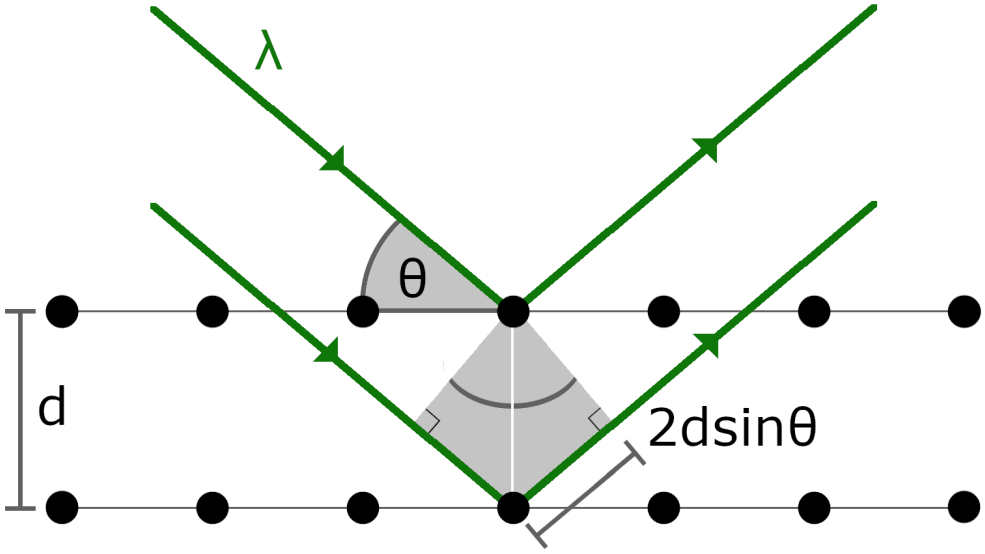


Figure 2.11: Bragg diffraction relation for the coherent interference of scattered beams from a crystalline lattice.

which defines the criteria for constructive interference of incident beams scattered by a crystal lattice. This principle is illustrated in Fig. 2.11. If a reflection is to be observed, the wavelength must be equal to an integer multiple, n, of the electron beam wavelength, $\lambda$. Therefore, the additional length traversed by a diffracted beam with respect to the next coherent beam is proportional to the crystal lattice spacing, d, multiplied by the sine of the angle of incidence, $\theta$. This relation can then be used to determine the atomic structure of the diffracting crystal [30].

Crystalline materials and structures can be identified and categorised by a set of defined symmetry relations [207]. The symmetry of a crystal correlates to the structure of its unit cell. In turn, this defines the set of positions that atoms can occupy, which can provide us with the indexable coordinates and corresponding reflections in diffraction patterns. These planes are defined by the Miller indices (h,k,l): integer numbers that, in combination, encapsulate the fundamental features of the crystallographic make-up of the sample, as introduced in Section 1.2 and to be discussed later. This principle can be spanned across multiple diffraction techniques (Section 2.6) in order to identify the sample, via analysis of the reflections.

Provided the crystal symmetry is then known, or can intuited, Bragg's relation can be used to obtain the lattice spacing of the system. The simplest instance of this is for the cubic system, where the lattice parameter relation to the Miller Indices is

given by

$$\mathrm{d} = \frac{\mathrm{a}}{\sqrt{h^2 + k^2 + l^2}} = \frac{\lambda}{2\sin(\theta)}. \tag{2.18}$$

Here the lattice constants, (a,b,c), are denoted by "a" alone (a=b=c) [207]. The right hand side of Eq. 2.18 gives the rearranged form of Bragg's law, such that it can be directly applied to indexing the diffraction patterns.

Cubic systems, such as AgCl, are defined most simply due to their uncomplex symmetry relations and right-angled bonds. However, once outside of such a unit cell, and into other systems, the relationships become more intricate, and harder to calculate without more specific information about the system. In the case of bulk SnSe, the equation becomes

$$\frac{1}{\mathrm{d}^2} = \frac{\mathrm{h}^2}{\mathrm{a}^2} + \frac{\mathrm{k}^2}{\mathrm{b}^2} + \frac{\mathrm{l}^2}{\mathrm{c}^2}, \tag{2.19}$$

since it is an orthorhombic system belonging to the "Pnma" space group, where $\mathrm{a} \neq \mathrm{b} \neq \mathrm{c}$ [207]. This is also true of $Sb_2Se_3$ and $Sb_2S_3$ [208].

However, the relation for a rhombohedral system, to which ($R\bar{3}m$) $Sb_2Te_3$ belongs, is more complex still and given by

$$\frac{1}{\mathrm{d}^2} = \frac{(\mathrm{h}^2 + \mathrm{k}^2 + \mathrm{l}^2)\sin^2(\alpha) + 2(\mathrm{hk} + \mathrm{kl} + \mathrm{hl})(\cos^2(\alpha) - \cos(\alpha))}{\mathrm{a}^2(1 - 3\cos^2(\alpha) + 2\cos^3(\alpha))}. \tag{2.20}$$

Whilst the lattice constants are all of equal value (a=b=c), the angles in the unit cell are no longer 90° ($\alpha = \beta = \gamma \neq 90°$) which therefore requires the introduction of angle-dependent terms. Therefore, in order to calculate the lattice spacings, or index the peaks in a diffraction pattern accurately, the angles in the lattice cell must be known. In standard single crystal samples, this is made more convenient by the presence of the regular repeating structure and sharp, bright spots in diffraction patterns with measurable intensities and distances - as depicted in Fig. 2.12 (a).

However, often the crystals in the specimen are not all in the same orientation with respect to the electron beam. Therefore, the effect is a set of overlapping lattices. This presents in SADPs as rings of sharp spots - as illustrated in Fig. 2.12 (b). As the number of different orientations increases, so too do the number of peaks. Eventually, these reflections can no longer be distinguished from one another, and the aspects morph into rings. This is the principle by which the characteristic rings of SWCNTs arise, which are clearly observed and indicated in Fig. 2.12 (c) and (d) and Fig. 2.13 [38]. The equatorial line - illustrated in Fig. 2.12 (d) - is normal to the bundle axis. The relative spacing of the reflections along, and parallel to, this line are dependent upon the specific chirality of each consituent SWNCT [209]. This is illustrated in the simulated SADP for a model of an individualised (10,10)

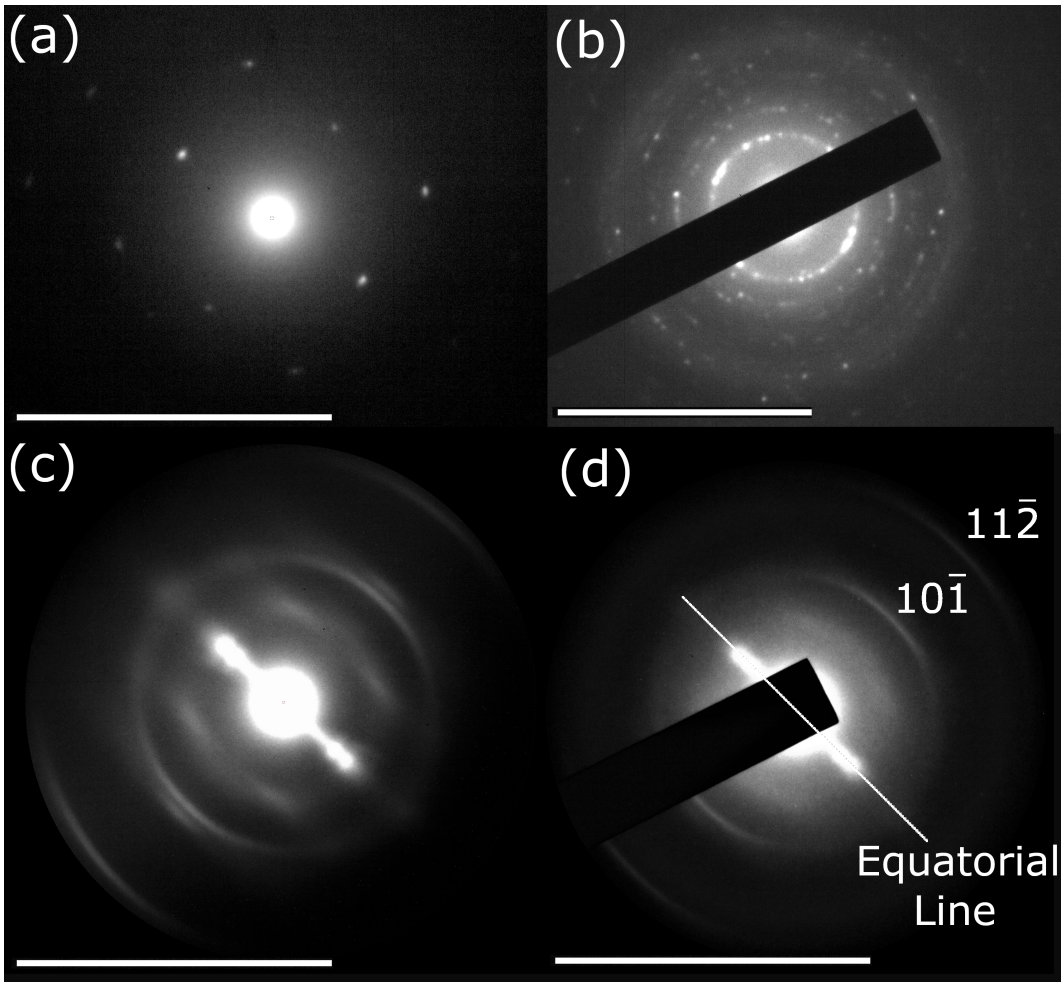


Figure 2.12: Examples of SADPs from (a) crystalline, (b) polycrystalline, (c) nano-confined crystalline, and (d) amorphous materials. The SADPs were obtained for (a) a single nanocrystal of $Sb_2Te_3$, (b) a thick, multi-faceted nanocrystal of $Sb_2Te_3$, (c) a bundle of filled $Sb_2Te_3$@SWCNTs, and (d) a bundle of SWCNTs filled with amorphous nano-confined $Sb_2Te_3$, respectively. The key characteristics of SWCNT bundles are identified in (d). Scale bars are 10 $nm^{-1}$.

armchair SWCNT filled with $Sb_2Te_3$ in Fig. 2.13 (a).
Since each nanotube is a single rolled sheet of monolayer graphene, the basis of the SADP is just that for multiple orientations of graphene. For an individual SWCNT this can be seen clearly, as the dots making up the equatorial line and rings can still be discerned - as depicted in the simulated SADP in Fig. 2.13 (a) [210–212]. In this case, (n,m) for the CNT can be calculated, based on the relative distances between the equatorial line and the radial dots - as described by the relations in Section 1.2 [213]. The TEM image and SADP shown in Fig. 2.13 (a) were simulated using clTEM - as outlined in Section 2.3 - from a model built in CrystalMaker of a fragment of $Sb_2Te_3$ nano-confined inside a (10,10) SWCNT. It is also possible to obtain "ideal" simulated electron diffraction patterns through the use of CrystalDiffract®. This software models the anticipated scattering from a given crystalline structure, when provided with an input model and specified parameters. As it belongs to the CrystalMaker™ suite of software, you can directly transfer between a structural model built in CrystalMaker™ and the modelled diffraction behaviour in CrystalDiffract™, in real time. Therefore, it is possible to quickly see the effect that rotating the crystal and view direction has on the diffraction pattern. However, this software does not account for the relative limitations and parameters of the TEM systems, unlike clTEM.
The lines of reflections parallel to the equatorial line - appearing as a line of spots along the centre of the SADPs in Fig. 2.13 - that typically contribute to the chracteristic SWCNT rings have been identified. The reflections arising from the nano-confined $Sb_2Te_3$ have also been indicated. Whilst the reflections in the experimental SADP given in Fig.2.13 (b) are sharp, some distinction has been lost to the reflections contributing to the equatorial line around the central beam spot. This is due to the fact that this is not an individualised filled SWCNT, but rather a thin bundle comprised of a few $Sb_2Te_3$@SWCNTs.
Once the SWCNTs are in bundles, with many chiralities aligned next to one another, the aspects blur into the characteristic rings - as can be seen in the SADP for the bundle of $Sb_2Te_3$ shown in the TEM image in Fig. 2.13 (c). The increased number of SWCNTs has also had a visible effect on the appearance of the parallel SWCNT reflections, which already appear more akin to the characteristic rings of a bundle (Fig. 2.13 (c)) than the spots of an individualised SWCNT (Fig. 2.13 (a)). The larger the bundle, and the wider the range of chiralities present, the brighter these rings will appear, but the more they will also appear to blur, similar to that of an amorphous sample. However, they will remain separated by the same radial distance as with the patterns for graphene [214]. Therefore, the CNT rings can be

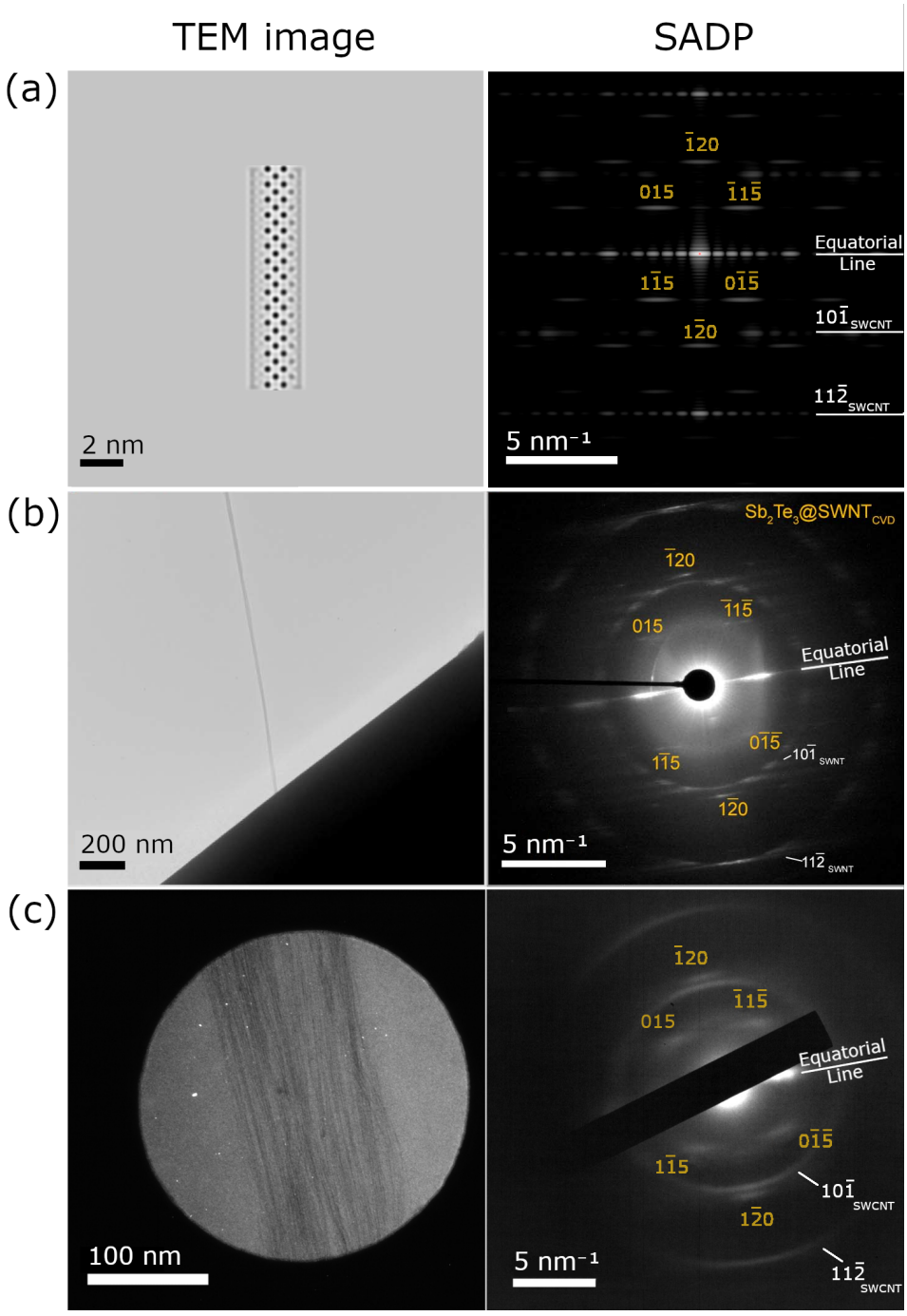


Figure 2.13: Experimental and simulated TEM images and SADPs of filled SWCNTs. (a) Simulated TEM image and SADP of a single (10,10) SWCNT filled with $Sb_2Te_3$. Simulated in clTEM using a model built in CrystalMaker. (b) Experimental TEM image and SADP - taken by J. Sloan - of a few SWCNTs $Sb_2Te_3$@SWCNTs in a thin bundle, suspended across a slit in a $Si_3N_4$ substrate - synthesised by J. Viner under the supervision of D. Smith. (c) Experimental TEM image - with selected area aperture - and SADP of a bundle of $Sb_2Te_3$@SWCNTs. The key reflections for the SWCNTs (white) and $Sb_2Te_3$ (yellow) have been indexed.

used to calibrate SADPs prior to quantitative analysis being conducted, provided any elliptical astigmatism has been corrected for (Fig. 2.14 (a)). Rings such as these can be indexed for known samples by looking at the ratios of their diameters, $\frac{\phi_n}{\phi_1}$, where $\phi_1$ is the first ring diameter. From this, phases can be identified from the combination of interplanar spacings present.

The samples presented in this research are, predominantly, crystalline materials constrained to one dimensional cylindrical structures. Therefore, in reality the sample is comprised of a bundle of nanocomposites, with a range of, pseudo-randomly orientated, structures. This presents as a smearing of the diffraction aspects and reflections into arcs (Fig. 2.12 (c)), and must be accounted for when analysing the patterns. In this respect, the diffraction patterns appear more akin to the diffuse rings formed by an amorphous sample. These arcs correlate to the average spacing between atoms. Amorphous samples do not possess the repeating crystal structure that determines the indexable characteristics of diffraction patterns from crystalline materials. However, in order to minimise the energy, the atoms in an amorphous sample will re-arrange to produce recurring average atomic separations. This presents as the blurred rings in SADPs, as can be seen by the blurred intensity in Fig. 2.12 (d) where crystalline aspects used to be in Fig. 2.12 (c). One way of analysing such samples and comparing them to their crystalline counterparts - as for Fig. 2.12 (c) and (d) - is via inspection of their radial intensity profiles, where the SADPs are analysed on the basis of intensity identification as a function of radius from the central beam spot. The intensity profile as a function of radius is extracted within a given line or angular range and can be isolated to particular regions or cones of interest.

SADPs - as for (S)TEM images - were viewed and collated in DigitalMicrograph$^{TM}$. This software is widely used for evaluating (S)TEM images and SADPs, and has the added benefit of the availability of a range of plugins - scripted by D. R. G. Mitchell - for image correction, filtering, and analysis [215]. "DiffTools" is a suite of tools which allows calibration, enhancement, formatting, measurement and analysis of SADPs, as well as calculation of simple crystallographic data.

An initial step is to calibrate the SADP to create a homogeneous base across all analysed patterns and samples. This was achieved through the use of the "Calibrate SADP" script, and then manually verified by measuring the radii of the SWCNT rings [216]. Again, this verification measurement can also be facilitated through the use of Mitchell's "Point and Measure" script. This code offers a quick and crude measurement of diffraction patterns by eye. All distances are calculated relative to the centre of the SADP, which must be defined using "Locate SADP Centre" in

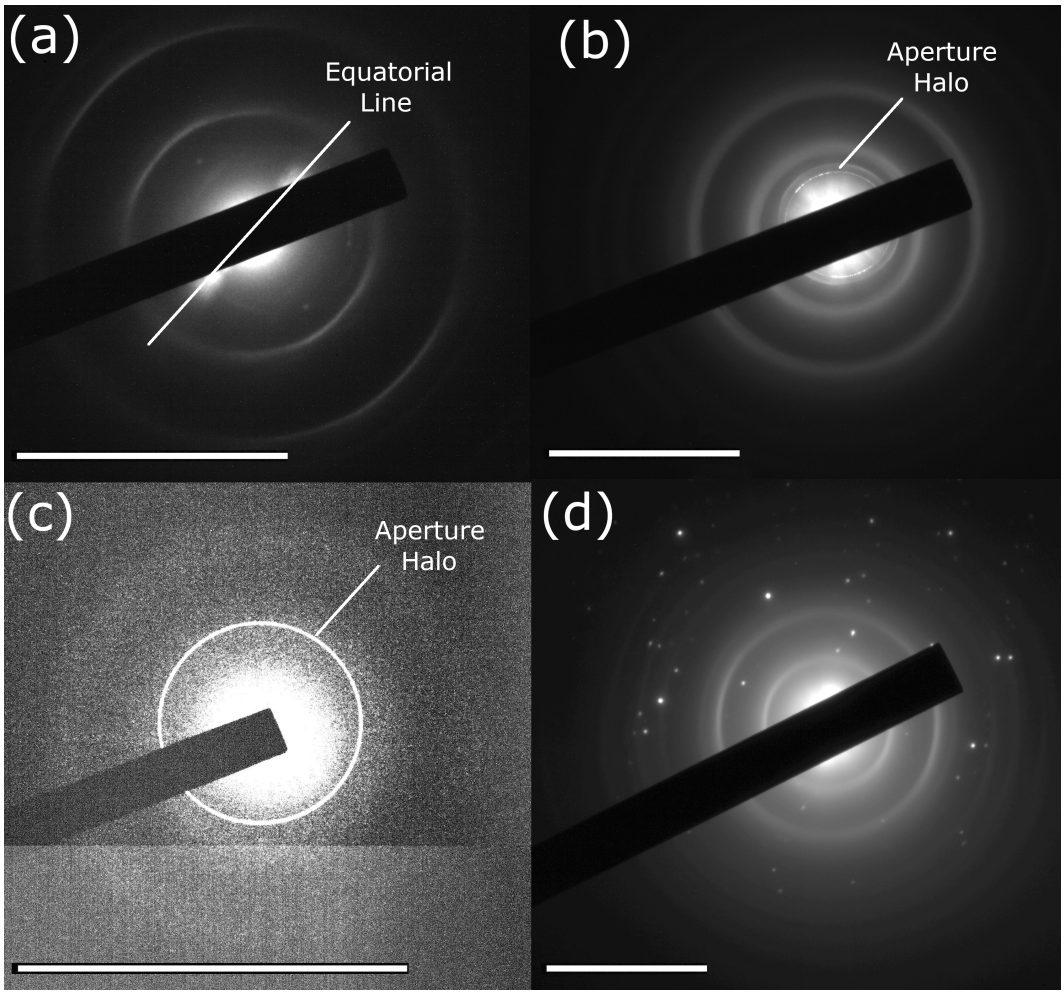


Figure 2.14: Examples of the issues that can arise in SAED. (a) Elliptical aberration of the rings in a SADP for a bundle of unfilled SWCNTs. (b) SADP of a mat of unfilled SWCNTs. A halo is also present - which is an artefact from scattering from an aperture. (c) If the beam is too weak, or not centred then low intensity is observed. The halo artefact is far more evident under these conditions. (d) Extraneous (polycrystalline) material on the outside of the SWCNT bundles appears as bright, sharp reflections with little or no seeming order or symmetry over the SADP. Scale bars are 10 $nm^{-1}$.

DiffTools, or "Centre Finder" in RDFTools. Points are then identified by manual point-and-click identification, which are marked with real d-spacing values. Whilst this is not very accurate, for some applications it provides a quick method for checking patterns.

A more involved process is to use the "CHT Diffraction Analysis script", which performs a circular Hough transform based automatic measurement of polycrystalline ring diffraction patterns. This can provide a method for accurately determining ratios to identify phases and materials in polycrystalline samples. However, the presence of reflections from other crystalline structures - such as those in Fig. 2.13 and Fig. 2.14 (d) - can interfere with these ratio calculations and skew the result.

The combined use of this suite of scripted diffraction tools allows for both qualitative and quantitive conclusions and comparisons to be drawn from polycrystalline and amorphous samples. The accuracy of the scripts can be seen in the calculation of the d-spacings from a SADP, where D. Mitchell quotes there to be a relative error of less than 0.65 % between the calculated values and the absolute measured values [216].

However, it is of primary import to ensure not only that the system is adequately aligned and free of aberrations (Fig. 2.14 (a)-(c)), but also that the sample is of good quality, well-dispersed, and free of external structures and extraneous crystalline material (Fig. 2.14 (b)-(d)). These factors will influence the breadth and complexity of the corrections that are required to accurately analyse the SADPs. A beam stop - which can be seen in the SADPs in Fig. 2.14 - is often used to prevent the central beam of highest intensity from destroying the pixels in the CCD. However, this can interfere with the analysis of SADPs, especially where scripts are used, due to the false "zero intensity" region (in terms of scattering from the sample) introduced by the beam stop.

In the case of Fig. 2.14 (a), the elliptical aberration - which can be caused by astigmatism ($A_1$) - to the SWCNT rings inhibits our ability to accurately measure, calibrate and characterise the SWCNT sample from its SADP. This can, however, be corrected for to a certain extent through the use of the "Ellipse Fitting Analysis" script, which facilitates the adjustment of the patterns when required. The script uses an ellipse fitting method to analyse SADPs from polycrystalline materials, and identifies and corrects any elliptical distortion which may be present. The pattern centre, ring dimensions and d-spacings, are reported in the output. These correction factors can be stored, thus allowing distortions in single crystal spot patterns to also be corrected.

Another issue that can be caused by a system that is not aligned optimally is the

appearance of a sharp, high contrast halo in SADPs - as illustrated in Fig. 2.14 (b) and (c)). This halo can appear to be aligned with the diffraction pattern of the sample - as in Fig. 2.14 (b) - or with a displaced centre - as in Fig. 2.14 (c). It is most likely an artefact of scattering from an aperture, and is difficult to remove from a pattern once present. Such an artefact can appear to have even higher contrast in patterns acquired using low beam brightness - as shown in Fig. 2.14 (c). This is particularly pertinent for beam sensitive samples such as those used in this research, as using a low beam brightness can limit the risk of damage to the sample from beam irradiation - as described in Section 2.2.5. However, this low dose regime can also significantly decrease the counts to the detector. Indeed, if the beam brightness is too low, then even the brightest reflections can be lost to background counts and noise - as seen in Fig. 2.14.

In contrast, often the sample itself can be the cause of the issues. If the sample is not well-dispersed, as is populated with multi-orientated bundle axis, then we are unable to isolate a distinct equatorial line, and the inner reflections from nano-confined crystalline material can be lost - as can be seen in Fig. 2.14 (b). Meanwhile, the SADP in Fig. 2.14 (d) of a bundle of unfilled SWCNTs shows a clear presence of polycrystalline structures on the upper portion of the observed area. These reflections can have poorly-defined order or symmetry and it can be difficult to isolate them from the main pattern. Therefore, the presence of such structures and reflections can greatly interfere with the analysis and characterisation of samples via their SADPs.

### 2.2.5 Irradiation Considerations

Considerations for the irradiation effects on the materials must be taken into account, as introduced in Section 1.4. These can present in several different ways, from added motion of the atoms, to the rearrangement and destruction of the nano-confined sstructures. The study of this dynamical behaviour of nanocrystals in TEM - including size, temperature or irradiation effects [217] - forms a distinct portion of this research.

In the case of inorganic nanostructures and SWCNTs, the two primary forms of radiation damage that we are concerned with are radiolysis and knock-on damage [29, 140, 142]. Knock-on damage is the dominant mechanism by which CNTs are damaged when irradiate by the electron beam. This effect results in displacement of carbon atoms in the lattice due to inelastic scattering events, which can be sufficient so as to expel the atom from the lattice completely. For CNTs, the critical voltage

for knock-on damage is $V_c = 86$ kV [16, 26]. Furthermore, the inelastic scattering events can incite secondary damage effects in the samples due to the generation and propogation of secondary electrons, phonons and free-radical species through the material [30]. Therefore, the electron beam accelerating voltages used in this research were maintained below this threshold - 80 kV for (S)TEM imaging.

Radiolysis is the dominant mechanism for beam-induced damage to CNTs at 80 kV. This has the effect of breaking, and making, of inter-molecular and chemical bonds due to electron-electron and ionisation interactions. Therefore, this is especially severe for organic matter. In the case of CNTs, this can lead to the occurrence of carbon free-radicals (unbonded carbon atoms) which can diffuse out of the sample, in a similar way to knock-on damage [30]. This can also be said for phase change materials, since knock-on damage does not normally occur at room temperature for these substances. Doses to the samples - as measured on the phosphor screen in terms of the current, or strength, of the electron beam incident on the sample per unit area ($pA{\cdot}cm^{-2}$) - and their effects were monitored across different brightnesses and beam intensities [56]. This is particularly important for the effects and mechanisms discussed in Section 2.2.4, 3.3, and 4.3. If we consider, for instance, STEM imaging at 80 kV, with a focal length of 8 cm, and using the smallest Condenser Lens aperture (CL1, which sets a semiangle of 22 mrad [218]), the electron beam current density incident on the sample is maintained at $\sim (0.5 \pm 0.1)$ $pA{\cdot}cm^{-2}$ - as measured on the phosphor screen. Provided the beam current has been measured and properly calibrated - for example with a Faraday cup - and sufficient parameters have been noted at the time of collection, then such beam current measurements could be converted to total electron dose to the sample.

In the case of encapsulated materials, which tend to be significantly heavier than carbon, interactions with the electron beam predominantly result in kinetic energy being imparted directly from the electrons to the atoms and dissipated along the structure. Indeed, the use of protective films and confining environments for the protection of samples from radiation damage is well-documented [219, 220]. However, there is a non-negligible possibility of the displacement of these heavier atoms. The observed movement and rotation of encapsulated structures under the electron beam can be significant and prevelant (Section 3.2). However, prolonged exposure of the filled SWCNTs to the electron beam has been shown to have adverse effects on certain nano-confined fillings. This can range from the rearrangement of the nano-confined structures - resulting in distinctly modified bond distances and long-range order (Section 3.3) - to the dissociation of the encapsulated material to clusters, as for nano-confined SnSe (Fig. 2.15). In all cases reported in this research,

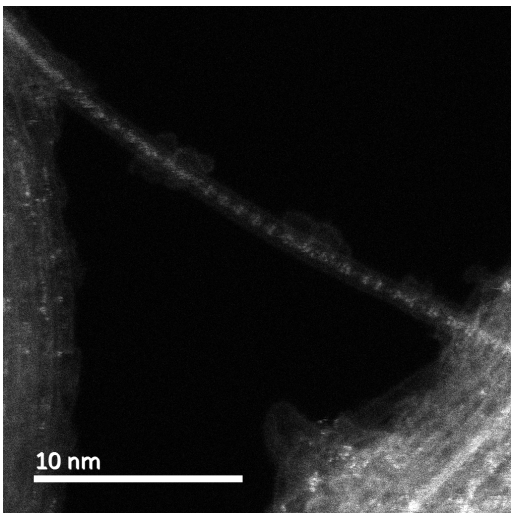


Figure 2.15: ADF-STEM image of clusters formed via dissociation of an encapsulated SnSe nanowire after >2 mins beam irradiation at $\sim 2.0$ pA·cm$^{-2}$. Imaging conducted at 80 kV.

the structure of the SWCNTs is observed to remain intact and devoid of defects.
The impact of interactions of the electron beam with the sample can be inhibited through the use of a cold stage - such as the reduction of diffusion of carbon by a factor of $\sim 10^5$ [140]. Radiolysis can also be reduced by increasing the accelerating voltage of the electron beam, since the energy of the incident electrons is corollary increased. Therefore, the electron scattering cross-section is reduced. However, this then increases the efficacy of knock-on damage. The damage to the sample due to both knock-on damage and radiolysis increases with increasing beam dose.
However, neither of these forms of radiation damage account for contamination effects, which commonly occur due to hydrocarbons on the surface of the sample (Fig. 2.16). This kind of contamination causes distortion to the sample and can be observed in TEM and SEM images [29, 221]. As an area of a sample is irradiated under the beam, the incoming electrons begin to polymerise the stray hydrocarbons. This presents as an amorphous residue on and around the sample, which causes blurring and distortion in imaging. Initially, this is best observed in BF-STEM imaging, due to low contrast of the polymer (similar to that of the CNT) with respect to the filling material (Fig. 2.16 (left)). However, the polymer increases in thickness over time, due to its low vapour pressure and surface mobility, with a higher beam dose inducing the process to occur more rapidly. This increased thickness therefore results in a higher contrast with respect to the surrounding sample, which can present as being significantly brighter than even nanocrystals in ADF-STEM iamging (Fig. 2.16 (right)).
In order to combat this, grids are baked at 90°C under vacuum prior to analysis,

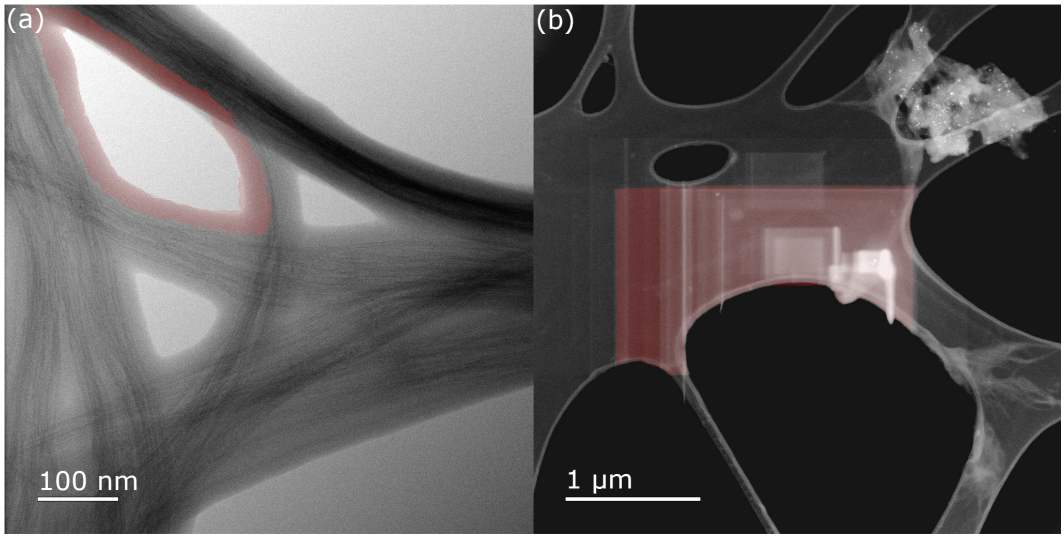


Figure 2.16: (a) BF- and (b) ADF-STEM images of contamination cause by hydrocarbons. Incoming electrons from the beam polymerise the surface hydrocarbons, which (a) appears as amorphous residue around the samples and causes blurring and distortion in imaging. (b) The polymer expands across the irradiated portion of the sample (field of view) and grows in thickness with increasing beam dose. This causes increased contrast with respect to the surrounding sample. Representative regions of beam induced contamination from hydrocarbons are highlighted in red.

particularly in the ARM. This low temperature annealing process is usually sufficent to remove hydrocarbons from the surface of the sample. This, therefore, prevents such distortions as those shown in the representative examples of a $Sb_2Te_3$@SWeNT after irradiation by the electron beam across multiple sites (Fig. 2.16) from interfering with EM analysis of samples.

Despite the issues and considerations outlined above, irradiation of the filled SWCNTs by the electron beam can also be exploited as a helpful tool. Beam irradiation has been observed to have potentially beneficial modifying effects on certain nano-confined fillings, such as rotation of the nano-confined structures (Section 4.2.2), and amorphisation of $Sb_2Te_3$ within SWCNTs [56]. Provided the energy of the electron beam is maintained at or below 80 kV, then the filling can be modified without electron beam knock-on damage to the SWCNT, meaning that the phase transition is potentially completely reversible as there should be no mass loss from the filling, only a rearrangement of the atomic structure.

Further to this, considerations must be made of how size can affect the melting temperature and phase transitions of a particle (Section 2.2.6 and 2.5), which is particularly relevant for nanoparticles with radii less than $\sim$10 nm [143]. From the theory and literature discussed earlier, and in Sections 1.4 and 2.1.3, we ex-

pect small particles and nano-confined materials to exhibit melt point depressions. However, it may be valid to work under the assumption that this principle also holds for other forms of energy input to such a system. It has been established that irradiation under the electron beam, at an accelerating voltage of 300 kV and a dose of $\sim$3000 electrons$\cdot s^{-1}\text{Å}^2$, can cause motion of the atomic constituents in gold nanoparticles to such an extent that sintering and merging of two, previously distinct, nanoparticles occurs within a fraction of a second, even at room temperature. After less than a minute, the nanoparticles had completely merged; the atomic arrangement of one had wholly rearranged to mimic the planes of the other [217]. Under these conditions and with certain assumptions, Buffat theorised [143] that the electron beam induced a thermal heating effect on the order of $(10^0 - 10^1)°\text{C}$. This thermal equilibrium temperature approximation is cited to be more representative of the average temperature for phonons.

When observing structures on the nanoscale, we can consider their structural to be dictated by growth-dominated behaviour, or classical nucleation theory [184, 222]. The first assumes a reformation of atomic bonds into a regular, uniform crystal lattice. In the latter scenario, recrystallisation of amorphised materials occurs from multiple nucleation sites, and is driven by the change in the Gibbs free energy of the system ($\Delta$G), such that

$$\Delta\text{G} = -\frac{4}{3}\pi\text{r}^3\Delta\text{G}_{\text{ac}} + 4\pi\text{r}^2\sigma_{\text{ac}} \tag{2.21}$$

where r is the radius of the nucleus, $\Delta\text{G}_{\text{ac}}$ is the difference in Gibbs free energy per unit volume between the amorphous and crystallise phases, and $\sigma_{\text{ac}}$ is the surface energy at the amorphous-crystalline interface [223]. This function reaches a maximum when $\text{r} = \text{r}_{\text{crit}}$, where

$$\text{r}_{\text{crit}} = \frac{2\sigma_{\text{ac}}}{\Delta\text{G}_{\text{ac}}}. \tag{2.22}$$

Under this principle, Zhu et. al saw a recrystallisation of amorphous $Sb_2Te_3$ films, via distinct nucleation points, under prolonged ($\sim$ 7 mins) exposure to an electron beam. Extensive and persistent alterations to the long-range structure was observed to occur after $\sim$ 20 mins [184].

Other, similar or more extensive, works present a complementary view of how beam irradiation affects samples, particularly when considering samples comprising hundreds of atoms, or fewer [29, 140, 142]. Crystal structure changes [224], or melting & re-solidification processes ("quasi-melting") [225–227], can be observed in these materials under beam irradiation, which is presented in Chapters 3 and 4. Chap-

ter 3 provides evidence and analysis into the observation of significant melting and recrystallisation of $Sb_2Te_3$ in the presence of an electron beam.

### 2.2.6 *in situ* Heating

Analysis of a sample via SAED can provide information on the crystallinity and structure of sample. Therefore, *in situ* analysis can be carried out, and diffraction patterns captured, across a phase transition. These can then be analysed - as outlined in Section 2.2.4 - to better understand the structural changes, amongst others, that the sample undergoes at each stage, as a function of time and temperature - as reported in Section 3.3).

*In situ* heating was achieved using the DENSsolutions Wildfire single tilt heating holder and heating-integrated MEMS chips [4] with silicon nitride thin film windows - as shown in Fig. 2.17. DENSsolutions have quoted that a resolution of $< 1$ Åcan routinely be achieved at 1000°C with these chips. However, the actual resolution is dependent on the specific TEM system. Nevertheless, the achievable resolution at elevated temperatures is reportedly as reliable as for a standard TEM holder.

The Wildfire system can tolerate any temperature between RT and 1100°C for the $SiN_x$ support chips, or 1300°C for the through hole chips. Low resolution SEM images depicting the analysis regions of the two types are given in Fig. 2.17 (a). The low scatter $SiN_x$ support films are electron transparent at $< 20$ nm thick and are stable up to 1100°C, with minimal deformation or change to the z-height. They give a uniform amorphous contribution to the background in TEM imaging (Section 2.2.2) and SAED (Section 2.2.4). The $SiN_x$ offers homogeneous support across the window, therefore enabling the standard dispersion method (see Section 2.1.5) to be used, with the $SiN_x$ acting in place of the usual amorphous carbon support that is present on the lacey carbon TEM grids.

With this in mind, whilst the through hole windows (Fig. 2.17 (I)) may seem like the better choice for diffraction experiments, given their zero background contribution and higher thermal limit, the lack of support makes them impractical for samples on the scale of those in this research. This can be seen in SEM images of a dispersion on $SiN_x$ windows in Fig. 2.17 (b-II): the SWCNT bundles are far to small to be stably supported by the edges of the holes alone. Indeed, almost all would simply pass through, and those that didn't would be unlikely to maintain two points of contact on hole edge. This is illustrated in part for the dispersion in Fig. 2.17 (b-I), where bulk sample is suspended in and across the holes by the remaining mass.

An image of the whole chip after dispersion and deposition of a PCM@SWCNT is given in Fig. 2.17 (c). It is important when depositing the dispersion onto the chip

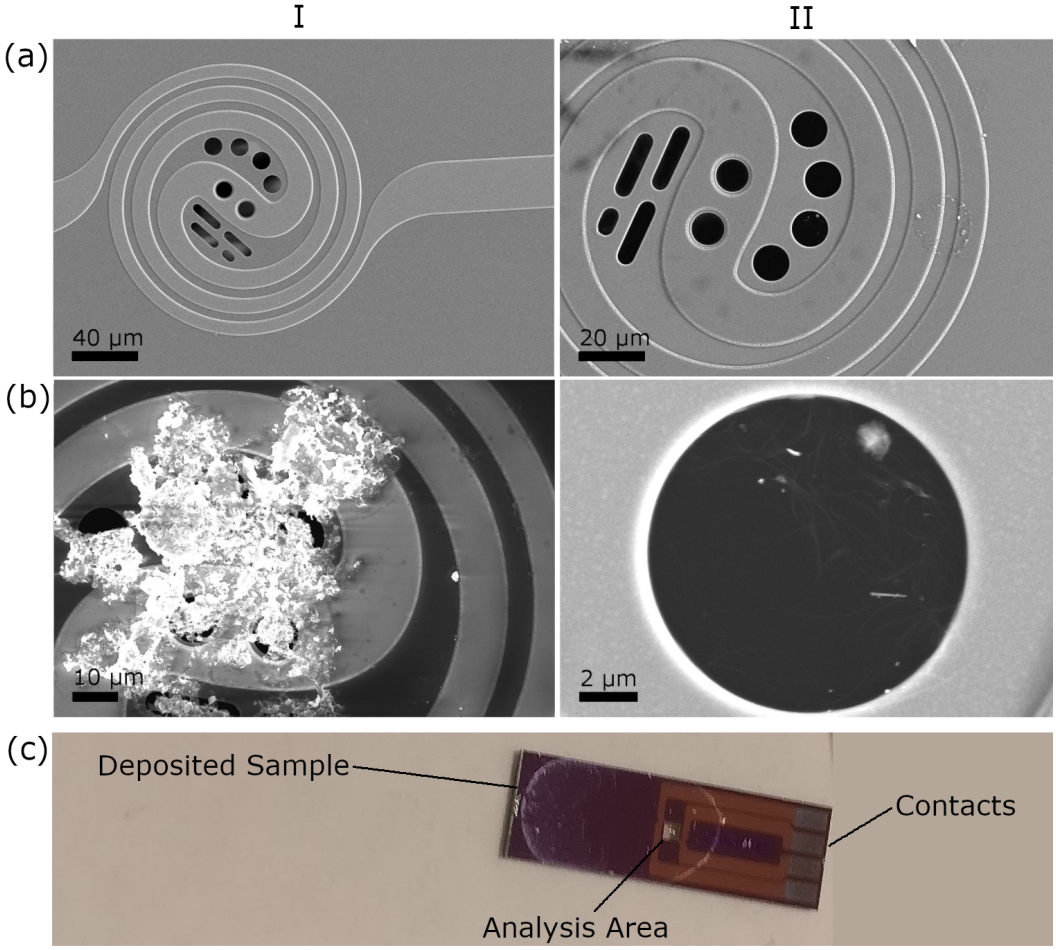


Figure 2.17: Images of the Wildfire MEMS chips that are used for *in situ* TEM and SAED heating studies of samples. (a) Low resolution SEM images of the configuration of the two main window types - (I) through hole and (II) $SiN_x$ support windows. (b) SEM images of (I) a bulk sample dispersed onto a through hole chip and (II) a SWCNT sample dispersed onto a SiN window chip. SEM images obtained at an accelerating voltage of 10 kV. (c) An image of a prepared $SiN_x$ window chip for analysis of a dispersed sample.

that no sample encroaches on the four silver contacts, as this will cause the chip to short out during use, thereby nullifying the temperature-control.
Further to this, to ensure efficient and reliable data is collected on the temperature-dependent phase properties of the materials, considerations must be made of how size can affect the melting temperature of a particle, which is particularly relevant for nanoparticles with radii less than ∼10 nm (as discussed in Sections 2.1.3, 2.2.2, and 2.2.4) [143]. This is discussed further in the context of thermal analysis measurements in Section 2.5, before being applied to the results gathered in this lab in Chapter 3.

## 2.3 Nanoscale Structure Analysis & Image Simulation

Experimental modelling and generation of crystal structures was conducted, both prior to and post experimental HR-imaging, using CrystalMaker® X. In the former case, models tend to be built on a predictive-basis, by taking slices of the bulk structure and projecting in different planes. Whilst the latter deals in atom placement and fragment building based on experimental (S)TEM imaging. Here, we use the relative intensities in ADF-imaging to gain an insight into the likely atomic composition and the bond distances can be measured from the images.
Where models have been built from bulk fragments, or unit cells, the input bulk structure has been taken from published databases [228–230], or directly from the CrystalMaker® library. The library compiles its material from (i) published structures, (ii) accepted models from experimental research database(s), (iii) theoretical models from research database(s). The reference for the the source of each model has been given, where the model has been supplied by - or adapted from - a previously published structure. In either circumstance, there will be some deviation of values for the lengths of interatomic bonds between different sources, which introduces an uncertainty into the bond distances & angles for the models presented here. Therefore, there is some iteration to the refinement processes of the generated models which is not confined solely to intensity-matching [131].
Once a likely model had been constructed (Fig. 2.18 (a)), atomically-resolved (S)TEM image simulations were then produced using clTEM - a multislice simulation software developed by M.A. Dyson and J.J.P. Peters [132, 231, 232]. Broadly speaking, the multislice method is an algorithm used to simulate how an electron beam interacts with matter elastically. It can also be extended to include scattering effects - such as diffuse scattering - through the use of extra parameters - such as

Debye-Waller factors [233]. Therefore, it has become the principle method by which atomic resolution TEM images are simulated [232].
The clTEM software takes the .xyz file (which is comprised of the atomic coordinates and constituents) of the proposed model, and reads the data slice by slice - the size of which are dictated by the user - in order to build up an image based upon the complex interactions of the electrons with the specified structure. The input parameters can be programmed to those most closely matching, or theoretically identical to, that for the experimental system. These include accelerating voltage, probe size, astigmatism values, detector angles and ranges, and even the inclusion of thermal vibrations - which impact the specific brightnesses of elements in ADF-STEM. Therefore, the output TEM, ADF-STEM & BF-STEM images (Fig. 2.18 (b-d)) can be used for intensity and bond length comparisons to a high degree of accuracy, in pseudo-3D. The objective aperture is set to 22 mrad, with a convergence angle of 0.5 mrad. The detector angle ranges are set to (45 - 180) mrad for ADF-STEM and (0 - 80) mrad for BF-STEM. When setting up the clTEM software parameters for ADF-STEM imaging, it is important to constrain the x dimension in the simulation, in order to access the maximum inverse angle necessary to encompass the full range for ADF imaging simulation (i.e. 150 mrad). A maximum inverse value below this threshold will result in an incomplete ADF simulation of the given model that gives representative, but non-quantitative images. A value below 45 mrad will cause the returned image to be comprised entirely of stray noise generated by the program. This is discussed in further detail in Section 4.2.2 and in the context of key experimental results in Section 4.2.3.
A key final parameter to incorporate when running the image simulations in clTEM is the defocus, which is the shift of the focus of the objective lens in (S)TEM - defined as "$C_1$" in the aberration function, $\chi(q)$, for high resolution experimental image formation (Eq. 2.13 in Section 2.2.3). If this value is not optimally chosen, then the resultant image - both in simulations and experiments - cannot be used for quantitative determination of atomic intensities. Indeed, in cases where the defocus deviates significantly from the optimum value, the atoms may become indistinguishable from one another in imaging. In simulations, the deviation can produce images with contrasts that would never be seen in experimental images. Examples of TEM image simulations run on the same model but with differing defocus values are given in Fig. 2.18 (e). Whilst a defocus value of 0 nm may well be the default, we can see from Fig. 2.18 (e-I) that it will not always give an optimally focused image. In the case of Fig. 2.18 (e-I), the image is significantly under-focused, with the atoms broadly appearing as well-defined white dots surrounded by black fringes. Similarly,

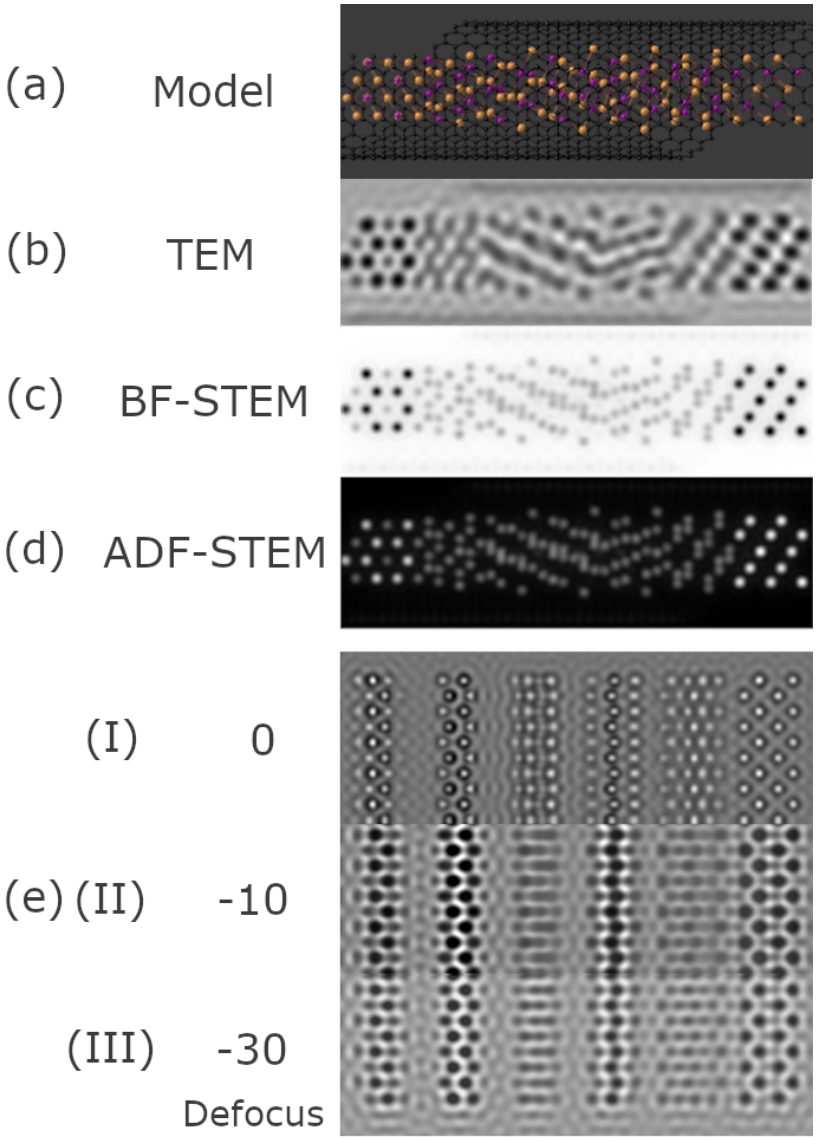


Figure 2.18: Example (S)TEM images simulated using clTEM from a input models. (a) A proposed model fragment - built in CrystalMaker® - for a $Sb_2Te_3$ encapsulated nanowire that has rotated about the SWCNT axis. The exported .xyz file for this model was input into clTEM to produce simulations of (b) TEM, (c) BF-STEM, and (d) ADF-STEM images. (e) TEM image simulations run on the same model of six $Sb_2Te_3$ fragments, with defocus values of (I) 0, (II) -10, and (III) -30. Defocus is given in nm.

to Fig. 2.18 (e-I), if the defocus is too far in the opposite direction (over-focus, as depicted in Fig. 2.18 (e-III)), then the subtler differences between the intensities of the atom columns can be lost. Whilst this may not be immediately obvious when viewing Fig. 2.18 (e-III) as a standalone image, it does become more apparent when compared to Fig. 2.18 (e-II) - which is closer to optimal defocus.

## 2.4 Energy Dispersive X-ray Spectroscopy

Energy Dispersive X-ray Spectroscopy (EDX) is a complementary technique to electron imaging. In this research it is used in conjunction with electron microscopy to identify the elemental constituents in a sample, as depicted in Fig. 2.7 in Section 2.2.1 and Fig. 2.8 in Section 2.2.2. This can be achieved via anlysis of a single point on the sample - which outputs the data as a spectrum of intensity against energy (Fig. 2.19 (a)) - and compositional mapping (Fig. 2.19 (b)). The former can provide quick quantitative data on the composition of the sample. The latter is useful for depicting the distribution of elements across the sample, as a visual overlay of an electron microscope image. Due to the increased area of the sample that that is being scanned in EDX mapping, acquiring sufficient counts to give an accurate rendering of elemental distribution tends to take a lot longer than for acquiring EDX point spectra.

In the case of SEM, an image of the surface of a sample is produced from the secondary electrons resulting from incident electron beam. The lateral resolution (probe size) of the electron beam dictates the volume of the specimen that emits X-rays - as discussed in Section 2.2.1 [196]. The electron probe size is typically on the scale of $\sim$3 nm for an SEM, or $\sim$1 nm for a TEM, although this is largely dependent upon the specifics of the system [202]. EDX utilises collected x-rays emitted from the sample (Fig. 2.7 in Section 2.2.1) and outputs as a spectrum of energy peaks (Fig. 2.19 (a) and Chapter 5).

Combinations of peaks at specific energies are the characteristic fingerprint used to identify the presence of specific elements. Therefore, a higher number of counts in a peak equates to an increased prevelance of a particular element, since there are more atoms present to radiate x-rays. These intensities are then analysed and output by the Aztec$^{TM}$ EDAX software as atomic or weight percentage ratios. Thereby providing quantitative results on the composition and stoichiometry of a sample, as well as the presence of contaminants.

In the case of the X@SWCNT nanocomposites grown in this lab, some of the extra-

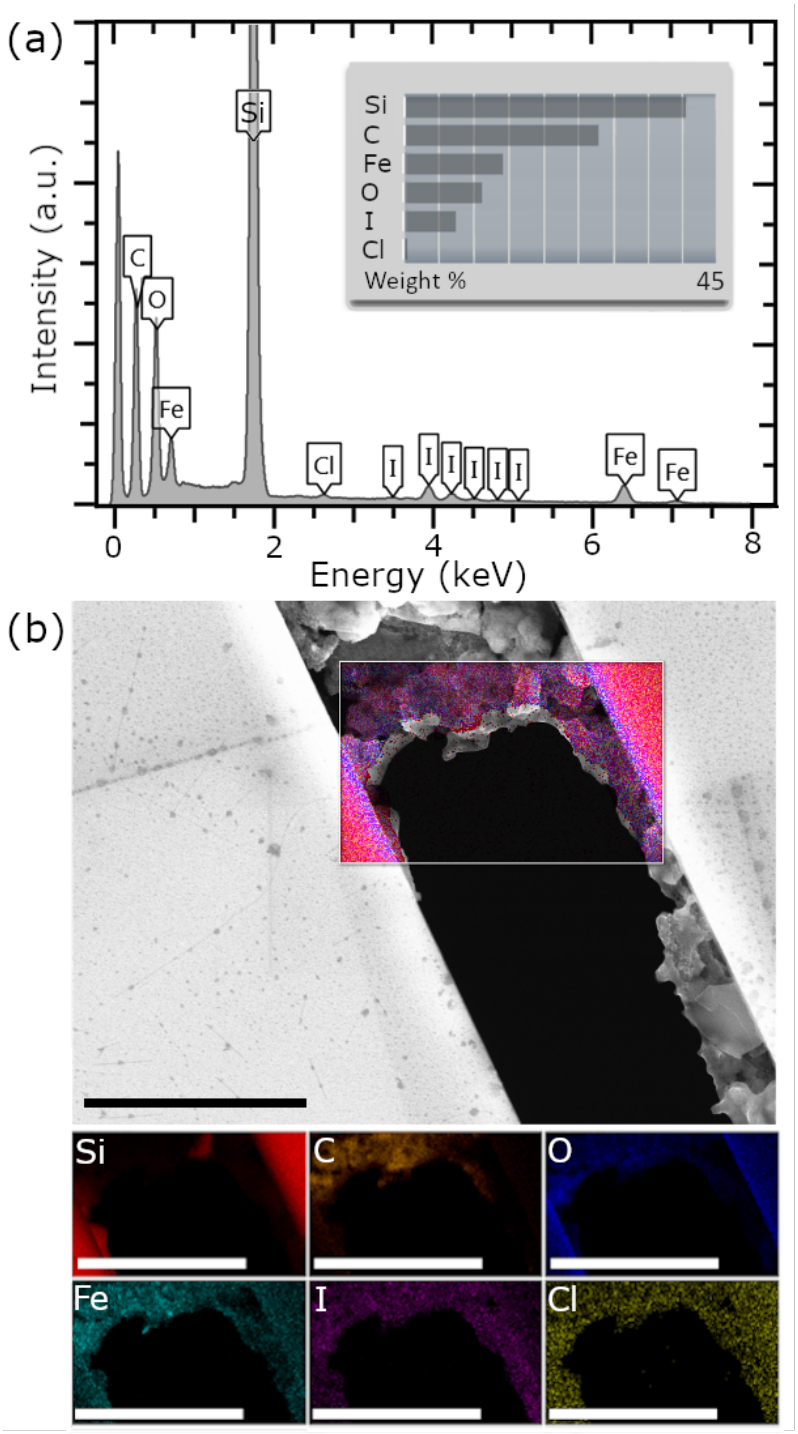


Figure 2.19: Example EDX analysis, conducted on a sample of I@CNTs grown, by J. Viner, on an etched $Si_3N_4$ substrate. (a) The spectrum shows the presence of silicon from the substrate, and carbon and iodine from the growth and filling processes. Traces of the substances utilised in the growth of the nanotubes are also present, in varying proportions. (b) The EDX map demonstrates how the elements are distributed across the analysed portion of the sample, as shown in the SEM image. Scale bars are 5 $\mu$m.

neous materials observed in the compositional analysis carried out on these samples can be attributed to the procedure for making the SWCNTs. This process involves the use of nickel, yttrium, cobalt, molybdenum, fluorine, and iodine (Section 1.2), and therefore their presence is often detected even in processed samples [24, 234]. Whilst the majority of these elements are removed during cleaning and dispersion, some traces have been observed to remain in final samples.

## 2.5 DSC/TGA

Thermogravimetric analysis (TGA) and differential scanning calorimetry (DSC) were used in combination in order to track the mass loss and heat flow characteristics, respectively, of milligram quantities of samples as a function of temperature. A Mettler Toledo STAR$^e$ combined thermal analysis instrument was utilised for these experiments, which captured DSC and TGA measurements simultaneously on each sample, according to a user-specified temperature profile [235].

The accompanying Mettler Toledo STAR$^e$ software allows the user to compose simplistic temperature profile programmes, which the instrument will then execute for a designated sample. An example profile, for one of the experiments outlined in Section 4.4, is given in Fig. 2.20 (a-I). The profiles can be programmed to have a cool down rate with a specified gradient - for example $10°C{\cdot}min^{-1}$ as shown in Fig. 2.20 (a) - or a step down - where the heating element is turned off. However, such a cool down profile is physically unrealistic. Therefore, extra time must be accounted for the actual - exponentially decreasing - cool down rate of the sample. If the sample were to be cycled through the profile in Fig. 2.20 (a-I), for example, then an additional $\sim$30 min will need to be incorporated into the total run time of the experiment for each complete cool down to 25°C required - as has been done for the profile in Fig. 2.20 (a-II).

The total run time of each experiment, as given by the software, is based solely upon the calculated run time of the theoretical profile given to it by the user, as shown above, at which point the data acquisition will stop. However, the next queued experiment will frequently be following a profile that commences at 25°C, although this is dependent upon the user. In such a case, the software will ensure that the measured instrument temperature is as required by the profile before beginning the data acquisition. Therefore, it is also necessary to account for this time interval between experiments when anticipating the total time or all samples, and/or profiles, to be fully processed.

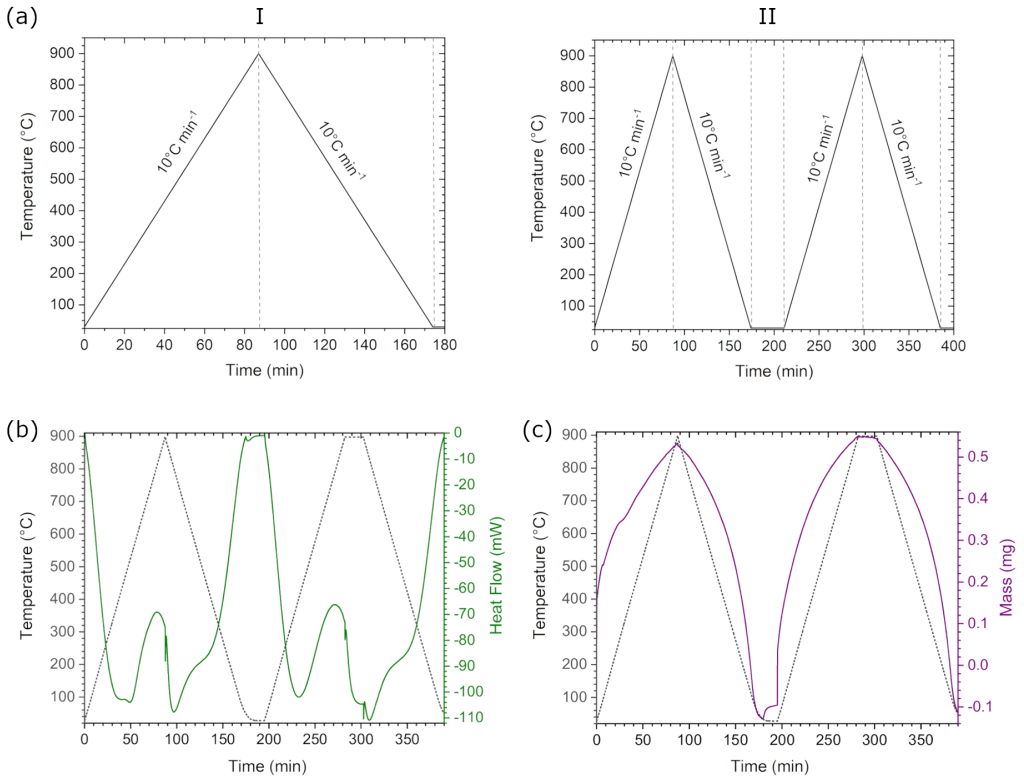


Figure 2.20: Examples of user-defined temperature profiles and calibration data for combined DSC/TGA experiments. (a) User-programmed temperature profiles using the STAR$^e$ software. (I) The temperature profile programme composed for a basic combined TGA/DSC experiment on bulk SnSe up to 900°C and back to room temperature. (II) An example of an extended programme designed to cycle the heating and cooling of the sample, which incorporates the ("hold") cool down interval required to ensure that the sample was at 25°C before proceeding with the second cylce. The dashed lines denote the limits of each stage in the profile. The (b) DSC and (c) TGA curves for a blank (empty) crucible that has been through the indicated (grey dashed) temperature profile. These act as a calibration for the system. There are discontinuities in the data caused by the transition from one segment of the programmed profile to another.

| t [s] | $T_s$ [°C] | $T_r$ [°C] | Value [mW] |
|---|---|---|---|
| 0 | 29.4123 | 25 | -0.201984 |
| 1 | 29.3825 | 25.1667 | -0.221495 |
| 2 | 29.3963 | 25.3333 | -0.234569 |
| 3 | 29.4356 | 25.5 | -0.249356 |

| t [s] | $T_s$ [°C] | $T_r$ [°C] | Value [mg] |
|---|---|---|---|
| 0 | 29.4123 | 25 | 38.7458 |
| 1 | 29.3825 | 25.1667 | 38.7454 |
| 2 | 29.3963 | 25.3333 | 38.745 |
| 3 | 29.4356 | 25.5 | 38.7446 |

Table 2.7: DSC and TGA tabular output file format for an experiment monitoring heat flow through and mass of a sample, with example data. "t" is the time step - relative to the first - at which the heat flow [mW] and mass [mg] "Value" was acquired. "$T_s$" and "$T_r$" are the temperatures of the sample and the programmed profile, respectively.

Each profile must be calibrated before commencing the experiment on samples. This entails running a blank (empty) crucible through the user programmed profile (Fig. 2.20 (a-II)). The resultant heat flow and mass loss curves - Fig. 2.20 (b) and (c), respectively - are then subtracted from future experimental curves for samples undergoing the same profile, on that system. The error margin for DSC instrumentation can be up to ±20°C. This deviation can arise due to heat exchange the sample pans, the sensor, and their surroundings [137, 236].

The evaluation portion of the STAR$^e$ software (Fig. 2.21) allows for completed experiments to be viewed, analysed, and exported as formatted text files. The incorporated experimental data includes the time step (discrete integer, in seconds) at which the data was taken with two temperatures - $T_s$ denoting the measured temperature at the sample in °C, and $T_r$ the temperature according to the input profile °C. The data file is then split into tabular sets, one for each measured output. For this research there were two "value" outputs, with units of mg and mW, denoting the mass remaining and heat flow through the sample, respectively (Table 2.7).

Furthermore, the acquisition of measurements ceases at the instant that the software believes the profile to have been completed - $T_r = 25$°C, as discussed above. Therefore, if $T_s = 25$°C is required, then it is necessary to also programme additional holding time in to the profile at the end of the experiment, which will see that both $T_r$ and $T_s$ are 25°C - as shown in Fig. 2.20.

Equally, it was pertinent to also determine the thermal characteristics of the SWC-

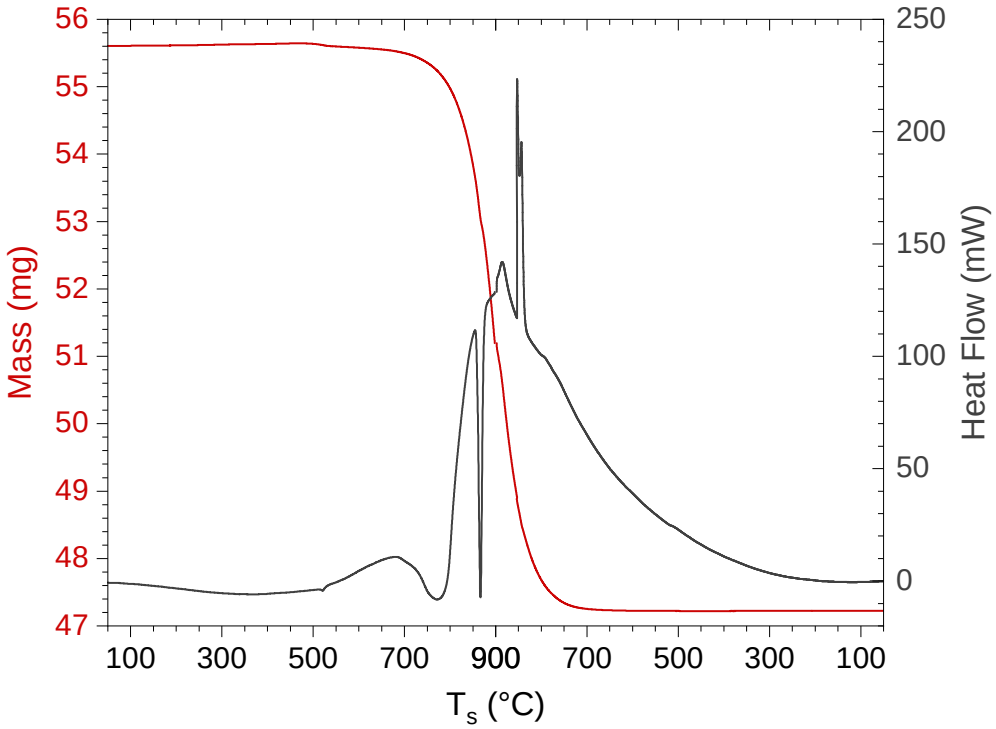


Figure 2.21: The evaluation plot for a combined TGA/DSC experiment on bulk SnSe up to 900°C, as presented when using the STAR$^e$ software. There is a discontinuity in the data at 900°C, caused by the transition from one segment of the programmed profile to another.

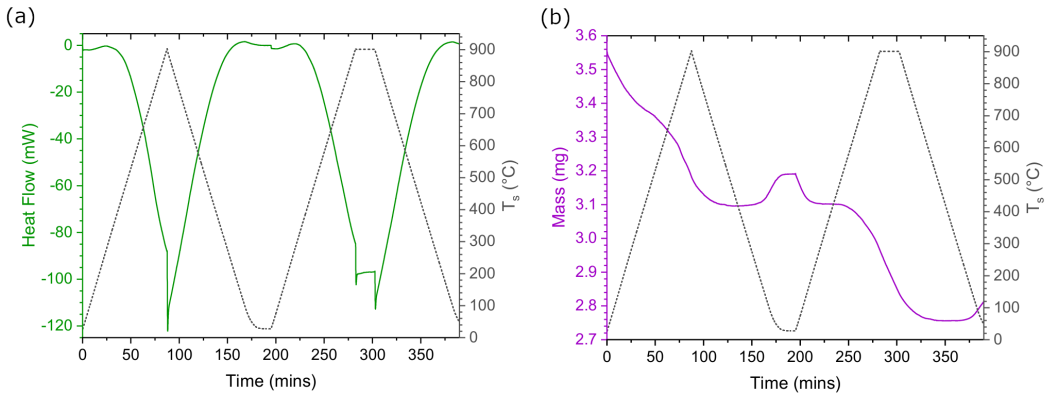


Figure 2.22: Combined DSC/TGA on unfilled SWCNTs, cycled twice through 900°C. Representative plots of combined (a) DSC and (b) TGA analysis on unfilled SWCNTs. The sample was cycled through 900°C and cooled to room temperature twice, as indicated by the black and dashed lines, which track the sample temperature over time.

NTs. Combined DSC/TGA experiments on unfilled SWCNTs (Fig. 2.22) demonstrated that the heat flow characteristics of the SWCNTs (Fig. 2.22 (a)) are almost identical to that of the blank (Fig. 2.20 (b)) - barring the regions of discontinuity, which appear random in their fluctuations. The SWCNTs exhibit no heat-induced phase changes. This confirms them to be suitable and stable as confining elements for this research, and can thus be ignored for the purposes of thermal analysis of the samples. Additionally, there is no significant mass loss (Fig. 2.22 (b)), when cycled through the same protocols as the filled samples. Indeed, in the case of high temperature DSC/TGA on the filled nanocomposites, the SWCNTs can be the dominant, or only, remaining mass in the post-analysis sample.

The acquired DSC/TGA data were used to not only characterise and compare the temperature dependent phase properties of a range of bulk and nano-confined samples, but also to identify temperature ranges of interest for *in situ* EM and SAED heating studies and treatment. They also proved useful for finding the most efficient and least destructive temperatures for exfoliation and processing of as-grown samples, as outlined in Section 2.1.5. Substantial differences in the average values for the heat flow curves between the samples can be attributed to the variance in the value of intial masses used for each sample.

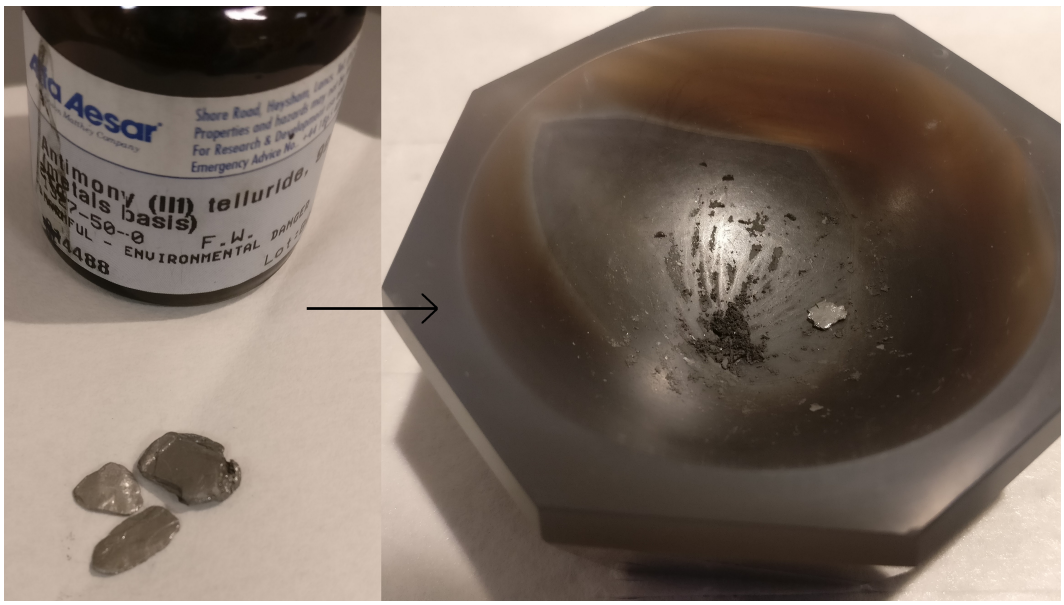


Figure 2.23: The as-supplied bulk crystalline material must be ground down to a fine powder for the XRD experiments. The powder should have no visible metallicity, since this will otherwise cause false intensities of some peaks due to prefential crystallographic orientiations.

## 2.6 XRD

### 2.6.1 Room Temperature

In SAED (Section 2.2.4), the diffraction pattern is collected from transmitted electrons through a finite nanoscale portion of a sample, brought into the image plane using a series of lenses (Section 2.2.2) and then viewed in real time in k-space. In contrast, powder XRD collects scattered x-rays from ∼milligram quantities of a powdered sample (Fig. 2.23) at different angles, and then outputs these as a plot of intensity against scattering angle, $2\theta$. The peaks in these patterns then correspond to distinct reflections from the crystal lattice of the structure.

For a peak to be observed in the diffraction pattern, the incident beams must be scattered in such a way that they are in phase and interfere constructively, as defined by Eq. 2.17 and Fig. 2.11 in Section 2.2.4. The peak positions are defined by the lattice spacings of {hkl}, and so provide information on the unit cell shape and size [237, 238]. The peak intensities can be used to determine the position, and atomic number, of the unit cell's constituent atoms. Therefore, grinding the as-supplied sample into a fine powder using a pestle and mortar (Fig. 2.23) ensures that the crystalline material is randomly distributed. The powdered sample should have no visible trace of metallicity, thereby minimising the chance of distorted peak intensi-

ties from scattering from crystals with specific orientations. Instrument parameters and temperature can determine the widths of the peaks. Although they can also provide information on crystal strain and size.

Therefore, when used in conjunction with accepted theory and experimental databases (ICDD)[228], the sample can be easily identified through the characteristic peaks and systematic absences in the diffraction pattern. This allows not only the composition of the sample to be determined, but also the phase, structure, and crystallinity. Therefore, phase transitions can be tracked *in situ*, as discussed in Section 2.6.2 and 3.5.

Indexing unknown patterns without the use of a database is more rigourous, and involves calculation of $\sin^2(\theta)$ (Fig. 2.11 and Eq. 2.17 in Section 2.2.4) for the major diffraction peaks in the acquired pattern. These values are then used to calculate the Miller indices from the relation between lattice parameter and Bragg's Law for a given crystallographic system. For example, for a cubic system, the expression would be

$$\frac{\sin^2(\theta)}{(\mathrm{h}^2+\mathrm{k}^2+\mathrm{l}^2)} = \frac{\lambda^2}{4\mathrm{a}^2} = \mathrm{A} \tag{2.23}$$

(rearranged from Eq. 2.18 in Section 2.2.4), where A is a constant given by $\frac{\lambda^2}{4a^2}$ [237]. If the symmetry of the crystal is also unknown, then an element of trial and error is required, until the most appropriate relation is identified for the given peak values [238].

Extensive literature has been published on the XRD patterns of CNTs grown by different methods [239–241]. These resources proffer insights into the differences between the characterstics of MWCNTs and SWCNTs of varying diameters and conformations, graphene and graphite, due to the identical base layered structure for these carbon forms.

The standard instrument configuration for powder XRD experiments carried out in this research is the tilted stage set-up employed by the Panalytical X-Pert Pro MPD $\mathrm{K}_{\alpha_1}$ powder diffractometer. This allows best access to a range of scattering angles, with optimised signal to noise. The filament emits electrons that have been accelerated through a voltage of 45 kV, which hits a copper target. A Johanson monochromator focuses the resultant incident beam to give very pure, high resolution copper $\mathrm{K}_{\alpha_1}$ radiation. Heating is accomplished by using an alternative stage and holder, which encapsulate the sample. The temperature, voltage, and other functioning particulars may be monitored by a displayed read-out on the machine. The experiments themselves are controlled and analysed by Panalytical$^{\mathrm{TM}}$ software.

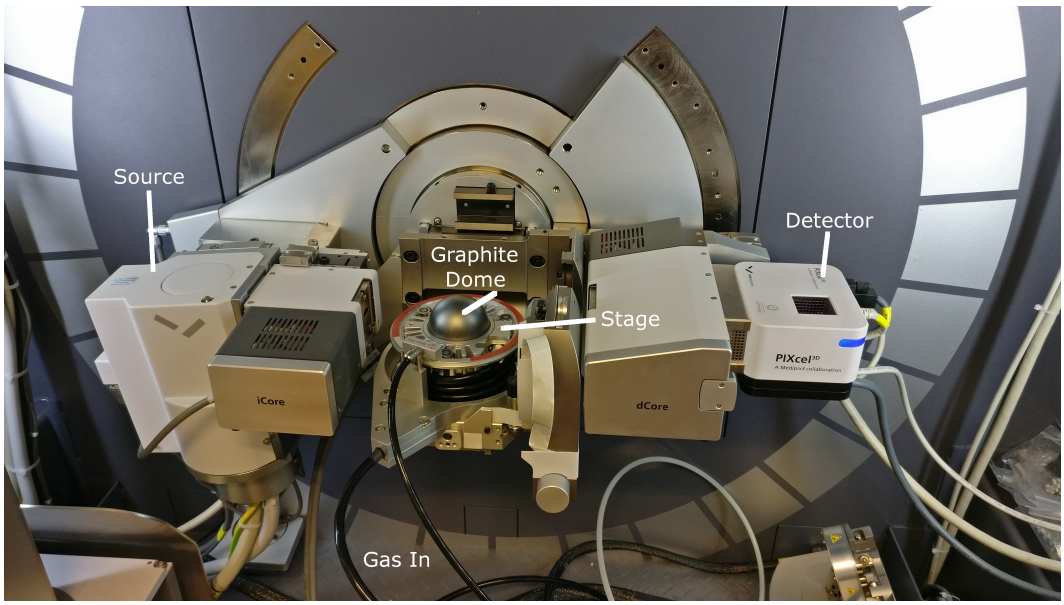


Figure 2.24: Annotated image of the static, flat stage set-up that is employed by the Panalytical Empyrean powder XRD system for heating samples *in vacuo* and under inert atmospheres.

### 2.6.2 Heating *in vacuo*

Initial heating experiments were undertaken using the standard tilted-stage set-up (Section 2.6.1) under vacuum, since the system has the capability to heat samples up to 1200°C under air, or vacuum. However, there were issues with slippage of the sample beyond a certain temperature (Section 3.5). This meant that an alternative had to be found. Early ideas and concepts included putting a silicon cap directly over the sample and stage, in order to secure the sample in place. Ultimately, a new XRD machine with a flat stage, capable of heating under a N vacuum, presented the best solution (Fig. 2.24).

The Panalytical Empyrean system also utilises a powdered sample, with a shallow sample holder that is clipped into the stage. However, the system is capable of maintaining a depressed atmosphere of $\sim 0.2$ bar under nitrogen around the sample. This is achieved through the use of an encapsulating graphite dome (as indicated in Fig. 2.24) which, although contributing a large graphite peak to the obtain patterns, allows the sample and hot stage (Anton Paar DHS 1100) to be wholly encased in an inert atmosphere, whilst being heated to up to 1100°C. The incorporation of a solid state PiXcel detector allows for greater sample intensities to be gathered, due to enhanced counting statistics. In fact, identification of phases can be accomplished after only 5 minutes for some samples. This also eliminates the requirement for a

beam attenuator, and so increases the sampled area and intensity over time. Whilst this allows for greater flexibility when studying polycrystalline samples, it also means that the total sample volume must be sufficient to wholly, and consistently, cover the entire sample holder. Should there be any shrinkage or loss of sample, then peaks corresponding to the mixed steel alloy holder will appear in the diffraction patterns, making compositional analysis and sample identification significantly more difficult, or impossible (Section 3.5).

### 2.6.3 Characterisation of X-Ray Diffraction Patterns

Whilst it is possible to determine the contributing elements and their phases via analysis and calculation of peak positions and intensities in XRD patterns, this is a time-consuming process that often requires the composition and approximate structure to be roughly known, prior to ananlysis. It is more common in the present day to cross-reference the obtained pattern with a database of published and accepted patterns using peak-matching software.

At Warwick, this is conducted using Panalytical$^{TM}$ software and its associated database of patterns. There are numerous room temperature XRD experiments on bulk samples of various compositions, stoichiometries, and symmetry groups in the literary domain, which have contributed greatly towards the databases that researchers draw from - which include the International Centre for Diffraction Data (ICDD), the Inorganic Crystal Structure Database (ICSD), and the National Institute of Standards and Technology (NIST) [228–230]. Several theoretical, or ideal, patterns were taken from this database, in order to compare and identify the relative aspects of experimental patterns obtained over the course of this research (Section 3.5). For instance, several patterns were found in published journals for antimony telluride bulk and platelet patterns through the use of these databases, which contributed greatly in the identification of key phases in the nano-confined samples in Section 3.5 [10, 242–244].

Diffraction patterns simulated from published structural models of, for example, stoichiometric $Sb_2Te_3$ with different phases were also used to compare against the experimental patterns (Section 3.5). These were obtained much in same way as the simulated electron diffraction patterns - as outlined in Section 2.2.4 - using CrystalDiffract®. This software simulated the scattering from a given crystal structure provided an input model and specified parameters. This offered "ideal" XRD patterns with which to compare the positions and relative intensities of different peaks.

# Chapter 3

# Encapsulated $Sb_2Te_3$

## 3.1 Introduction

This chapter outlines and discusses the growth and characterisation of encapsulated $Sb_2Te_3$@SWCNTs, on scales less than $\sim 2$ nm in diameter. The first section explores the stoichiometry, quality and structural characteristics of the grown samples, in both bulk and low dimensional structures. Energy Dispersive X-ray analysis is utilised in conjunction with Electron Microscopy to understand the effects of the different growth processes on the resultant samples. Purified $Sb_2Te_3$-filled nanotubes were then analysed using Aberration Corrected Scanning Transmission Electron Microscopy in order to identify the $Sb_2Te_3$@SWCNT structures. High resolution TEM images demonstrated that the sample contained nanotubes with diameters in the range of $(0.7 - 1.7) \pm 0.3$ nm, with few outliers. This diameter range was achieved through the use of SWCNTs from three different suppliers, as outlined in Section 1.2. Further analysis led to the identification of the crystal structures that form when $Sb_2Te_3$ is nano-confined to specific diameter ranges. Atomic modelling and (S)TEM simulation, in correlation, enabled the accurate determination of these nano-confined structures, which have been constructed into a catalogue.
The second section investigates the Selected Area Electron Diffraction characteristics of these nanocomposites, and analyses *in situ* the effect of electron beam irradiation and heating on these samples. The obtained Selected Area Diffraction Patterns are analysed using radial intensity profiles. These results are then compared with modelled - experimental and *ab initio* Molecular Dynamics - diffraction behaviour and simulations in order to build a full picture of the amorphous-crystal phase transition.
The third section moves into characterising the thermal behaviour for the different

forms of $Sb_2Te_3$. Differential Scanning Calorimetry and Thermogravimetric Analysis were used in combination in order to determine the transitional temperatures and mass loss behaviour, respectively, of bulk and nano-confined $Sb_2Te_3$. These investigations revealed a melt point depression in encapsulated $Sb_2Te_3$ in comparison with the bulk.
The fourth section analyses the composition and phase of different crystalline structures of bulk rhombohedral ($R\bar{3}mh$) and nC-$Sb_2Te_3$ via XRD analysis at room temperature. The effects of temperature and heat cycling on the samples were also investigated. This showed the appearance and recedence of different reflections and phases, which potentially includes the metastable $R\bar{3}mf$ cubic $Sb_2Te_3$ phase.

## 3.2 Structural Analysis

### 3.2.1 Large Scale Structure & Composition

The fabrication of $Sb_2Te_3$-filled SWCNT samples was carried out using the melt method (as described in Section 2.1). An important initial step in analysing the grown samples is verifying their composition and structure. This can be achieved via direct analysis of the $Sb_2Te_3$@SWCNTs sample. However, this requires the nano-confined sample to be processed and dispersed onto a TEM grid, as outlined in Section 2.1.5. A quicker method is to analyse the bulk remnant material from the growth in the SEM. This has the additional benefit of allowing for direct comparison with the as-supplied bulk $Sb_2Te_3$. This can be achieved via EDX analysis, and combined with SEM imaging, to quickly and efficiently compare the effects of different growth protocols on the composition and large scale structure of the samples.
The as-supplied bulk $Sb_2Te_3$ is a layered rhombohedral crystal (Fig. 3.1 (a)) and belongs to the $R\bar{3}m$ space group. As such, it has underlying trigonal and hexagonal symmetry (Fig. 3.1 (a) [001]), which is expected to strongly present in the bulk crystals.
A comparison of the structural appearance at the surface of the bulk samples reveals rudimentary similarities and differences (Fig. 3.1 (b)-(d)). The source bulk $Sb_2Te_3$ for the growth experiments is supplied by Alfa Aesar in the form of flakes with dimensions on the order of millimeters to centimeters. Due to the layered nature of bulk $Sb_2Te_3$, these flakes are readily cleaved and broken into smaller fragments, which results in micrometer flakes and powdered material also being present. Therefore, when analysing the large scale structure of the as-supplied $Sb_2Te_3$ (Fig. 3.1 (b)), the surface of the ($\sim$ 100s $\mu$m) flakes is often populated by further microstructures.

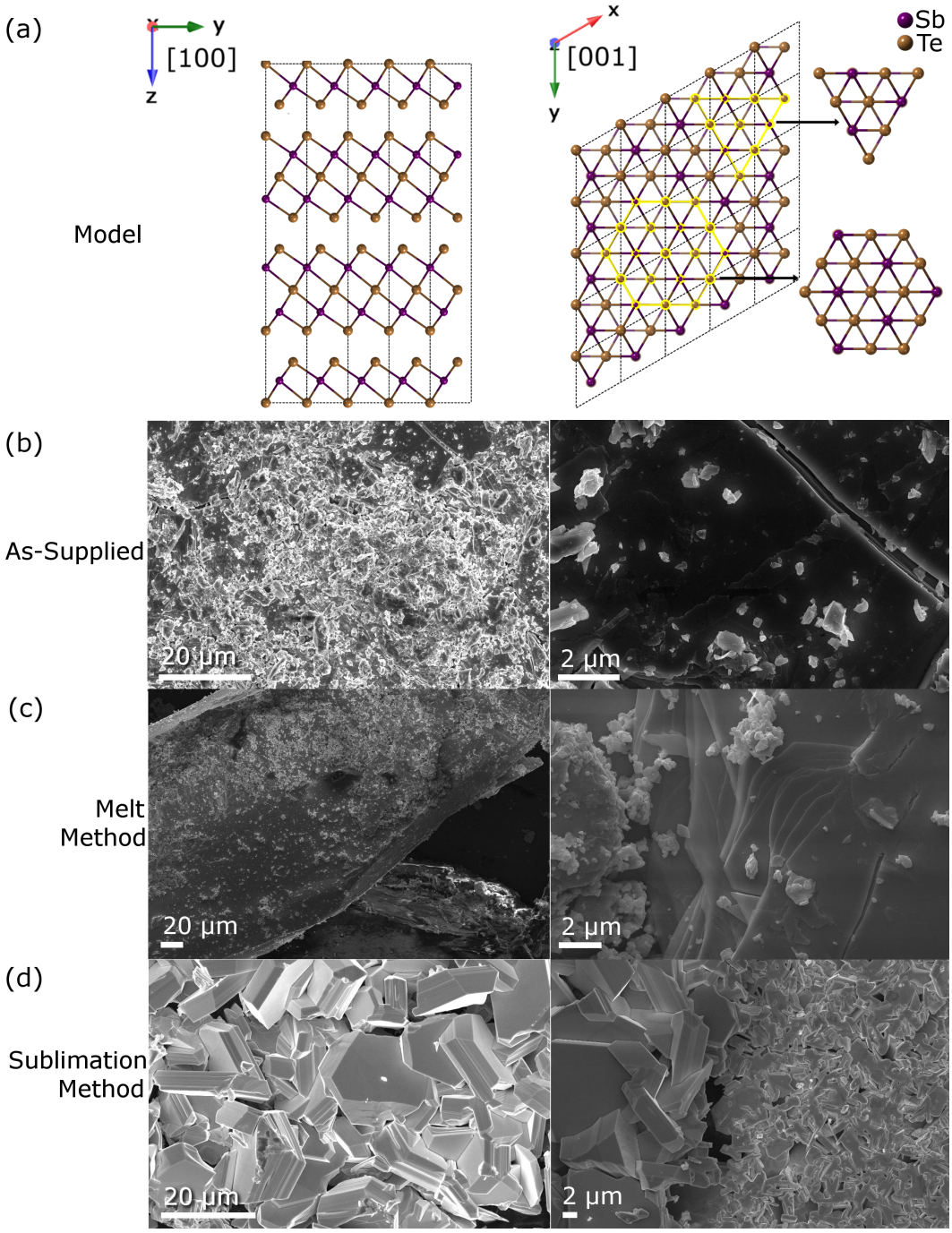


Figure 3.1: Structural model of bulk $Sb_2Te_3$ and SEM images comparing the large scale structure of post-growth and as-supplied bulk $Sb_2Te_3$. (a) Structural model of bulk $Sb_2Te_3$, in different projections, and depictions of the uderlying trigonal/hexagonal symmetry. The black lines denote the unit cell. The arrows indicate the view direction in cartesian coordinates. (b) The microstructure of as-supplied bulk $Sb_2Te_3$. (c) $Sb_2Te_3$@SWCNTs samples grown by the melt method looked visually very similar to the as-supplied bulk. (d) The microstructures formed during sublimation growth of the $Sb_2Te_3$@SWCNT samples appear to be a combination of cubic-like and more hexagonal structures. Images were obtained at an accelerating voltage of 10 kV.

Some of these are facets of the larger flake, whilst others are powdered material. The powdered microstructures can be rudimentarily distinguished in the SEM by the relatively high contrast at their edges, and significantly lower contrast on the flake - which is indicative of shadowing.

If we then compare these observations to SEM images of the melt procedure at 670°C (Fig. 3.1 (c)), we see that this growth method results in a sample that appears structurally similar to that of the as-supplied bulk source material, with micrometer grains being further populated by smaller nano-/micro-structures and facets. In contrast, the remnant bulk $Sb_2Te_3$ from the sublimation growth procedure at 670°C (Fig. 3.1 (d)) shows more cubic-like morphology, alongside some of the anticipated hexagonal formations, indicating the possible presence of alternative additional phases.

Combining these results with EDX mapping (Fig. 3.2) demonstrates that, for the melt filling process used here, the $Sb_2Te_3$ remains stable in composition (Fig. 3.2 (a)-(b)), with the ratio of Sb:Te remaining at 40:60±1 at.%. These results are consistent across all repeat samples grown using these same parameters. Further analysis of the bulk $Sb_2Te_3$ samples via DSC/TGA and XRD in Sections 3.4 and 3.5 validates these data presented here. XRD measurements consistently show the presence of peaks characteristic to the phases and symmetry of the original bulk $Sb_2Te_3$ precursor, as described in Section 3.5. Furthermore, despite the differing visual appearance of the post-sublimation method bulk material to the as-supplied $Sb_2Te_3$, EDX analysis (Fig. 3.2 (c)) indicates the composition to be consistent with that for the other bulk samples (40:60±1 at.%). Therefore, the differing appearances may be due to annealing at alternate temperatures.

Once this initial quantification of the sample composition has been conducted (Fig. 3.2), more probing analysis can be confidently performed. The sensitivity of ADF-STEM images to the atomic number of a material (Chapter 2) allows the $Sb_2Te_3$ nanocrystal confined within the SWCNTs to be clearly visualized. A high filling fraction ($\geq$ 50 %) of SWCNTs with $Sb_2Te_3$ has been observed across all samples, when using the melt growth protocol at 670°C [146]. This can be observed in the low magnification ADF-STEM images (Fig. 3.3 (I)), where the filling material shows up as bright white lines due to the significantly higher atomic number of both antimony and tellurium than carbon. Although ADF imaging is a chemically sensitive technique, the composition of the encapsulated nanocrystal was also determined quantitatively using EDX analysis. This analysis gave a Sb/Te ratio of two to three (Sb to Te as 40 ± 1 at.% to 60 ± 1 at.%, respectively). Additional investigations on other $Sb_2Te_3$@SWCNT bundles, samples and bulk materials, gave consistent results

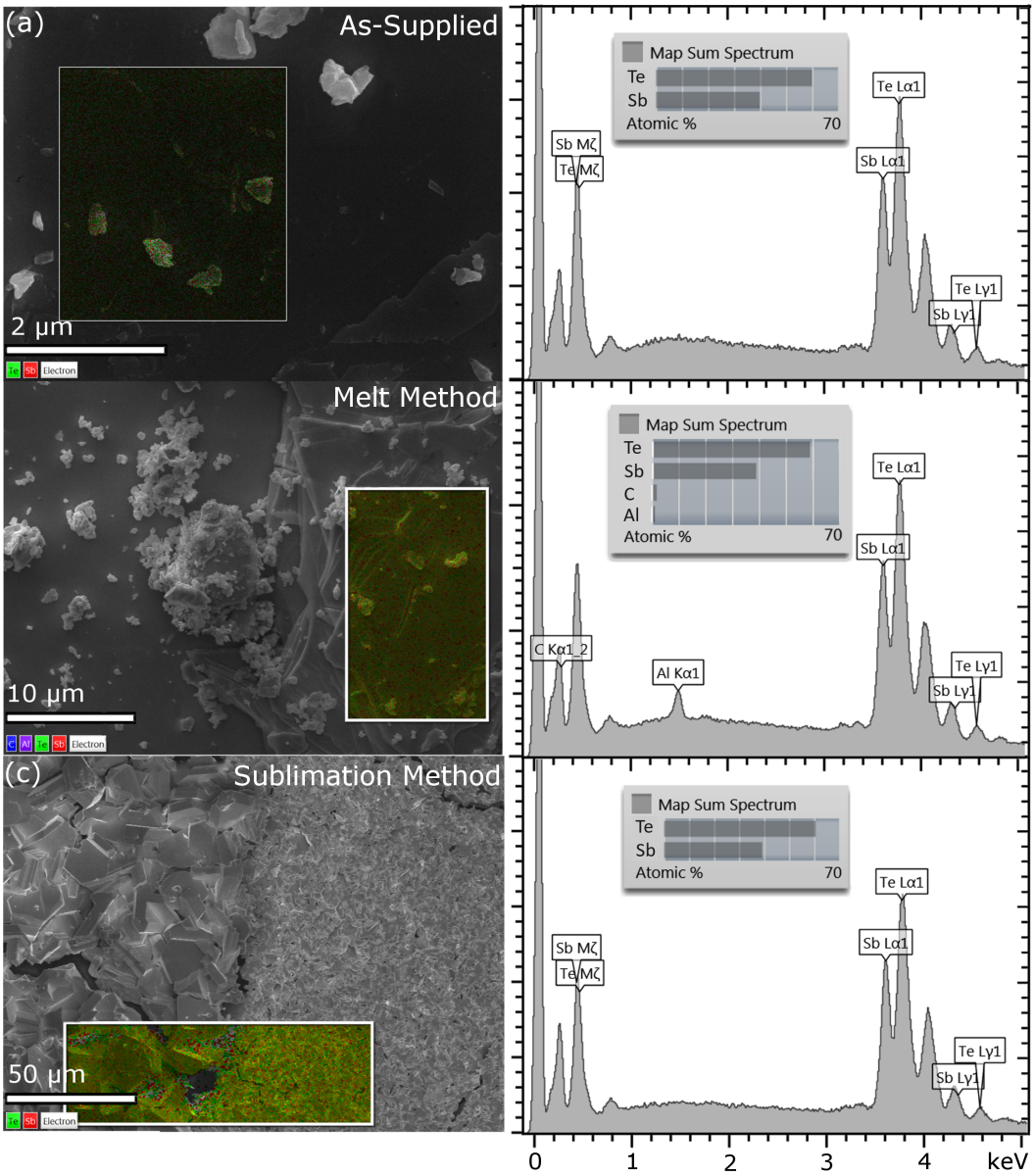


Figure 3.2: EDX mapping and sum spectra on three bulk forms of $Sb_2Te_3$. Compositional analysis on $Sb_2Te_3$ (a) bulk supplied by Alfa Aesar and bulk remnant material from (b) melt and (c) sublimation growth procedures at 670°C, showed all samples to possess the stoichiometric $Sb_{40}Te_{60}$ at. %, within error. The differing appearances may be due to the presence of other phases, caused by annealing at alternate temperatures. Images and spectra obtained at an accelerating voltage of 10 kV.

with the SEM EDX analysis outlined above, and confirmed the desired 2:3 stoichiometry of Sb:Te. The diameter of the SWCNT did not appear to negatively hinder the resultant proportion of filled CNTs, as a high filling fraction was observed for $Sb_2Te_3$@NI ($2.1 \geq d_{SWCNT} \geq 1.3$ nm), $Sb_2Te_3$@SWeNT ($1.4 \geq d_{SWCNT} \geq 0.7$ nm), and $Sb_2Te_3$@CHASM ($1.1 \geq d_{SWCNT} \geq 0.7$ nm) samples (Fig. 3.3 (a)-(c), respectively).

Furthermore, whilst ADF imaging allows the nanocrystals to be precisely visualised, BF imaging facilitates the effective and complementary analysis of the CNTs (Fig. 3.3 (II)). This is due to the contrast mechanism in BF, which is more sensitive to lighter elements - including carbon. This presents as a significantly lower contrast between the $Sb_2Te_3$ and the SWCNTs in BF-STEM images, so the widths of the SWCNTs can be more readily visualised. Therefore, candidate (n,m) CNTs can be identified from their measured diameter, taking into account the diameter relation in Eq. 1.1 in Section 1.2.

Whilst the filling fraction is high, there is also a prevelance of external material on the outside of the SWCNTs following synthesis. Extraneous crystals and the filling material shows as high contrast in ADF-imaging, whilst BF-STEM allows the CNTs to be clearly resolved. Some of this extraneous material is indicated in Fig. 3.4 (a), which appears as bright white in ADF imaging (I) and black in BF imaging (II). This can also be seen, on a less pronounced scale, in Fig. 3.3 (b). Due to this, additional processing is required to remove this material in order to accurately analyse the samples. As outlined in Section 2.1.5, this can be achieved through exfoliation - extraneous material can be sublimed off by heating the samples in a vacuum to just below the melting temperature of the bulk. This causes the external material to be vapour phase transported down a temperature gradient and away from the SWCNTs, whilst leaving the filling material intact. Exfoliation *ex situ* of samples resulted in bundles of $Sb_2Te_3$@SWCNTs that were free from external crystalline structures, whilst maintaining their high filling fractions (Fig. 3.4 (b)). The direct visual comparison between as-grown $Sb_2Te_3$@SWCNTs and the same sample post-exfoliation illustrates the significant reduction in the presence of extraneous crystalline structures - especially $Sb_2Te_3$ that this additional step in processing provides.

Furthermore, whilst exfoliation makes it more convenient when gathering high resolution images of the samples, it can also have a significant constructive impact on low-resolution EDX and SAED, DSC/TGA, and XRD analysis of samples (Section 3.3, 3.4, and 3.5). This is simply due to the fact that the signal from the external crystals cannot be isolated from that of the nC-$Sb_2Te_3$ in the as-grown samples

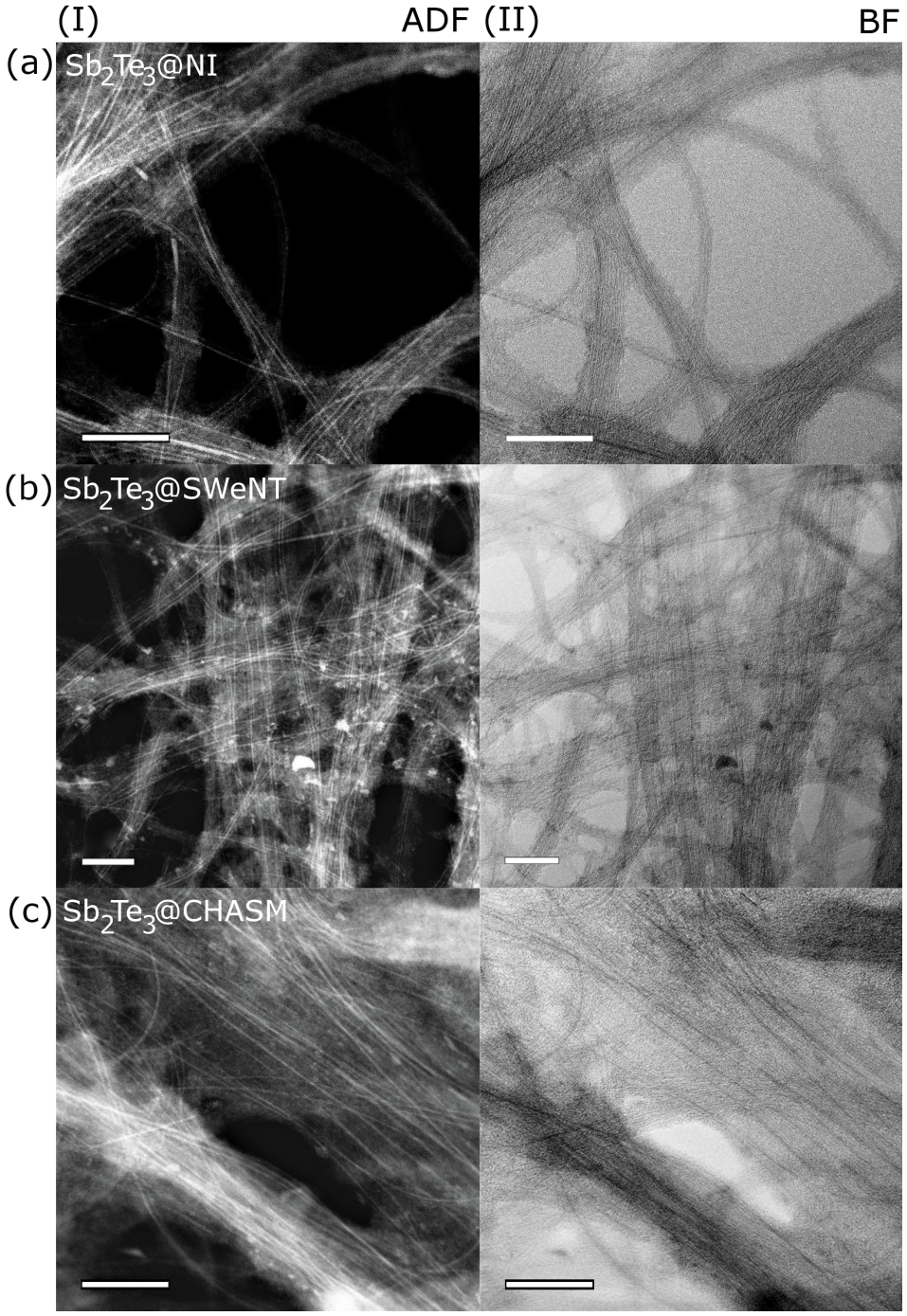


Figure 3.3: ADF- and BF-STEM imaging shows a high fraction filling of the SWCNTs with $Sb_2Te_3$ across all samples grown at 670°C via the melt method. The high Z-dependence of (I) ADF-STEM imaging shows the filling clearly as bright white, whilst the intensity from the carbon is very feint. Complementary (II) BF-STEM imaging allows for the carbon, and therefore the diameters and sizes of the bundles, to be resolved. The diameter of the SWCNT did not appear to negatively hinder the resultant proportion of filled CNTs, as a high filling fraction was observed for (a) $Sb_2Te_3$@NI, (b) $Sb_2Te_3$@SWeNT, and (c) $Sb_2Te_3$@CHASM samples. Scale bars are 20 nm. Images were obtained at 80 kV.

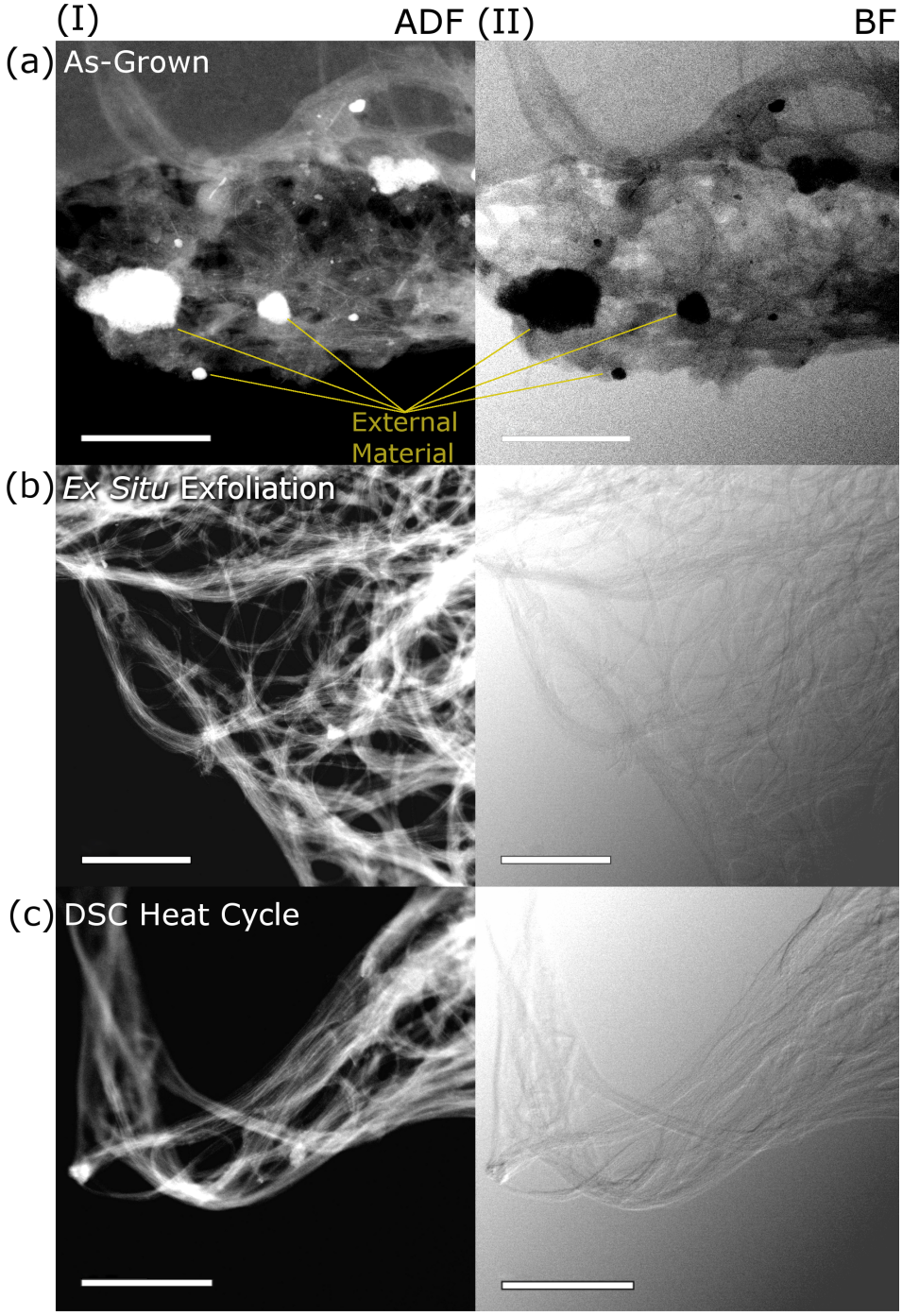


Figure 3.4: ADF- and BF-STEM images illustrating the impact of exfoliation on the $Sb_2Te_3$@SWCNT samples. (a) The as-grown $Sb_2Te_3$@SWCNTs show a significant proportion of external crystalline formations, which appear as very bright white in ADF (I), and black in BF (II). The post-exfoliation images illustrate the impact of (b) the *ex situ* method and (c) a DSC/TGA analysis cycle through 800°C on the $Sb_2Te_3$@SWCNT samples. The exfoliated samples are virtually devoid of these structures, whilst maintaining a high filling fraction. Scale bars are 100 nm. Images were obtained at 80 kV.

for these methods. Therefore, if the prevalence of extraneous material is sufficient enough, the contribution from the $Sb_2Te_3$@SWCNTs can be overwhelmed by that of the bulk material, as will be demonstrated in Section 3.4. Similarly, complementary results to those presented for *ex situ* exfoliation (Fig. 3.4 (b)) have been obtained for a $Sb_2Te_3$@SWeNT sample that had been cycled through 800°C once under nitrogen at atmospheric pressure during a DSC/TGA thermal analysis experiment (Fig. 3.4 (c)).

### 3.2.2 Atomic Resolution Structure Catalogue

The ability to produce high quality samples consistently has important ramifications in terms of the reproducibility of experiments and the confidence in obtained results. Furthermore, effective processing and refining techniques make conducting analysis on samples far easier and more accurate, whilst increasing the viability of upscaling growth mechanisms in the future. This is especially important when looking at the atomic-scale, and bundled characteristics; the slightest contaminant could disrupt the formation and stability of an entire nano-confined structure, and interfere with the atomic-scale analysis of the sample.

As previously discussed, the use of a variety of SWCNTs provided a larger diameter range within which to encapsulate materials. Therefore, we were able to study to structures that form when nano-confined in a cylindrical volume with cross-sectional areas as small as 1 $nm^2$ [245]. This results in a variety of arrangements that would in principle never appear, or be stable, in the bulk, due to the reassessment of the energy minima imposed by the SWCNT confining surfaces. However, the extension of this range to larger diameters ($\geq$2 nm) means that structures resembling the bulk are also observed to form. Furthermore, high resolution (S)TEM imaging of the $Sb_2Te_3$@SWCNT samples revealed the co-existence of a variety of different structures (Fig. 3.5). This is due to the bundles being comprised of SWCNTs with a range of diameters. The insets in Fig. 3.5 show three examples of the coexisting forms present. Each bundle was confirmed to have the desired stoichiometry for $Sb_2Te_3$ via EDX analysis, and the structures within were able to be modelled as such. These were then arranged by the diameter range in which they were observed to have formed and placed into the compiled catalogue of nC-$Sb_2Te_3$ structures, from narrowest to widest accommodating SWCNT (Fig. 3.6 (a)-(e)). Linear chain has been observed to form inside CNTs with d$\leq$0.7 nm (Fig. 3.6 (a)), as outside this diameter the zig-zag chain (Fig. 3.6 (b)) and single helix chain (Fig. 3.6 (c)) begin to become more prevelant and dominate, as the additional volume allows

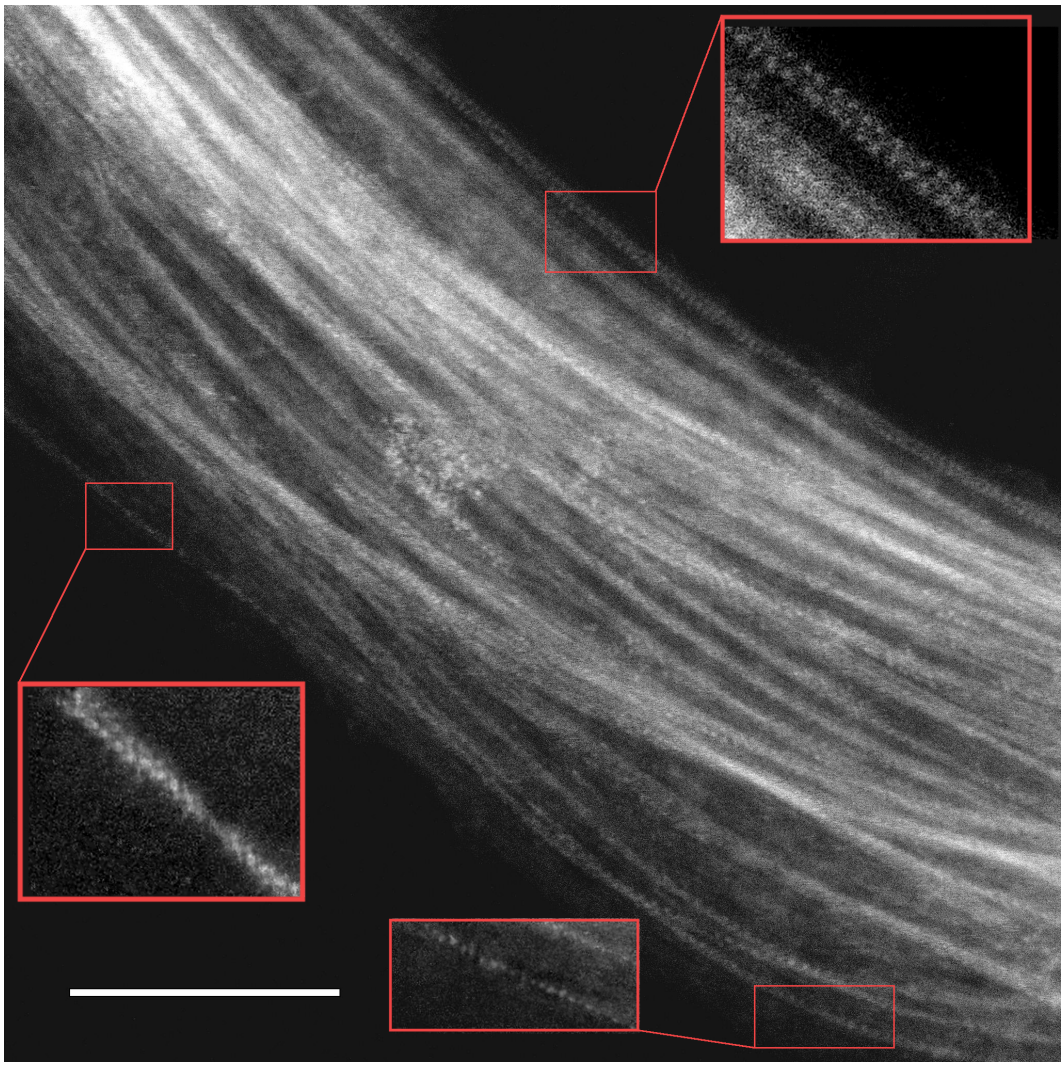

Figure 3.5: ADF-STEM image of the coexistence of a variety of forms of nC-$Sb_2Te_3$ in a bundle of exfoliated $Sb_2Te_3$@SWeNT. The insets show three examples of some of the coexisting forms present. Scale bar is 10 nm. Images were obtained at 80 kV.

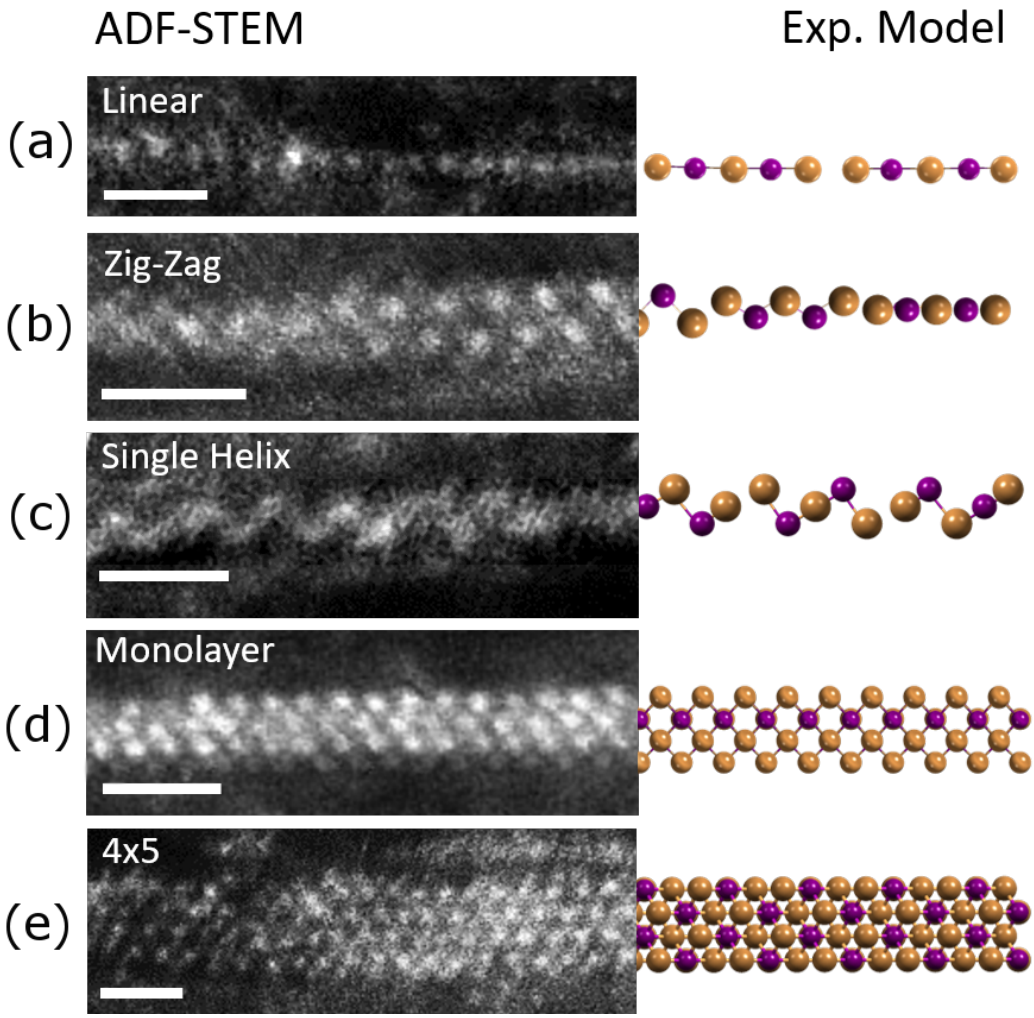


Figure 3.6: ADF-STEM images of the observed forms of nC-$Sb_2Te_3$, alongside their their derived atom models, based on fragmenets of $Sb_2Te_3$. The nano-confined structures have been arranged by diameter of the accommodating SWCNT, with (a) linear chain being observed to form inside CNTs with d≤0.7 nm (SWeNT), and (e) 4x5 inside d≥1.7 nm (NI). Scale bars are 1 nm.

the atoms more room to contract bonds and twist. We see the appearance of the monolayer-like nano-confined form (Fig. 3.6 (d)) - so called as it is a direct analogue to a monolayer slice of the bulk structure - at diameters of $\sim$ 1.1 nm. This structure dominates the samples, being the most observed nano-confined form and comprising $\sim$ 60% of the samples. This is, in part, due to the fact that the average diameter of SWCNT across the samples is $\sim (1.1 - 1.4)$ nm (Section 1.2). However, the range that this structure forms inside is relatively large, and unpopulated by alternative nano-confined structures. Indeed, the next encapsulated structure (4x5) is not observed - or modelled in principle - to form until a minimum diameter of $\sim$ 1.7 nm (Fig. 3.6 (e)). As was demonstrated in Section 3.2.1, the distribution and occurence of these observed structures is not affected by *ex situ* exfoliation, or careful heat treatment, of the sample.
(S)TEM analysis was conducted at 80 kV, in order to reduce the risk of damage to both the SWCNTs and the encapsulated structures. Despite this, beam irradiation still causes substantial vibration and motion of the atoms in the analysed structures. Therefore, succesfully resolving the structures on an atomic scale, without prolonged beam irradiation, is challenging. This can be counteracted through stack imaging, when multiple brief snapshots of the structures are taken and an image of the structure, or movie of the rotation, can be built up later. This method has the additional advantage of being able to see when the specimen begins to change. Alternatively, a more stable environment can be achieved through supercooling with liquid nitrogen. This significantly reduces motion of the atoms and allows for cleaner images to be obtained, as well as reducing the impact of imparted energy from the electron beam and scattering events. However, such high resolution cryo-EM is beyond the capabilities of this lab. Therefore, further investigation would have to be conducted off-site, which is beyond the time restriction of this thesis.

### 3.2.3 Nanoscale Structure Analysis & Image Simulation

Further to the catalogue of observed structures outlined above, pre-emptive structural modelling was carried out in order to try and experimentally predict the structures that we might observe, prior to analysis being carried out. Such a method is sometimes referred to as "Top-Down" modelling, wherein existing structures and geometries are used to define and build up likely models for nano-confined materials. In the case of modelling prior to experimental imaging, this was primarily achieved by taking slices through a room temperature model of bulk $R\bar{3}m$ $Sb_2Te_3$ (Fig. 3.7 (a)), obtained from the crystallographic database compiled by CrystalMaker 9 of

published structures [168].
Some of these structures were subsequently observed experimentally, as well as the observation of additional configurations that have no direct analog in the bulk, such as linear chain and zig-zag (Fig. 3.6 (a)-(b) in Section 3.2.2). ADF- and BF-STEM image simulations were also run using clTEM (Section 2.3) for the remainder of those models that had been constructed via the "Top-Down" method, but not observed. These models and ADF-STEM simulations are shown in Fig. 3.7 (b). The models depicted in Fig. 3.7 were built by taking sections through the $R\bar{3}m$ bulk structure of $Sb_2Te_3$. These sections are shown as overlays on the [100] and [001] projections in Fig. 3.7 (a), where the specific colours correspond to the models (I-IV) given in Fig. 3.7 (b).
However, the primary method for modelling the nano-confined crystals comprised analysing the obtained experimental HR-(S)TEM images and reactively building models. This method requires bond distances to be measured from the HR-(S)TEM images, whilst the relative contrast between atoms in ADF-STEM images can be used to identify possible atomic constituents, or combinations thereof, since elements with higher atomic numbers appear brighter in ADF-STEM imaging - as outlined in Section 2.2.2. clTEM is then employed to simulate (S)TEM images from the resultant model, which can be compared with experimental images to qualitatively determine the accuracy of the model to the real structure. Therefore, the more projections of the $Sb_2Te_3$@SWCNT structure that can be viewed, the more accurate and complete a model we are able to build. Therefore, the rotation of the nano-confined structures under the electron beam can be exploited.
In addition to those models already reported, some non-stoichiometric models were also built in the same manner. These had direct originators in the bulk rhombohedral $Sb_2Te_3$ model, as before. However, they comprised recurring units containing Sb:Te ratios other than 2:3, such as 1:1 or 4:7. they have yet to be observed experimentally in our samples, due to their stoichiometries being different to that discerned in our samples. These are not reported here, but form part of a growing database of possible nano-confined structures that may be observed in further samples and materials.

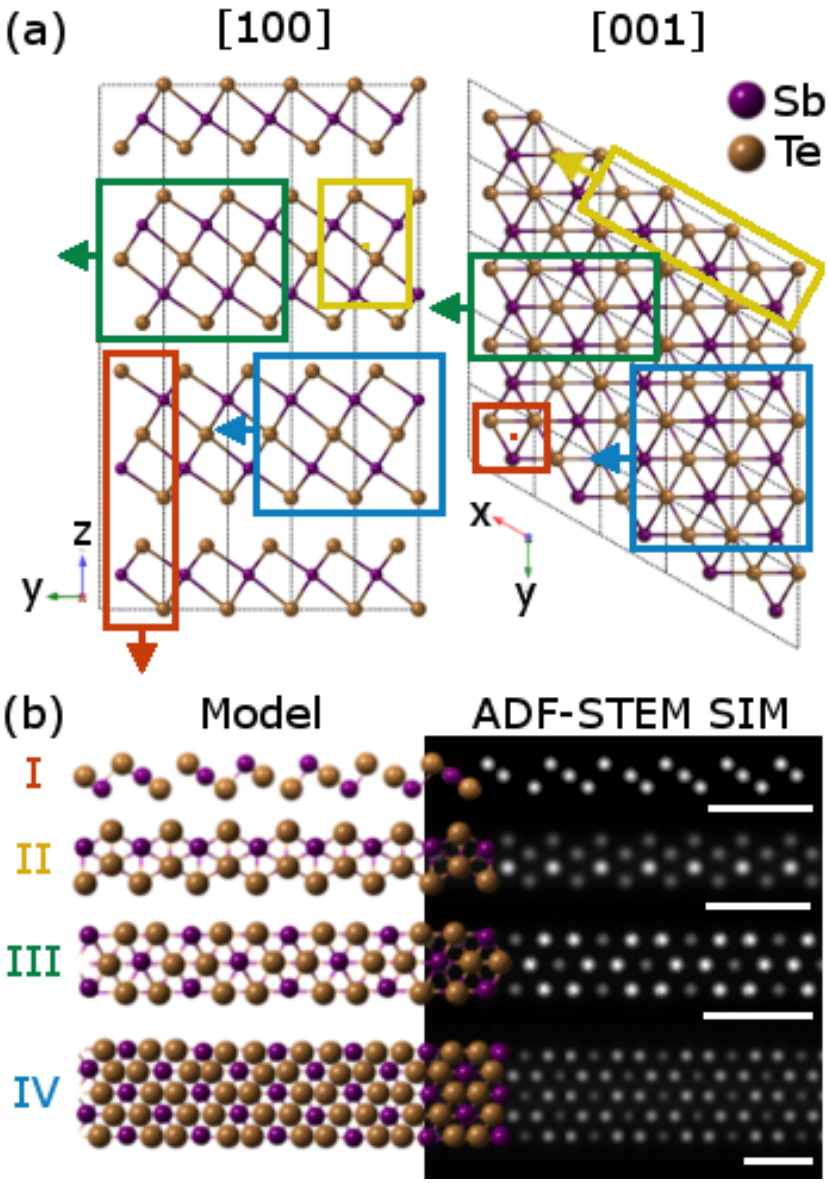


Figure 3.7: "Top-Down" modelling of possible stoichiometric nano-confined $Sb_2Te_3$ structures from the rhombohedral bulk. (a) The atomic structural model for rhombohedral $R\bar{3}m$ $Sb_2Te_3$, as viewed along the [100] and [001] directions, respectively. The slices used to obtain the models given in (b) are depicted by the overlays, including extrapolation direction. (b) Further top-down modelled nano-confined structures for stoichiometric $Sb_2Te_3$, that were not subsequently observed in our samples. They are shown alongside their corresponding ADF-STEM simulated images. Scale bars are 1 nm. The dashed lines in the bulk indicate the unit cell. The arrows indicate the view direction in Cartesian coordinates.

## 3.3 SAED

### 3.3.1 Room Temperature

Further to visual inspection of the samples on a bulk- (Section 3.2.1) and atomic-scale (Section 3.2.2), studying the electron diffraction characteristics provides us with significant additional information about the structure of the samples. Investigations into the room temperature electron diffraction of $Sb_2Te_3$@SWCNTs were conducted on samples that had been dispersed onto lacey carbon TEM grids (as outlined in Sections 2.1.5 and 2.2.4). This established sufficient support for the SWCNTs to spread across, whilst also providing areas of vacuum-only background to the TEM images and SADPs (Fig. 3.8 (a)). TEM imaging and SAED were carried out at 80 kV, and electron beam doses (current densities) were monitored throughout and maintained at sufficiently low levels ($\leq$70 pA·cm$^{-2}$ for low magnification TEM imaging and electron diffraction at 80 kV). This not only ensured accurate reproducibility of the SAED experiments, but also provided valuable quantification of the robustness of the nanocomposites under beam irradiation.
The obtained experimental SADPs of bundles of $Sb_2Te_3$@SWCNT show clear additional reflections (highlighted in yellow in Fig. 3.8 (a-I)) that cannot be attributed to the SWCNTs (the diffraction characteristics of SWCNTs are outlined in Section 2.2.4). These features are consistently present in SADPs of larger diameter $Sb_2Te_3$@SWCNT bundles (Fig. 3.8 (a-II)). We can analyse these SADPs and features in order to calculate the lattice parameters, as outlined in Section 2.2.4. From given symmetry relations, we can then determine the allowed Miller indices using Eq. 2.20 from Section 2.2.4 in the case of the rhombohedral bulk $Sb_2Te_3$ system.
However, this method of indexing requires the symmetry and phase of the contributing crystal structure to be known. Therefore, cross-referencing the diffraction aspects with observed structures and their corresponding models and simualtions dramatically narrows the dataset and, therefore, the time taken to index the diffraction features. This is the method by which the simulated SADP (Fig. 3.8 (b-I) "SIM"), corresponding to a section through a structure of $Sb_2Te_3$ (Fig. 3.8 (c-*)), was obtained. This corroborates the research carried out by S. Marks, J. Sloan and K. Morawiec [56, 163]. Furthermore, these electron diffraction results are concurrent with SADPs extracted from bulk rhombohedral $Sb_2Te_3$. The experimental SADP (Fig. 3.8 (b-I) "EXP"), from the crystal depicted in the corresponding TEM image (Fig. 3.8 (b-II)), has been overlayed with simulated diffraction data (Fig. 3.8 (b-I) "SIM") for a model extracted from the rotated [001] projection of the bulk $Sb_2Te_3$ given in Fig. 3.8 (c). The yellow diffraction spots correspond to the indicated slices -

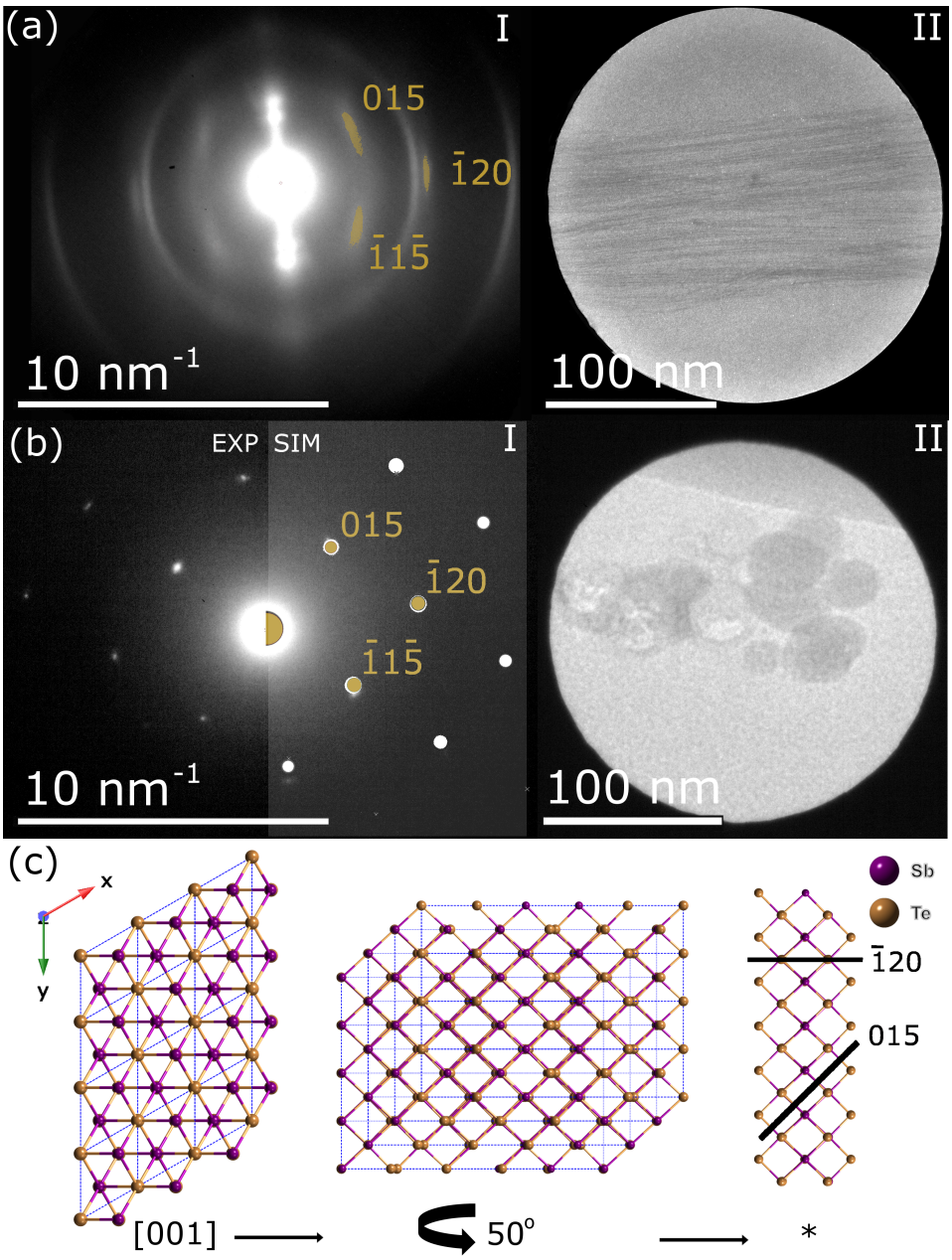


Figure 3.8: (a) Experimental SADP (I) showing the key diffraction aspects seen for nC-$Sb_2Te_3$ and the SWCNTs, alongside the corresponding TEM image of the bundle (II). The aspects that can be attributed to the nC-$Sb_2Te_3$ are highlighted in yellow. (b) The experimental SADP (I), "EXP", from the crystal depicted in the corresponding TEM image (II), has been overlayed with the simulated diffration pattern, "SIM", for the model of bulk $Sb_2Te_3$ given in (c). The yellow indicates the key reflections of interest. The white shows the extended pattern for a full crystal. (c) The yellow diffraction spots in (b-I) "SIM" correspond to the indicated slices through the crystal shown (*). This crystal can be pulled directly from the a 50° rotation about the y axis of the [001] projection of the bulk rhombohedral structure, and arises due to nano-confinement of the $Sb_2Te_3$. Here it is constrained in the vertical direction to [010] and viewed along lattice vector direction [$\bar{2}$ $\bar{1}$ 0]. The dashed lines depict the unit cell. The arrows indicate the view direction in Cartesian coordinates.

$\{\bar{1}20\}$ and $\{015\}$ - through the crystal shown in Fig. 3.8 (c-*) - which is the "Monolayer" structure depicted in Fig. 3.6 (d) in Section 3.2.2. The white overlay shows the extended pattern for a full crystal. This crystal can be pulled directly from the a 50° rotation about the y axis of the [001] projection of the bulk rhombohedral structure, and arises due to nano-confinement of the $Sb_2Te_3$.

As shown in Fig. 3.8 (a-I), the SADPs of the $Sb_2Te_3$@SWCNTS do not possess well-defined spots - as in a bulk crystal sample. This is due to the fact that the samples are comprised of bundles of crystalline materials constrained to one dimensional cylindrical structures (Fig. 3.8 (a-II)), with a range of, pseudo-randomly orientated, structures. This presents as a smearing of the diffraction aspects and reflections into arcs (Fig. 3.8 (a-I)). In this respect, the diffraction patterns appear more akin to the diffuse rings formed by an amorphous sample. These arcs correlate to the average spacing between atoms. Similarly, amorphous samples do not possess the repeating crystal structure that determines the indexable characteristics of diffraction patterns from crystalline materials. However, in order to minimise the energy, the atoms in an amorphous sample will re-arrange to produce recurring average atomic separations. This presents as blurred rings in SADPs.

These indexed reflections from the crystalline nC-$Sb_2Te_3$ are observed to blur after prolonged beam irradiation (Fig. 3.9). Eventually, these spots fully fade, and disappear into an intensity akin to an amorphous background. This is indicative of the beam-induced amorphisation of the encapsulated $Sb_2Te_3$. This result was consistent across SADPs obtained for multiple bundles of $Sb_2Te_3$@SWCNT, and for all analysed samples. The energy input by the beam irradiation causes vibration of the atoms, and eventually lengthening, and breaking, of the bonds holding the crystals together occurs (as depicted in Fig. 3.9) [56, 183]. Once this process has transpired, the structures, and SADPs, were observed to remain as such. Further energy input by the electron beam was insufficient to induce recrystallisation of the nano-confined structures over the timescales ($\leq$30 mins) and electron beam current densities ($\leq$70 pA·cm$^{-2}$) investigated - as described in Section 2.2.5.

As will be demonstrated in Section 3.3.2, the encapsulated $Sb_2Te_3$ has been observed to remain crystalline after approximately 7 mins of consecutive beam irradiation at a beam current density of 19 pA·cm$^{-2}$. However, the filling material will undergo complete amorphisation after less than 2 mins irradiation at 120 pA·cm$^{-2}$. This relatively high beam dose appeared to have no damaging effects on the encapsulated $Sb_2Te_3$ over this timescale. This remained valid for beam doses (current densities) up to $\sim$ 300 pA·cm$^{-2}$ in standard TEM, with the amorphisation of filling becoming more rapid with the correlative increase, but no irradiation-induced dissociation

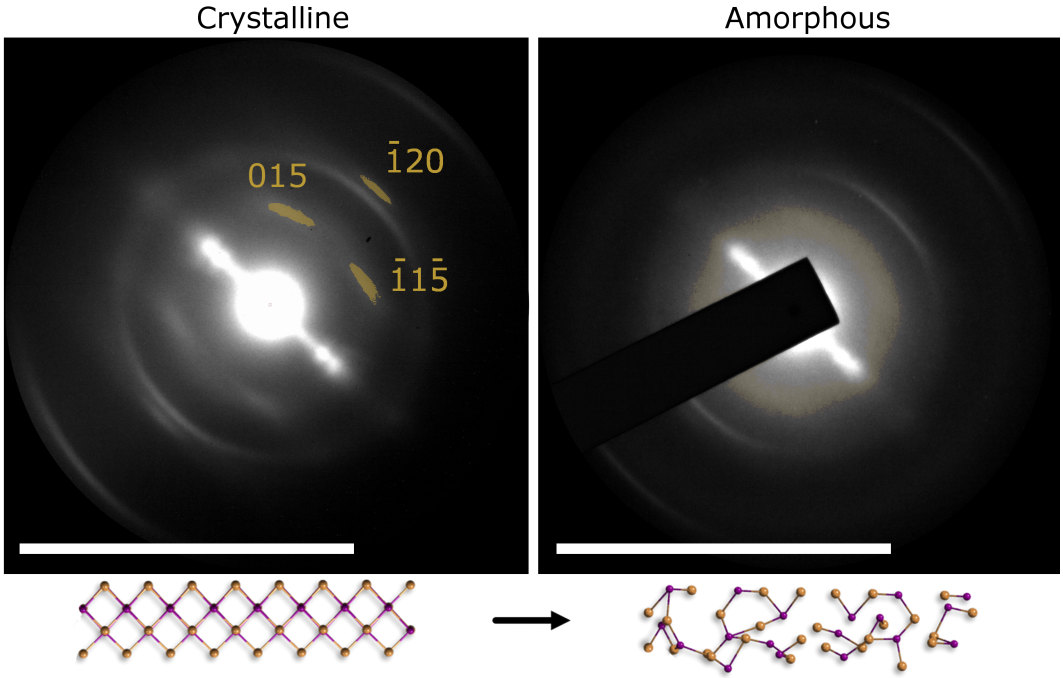


Figure 3.9: SADPs of a bundle of crystalline and amorphous $Sb_2Te_3$@SWCNT, with indicative models of the corresponding nano-confined structures. Amorphisation was induced *in situ* via prolonged irradiation under the electron beam. The distinct diffraction aspects in the SADP, attributed to the nano-confined crystalline $Sb_2Te_3$, fade and eventually disappear into an intensity akin to an amorphous background. The energy input by the beam irradiation causes lengthening, and breaking, of the bonds holding the crystals together. These patterns were obtained for a bundle of $Sb_2Te_3$@SWeNT, dispersed on a lacey carbon TEM grid.

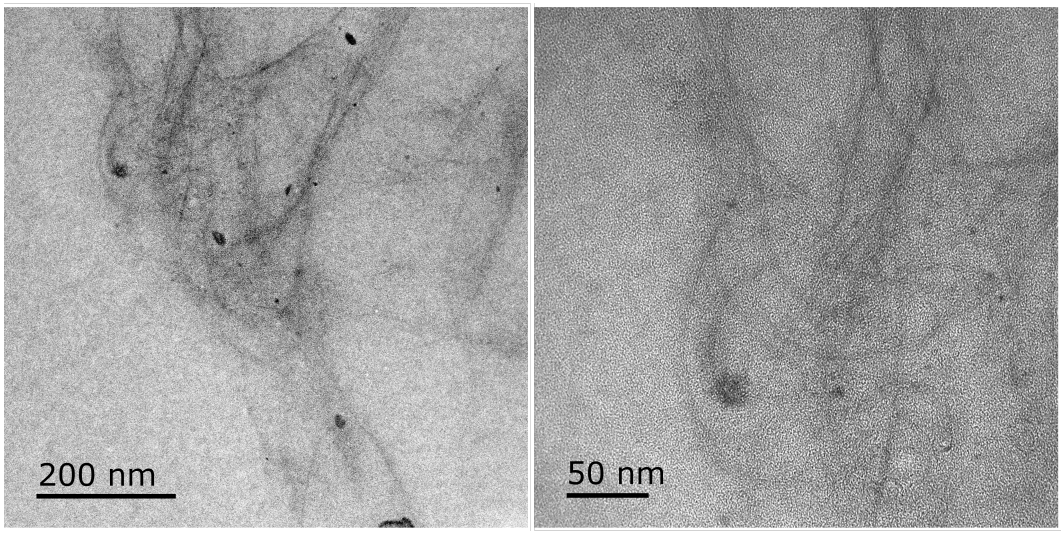


Figure 3.10: TEM images of $Sb_2Te_3$@SWeNT dispersed onto the silicon nitride window of a MEMS heating chip for *in situ* temperature experiments.

being observed over timescales of $\leq 200$ s. Recrystallisation was not observed to be induced via beam irradiation during this time.

### 3.3.2 *in situ* Heating

As outlined above (Section 3.3.1), the amorphisation of the encapsulated $Sb_2Te_3$ can be induced via beam irradiation. However, we have found that this structural change can be made reversible, via *in situ* heating. Following the procedure outlined in Section 2.2.6, samples were dispersed onto MEMS chips with temperature control capabilities. TEM images of a representative dispersion of a $Sb_2Te_3$@SWeNT sample onto a silicon nitride film window MEMS heating chip are given in Fig. 3.10, which shows the clear presence of a uniform amorphous background - from the $Si_3N_4$ - in the images. Despite this background, the $Sb_2Te_3$@SWCNT bundles can still be discerned, with external crystal structures and filled SWCNTs exhibiting higher contrast (darker) than the empty SWCNTs and surrounding silicon nitride. This configuration allowed the amorphous-crystalline phase transition to be tracked *in situ* whilst heating the sample to up to 1100°C - the thermal stability limit of the silicon nitride window.

Whilst tracking this transition, we want to ensure that the acquired diffraction data are not contaminated by the inclusive of non-encapsulated material. Therefore, it is important to efficiently process and clean the samples of extraneous material,

as introduced in Section 2.1.5 and further discussed in Section 3.2.1. This can be achieved by exfoliation: external crystals can be removed from the $Sb_2Te_3$@SWCNT bundles by annealing the sample in a furnace at a pre-requisite temperature, specific to the material of interest - 600°C, with the sample being annealed for 5 hours, in the case of $Sb_2Te_3$.

However, we have now found a method by which exfoliation of the samples can be carried out *in situ* (Fig. 3.11), after depostion. Experiments conducted in this research have shown that, despite the melt transition of bulk $Sb_2Te_3$ occuring at 620°C under inert atmospheric (to be discussed further in Section 3.4), the extraneous material begins to undergo changes from $\sim$ 350°C under an *in situ* TEM environment (Fig. 3.11 (a)). Furthermore, material is not observed to be exfoliated from the bundles until $\sim$ 500°C, but this is still $>$ 100°C below the reported atmospheric melting temperature of bulk $Sb_2Te_3$. Annealing at this temperature is sufficient to remove significant mass ($\sim$ 30 %) from the bulk and external crystalline material (Fig. 3.11 (b)). Smaller crystals are discerned to visibly alter their appearance, and rapidly melt, far in advance of the larger crystals. Evidence of this can be seen in both the high, and low, resolution temperature-resolved TEM images in Fig. 3.11 (a) and (b), and is as expected from previous studies and theory [217].

Further to this, the standalone crystalline material was observed to shrink and dissipate faster than that attached to SWCNTs. As the temperature was increased beyond 500°C, an exponential correlative increase in the rate of disintegration of external deposits was observed. However, full exfoliation of the sample (across the entire chip) was not observed to occur until $\sim$ 700°C. This could in part be due to the variation in the actual temperature across the chip (Section 2.2.6), and the potential bonding - and so the additional required energy - of the crystals to the bundles. Furthermore, the purging of extraneous material resulted in scarring of the $SiN_x$ window (Fig. 3.11 (a)), and the SWCNTs. An example of the observed scarring to the SWCNT bundles is highlighted in yellow in Fig. 3.11 (c).

Whilst the aim of the high temperature treatment is to efficiently remove the extraneous crystals, it was important to confirm that the encapsulated $Sb_2Te_3$ remained intact during this process. This is observed to be valid, up to 700°C, as can be seen by the dark lines of contrast in the post-treatment bundle in Fig. 3.11 (c). Furthermore, the filling is nC-$Sb_2Te_3$, as can be seen by the inset SADP of the bundle (Fig. 3.11 (c)). However, if the samples are heated to temperatures above 800°C, then loss of the filling material is observed, with this loss becoming rapid and significant at 900°C.

The results of combined DSC and TGA measurements (Section 3.4) on the bulk

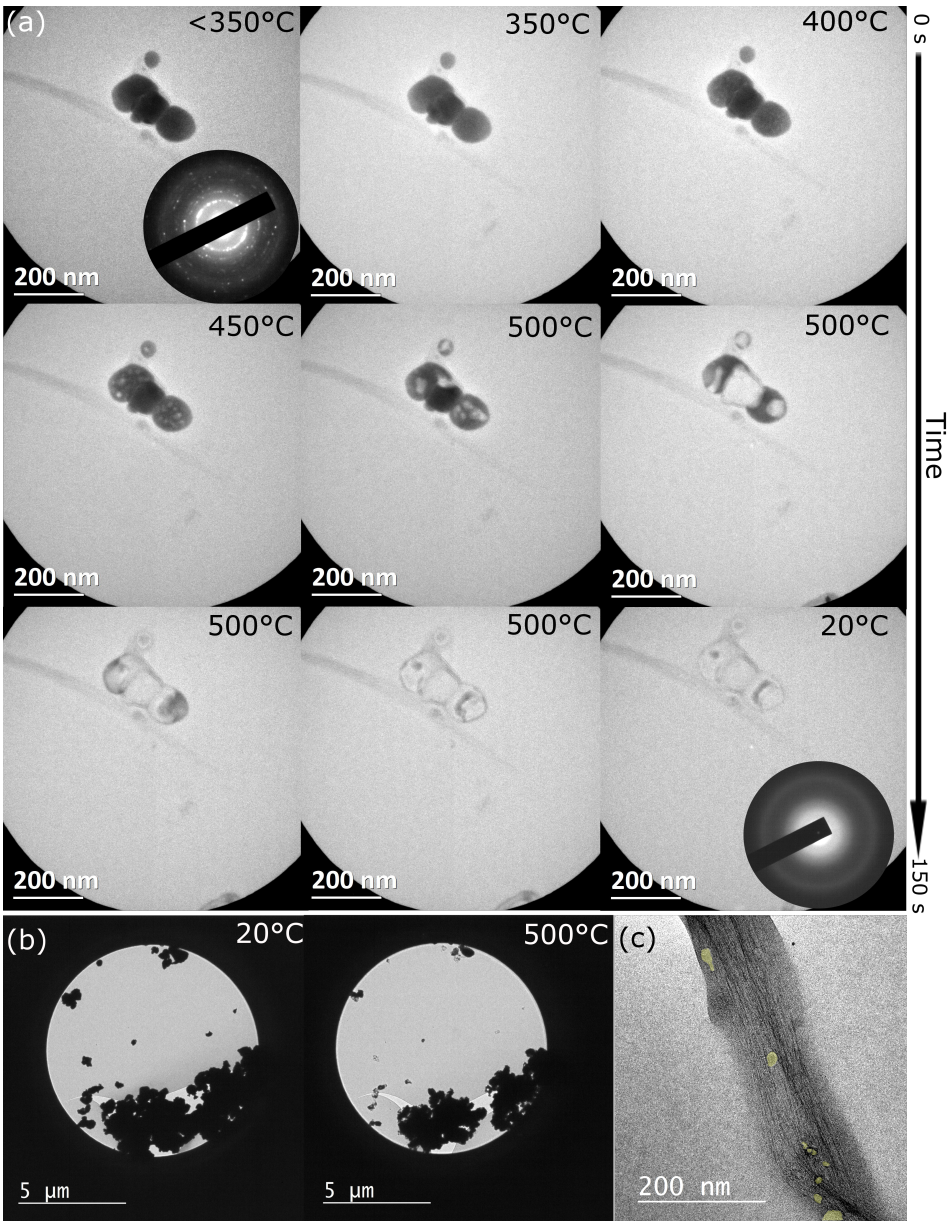


Figure 3.11: Temperature-resolved TEM imaging and SADPs of the *in situ* exfoliation of bulk $Sb_2Te_3$. (a) Temperature and time resolved TEM images illustrating the effect that heating the $Sb_2Te_3$@SWCNT samples to 500°C *in situ* has on extraneous crystalline structures. The inset SADPs evidence the complete removal of the originally polycrystalline material upon completion of heating cycle. Resultant scarring of the $SiN_x$ membrane is shown. (b) Low resolution TEM images of bulk $Sb_2Te_3$ on the larger membrane area. The crystals are observed to have shrunk by approximately 30 % after 10 s at 500°C, with the smaller of these having completely disintegrated. Annealing for longer results in the complete removal of these crystals *in situ*. Increasing the temperature to 800°C rapidly increases the rate of vaporisation, and removes all trace materials. (c) The scarring from the melting and vaporisation of the crystals also affects the SWCNTs, here indicated in yellow. The filling material is observed to remain intact after heating to 800°C. Images were obtained at 80 kV, and beam current densities were limited to 70 $pA \cdot cm^{-2}$.

$Sb_2Te_3$ and $Sb_2Te_3$@SWCNT samples were used to identify and isolate potential temperature ranges of interest. This process was particularly helpful in determining the point at which the nC-$Sb_2Te_3$ melts, without losing significant mass from the filling material. The data provided by the thermal measurements have proven complementary to the *ex situ* and *in situ* exfoliation of $Sb_2Te_3$@SWCNT bundles, as outlined above.

Furthermore, it has also been observed that heating the sample to 800°C, and then cooling to room temperature, induces the recrystallisation of amorphised encapsulated material. The full amorphisation and recrystallisation process was tracked via time resolved SADPs and stack movies (Fig. 3.12). The encapsulated material was not observed to recrystallise until $\sim$ 250°C on the cooling curve. This is due to the fact that the glassy phase can also be induced by heating [246]. The onset of this phase can be observed at $\sim$ 300°C in the heating curve, with recrystallisation occurring at a similar point in the cooling curve as heat treated samples that have undergone beam-induced amorphisation. Similarly, heating temperatures below 650°C result in incomplete, or no, recrystallisation of the nC-$Sb_2Te_3$. These results can be correlated with the observed mass loss behaviour when heated above 700°C. It appears that it is not sufficient for the nano-confined material to just melt when encapsulated, further energy must be provided to the system to induce the reformation of the crystalline bonds. However, once the material begins to degrade chemically, this recrystallisation of the encapsulated $Sb_2Te_3$ becomes irreversible. Recent *in situ* TEM and EDX analysis conducted by J. Tyler and S. Bradley, under the supervision of J. Sloan, has shown that the external material begins to degrade at $\sim$ 630°C, with one element (Te) being removed preferentially.

As shown in the time-resolved SADPS in Fig. 3.12, the recrystallised sample shows identical diffraction features and behaviour to the original structure, which is also qualified by radial intensity analysis of the SADPs (Fig. 3.13). Furthermore, this process can be continuously cycled. Whilst the lifetime of the sample has not been investigated, the current cyclable abilities of the encapsulated $Sb_2Te_3$ seems promising, with no signs of degradation being apparent after three cycles of continuous beam irradiation and heat cycling.

The impact of beam dose has been investigated extensively over the course of this research (Chapter 2), and nC-$Sb_2Te_3$ has been observed to remain structurally stable under low dose (beam current density) conditions, as outlined in Section 3.2. This has also been verified via SAED tracking of the diffraction aspects. The encapsulated $Sb_2Te_3$ has been observed to remain crystalline after approximately 7 mins of consecutive beam irradiation at a beam current density of 19 pA·cm$^{-2}$ (Fig. 3.14).

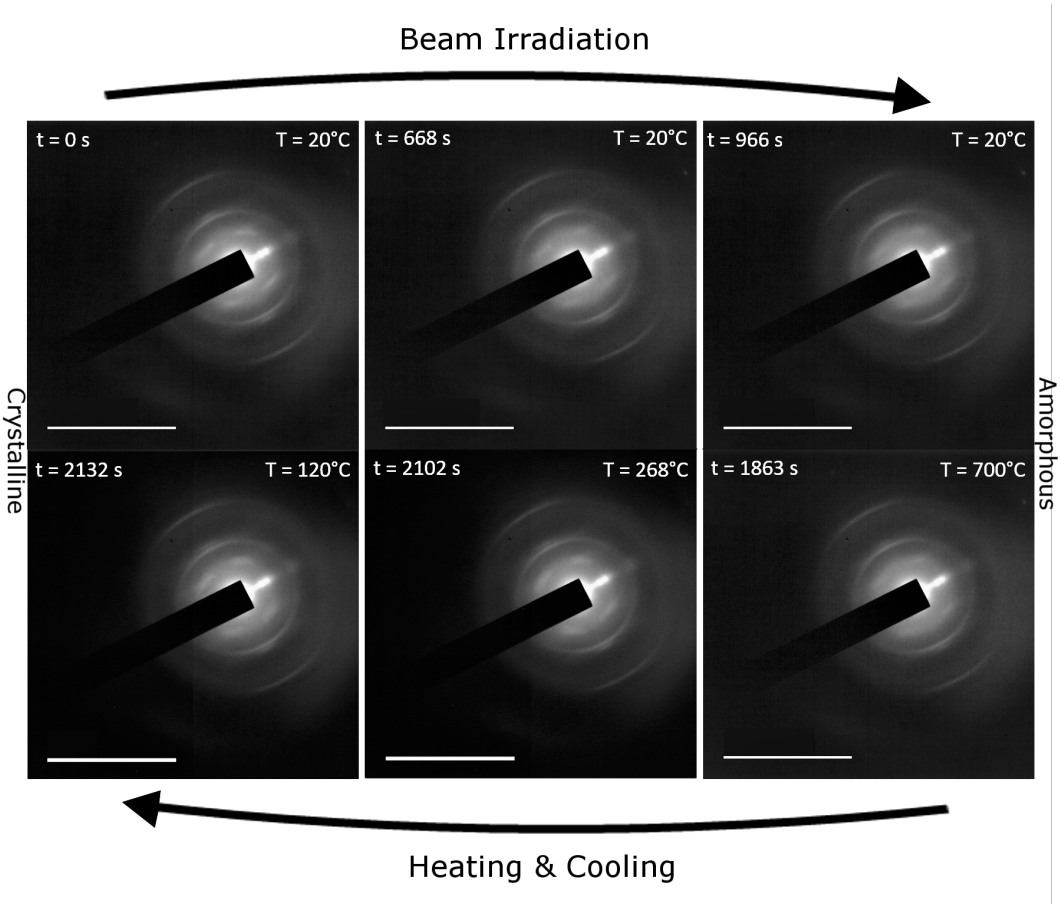


Figure 3.12: Time-resolved SADPs tracking the amorphisation and recrystallisation of encapsulated $Sb_2Te_3$ via *in situ* beam irradiation and sample heating, respectively. The blurring of the diffraction aspects can be attributed to the lengthening of bonds and rearrangement of the atomic structure. The sample was subjected to a continuous beam current density of 23 pA·cm$^{-2}$, over the times indicated. The SADPs track one cycle of beam-induced amorphisation and heat treatment, as described by the corresponding temperatures on each SADP. Scale bars are 1 Å$^{-1}$.

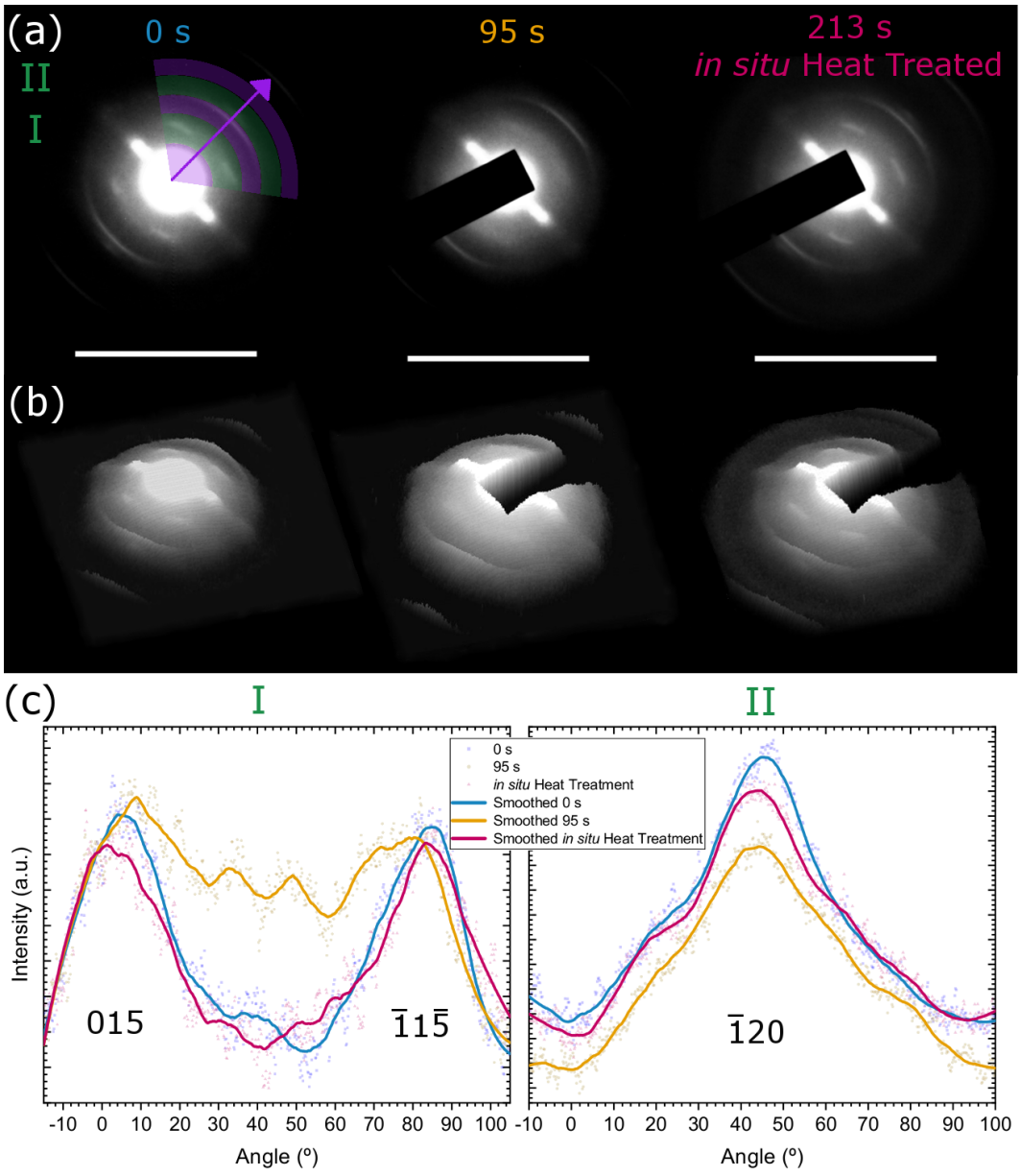


Figure 3.13: (a) Time-resolved SADPs tracking the amorphisation and recrystallisation of encapsulated $Sb_2Te_3$ via *in situ* beam irradiation and sample heating, respectively. The sample was subjected to a beam dose of 120 pA·cm$^{-2}$, over the times indicated. Scale bar is 1 Å$^{-1}$. (b) Intensity surface plots of the SADPs to better show intensity of the reflections. (c) Analytic plots of the intensities of the indexed reflections for nC-$Sb_2Te_3$. There is a clear smoothing of the intensity in the $\sim 0.3$ Å$^{-1}$ aspect in the SADP for the amorphised material, and a corresponding reduction in intensity in the $\sim 0.5$ Å$^{-1}$ aspect. Data was smoothed using the Savitzky-Golay method to the second order, in OrginPro 2019, to better show trend.

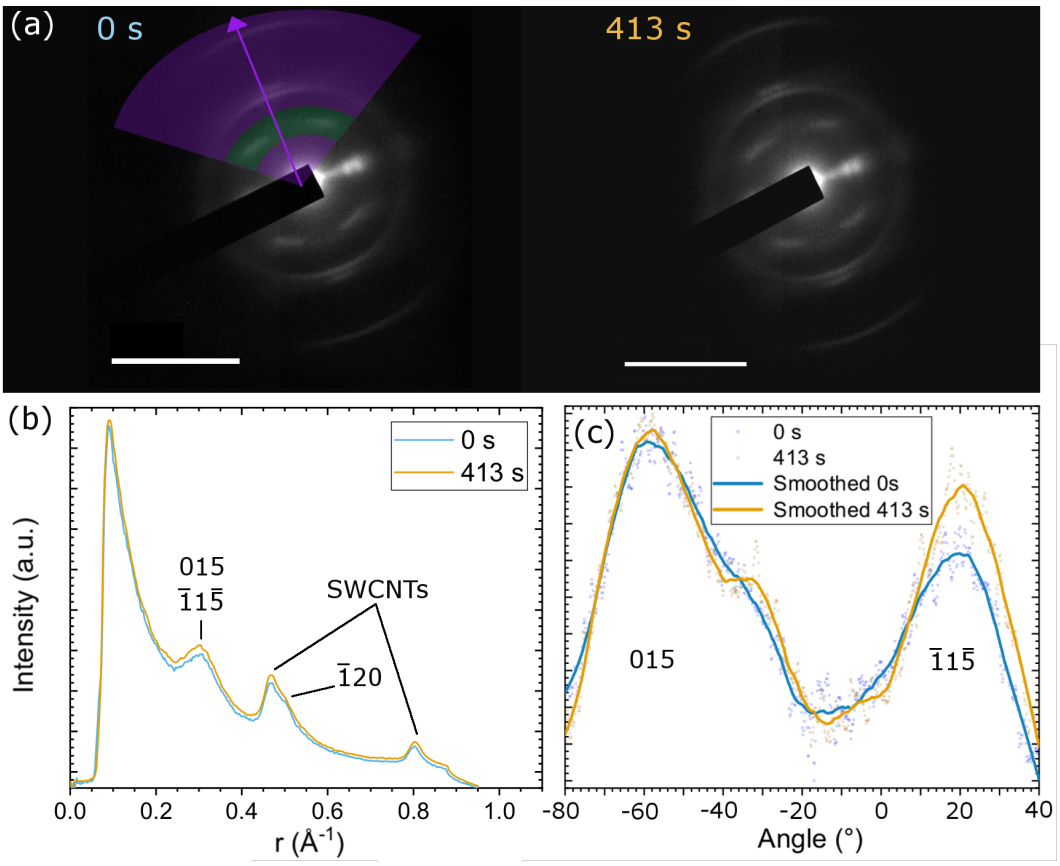


Figure 3.14: Radial SADP characteristics of beam irradiated $Sb_2Te_3$@NI after prolonged irradiation under low dose conditions. (a) A comparison of time-resolved SADPs for $Sb_2Te_3$@NI before and after beam irradiation at 19 pA·cm$^{-2}$ for 413 s. The (b) radial rotational averages and (c) angle-resolved intensity - indicated in pink ad green in (a), respectively - show no clear change in the diffraction aspects or crystallinity of the encapsulated material. Scale bars are 0.5 Å$^{-1}$.

However, the filling material will undergo complete amorphisation after less than 2 mins irradiation at 120 pA·cm$^{-2}$ (Fig. 3.13). This relatively high dose appeared to have no damaging effects on the encapsulated $Sb_2Te_3$ over this timescale. This remained valid for beam current densities up to $\sim$ 300 pA·cm$^{-2}$ in standard TEM, with the amorphisation of filling becoming more rapid with the correlative increase, but no irradiation-induced dissociation being observed over timescales of $\leq$ 200 s. Recrystallisation was not observed to be induced via beam irradiation during this time.

## 3.4 DSC/TGA

Extensive thermal analysis has been carried out on $Sb_2Te_3$ at 1 atm under a nitrogen atmosphere. The work presented here is a continuation of that started by K. Bal and L. Carnohan under the supervision of J. Sloan. By conducting combined DSC and TGA studies on numerous forms of the material, it allowed us to identify characteristic properties of each, such as the melting point of the materials. The data was used to establish key differences in the nano-confined $Sb_2Te_3$, when compared to the bulk, and to expected transition temperatures for bulk $Sb_2Te_3$ ($T_m(Sb_2Te_3) = 620°C$ as given in Table 3.1) [143]. The results of these measurements on the bulk $Sb_2Te_3$ and $Sb_2Te_3$@SWCNT samples were used to identify and determine potential temperature ranges of interest. This process was particularly helpful in determining the point at which the nC-$Sb_2Te_3$ melts without losing significant mass from the sample. The data provided by the thermal measurements proved complementary to the *ex situ* (Section 3.2.1) and *in situ* (Section 3.3.2) exfoliation of $Sb_2Te_3$@SWCNT bundles, due to the identification of specific temperature-induced transitions, and their possible impact on the samples. This included the determination of melt point of the materials, and how further heating affects the mass lost from the sample.
Therefore, in the primary stages of these investigations, it was first important to establish the thermal characteristics of the bulk $Sb_2Te_3$. Initial DSC measurements on as-supplied (from Alfa Aesar) bulk $Sb_2Te_3$ showed that repeated heating to 750°C and cooling to 25°C cycling resulted in an alteration to the characteristic peaks - which suggests the occurrence of a phase transition - in the heating curve of the second cycle ($T_{m_2}$), in comparison with first ($T_{m_1}$), as depicted in Fig. 3.15 (a). There is also an apparent splitting of this transition - indicated by $T_{m_2}^{(I,II)}$ in Fig. 3.15 (a). A negative peak in heat flow is indicative of a melt transition, which is corroborated

| Chemical | Melting Temperature (°C) | Boiling Temperature (°C) |
|---|---|---|
| $Sb_2Te_3$ | 620 | - |
| $TeO_3$ | 430 | - |
| Te | 450 | 990 |
| $SbTe_3O_8$ | 480 | - |
| Sb | 631 | 1587 |
| $Sb_2O_3$ | 656 | 1425 |
| $TeO_2$ | 733 | 1245 |
| $SbO_2$ | 930 | - |

Table 3.1: Basic transitional temperatures for $Sb_2Te_3$ and its constituent elements and oxidation products, ranked by melting temperature at atmospheric pressure [182, 247].

by the near-exponential mass loss (Fig. 3.15 (b)) observed beyond $T_{m_1} \simeq 620°C$ in the first heating curve. We also see a correlative decrease in the solidification transition - indicated by a positive peak in heat flow - between the first and second cooling curves. Despite the apparent $\sim (30-70)°C$ drop in the melt point observed in the second heating curve ($T^{I}_{m_2} \simeq 550°C$, $T^{II}_{m_2} \simeq 590°C$) when compared with the first ($T_{m_1} \simeq 620°C$) depicted in Fig. 3.15 (a)), the mass loss in the second heating curve (Fig. 3.15 (b)) is $< 1$ % of the total starting mass, compared with $\sim 7$ % in the first. Similarly, the proportional mass loss in the second cooling curve is far smaller than that of the first, despite the difference being less pronounced than that of the heating curves. The results presented in Fig. 3.15 are shown over the temperature range (300-750)°C, in order to better highlight the transitions.

Subsequent SEM images of the cycled bulk $Sb_2Te_3$ samples revealed bimodal crystal growth, therefore indicating that the $Sb_2Te_3$ underwent a complex recrystallisation (Fig. 3.16 (a)). This was characterised by the formation of triangular microstructures on the originating planes of the bulk crystal lamellae - highlighted in blue in Fig. 3.16 (a). This morphology can arise due to the layered structure of $Sb_2Te_3$, and the fact that it has hexagonal symmetry (Fig. 3.16 (b)). The layered nature results in a crystal that will readily form platelets which, depending on the substrate and conditions of nucleation, will comprise either hexagonal platelets or triangular ones [248]. Mathematically, these structures can be extracted from the bulk arrangement, as depicted in the [001] projection of a model of bulk $R\bar{3}m$ $Sb_2Te_3$ shown in Fig. 3.16 (b).

However, the formation of these smaller platelets is unlikely account for the $\sim (30-70)°C$ drop in the melt transition observed in the second heating curve ($\sim (550-590)°C$) when compared with the first ($\sim 620°C$, as expected from bulk $Sb_2Te_3$). As although it has been firmly established that the size of a structure impacts the melting temperature, this is usually the case for structures on the nanometer scale, not the micrometer. Buffat et. al have observed a depression in the melting temperature of gold nanoparticles with decreasing radius. They also saw an exponential drop off of the melting temperature for radii less than 5 nm [143]. Such studies may explain why a double melt transition were observed if there were nanostructures present, with the significantly smaller platelets melting first and the larger bulk lamellae persisting to the characteristic transitional temperature - within error.

Taking a different approach, the observed change and split in the melt point could be explained by the coexistence of two different structures - the anticipated hexagonal [001] structure ($R\bar{3}mh$), and a cubic [111] structure ($R\bar{3}mf$). This coexistence could

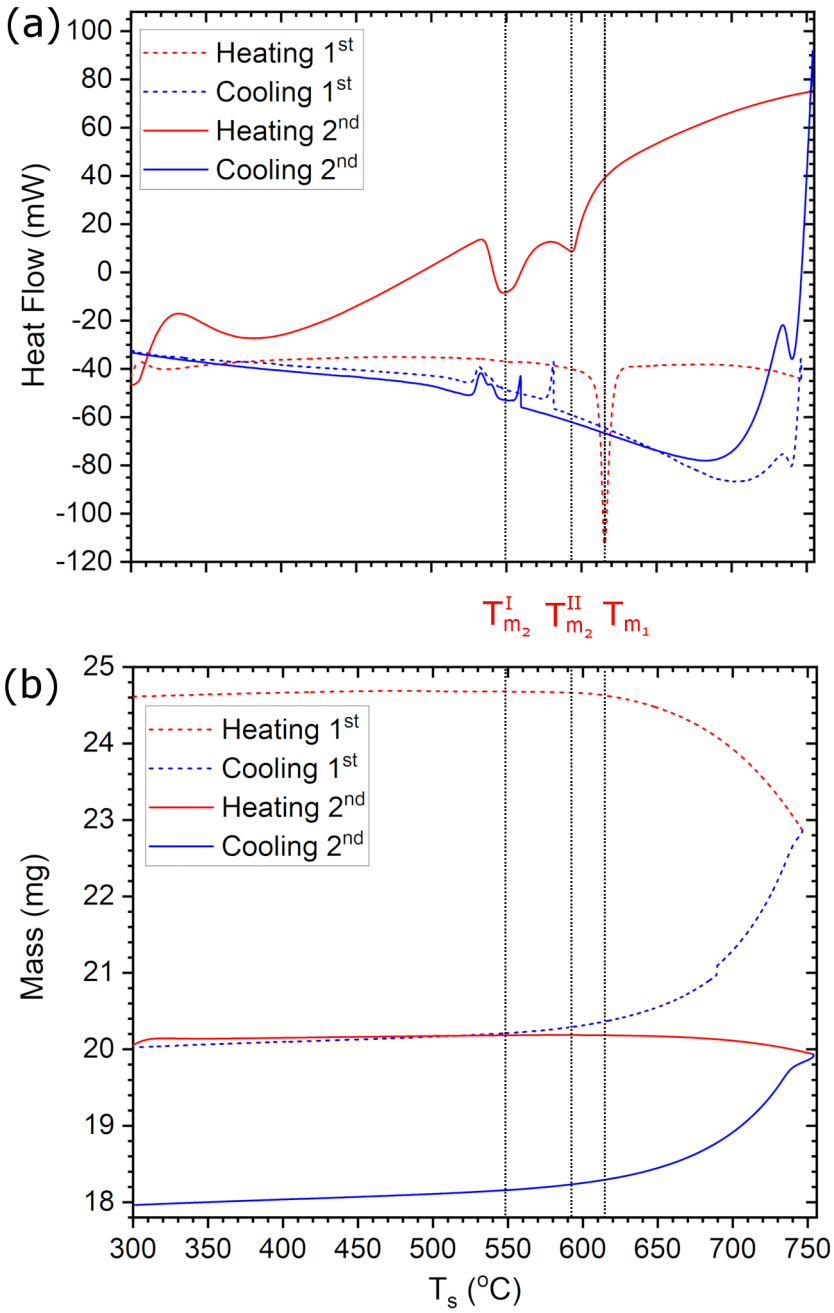


Figure 3.15: TGA and DSC plots for as-supplied (Alfa Aesar) bulk $Sb_2Te_3$ when cycled through 750°C and cooled to room temperature twice. The temperature range (300-750)°C is shown. (a) Cycling the heating and cooling of the as-supplied bulk $Sb_2Te_3$ results in a shift of the characteristic peaks in the DSC heating curves. This is evidenced by the drop in temperature from $T_{m_1}$ to $T_{m_2}$, where $T^{I,II}_{m_2}$ describe a splitting of the melt transition in the second heating curve. (b) The combined TGA plot depicts a near exponential rate of mass loss beyond $T_{m_1}$ in the first heating curve curve, with the first cooling curve exhibiting similar behaviour. The second heating curve exhibits no such behaviour, with $< 1$ % of the total starting mass being lost during this time.

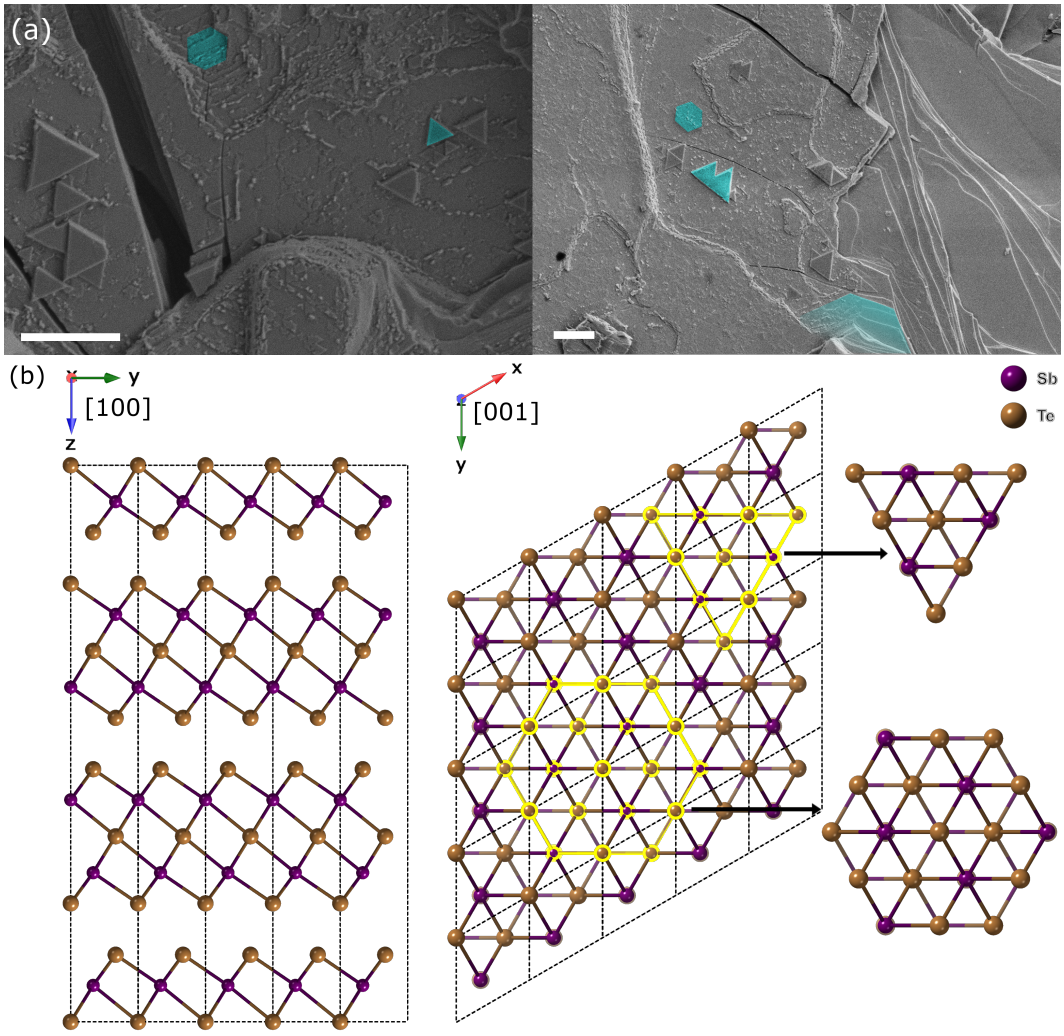


Figure 3.16: Characterisation of the complex recrystallisation observed in post-DSC/TGA bulk $Sb_2Te_3$ via SEM. (a) SEM images reveal that the heat cycling through 750°C of the sample during TGA/DSC results in bimodal crystal growth and complex recrystallisation of the bulk $Sb_2Te_3$. This process prompts the formation of triangular [001] $R\bar{3}mh$ projections on the large hexagonal platelets of the original bulk crystal. The metastable $R\bar{3}mf$ phase can also result in triangular formations (cubic [111]). Images were obtained at an accelerating voltage of 5 kV. Scale bars are 5 $\mu$m. (b) Atomic models depicting the layered rhombohedral structure of bulk $R\bar{3}mh$ $Sb_2Te_3$, and how the microstructures that form during recrystallisation of the $Sb_2Te_3$ can be extracted directly from the [001] projection. The underlying hexagonal symmetry of the structure causes sharp, angular step edges to form during the crystal growth. The dashed lines depict the number of unit cells present in the model. The arrows indicate the view direction in cartesian coordinates.

also explain the triangular formations observed in the recrystallised bulk sample in Fig. 3.16 (a). The latter is accessible to $Sb_2Te_3$ due to a metastable face-centred cubic phase, which holds a distorted octahedron basis, held together by strong covalent like bonds between the Sb and Te atoms [57, 246]. However, the metastable f-phase is conventionally a low temperature one, which converts to the h-phase at temperatures above 220°C [59, 246].

If we instead assume that heating the $Sb_2Te_3$ much past its melting point (620°C) causes a chemical degredation in the material, as has been observed in *in situ* work conducted under the supervision of J. Sloan in this lab, and look at the temperature-composition phase diagrams for the Sb-Te system, then a melt temperature of 550°C would be associated with $Sb_7Te_3$[249]. However EDX analysis of the post-DSC/TGA samples showed the composition to be correct for stoichiometric $Sb_2Te_3$.

Furthermore, if we compare these results with the corresponding SEM images of post-growth and as-supplied $Sb_2Te_3$, outlined in Section 3.2.1, then we see a similarity between the recrystallised $Sb_2Te_3$ and both the post-melt bulk and as-supplied source material. As described before, this is as expected for rhombohedral $R\bar{3}m$ $Sb_2Te_3$, and has been verified via EDX analysis and mapping. This demonstrates that the $Sb_2Te_3$ remains stable, both in stoichiometry and composition, and in structural symmetry after undergoing DSC/TGA analysis. Further analysis of the bulk $Sb_2Te_3$ samples via XRD validates these data. XRD patterns consistently show the presence of peaks characteristic to the phases and symmetry of the original bulk $Sb_2Te_3$ precursor, as will be demonstrated in Section 3.5.

Thermal investigations of $Sb_2Te_3$@SWCNTs via combined DSC/TGA analysis revealed many interesting characteristics: initial DSC/TGA measurements on as-grown $Sb_2Te_3$@SWeNT (Fig. 3.17 (a)) demonstrated its behaviour to be identical to that of the bulk, up to 800°C. A negative peak in heat flow was observed at $T_m = 620$°C, which coincided with a progressive, rapid mass loss - which corroborated the feature being a melt transition. Furthermore, when a maximum temperature of 800°C is used under nitrogen at atmospheric pressure, a negative peak in heat flow at $\sim 620$°C was observed in remnant bulk $Sb_2Te_3$ that has been subjected to the same growth procedure (72 h @ 670°C) as the $Sb_2Te_3$@SWeNT sample (Fig. 3.17 (b)). This is consistent with the anticipated and experimentally observed melt transition temperature for as-supplied bulk $Sb_2Te_3$ outlined in Fig. 3.15 (a) and 3.17 (b). The observed mass loss for all samples was $\sim 3$ mg, for starting total masses of (30-50) mg. Inspection of the bulk material post-analysis revealed the formation of metallic balls, where repeated high temperature melting and recrystallisation had occurred, with minimal proportional mass loss. Furthermore, there is an additional,

smaller negative peak at $\sim 255°C$ in the plots for all three samples in Fig. 3.17 (b), which could be indicative of a low-temperature minor phase transition. This transition may be the melting of small particles, or a structural change - such as the hexagonal-cubic transition outlined above.

However, when measurements were conducted for $Sb_2Te_3$@NI using the same parameters (Fig. 3.17 (c)), a distinct shift was observed in the primary melt transition for the sample, in comparison with the as-grown $Sb_2Te_3$@SWeNT and bulk samples (Fig. 3.17 (b)). A comparison between TGA and DSC curves for the $Sb_2Te_3$@NI - as taken by K. Bal and L. Carnohan, under the supervision of J. Sloan - show that the sample simultaneously gains mass and exhibits a positive heat flow up to 500°C, as shown in Fig. 3.17 (c). This is most likely due to a calibration offset and settling in the equipment. However, this does not account for the sharp drop in heat flow at $\sim 530°C$. Whilst oxidising remnant $Sb_2Te_3$ would account for the fluctuations in heat flow [247], the measurements are taken under an inert nitrogen atmosphere. Furthermore, as can be seen in Table 3.1, no products of the oxidation of $Sb_2Te_3$, or any combination thereof, has a melt temperature in the required vicinity. Therefore, this is most likely indicative of a suppression of the melt temperature, in comparison with the bulk. The, comparatively, small drop in heat flow at 620°C indicates that bulk $Sb_2Te_3$ is still present in the sample in sufficient quantities to exhibit a semblance of the behaviour observed for its bulk forms (Fig. 3.17 (b)). Furthermore, a progressive, near exponential mass loss is observed from the melt point ($T_m$), as with the other samples (Fig. 3.17 (a-b)).

The difference in relative intensities between the heat flows for the bulk and encapsulated samples can be explained by the disparity in mass utilised for each sample. An indication of this is seen in the climbing heat flow observed in the second bulk heating curve, when compared with the first in Fig. 3.15 (a). By the second heating curve significant mass loss has already occurred in the bulk sample - as indicated in Fig. 3.15 (b).

In contrast, the results presented in Fig. 3.17 (c) indicate that the encapsulated $Sb_2Te_3$ - when nano-confined inside NI SWCNTs - exhibits a different temperature-dependency to that of the bulk, in terms of its melt point ($T_m \simeq 540°C$). However, this is in direct opposition to the result for as-grown $Sb_2Te_3$@SWeNT in Fig. 3.17 (a-b), which demonstrates a high correlation to the data obtained from the bulk forms. The most likely explanation for this is the presence of significant extraneous crystalline $Sb_2Te_3$ structures on the outside of the $Sb_2Te_3$@SWeNT bundles, which exhibits similar thermal characteristics to the bulk samples (Fig. 3.15 (a) and 3.17 (b)). The presence of external crystalline material was confirmed by TEM imaging

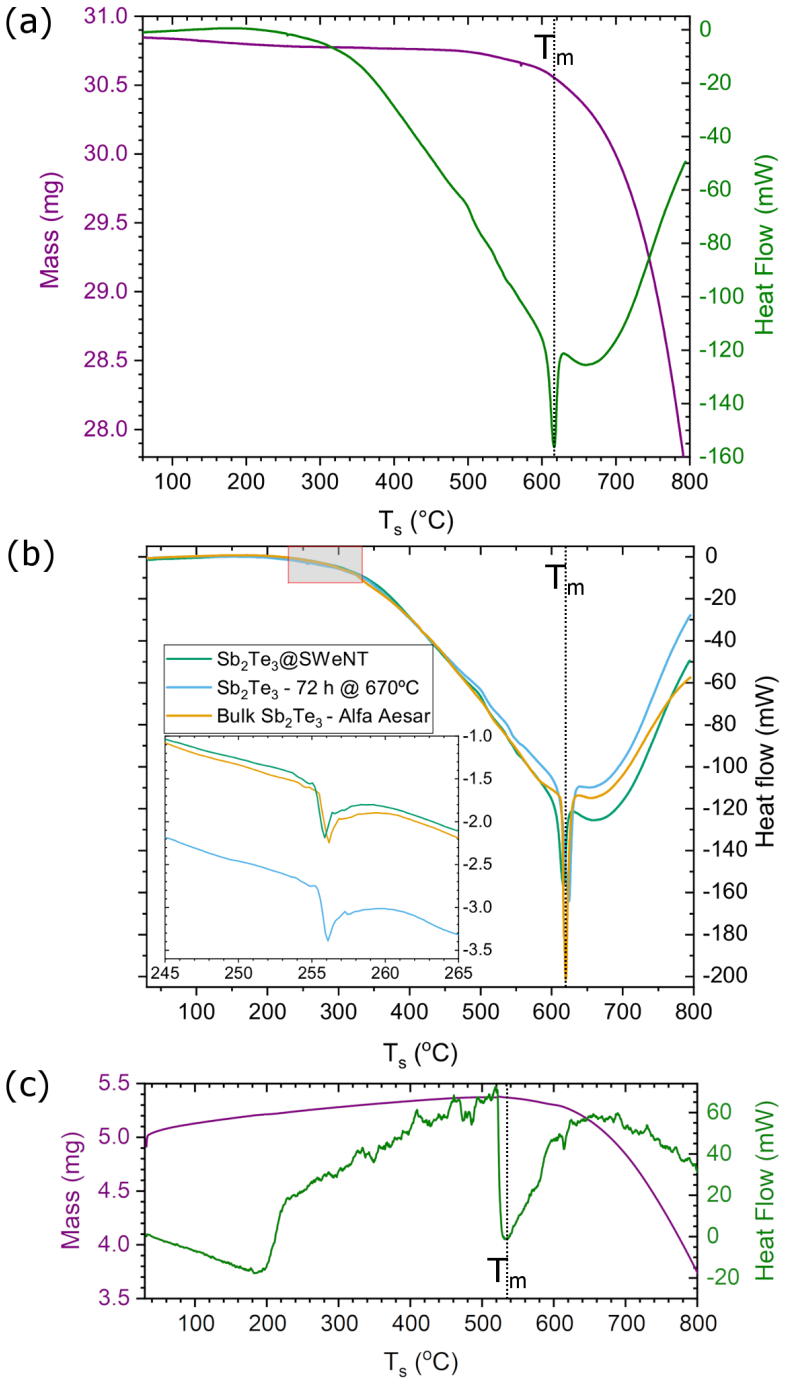


Figure 3.17: TGA and DSC plots comparing bulk and encapsulated forms of $Sb_2Te_3$, up to 800°C. Negative peaks in heat flow are indicative of melt points ($T_m$). (a) Combined TGA/DSC plots for as-grown $Sb_2Te_3$@SWeNT sample ($0.7 \leq d_{SWCNT} \leq 1.3$ nm). $T_m = 620$°C coincides with a progressive, rapid mass loss. (b) DSC plots for measurements on as-grown $Sb_2Te_3$@SWeNT, remnant bulk $Sb_2Te_3$ from the growth of the $Sb_2Te_3$@SWeNT sample (72 h @ 670°C), and as-supplied bulk $Sb_2Te_3$ from Alfa Aesar. Inset shows the peak at $\sim 255$°C, which is consistent in all samples. $T_m = 620$°C is consistent with previous results for bulk $Sb_2Te_3$. (c) Combined TGA/DSC plots for the exfoliated $Sb_2Te_3$@NI sample ($1.2 \leq d_{SWCNT} \leq 2.0$ nm). Above $T_m \simeq 540$°C there is a progressive, rapid mass loss.

of the pre-DSC/TGA $Sb_2Te_3$@SWeNT sample. The relative population of these structures was sufficient to swamp the contribution from the encapsulated $Sb_2Te_3$. Therefore, the extraneous material must be removed if we are to see the true characteristics of the $Sb_2Te_3$@SWCNT samples, across all diameter ranges. These results, shown in Fig. 3.17, illustrate the importance of the exfoliation of samples to remove external crystalline material.

Once exfoliated *ex situ*, the $Sb_2Te_3$@SWeNT sample exhibited a high correlation to the data obtained from the $Sb_2Te_3$@NI (Fig. 3.18 (a)). As with the $Sb_2Te_3$@NI sample, there is a smaller peak in heat flow observed at 620°C, which indicates the presence of stoichiometric $Sb_2Te_3$. This demonstrates the successful exfoliation of the $Sb_2Te_3$@SWeNT, and the emergence of a consistent melt suppression of $\sim 80$°C for $Sb_2Te_3$@SWCNTs ($T_m^{nC}$) compared with the bulk ($T_m^{\infty}$). The former was verified via TEM, wherein a complete removal of external crystalline structures was observed whilst maintaining filling density, as outlined in Section 3.2.1.

In order to verify this behaviour, as-supplied bulk $Sb_2Te_3$, and exfoliated $Sb_2Te_3$@ SWeNT were subjected to the temperature profile outlined in Section 2.5, which cycles through 900°C twice (Fig. 3.18 (b)). The resultant DSC curves show a distinct suppression in the primary melt point in nC-$Sb_2Te_3$ ($T_m^{nC} \simeq 540$°C) when compared with bulk $Sb_2Te_3$ ($T_m^{\infty} \simeq 620$°C). This shift is consistent with the results obtained for encapsulated $Sb_2Te_3$ outlined in Fig. 3.18 (a). The melt transition is as expected for bulk $Sb_2Te_3$; there is a consistent primary dip in heat flow at $\sim 620$°C in all bulk $Sb_2Te_3$ heating curves, which also appears as a secondary melt point in $Sb_2Te_3$@SWCNT (Fig. 3.18).

The cycling of the samples provided data on the consistency of the behaviour of the different forms, as well as indications of the recrystallisation temperatures for each when cooling ($T_r$). These transitions are characterised by positive peaks in heat flow, such as those seen in the cooling curves in Fig. 3.18 (b). In the $Sb_2Te_3$@SWeNT sample, recrystallisation occurred at $T_r \simeq 520$°C, which is consistent with the melt point observed in the heating curve, within error. However, the apparent recrystallisation point of bulk $Sb_2Te_3$ is $T_r \simeq 500$°C, according to the results given in Fig. 3.18 (b) for the first cooling curve. This may explain the subsequent drop in the melt point observed in the second heating curve for $T_m^{\infty}$ compared with the first, as it could be that the ramping to high temperature is inducing the formation of an alternative structure - such as cubic [111] described earlier (Fig. 3.16). By the second cooling cycle (Fig. 3.18 (b)), no thermal behaviour is evident in the bulk sample, whilst the $Sb_2Te_3$@SWCNTs exhibit a reduced intensity $T_r$ value that is consistent with the first cooling cycle, within error ($\sim 530$°C). The reduced intensity

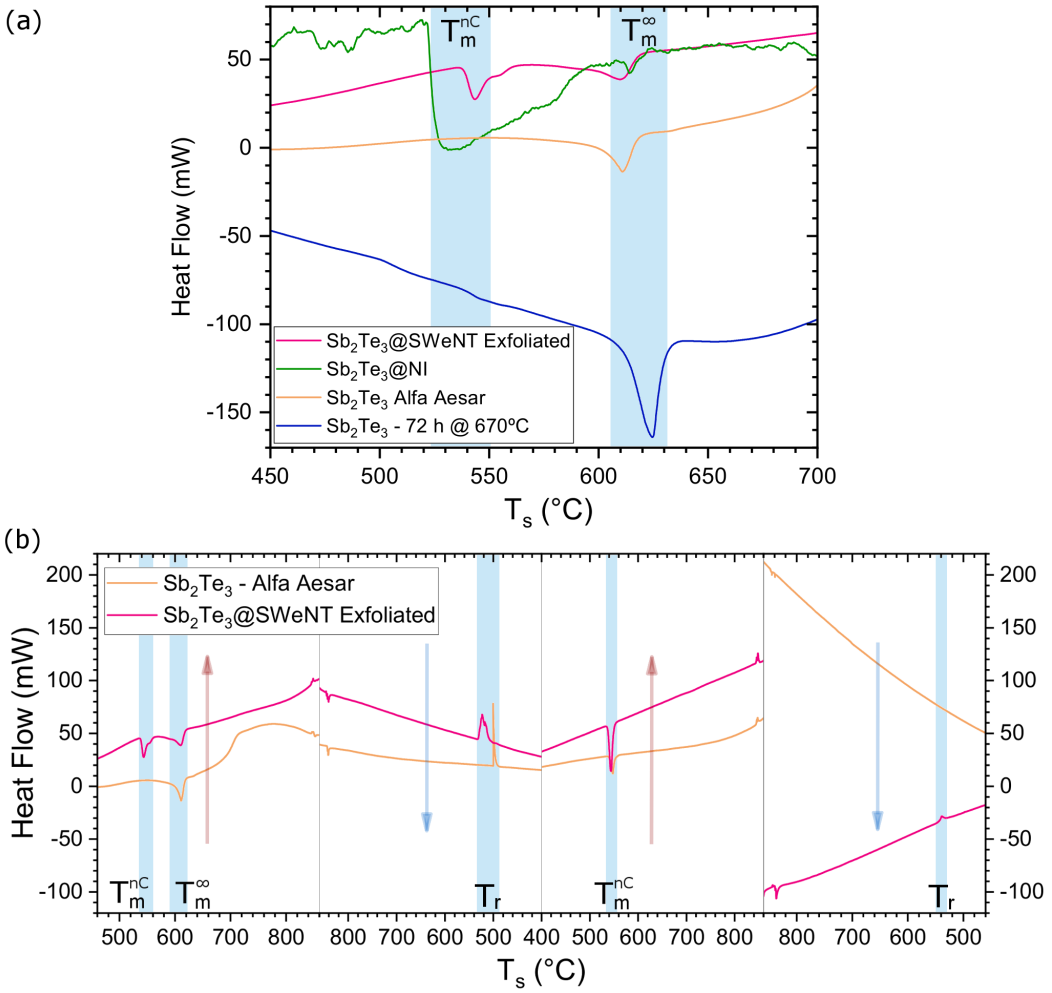


Figure 3.18: Comparative DSC analysis on bulk and nano-confined $Sb_2Te_3$. (a) Experimental DSC plots up to 700°C for exfoliated $Sb_2Te_3$@SWCNTs, remnant bulk $Sb_2Te_3$ from the growth of the $Sb_2Te_3$@SWeNT sample (72 h @ 670°C), and as-supplied bulk $Sb_2Te_3$ (Alfa Aesar) which show a clear, and consistent, suppression in the melt transition between encapsulated $Sb_2Te_3$ ($T_m^{nC}$) and bulk $Sb_2Te_3$ ($T_m^{\infty}$). (b) DSC plots for heat cycling twice through 900°C of exfoliated $Sb_2Te_3$@SWeNT and as-supplied bulk $Sb_2Te_3$ (Alfa Aesar). Melting ($T_m^{nC}, T_m^{\infty}$) and recrystallisation ($T_r$) points are illustrated. Heating and cooling phases are indicated by the red and blue arrows, respectively.

is due to the significant mass loss experienced by the samples. In the case of the bulk $Sb_2Te_3$, $\geq$ 95 % of the total mass was removed by this cycling process. In contrast, the $Sb_2Te_3$@SWeNT sample persisted at $\sim$ 25 % mass remaining, where $\sim$ 15 % can be attributed to the SWCNTs.

The significant mass loss observed in this research in all samples, when subjected to temperature cycling through 900°C, demonstrates that both bulk and encapsulated material is lost when subjected to these conditions. However, complementary ADF-STEM imaging on a post-DSC/TGA sample (Section 3.2) shows that a single heating cycle through 800°C at atmospheric pressure in nitrogen will remove extraneous material, whilst leaving the encapsulated $Sb_2Te_3$ intact (Fig. 3.4). Therefore, whilst we see a melt suppression in the nC-$Sb_2Te_3$ (Fig. 3.18), the material appears to be wholly contained by the SWCNT and so remains encapsulated during this phase, up to at least 800°C at atmospheric pressure. However, the bulk material has no such stabilising phenomena, and so sublimation and loss of material mass occurs more readily under these conditions. Therefore, this process provides us with a third method by which to purify the samples of extraneous material. Unlike the *in situ* exfoliation method described in Section 3.3.2, no scarring of the SWCNTs is observed using this method - as evidenced in the comparative images given in Section 3.2.

Other ongoing work conducted in this lab under the supervision of J. Sloan has found that the $Sb_2Te_3$ begins to decompose between (600-900)°C. The sample is most likely preferentially losing Te, which is more voltaile and has a lower melting temperature (450°C) than Sb (630°C), but both of which will be molten above 620°C - the melting point of $Sb_2Te_3$. As mentioned before (Section 3.3.2), recrystallisation becomes irreversible if the composition of the nC-$Sb_2Te_3$ begins to changes.

Substantial differences in the average values for the heat flow curves between the samples could be the result of the varying intial masses used. It was pertinent to also determine the thermal characteristics of the SWCNTs. Combined DSC/TGA experiments on unfilled SWCNTs demonstrated that the heat flow characteristics of the SWCNTs (Fig. 3.19 (a)) are almost identical to that of the blank (Section 2.5); the SWCNTs exhibit no heat-induced phase changes. This confirms them to be suitable and stable as confining elements for this research, and can thus be ignored for the purposes of thermal analysis of the samples. Therefore, all peaks are confirmed to be from the $Sb_2Te_3$. Additionally, there is no significant mass loss, when cycled through the same protocols as the filled samples. Indeed, in the case of high temperature DSC/TGA on the filled nanocomposites, the SWCNTs can be the dominant, or only, remaining mass in the post-analysis sample (Fig. 3.19 (b)).

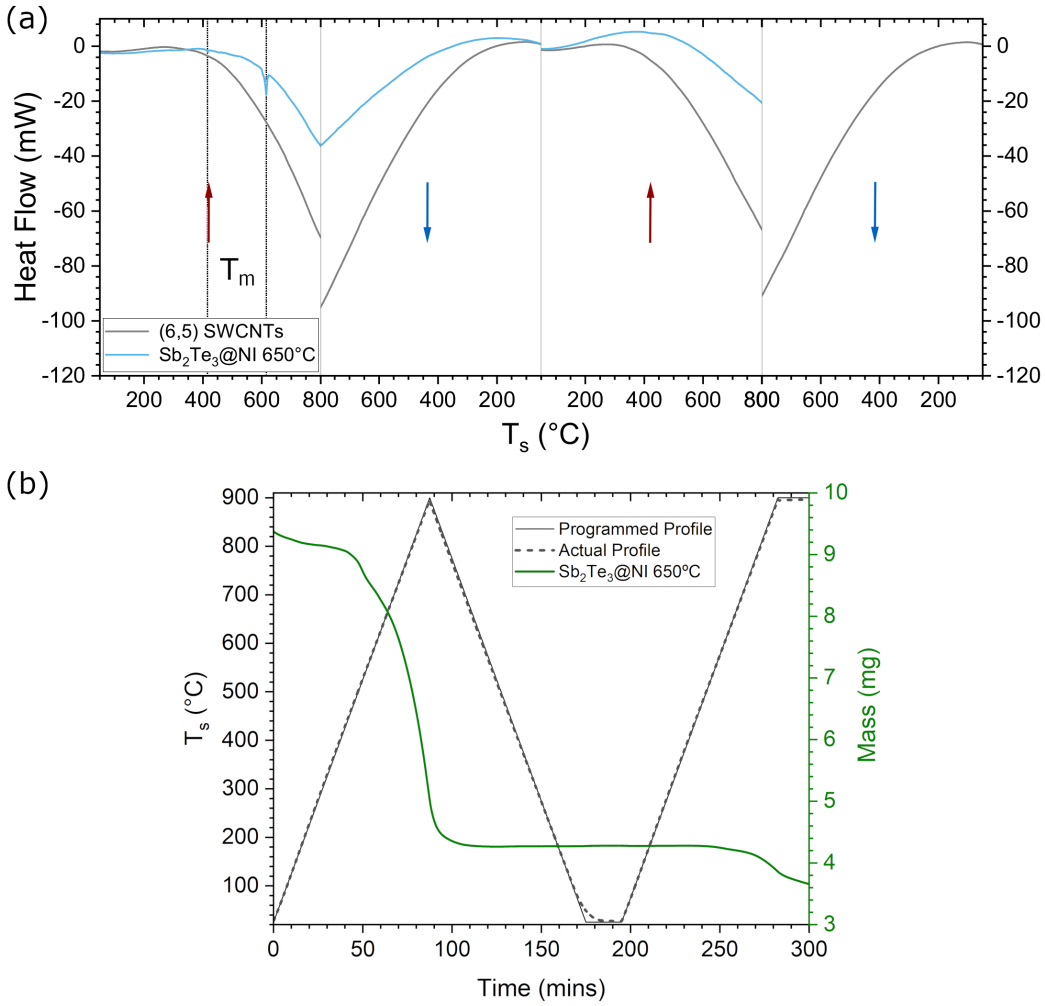


Figure 3.19: Combined DSC/TGA measurements on $Sb_2Te_3$@NI grown at 650°C via the melt method and comparison with (6,5) SWCNTs. Experimental (a) DSC and (b) TGA plots for $Sb_2Te_3$@NI, grown at 650°C, and cycled through 900°C twice. (a) There is the anticipated drop in heat flow at 620°C, however the additional drop in heat flow is significantly lower in intensity and temperature ($\sim$ 420°C) than the nano-confined samples grown at 670°C. The DSC curve appears almost identical to that of the raw SWCNTs in the second heating curve. (b) There is a near complete loss of mass of nC-$Sb_2Te_3$ after a single heating curve, with only SWCNTs comprising the final sample, as indicated by the plateau in the second heating curve. Heating and cooling phases are indicated by the red and blue arrows, respectively.

These investigations were further expanded to the heat flow and thermal properties of samples with alternative growth protocols. Growth by sublimation has already been determined to provide undesired results, as outlined in Section 2.1, so was discounted from these experiments. However, investigations into the effect of using alternative temperatures for the melt growth of $Sb_2Te_3$@SWCNTs (Section 2.1) have demonstrated that the as-grown samples can comprise a considerably lower filling fraction, alternative stoichiometry, or exhibit a distinct shift in the properties. This is true for samples grown at 650°C or lower.
Thermal analysis of a filled sample grown via the melt method at 650°C demonstrates such $Sb_2Te_3$@SWCNTs to exhibit altered heat flow properties (Fig. 3.19 (a)), when compared with those grown at 670°C. The mass loss characteristics show a plateau during the second heating curve, indicating the near complete loss of nC-$Sb_2Te_3$ and the persistence of the SWCNTs only. The shift in heat flow and observation of complete mass loss of filling material (Fig. 3.19 (b)) suggest that the encapsulated material either contains non-stoichiometric components (unlike the 670°C samples), or is in a distinctly altered phase (Table 3.1) [248].
Further to these considerations, the pressure exerted on the sample must also be taken into account. For example, $Sb_2Te_3$ has been observed to undergo a phase transition at a pressure of $\sim 72 \cdot 10^3$ atm [101, 167]. At 1 atm, the established melting temperature of R$\bar{3}$m bulk $Sb_2Te_3$ is 629°C, whilst the melting points of bulk R$\bar{3}$m Sb and bulk P321 Te are 631°C and 450°C, respectively [250, 251]. Table 3.1 provides us with a basic understanding of the transitional and formation temperatures of the oxides of these $Sb_2Te_3$ elements. This aspect of the work has been investigated further, and is evidenced in Section 3.5, wherein the observed formation of such oxides at $\sim$ 300°C, when the $Sb_2Te_3$ sample is heated in air at 1 atm, has been described.

## 3.5 XRD

SEM images of the remnant bulk $Sb_2Te_3$ from growth procedures has more cubic-like morphology, alongside the hexagonal formations, as outlined in Section 3.4. These are as expected for rhombohedral R$\bar{3}$m $Sb_2Te_3$. Although they could also indicate the presence of a metastable low-temperature cubic phase of $Sb_2Te_3$ [59, 252]. Combining these results with EDX mapping demonstrates that, for the growth and filling processes used here, the $Sb_2Te_3$ remains stable in composition. However, we cannot discern the symmetry of the material via these methods. XRD analysis of the bulk $Sb_2Te_3$ samples validates the persistence of the R$\bar{3}$m $Sb_2Te_3$ structure

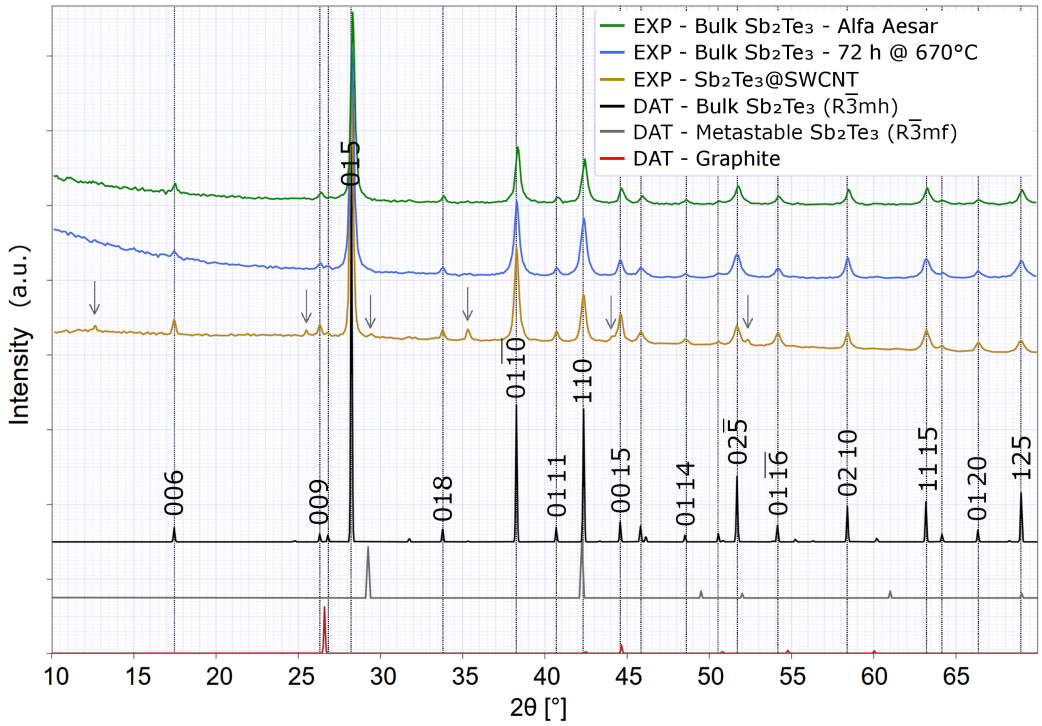


Figure 3.20: A comparison of the room temperature XRD patterns for three forms of $Sb_2Te_3$, and simulated XRD patterns for models of bulk $Sb_2Te_3$ and graphite. The metastable cubic $Sb_2Te_3$ ($R\bar{3}mf$) pattern was simulated from data published by Zheng et. al [246] and Yin et. al [59]. The peaks from the database model for bulk $Sb_2Te_3$ ($R\bar{3}mh$) are indicated with dashed lines. Those with higher intensities are indexed with their hkl values. For $Sb_2Te_3$@SWCNTs, we also see the appearance of additional new reflections - as indicated by the grey arrows - that cannot be attributed to bulk $Sb_2Te_3$ ($R\bar{3}mh$), nor the graphitic carbon model. The $Sb_2Te_3$@SWCNT peaks at 29° and 42° coincide with the highest intensity peaks for metastable $Sb_2Te_3$ ($R\bar{3}mf$).

(Fig. 3.20). Powder XRD diffraction patterns consistently show the presence of peaks characteristic to the phases and symmetry of the original bulk $Sb_2Te_3$ precursor for those samples whose composition has been confirmed via EDX as being stochiometric $Sb_2Te_3$.

Comparing the XRD patterns of the pertinent forms of $Sb_2Te_3$ (Fig. 3.20) at room temperature gives a good grounding for identifying the fundamental differences and aspects present in each [242–244]. A combined figure for the room temperature patterns exhibited by as-supplied bulk $Sb_2Te_3$, $Sb_2Te_3$@SWeNT, and the remnant bulk $Sb_2Te_3$ from the growth of $Sb_2Te_3$@SWeNT is shown in Fig. 3.20. Theoretical patterns for bulk $Sb_2Te_3$ and graphite are also given, to directly compare the sources of the characteristic peaks in the experimental patterns. These were ob-

tained by simulating XRD scattering in CrystalDiffract$^{TM}$ of modelled structures provided in the CrystalMaker and ICDD databases (Section 2.6). The metastable cubic $Sb_2Te_3$ pattern - identified by "DAT - Metastable $Sb_2Te_3$ R$\bar{3}$mf" in Fig. 3.20 - was simulated from data published by Zheng et. al [246] and Yin et. al [59]. The line broadening observed in the peaks in the experimental patterns can be caused by strain in the material, defects and varied crystal sizes, which are not accounted for in the ideal, simulated patterns [253–256].

The bulk forms of $Sb_2Te_3$ shown in Fig. 3.20 clearly exhibit the characteristic peaks expected for rhombohedral $Sb_2Te_3$, as given by the overlap of experimental peaks with the dashed lines - which indicate reflections in the simulated $Sb_2Te_3$ pattern. Reflections with higher intensities have been overlayed with their indexed hkl values. However, in the case of $Sb_2Te_3$@SWCNTs, we see the same expected peaks, but also the appearance of new additional reflections - indicated by the grey arrows in Fig. 3.20 - that can be attributed to neither the bulk $Sb_2Te_3$, nor the graphitic carbon model [239–241]. This is true when compared with both the experimental and theoretical (simulated database) patterns. Since the compositional ratios of the sample has already been checked and consistently confirmed (Section 3.2), these peaks are most likely indicative of new phases and bonding that are not present in any capacity in the bulk form. However, this would need to be verified via further investigation of filled and unfilled SWCNTs.

Furthermore, it can be expected that some peaks may be absent in the XRD patterns for $Sb_2Te_3$@SWCNTs, when compared with bulk $Sb_2Te_3$. Whilst this does not appear to be the case for the room temperature pattern shown in Fig. 3.20, such absences could be due to a lack of interactions and bonding from the van der Waals planes that are present in the layered bulk material, that are not in the encapsulated form, for example. The appearance of any additional, low-angle, peaks in the nC-$Sb_2Te_3$ patterns would be as expected due to hexagonal packing of SWCNTs. These would appear at low scattering angles due to the large scale distances of these interactions (Section 2.6). We see the appearance of one such peak at $\sim 12.5^{\circ}$ in the $Sb_2Te_3$@SWCNT pattern in Fig. 3.20.

Further to this investigation, as introduced and outlined in Sections 3.4 and 3.3, it is interesting to look at, and compare, the temperature-dependent characteristics of the various forms of $Sb_2Te_3$. However, to do this, the pressure and atmosphere exerted on the sample must be taken into account. At 1 atm, the established melting temperature of R$\bar{3}$m bulk $Sb_2Te_3$ is 620°C, whilst the melting points of bulk Sb and bulk Te are 631°C and 450°C, respectively [182]. The melting and formation temperatures of the oxides of these elements, in combination, are given in Section

3.4. Furthermore, these materials have distinct XRD charateristics, with little or no overlapping of peak positions occuring between simulated XRD patterns for the different materials (Fig. 3.21 (a)). This should make the emergence, and coexistence, of any oxidation products easier to identify in the experimental patterns (Fig. 3.21 (b)). An additional question arises as to whether we need to consider the affect, if any, that relatively small differences in pressure has on the formation of these undesirable compounds.

In the simplest case, when heated at 1 atm in air, we see the formation of such oxides at around 300°C (Section 3.4). This observation was tracked via the the changing peaks in XRD as bulk $Sb_2Te_3$ was heated to 600°C, and then cooled to room temperature. The progression of the XRD patterns with temperature from bulk powdered $Sb_2Te_3$, under these conditions, is given in Fig. 3.21 (b).

The sample appears to remain stable in its rhombohedral form until approximately 300°C, at which point the relative intensities of the existing peaks begin to change. Emerging and receding peaks are indicated by arrows in Fig. 3.21 (b). This is concurrent with the behaviour exhibited by bulk crystalline $Sb_2Te_3$ deposits when subjected to *in situ* heating in the TEM, as outlined in Section 3.3.2. By 400°C, we see a dramatic decrease in the overall intensity from the sample, with the majority of the room temperature $R\bar{3}m$ $Sb_2Te_3$ peaks having diminished or disappeared. Despite the elevated temperature, some new peaks can be identified from the database as potential oxidation products of antimony and tellurium [257, 258]. These new peaks are indicated from the instance of their appearance in the temperature-resolved XRD patterns by dark grey arrows in Fig. 3.21 (b). Similarly, receding $Sb_2Te_3$ peaks, amongst others, are denoted by light grey arrows. These products display consistent and stable diffraction characteristics as the sample continues to be heated to 600°C and then cooled back to room temperature. The final room temperature pattern exhibits none of the characteristic peaks of its originator. Instead, the final sample is now wholly comprised of Te, $TeO_3$, and $SbTe_3O_8$. This is consistent with the melting and formation temperatures given in Section 3.4, and is corroborated by the altered appearance of the once grey powdered sample to a yellow-white (Fig. 3.21 (c)).

Considering the significant effects that heating under standard atmospheric conditions have on the bulk $Sb_2Te_3$, vacuum or an inert atompshere is required to track phase changes to bulk $Sb_2Te_3$, whilst maintaining stoichiometry when heating. Therefore, the heated experiment was repeated under a vacuum of $\sim 10^{-6}$ atm (Fig. 3.22) using a standard tilted stage XRD (Section 2.6.2). However it was discovered that, in this configuration, the sample becomes less cohesive with the surface

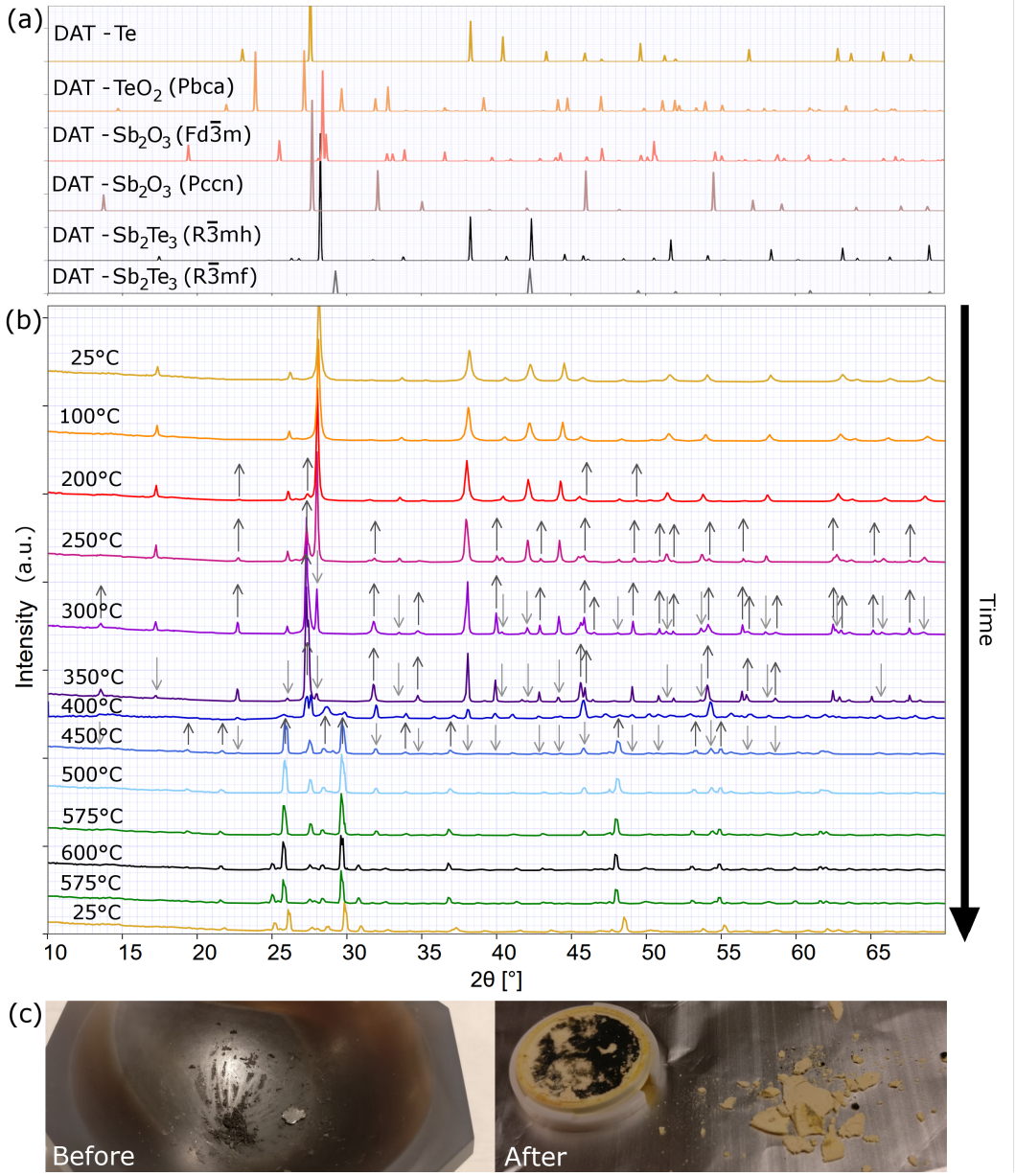


Figure 3.21: The progressive oxidation of bulk $Sb_2Te_3$ when heated in air at 1 atm to 600°C and then cooled to room temperature. (a) Simulated XRD patterns for - bulk rhombohedral ($R\bar{3}mh$) and metastable cubic ($R\bar{3}mf$) - $Sb_2Te_3$ and its oxidation products. (b) XRD patterns display a reduction in the overall peak intensity as the heating, and initial oxidation, of the sample progresses. The relative intensities of the $Sb_2Te_3$ peaks start to change at $\sim$ 300°C. Some of these have disappeared by $\sim$ 400°C, whilst new peaks corresponding to antimony and tellurium oxides begin to appear. Beyond this, any remaining peaks from $Sb_2Te_3$ display a systematic shift from accepted positions at room temperature. The final scan, acquired at room temperature, confirms the sample to have completely oxidised; peak analysis detected the presence of Te, $TeO_3$, $Sb_2O_3$, and trace others. Emerging and receding peaks are indicated by the arrows. (c) Visual inspection of the post-heating sample reveals a distinct alteration in its appearance before and after.

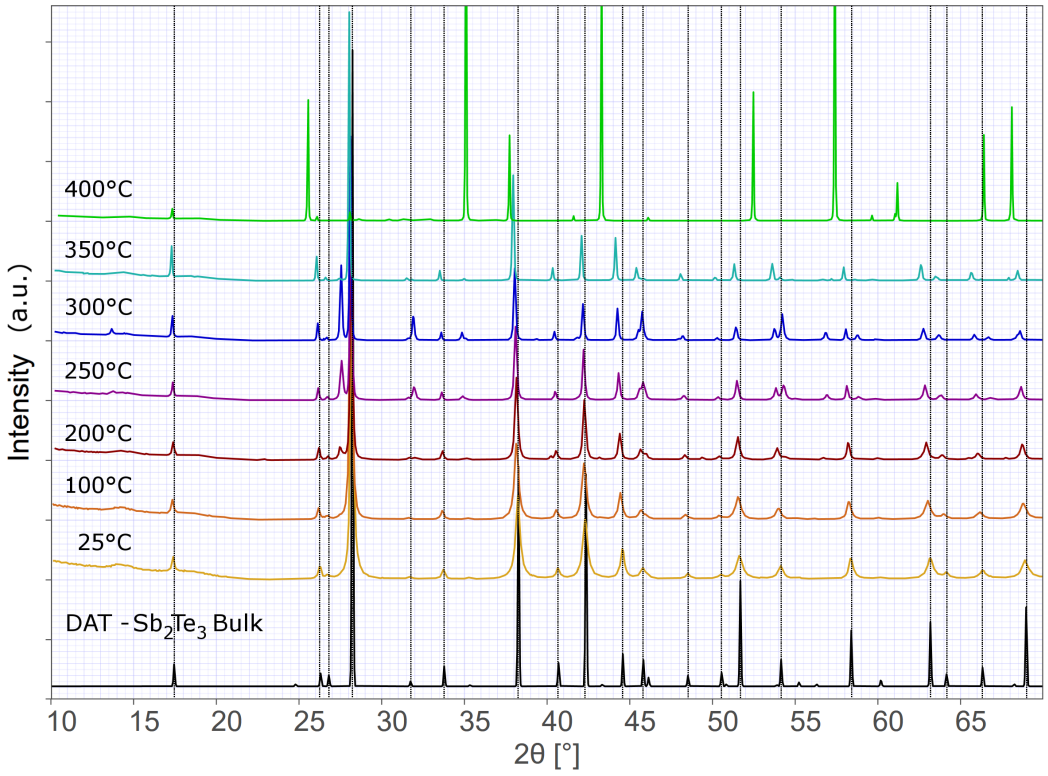


Figure 3.22: XRD patterns tracking progression of bulk $Sb_2Te_3$ when heated under vacuum using the tilted stage configuration. The peaks can be seen to begin to shift as the sample is heated, before slippage begins to occur at 350°C. Therefore, by the 400°C measurement the sample is observed to be almost entirely lost to the vacuum. The dashed lines indicate the higher intensity peaks that appear in the simulated bulk rhombohedral $R\bar{3}m$ $Sb_2Te_3$ pattern.

of the stage and slippage occurs, such that the sample either sublimes or is sucked down the vacuum at $\sim 400°$C. There is the onset of some indicative changes to the XRD pattern at $\sim 350°$C, as shown in Fig. 3.22. The simulated XRD pattern for a model of rhombohedral $Sb_2Te_3$ is also given, with dashed lines showing key peak positions. Heating induces a small, but proportional, offset in the scattering angles, as can be seen by the shift of characteristic peaks to lower angles with increasing temperature in Fig. 3.22. By 350°C, the higher angle peaks have shifted by $\sim 0.6°$, with respect to the room temperature (25°C) pattern, whilst the 17.5° peak at room temperature appears at 17.4°. By 400°C, almost the entire sample has been lost, with only a minor contribution to the resultant pattern being observed (after adjusting for the angle offset). The remainder of the reflections in the XRD data at this temperature originate from the holder.

In order to combat both of the issues outlined above, a new machine with a static stage (as described in Section 2.6.2) was utilised. The sample was powdered and arranged as before, and then encased in a graphite dome and evacuated to $\sim 0.2$ bar under nitrogen. The bulk $Sb_2Te_3$ was then heated to 600°C and cooled to room temperature, with XRD data being obtained at 50°C intervals. As before, we see a shift of the peaks to lower angles, as the temperature increases Fig. 3.23. This can be observed most clearly at higher scattering angles, where the positions of the reflections appear to deviate most significantly from those in the room temperature data (dashed lines).

The graphite dome caused a large graphite peak at $\sim 28°$ to be consistently present in the diffraction patterns, as seen in Fig. 3.23. This peak overlaps with, and dominates, the strongest peak for bulk rhombohedral $Sb_2Te_3$, as shown in the "DAT" pattern in Fig. 3.22. Depsite this, clear characteristic peaks of the $Sb_2Te_3$ could be identified in the initial room temperature pattern. These peaks persist up to $\sim 350°$C, at which point the pattern begins to change. The arrows in Fig. 3.23 denote emerging and receding reflections. This is indicative of the sample undergoing a distinct phase transition, or alteration. This change is similar to that seen by Yin et. al for the $Sb_2Te_3$ $R\bar{3}mf - R\bar{3}mh$ phase transition - where the structure transitions from face centred cubic (f-phase) to hexagonal (h-phase) [59]. However, the metastable f-phase is conventionally a low temperature one, converting to the h-phase at temperatures above 220°C [59, 246, 252].

In Fig. 3.23, by 500°C the phase that emerged at 250°C has almost entirely disappeared, and the pattern appears to revert to one that is more akin to the room temperature $Sb_2Te_3$ rhombohedral phase, with a (0.5-1.0)° offset in peak positions. This behaviour persists through additional heating to 600°C, and only re-emerges

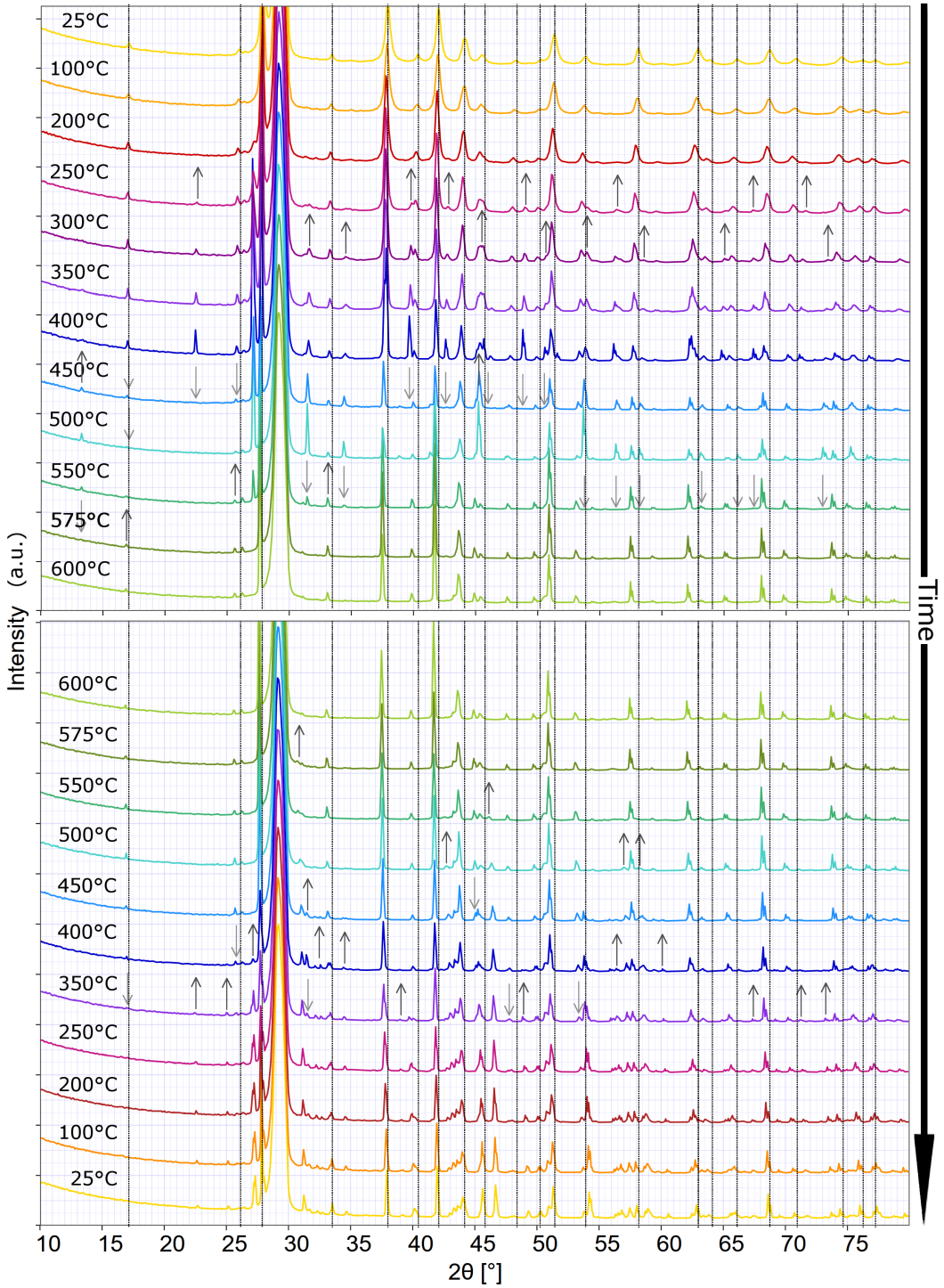


Figure 3.23: XRD patterns tracking the progression of bulk $Sb_2Te_3$ when heated through 600°C and cooled to room temperature under nitrogen at $\sim 0.2$ bar, using the static stage set-up. The peaks can be seen to begin to shift and new peaks appear at 350°C as the sample is heated. These then begin decrease in intensity, or have completely disappeared, by $\sim 450$°C. Once the peak temperature of 600°C has been reached, the pattern has almost returned to that seen at room temperature. Dashed lines indicate peak positions in the initial room temperature pattern. Arrows denote emerging, and receding, reflections.

at $\sim 450$°C on the cooling curve. Conversely, some low-angle peaks can be observed to disappear and reappear at these benchmark temperatures in the heating and cooling curves. This could be indicative of the loss and re-emergence of long-range order and bonding in the sample. The phases stored in the database, and used for the identification of materials are room temperature patterns. Therefore, although the high temperature patterns appear similar to room temperature rhombohedral $Sb_2Te_3$ (Fig. 3.20 - 3.23), it is difficult to accurately quantify the phases at elevated temperatures [257, 258]. This is due to broadening and peak shifting that can be caused by heating alone. However, it was also possible for some aspects in the lower temperature patterns to be attributed to rhombohedral $Sb_2Te_3$, hexagonal $Sb_2Te$, and cubic Te. This is concurrent with compositional changes observed for $Sb_2Te_3$ films that have been annealed at different temperatures up to 300°C by Chen et. al [259], where a mixture of $Sb_2Te_3$, $Sb_2Te$ and Sb was seen to form.

Beyond this, it is difficult to identify the dominant phase and composition of the resultant sample when returned to room temperature, due to the emergence of peaks from the steel alloy holder (Fig. 3.23). This can be attributed to the recystallisation of the sample, which was also suggested by the change in the diffraction patterns around $\sim 450$°C. Visual inspection of the post-experiment sample showed this to be the correct. Additionally, some shrinkage in the sample mass had occurred, which was particularly evident around the edges of the sample holder (Fig. 3.24). This resulted in significant portions of the steel alloy holder becoming exposed, which was evidenced by the appearance of corresponding additional peaks in the diffraction patterns (Fig. 3.23). The material had a distinctly increased metallic appearance to the inserted powdered material (Fig. 3.24). This would explain, in part, the changes seen to the diffraction aspects on the cooling curve. In particular, the onset of peak splitting and the sharpening of peak widths, could be explained by the formation of crystallites in the sample. Despite these issues, it was possible to identify the presence of $Sb_2Te_3$, $Sb_2Te$, Sb, Te and possible trace $SbTe_3O_8$ in the final room temperature pattern (Fig. 3.23).

However, if we consider these results alongisde those for the nC-$Sb_2Te_3$ (Fig. 3.25), then some interesting comparisons can be drawn. As with the room temperature studies of the nano-confined and bulk samples (Fig. 3.20 at the beginning of this section), we see the appearance of additional peaks in the encapsulated sample. Some of these can be easily attributed to the CNTs (Section 2.6), whereas others have no trace association with rhombohedral $Sb_2Te_3$, C, CNTs, or any speciation products of such. These peaks are present and consistent in all room temperature XRD studies, including those taken post-heat-treatment and cycling. The dashed


Figure 3.24: Images of the as-supplied bulk $Sb_2Te_3$ prior to, and immediately after, heating under nitrogen atmosphere and cooling to room temperature, using the static stage XRD configuration. The as-supplied bulk sample was finely ground prior to XRD. Visual inspection of the post-experiment sample showed the heat cycling to have caused shrinkage to centre of holder, and a loss of mass. This resulted in significant portions of the steel alloy holder becoming exposed.

lines in Fig. 3.25 indicate reflections observed in the initial room temperature measurement, which are then used as a benchmark for comparison with those seen at elevated temperatures, and in the cooling cycle.

Furthermore, as with the temperature dependent XRD measurements for bulk $Sb_2Te_3$ (Fig. 3.23), we see the onset of changes at $\sim$ 200°C, with the most notable alterations occuring from 350°C. As with the bulk $Sb_2Te_3$ sample, we see the emergence of new peaks, and the recedence of existing ones, which could be indicative of the formation of an alternative phase that may be in coexistence with the rhombohedral bulk phase at elevated temperatures (Fig. 3.25). However, as before, this phase almost entirely disappears by 575°C, being replaced by one that exhibits almost identical XRD characteristics to the room temperature structures present in $Sb_2Te_3$@SWCNTs. Furthermore, this pattern of reflections, beyond 550°C in the heating curve, persists to 600°C, and all through the cooling curve. This behaviour exhibited by the $Sb_2Te_3$ is unlike the bulk $Sb_2Te_3$ (Fig. 3.23), which displayed mirrored peak changes on the cooling curve to that of the heating curve.

Therefore, it may be that the confining environment of the SWCNTs allows the $Sb_2Te_3$ to rearrange whilst encapsulated at elevated temperatures, exhibiting a loss of long range order, and then remain stable in these new forms. Whereas the bulk $Sb_2Te_3$ has no such confining phenomenon (the crystal edges tend to inifinity), there-

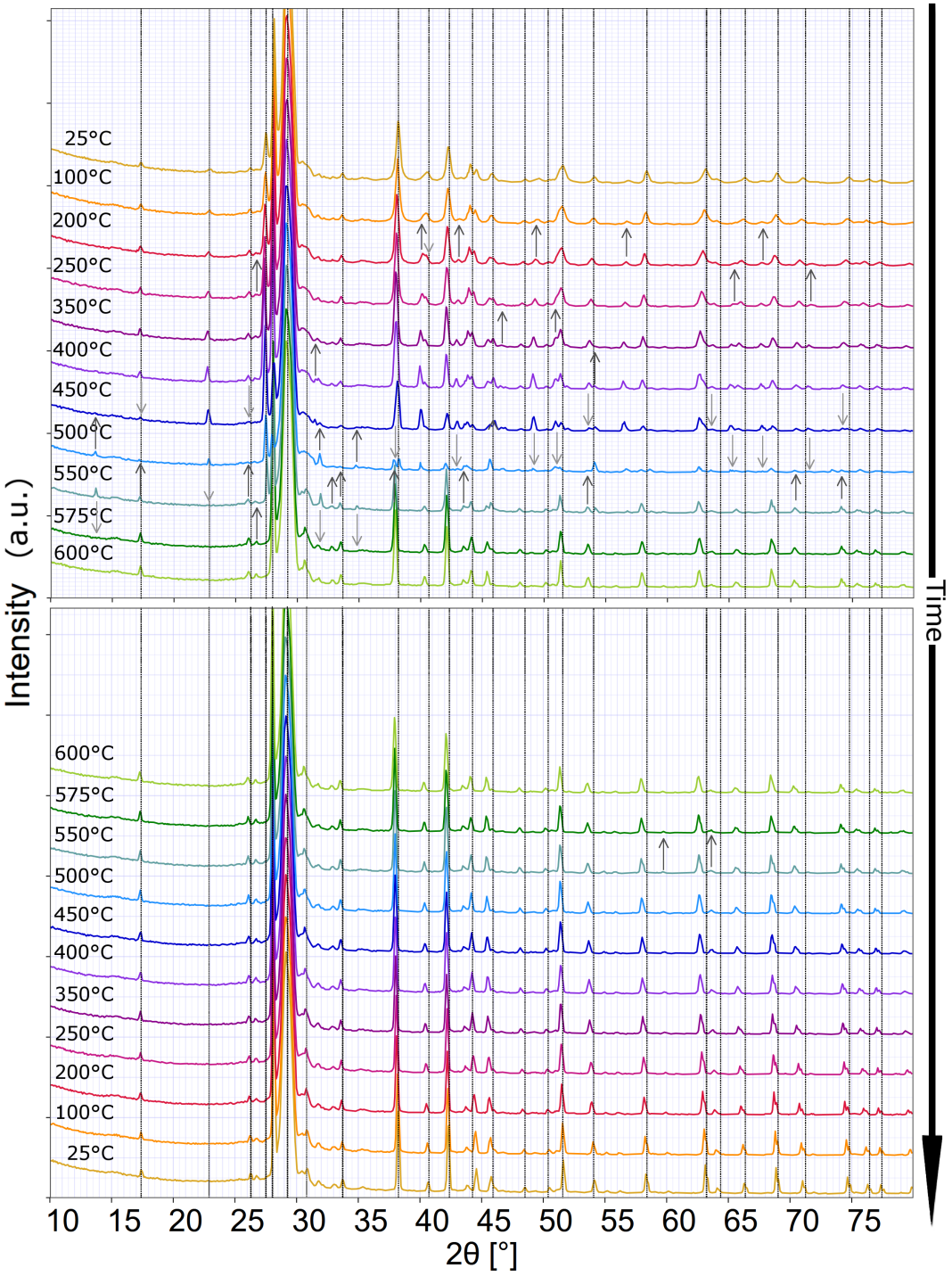


Figure 3.25: XRD patterns tracking the phase and composition changes in nC-$Sb_2Te_3$ when heated to 600°C and cooled to room temperature under nitrogen at ∼ 0.2 bar, using the static stage set-up. The $Sb_2Te_3$@SWCNTs sample comprised $Sb_2Te_3$ encapsulated in predominantly (6,5) SWCNTs. Dashed lines indicate peak positions in the initial room temperature pattern. Arrows denote emerging and receding reflections as the sample is heated and cooled. See also Fig. 3.20, 3.21, and 3.23.

fore is predispositioned to reorder to its lowest energy state - the rhomobohedral phase that it began in, since there has been no apparant chemical degradation.

## 3.6 Conclusion

Three methods of removing external crystalline structures from $Sb_2Te_3$@SWCNTs samples have been identified and discussed. These include *ex situ* exfoliation - a sealed ampoule is heated under a vacuum of $\sim 10^{-6}$ atm to 500°C - (Section 3.2.1), *in situ* heating to 900°C (Section 3.2), and heating to 800°C under nitrogen at atmospheric pressure (Section 3.4).

In addition to the *in situ* experiments tracking and analysing the phase transition in $Sb_2Te_3$@SWCNTs, early-phase *ex situ* experiments have shown promise in capturing the glassy phase of the nC-$Sb_2Te_3$, but this forms part of future work, which shall be discussed further in Section 6.

Possible new phases have been observed in the room temperature XRD patterns for nC-$Sb_2Te_3$, that cannot be attributed to the bulk form of the material. Additionally, a distinct phase transition or alteration has been identified in bulk $Sb_2Te_3$ when heated to 350°C. This phase wholly disappears and reverts to the room temperature $Sb_2Te_3$ rhombohedral phase by 500°C. This behaviour persists through additional heating to 600°, and only re-emerges at $\sim$ 450°C on the cooling curve.

# Chapter 4

# Encapsulated SnSe

## 4.1 Introduction

SnSe has been chosen for encapsulation due to its established applications in photovoltaics and memory-switching devices, and its phase change behaviour [9, 99, 100, 126]. This behaviour has been repeatedly investigated and applied in the bulk material, and has been observed to persist when SnSe is in a thin film form. Therefore, the question of whether these properties extend to stoichiometric nC-SnSe - where the structures are significantly modified with respect to those of the bulk - is what prompted the investigation into the growth of SnSe@SWCNTs. The research presented in this chapter lays the groundwork to these extended studies.

The first section examines the growth of SnSe@SWCNTs, and how the structures that form compare with bulk. A particular focus is made on investigations into the variation of the structure of the encapsulated material as a function of the diameter of the NT, alongside a confirmation of the desired Sn:Se composition ratio of 1:1. A full catalogue of these observed structures has been compiled, which includes an analysis, and modelling, of a newly observed form of nC-SnSe.

This cataloguing is complementary to the analysis of the amorphisation of the nC-SnSe, which has been observed in live TEM imaging, but has been captured and evidenced by time-resolved SAED, which is outlined in the second section.

Further temperature-dependence and compositional analysis of the various forms of SnSe have been conducted, and were facilitated by DSC/TGA. These data and results are reported in the third section. The experiments sought to illustrate the phase and temperature characteristics and the corresponding response of the nC-SnSe, in comparison with the bulk.

## 4.2 Structural Analysis

### 4.2.1 Large Scale Structure & Composition

The fabrication of SnSe-filled nanotube samples was carried out using vapour phase transport via the sublimation method at 700°C (Fig. 4.1). The SnSe@NI sample growth was carried out in a 3-zone furnace, where the 20 cm long ampoule spanned two zones only; one being held at 700°C, the second at 265°C (Section 2.1). The SnSe@SWeNT sample was grown in a single-zone furnace, as described in Section 2.1. The metallic mirror observed on the interior of the ampoule in the SnSe@SWeNT image in Fig. 4.1 is from vacuum evacuation and sealing of the silica quartz ampoule. This process can cause negligible quantities of powdered bulk material to be drawn towards the point of sealing, which then rapidly melts and recrystallises on the walls of the ampoule. The as-supplied bulk SnSe is orthorhombic and belongs to the Pnma space group (Fig. 4.2 (a)). As such, it has underlying distorted NaCl structure which is expected to strongly present in the bulk crystals (Fig. 4.1 and 4.2). The visual appearance of the crystalline material gives an indication of its underlying structure, which can be clearly observed in the SnSe@SWeNT system. Similarly, the placement of the deposited bulk material provides a suggestion of the likelihood of a high filling fraction of the SWCNTs with SnSe. The high population of crystal material before the neck of the ampoule - and away from the SWCNT flakes - in the SnSe@SWeNT system shown here indicates that the relative proportion of filled SWCNTs may be low.

Research into the phase behaviour and Antoine equations (Section 2.1) of SnSe prior to filling placed it as a good candidate for vapour phase transport, since it melts, and sublimes, congruently [151, 260] from a stoichiometric source material, up to a specific pressure and temperature [173, 174, 180]. Review of the literature for the SnSe system gives experimentally determined values to these. Boone et. al reported the congruency of SnSe at a melting temperature of 1163 K at atmospheric pressure [166], and Hirayama et. al observed vapour pressures on the order of (1-10)$\cdot 10^{-6}$ atm in the range (773-898) K [179]. The latter quoted the specific use of an Antoine equation of the form

$$\log_{10}(\mathrm{P[atm]}) = 7.318 - \frac{10495 \pm 151}{\mathrm{T[K]}}, \tag{4.1}$$

which was experimentally calculated and observed to be valid within the stated temperature range. Whilst this is published data and is theroretically accepted, it is important to verify the quality of the grown nanocomposites in this lab. This is

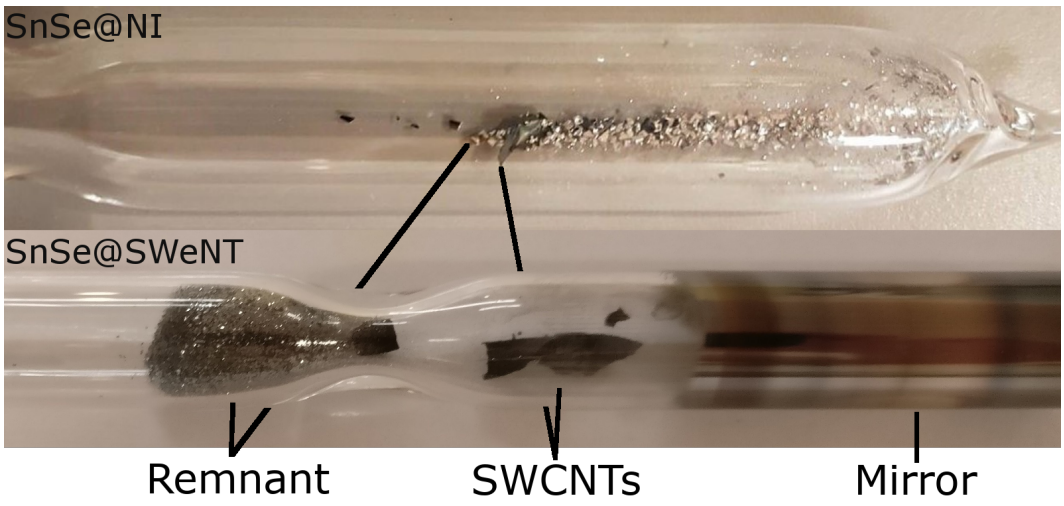


Figure 4.1: As-grown SnSe@SWCNT samples in evacuated growth ampoules. Both samples were grown via the sublimation method at 700°C. The SnSe@NI sample growth was carried out in a 3-zone furnace, whereas the SnSe@SWeNT sample was grown in a single-zone furnace. The metallic mirror observed on the interior of the ampoule in the SnSe@SWeNT image is from vacuum evacuation and sealing of the silica quartz ampoule. The silver appearance of the crystals is as expected for SnSe.

especially significant given that the temperature used for growth (700°C) - a suitable temperature for the vacuum pressure used ($\sim 10^{-6}$ atm), as indicated by Eq. 4.1 and additional research into the Antoine equations for SnSe [179, 180] - is $> 150$°C lower than the atmospheric melt temperature of SnSe (861°C) [174, 180].
Therefore, an initial step in analysing the samples is verifying their composition and stoichiometry, which can be achieved via direct analysis of the SnSe@SWCNTs. However, this requires the nano-confined sample to be processed and dispersed onto a TEM grid, as outlined in Section 2.1.5. A quicker method is to analyse the bulk remnant material from the growth. This has the additional benefit of allowing for direct comparison with the as-supplied bulk SnSe. Indeed, sometimes this can be discerned from the appearance of the newly grown sample when it is still in the ampoule (Fig. 4.1). The shape, colour, and structure of the remnant crystalline material - as indicated in Fig. 4.1 - gives a rudimentary idea of the underlying morphology. In the case of the as-grown material shown in Fig. 4.1, the bulk crystals have a silver-grey, cuboid appearance, as is expected for SnSe (Fig. 4.2 (a)) [179]. However, if the crystals are smaller, or less well-defined then a more in depth appraisal of the surface and structures are required. This can be achieved via SEM imaging, and combined with EDX analysis, in order to quickly and efficiently compare the effects of different growth protocols on the structure and composition of

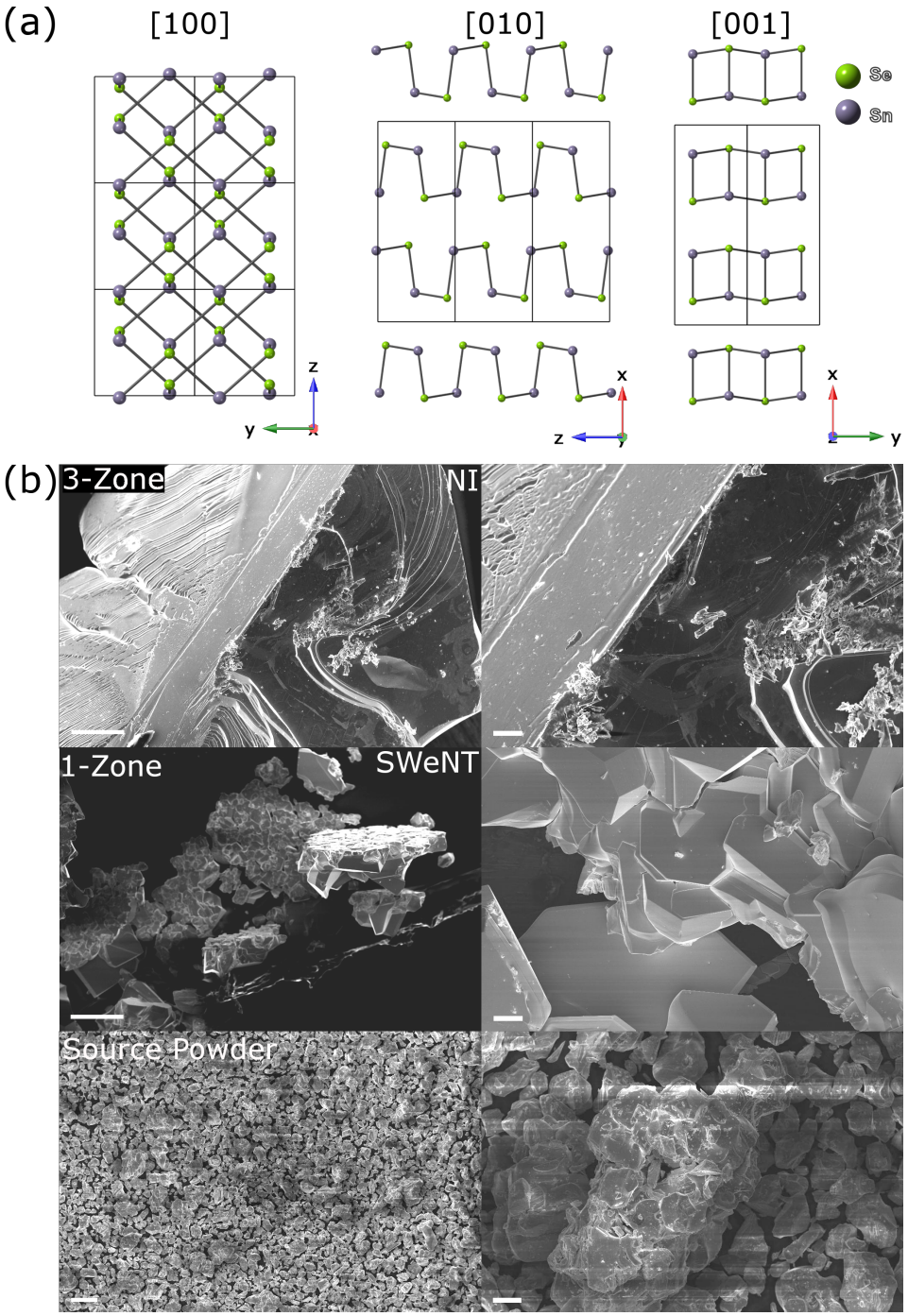


Figure 4.2: The structure of bulk Pnma SnSe and SEM images comparing the large scale structure of as-supplied SnSe, and post-growth remnant bulk material for two representative samples. (a) Structural models of the main projections of bulk Pnma SnSe. The black lines shown the unit cell. (b) SEM images of post-growth bulk material from protocols utilising a 3-zone or single-zone ("1-zone") furnace, and the as-supplied growth source powder. Scale bars are 100 $\mu$m (left) and 20 $\mu$m (right).

the samples.

SEM images of the different bulk samples reveals a complex combination of facets and crystals presenting at the surface of the material (Fig. 4.2 (b)). In some samples, the underlying distorted orthorhombic symmetry is visually more apparent, such as in the distorted cuboidal remnant crystals from the SnSe@SWeNT ("1-zone") sample growth shown in Fig. 4.2 (b). In contrast, the remnant material from the growth of the SnSe@NI ("3-zone") sample shown in Fig. 4.2 (b) takes the form of much larger crystals - one of which is shown here - with sweeping step edges, and clusters of small, irregularly-shaped crystals on the surface. Furthermore, from these SEM images (Fig. 4.2 (b) the remnant crystals from the SnSe@SWeNT growth also appear more similar to the source SnSe powder than those from the SnSe@NI. This comparison of the large scale structure of the post-growth samples and the as-supplied bulk material, indicates the impact of using a 1-zone or a 3-zone furnace for growth. The remnant bulk material from the two growths appear to show a semblence of similarity between the step edges at the surface of the 3-zone remnant crystal, and the edges of the smaller crystals in the 1-zone remnant material alone. These images, in combination with EDX investigations (Fig. 4.3), provide a rudimentary understanding of the structural effects that the sublimation and heat treatment has on the growth precursors, and how this compares with the as-supplied bulk SnSe.

Although the bulk forms present differently on the microscale (Fig. 4.2), the EDX mapping investigations reveal the composition of the samples to all be stoichiometric. Therefore, the varying visual appearances of the materials could be symptomatic of the differing temperature gradients and deposition zone annealing temperatures imposed during growth. These variables are dictated by the use of a 1-zone or 3-zone furnace, due to the length of the furnaces and the range of the heating elements (as discussed in Section 2.1). The temperature gradient largely instructs the temperature and placement of the deposition zone, which in turn has significant ramifications on the quality and filling fraction of the material. Further investigations revealed the resulting structures and compositions from growth in a single-zone furnace to be far more variable than those from a 3-zone. These results can be correlated with atomic scale imaging (Section 4.2.2), and further compositional and thermal analysis (Section 4.4) to better understand the samples and the effects of the processes that they undergo.

Similarly, an initial indication of the anticipated filling fraction of the SWCNTs with SnSe can be discerned from the position of the majority of the deposited material in relation to the CNTs in the ampoule. The post-growth SnSe@SWeNT system

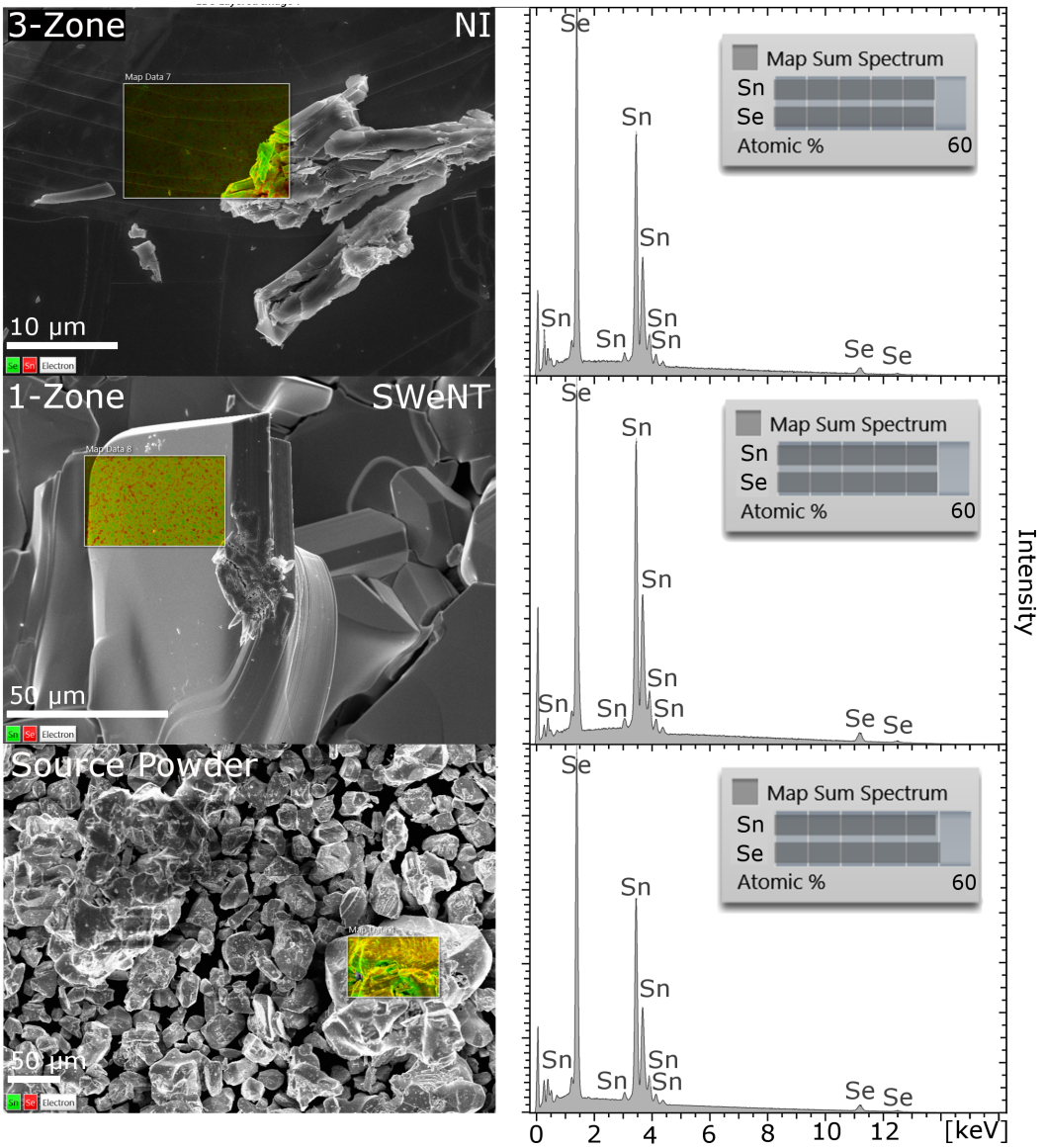


Figure 4.3: SEM imaging and EDX of the large scale structure of the bulk SnSe source powder, in comparison with the post-growth remnant material for two representative samples, showing the impact on composition (at. %) of using a 1-zone or a 3-zone furnace for growth of the SnSe@SWCNT samples.

shown in Fig. 4.1 has a high population of crystal material before the neck of the ampoule, and away from the NI flakes. This indicates that the relative proportion of filled SWCNTs may therefore be low. However, nanoscale and density probing analysis of the SWCNT bundles is required to confirm this.

This can be achieved via high resolution (S)TEM - where the atomic arrangements and filling can be discerned. Since annular dark field STEM is sensitive to the atomic number of the analysed materials, the filling material can be clearly observed (as shown by the bright lines of contrast following the axis of the bundle in Fig. 4.4). Images were obtained using both a STEM-capable SEM at 10 kV (Fig. 4.4 (a)), and a high resolution STEM system at 80 kV (Fig. 4.4 (b)), as described in Section 2.2. Analysing the filling proportion in the SnSe@SWCNT samples is made a lot faster through the use of a STEM-capable SEM. However, the highest resolution is on the order of 100s nm to 1 $\mu$m, which is far below that of the ADF-STEM on the AR-TEM system. The high fraction filling of SWCNT with SnSe depicted in the dark field STEM imaging in Fig. 4.4 - observed particularly for the growth processes conducted in a three-zone furnace, as for the SnSe@NI sample shown in Fig. 4.1 - was consistently observed in all repeated growths conducted using the same protocols. Furthermore, the relative population and prevalence of extraneous crystals across all dispersed samples is low. This can be seen in the dark field STEM images of SnSe@SWCNT bundles in Fig. 4.4, where there is almost no bright "bulk" contrast to be associated with the extraneous crystal, as previously shown in Fig. 3.4 in Section 3.2.1. The dark field STEM images shown in Fig. 4.4 are representative of the low population of external crystals observed across all of the high yield SnSe@SWCNT samples.

Therefore, the growth procedure can be considered to be relatively efficient. It also means that fewer processing stages are required for the as-dispersed sample to adequately prepare it for analysis and characterisation, which reduces the risk of introducing chemical-born contaminants to the samples. Not only does this prove promising for the scalability of the consistent growth of high quality samples, but it also provides an improved signal for EDX and compositional analysis, particularly over very localised areas. Representative high resolution imaging and EDX analysis is shown in Fig. 4.5.

The EDX analysis of SnSe@SWCNTs bundles routinely gave a Sn/Se ratio of one to one, within error (Sn to Se as 50 $\pm$ 1 at.% to 50 $\pm$ 1 at.%, respectively). Additional EDX investigations of other areas and SnSe@SWeNT specimens, as well as the VPT remnant material SnSe outlined above in Fig. 4.3, gave congruent Sn/Se ratios for both wt.% and at %, which confirmed the pursued 1:1 stoichiometric SnSe ratio of

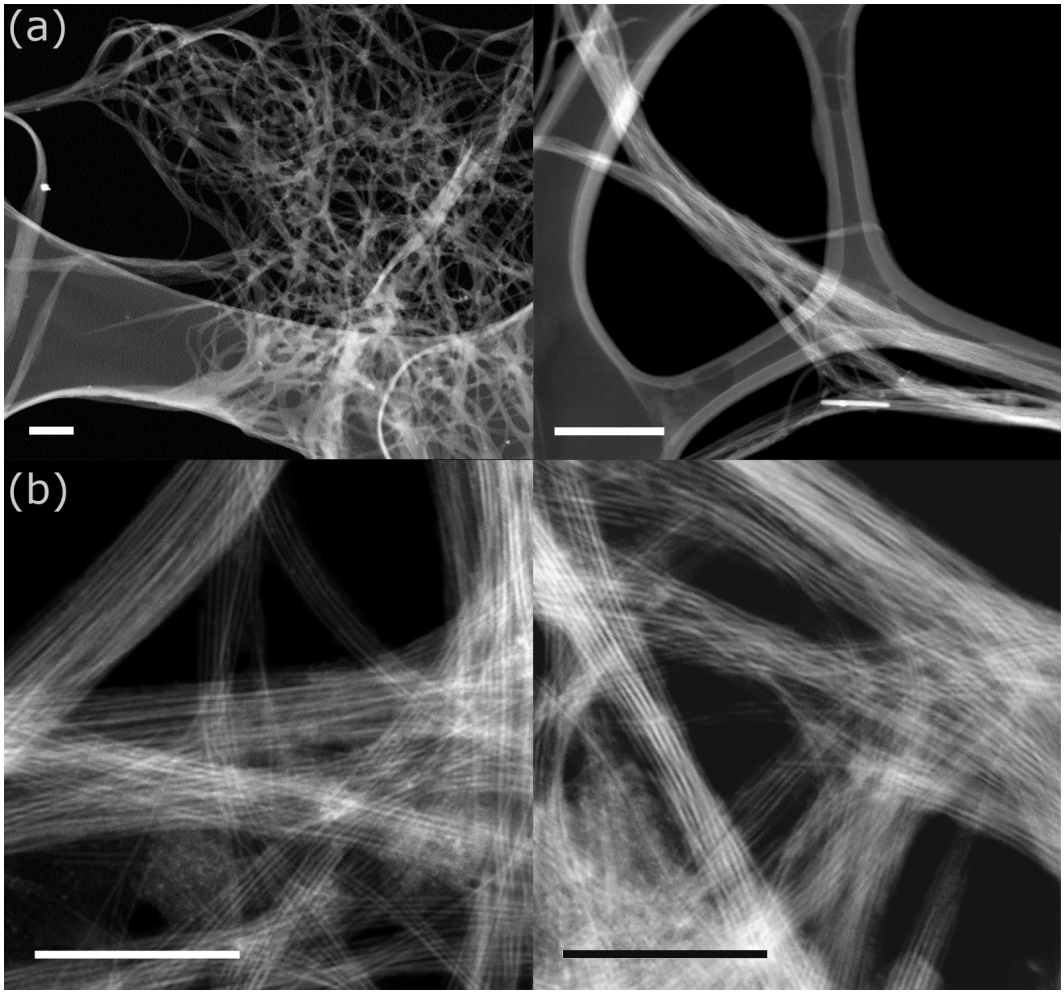


Figure 4.4: ADF-STEM imaging showing a high fraction filling of the SWCNTs with SnSe. Images were obtained using both a (a) STEM-capable SEM at 10 kV and (b) a high resolution ADF-STEM system at 80 kV. The images are also representative of the low population of external crystals observed across all of the high yields samples. Scale bars are (a) 200 nm and (b) 50 nm.

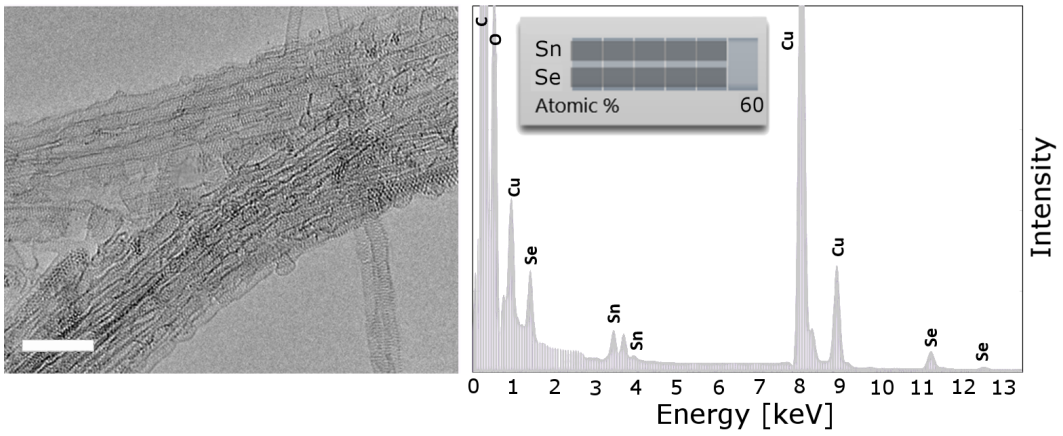


Figure 4.5: High resolution representative EDX analysis of a SnSe@SWCNT bundle. The EDX spectrum was acquired for the bundle of SnSe@SWCNTs shown in the HR-TEM image. Compositional analysis of the relative proportions present in the spectrum gives values concurrent with stoichiometric SnSe. The strong copper peaks originate from the TEM grid. Very trace silicon was also detected across the sample. Scale bar is 50 nm.

the SnSe encapsulated SWCNTs. This is consistent with studies conducted on the bulk material, as shown in the representative analysis depicted in Fig. 4.3.

### 4.2.2 Atomic Resolution Structural Analysis

The fabrication of SnSe-filled nanotube samples was carried out using VPT via the sublimation method (as described in Section 2.1). The van der Waals forces at the internal surfaces of the SWCNTs act to constrain the encapsulated material to confined cylindrical volumes with cross-sectional areas down to <1 $nm^2$ ($d_{SWCNT} < 1$ nm) [245]. This results in structures that can often vary wildly from that of the bulk form of the material (Fig. 4.6). The purified filled nanotubes were analysed using AC-(S)TEM at 80 kV. High resolution TEM images demonstrated that the sample contained nanotubes in the range of $0.7 - 1.7$ nm, with few outliers. The SnSe nanocrystal confined within the SWCNTs was clearly visualized in ADF-STEM images, which also resulted in the observation of the coexistence of different structures in a single bundle of SnSe@SWCNTs, as shown in the case of a 2x1 and novel tubular structure - never reported before for SnSe [124] - in Fig. 4.7. Low magnification ADF-STEM images (as shown in Fig. 4.4 in Section 4.2.1) revealed high filling fraction ($\sim 50 - 60$ %) of SWCNTs with SnSe, whilst also exhibiting a sparse - negligible - population of external SnSe deposits and structures following synthesis and deposition. The filling fraction was, in the first instance, rudimentar-

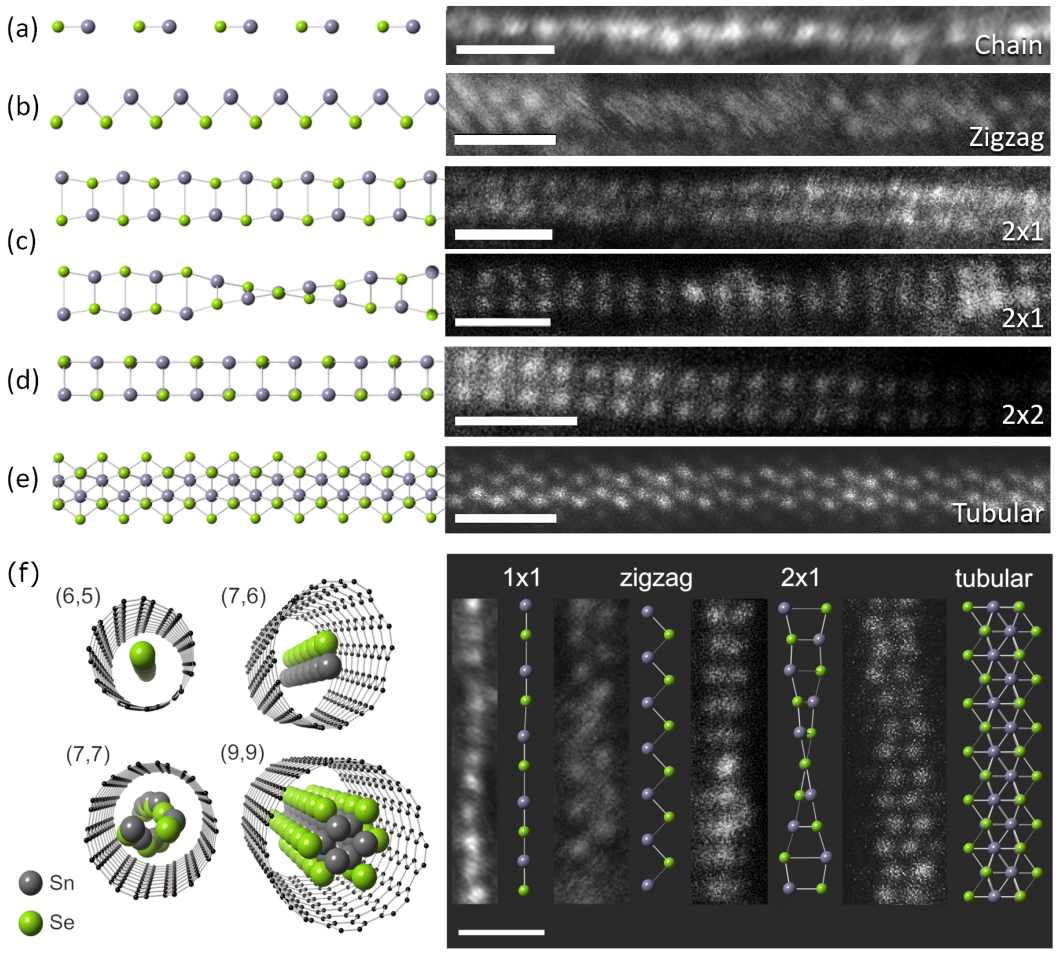


Figure 4.6: ADF-STEM images of all of the observed forms of encapsulated SnSe nanowires inside SWCNTs, alongside their structural models. The structures are ordered by the mean diameter in which they form. (a) Linear dipole chain. (b) Zig-zag. (c) 2x1. (d) 2x2 cubic. (e) New tubular structure. (f) Four of these observed structures are then shown inside SWCNTs with suitable chiralities. Scale bars are 1 nm.

ily estimated from the proportion of visually observed filling material (high contrast lines) to the size of the bundle (low contrast) in ADF-STEM images.

Although ADF imaging is a chemically sensitive technique, the composition of the encapsulated nanocrystal was also confirmed by EDX - as shown in Fig. 4.5 in Section 4.2.1. The EDX analysis of SnSe@SWCNTs bundles routinely gave a Sn:Se ratio of 1:1 (Sn to Se as 50 ± 1 at.% to 50 ± 1 at.%, respectively). Additional EDX investigations of other areas and SnSe@SWeNT specimens, as well as the VPT remnant material SnSe, gave congruent Sn:Se ratios for both wt.% and at %, which confirmed the pursued 1:1 stoichiometric SnSe ratio of the SnSe encapsulated SWCNTs.

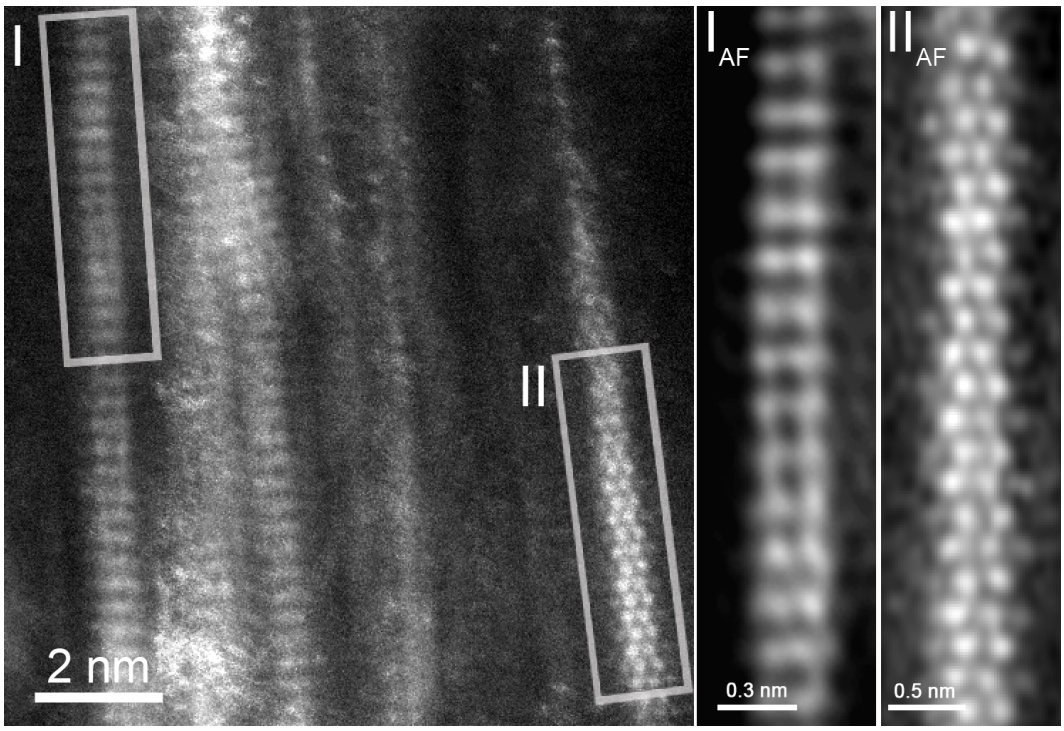


Figure 4.7: ADF-STEM image showing the co-existence of a 2x1 SnSe fragment (I) with a "tubular" (MoSe-like) SnSe nanostructure (II) in a bundle of SnSe@SWCNTs. The indicated details are subjected to adaptive filters in insets $I_{AF}$ and $II_{AF}$, respectively.

Five different structural forms of one-dimensional SnSe nanocrystals were observed over the nanotube diameter range studied ($0.7 - 1.7$ nm). The compiled catalogue of the observed structures of SnSe@SWCNTs, alongside the atomic models for each are shown in Fig. 4.6. All of the structures presented were obtained during the same encapsulation process, using identical fabrication conditions. Therefore, the presence of different SnSe structures is related to the medium and narrow distribution of SWCNT diameters. Each structure forms within a characteristic diameter range, so it is possible to order them by the mean diameter of the associated SWCNTs. Typical SWCNTs with confining diameters that can accommodate four of the different structures are modelled in Fig. 4.6, and are identified by their specfic chiralities, (n,m). The 2x2 cubic form is excluded as it has already been extensively modelled and reported in the literature [126]. The previously reported 2x2 cubic structure of encapsulated SnSe in narrow (d = 1.1 nm) SWCNTs was observed both by ADF-STEM and BF-STEM images (Fig. 4.8) [126]. The 2x2 structure (Fig. 4.6) is characterised by an interatomic distance a = 0.28 nm, as shown in the annotated ADF-STEM image in Fig. 4.8. The values for a and d were obtained by careful analysis of multiple calibrated ADF- and BF-STEM images, primarily via repeated line profile measurements. Furthermore, distance measurements, via line profile analysis, of images of the cubic (Fig. 4.8) and tubular (Fig. 4.9) structures show that the SWCNTs that accommodate the novel tubular structure are $(21 \pm 1)$ % larger than those in which 2x2 cubic SnSe forms.

Additional structures were also seen to have formed in the same SnSe@SWCNT samples, such that it was necessary to compile a catalogue of the full set of observed nano-confined forms as a function of confining diameter - from narrowest to widest. This catalogue is reported in Fig. 4.6 and incorporates the (a) linear atomic chain, (b) zig-zag, (c) 2x1, (d) 2x2, and (e) tubular SnSe forms, alongside their atomic models. An indication of the relative cross-sectional size of four of these structures inside specific chirality (n,m) SWCNTs with minimum appropriate confining diameters is also depicted in Fig. 4.6 (f). The 2x2 SnSe form has already been extensively reported in the literature, and so has been excluded from this final arrangement [126, 245]. It was common to observe the coexistence of different structures in a single bundle of SnSe@SWCNTs, as depicted in the ADF-STEM image in Fig. 4.7 for a 2x1 and novel tubular structure. There is also the obvious presence of further structures - which could possibly be additional 2x1 and tubular structures, as well as a zig-zag and a linear atomic chain - in this bundle (Fig. 4.7), however these cannot be clearly visualised in this image.

An approximation of the lowest possible diameter that can accommodate these struc-

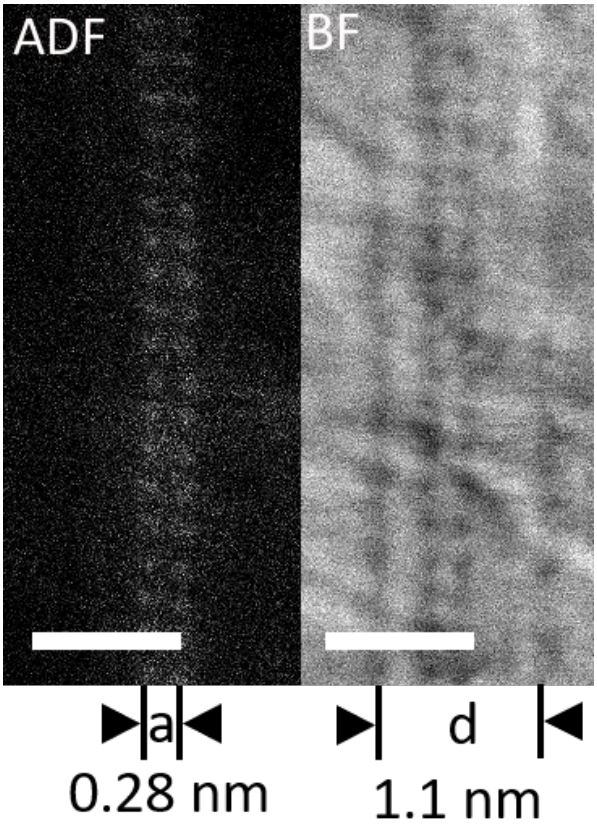


Figure 4.8: ADF and BF-STEM images of the 2x2 cubic form of nC-SnSe inside a SWCNT. The atomic spearation, a, and the measured diameter of the confining SWCNT, d, are indicated. Scale bars are 1 nm.

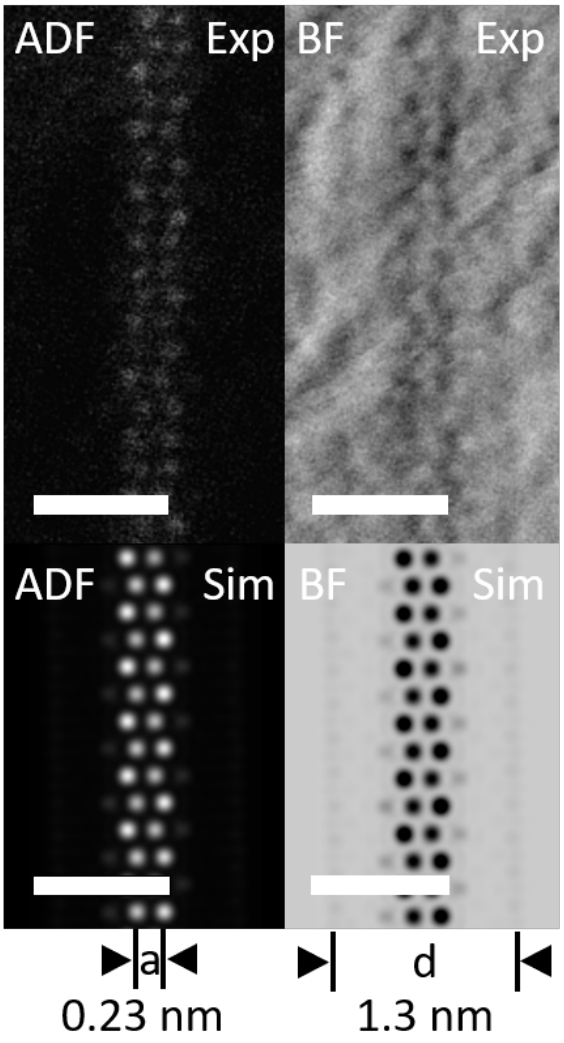


Figure 4.9: ADF and BF-STEM images of the newly observed "tubular" form of nC-SnSe, alongside the simulated counterparts. The simulated images were produced from a tubular SnSe fragment inside a (10,10) SWCNT. The indicated measurements are for the diameter of the confining SWCNT, d, and the atomic separation of the SnSe, a, which are concurrent for the experimental and simulated images. Scale bars are 1 nm.

tures (Fig. 4.6) could be crudely specified by the outside of the structure plus just slightly less than the diameter of another layer of atoms, Sn or Se. These diameter ranges can also be approximated based on more fundamental structural phenomena. An estimate of the lowest possible diameter can be given by calculating the outside diameter of the structure we have obtained according to experimental TEM images, taking into account the likely atomic radii, plus the van der Waals diameter of carbon (Chapter 1). Such a method exhibits why the 2x2 nC-SnSe structure is stable inside an (8,8) SWCNT, but not a (7,7) [126]. Similarly, an upper limit could be crudely approximated the outside of the nano-confined structure plus the diameter of another layer of (Sn or Se) atoms, less a reasonable margin. Thus giving a loose approximation for the diameter range in the absence of predictive modelling methods including Molecular Dynamics (MD) [261], Density Functional Theory (DFT) [114, 115] and *Ab Initio* Random Structure Searching (AIRSS) [60, 117, 119]. If the formation energy is positive, then the structure will not form, but a negative formation energy would indicate a likelihood of existence. The spontaneous shrinking and twisting of SWCNTs occurs even when they are unfilled, as introduced in Chapter 1. Therefore, it is unsurprising that the structures that form can also cause deformations to the SWCNTs from cylindrical, such as in the case of a 2x1 nano-confined structure. This deformation can be seen in Fig. 4.6, where the zig-zag nanowire cause a stretching of the confining (7,6) SWCNT. A similar phenomenon can also be observed in the case of the encapsulated 2x1 SnSe form. However, it is also common for this structure to twist, which can result in the confining SWCNT to appear to undergo no discernible deformation, as depicted in Fig. 4.6 for the (7,7) SWCNT. An arrangement of 3x2 SnSe would be expected to be unstable when encapsulated due to significant deformation of the NT, and a 3x3 (rocksalt) structure is larger than the "tubular" structure.

When the diameter of the encapsulating SWCNT is $\sim (1.3 - 1.4)$ nm, the SnSe filling self-assembles into an unprecedented new crystalline form (Fig. 4.6 (e) and 4.9), which has not been reported by any other group, to our knowledge, for SnSe [124]. As mentioned above, ADF-STEM allowed the atomic positions of the nC-SnSe to be clearly visualised (Fig. 4.9 ADF), and the contrasting atom intensities analysed (Fig. 4.10). In contrast, BF-STEM imaging allowed for the carbon walls to be resolved (Fig. 4.9 BF). Further observations of the appearance of this novel tubular form of nC-SnSe - as shown in Fig. 4.11 - demonstrate that it is a stable and consistently occurring structure in our SnSe@SWCNT samples. Thus, based upon the analysis and measurements of experimental (S)TEM images, an armchair (10,10) SWCNT was considered to be one of the appropriate conformations for ini-

tial modelling and image simulation of the new structure (Fig. 4.11 (b) and 4.12 (a)). This conformation lies firmly within the observed diameter range and the confining walls of the SWCNT present as continuous lines in experimental TEM images, as opposed to distinct points, which give an indication of the chirality of the SWCNT. Such a SWCNT would be metallic. However, the observed diameter range for this structure spans a combination of metallic and semiconducting SWCNTs, with the majority being the latter, affording more options to study properties such as changes in conductivity in embedded phase change materials [183] or enhanced thermoelectric characteristics as a result of nanostructuring [112] when these are to be considered.

Although this novel "tubular" crystalline form has not been reported previously for SnSe [124], it should be noted that the structure is isostructural with observed in monochalcogenide nanowires (MoS, MoSe, and WSe) suspended *in-vacuo* [262, 263]. The detailed intensity profile obtained from the ADF-STEM simulated image - corresponding to the 60 ° rotation model (Fig. 4.12) - can be clearly correlated with that of the experimental ADF-STEM image, as shown in Fig. 4.10 (a-c). The direct comparison between the line profiles and measured interatomic distances (Fig. 4.10 (c)) for correlative slices through simulated (Fig. 4.10 (a)) and experimental (Fig. 4.10 (b)) ADF-STEM images of the novel tubular structure, show a high level of agreement between the obtained values. Thus, this provides us with a quantification of the fit of the proposed model for the novel tubular structure (Fig. 4.10 (d), 4.11 (b-c), and 4.12) with the experimental data (Fig. 4.9 and 4.11 (a)). In addition, the geometrical analysis of bonding in the new structure (Fig. 4.10 (d) and 4.11 (c)) shows the Sn-Se bond distances to be similar to that observed in bulk (0.272 nm), which is in agreement with previous research on encapsulated SnSe [126].

We further explored the new SnSe crystalline form by analysing the interaction of this structure under beam irradiation. Whilst SWCNTs are only selectively sensitive to electron beam irradiation [141], the nC-SnSe has been observed to exhibit a variety of behaviours. The most basic of which are for the structure to vibrate and move inside the SWCNTs. This is more pronounced under prolonged exposure to the electron beam. Such motion can include rotations and translations. Therefore, despite the consistently recurring observation of the tubular structure along the view direction depicted in the STEM images in Fig. 4.9, 4.10 and 4.11, we must also assess the appearance of this structure when it rotates inside the SWCNT. This is depicted in Fig. 4.12, which shows the built model for the novel tubular nC-SnSe structure - inside a (10,10) SWCNT - at rotational intervals of 15 °, from 0 ° to 90 ° - where 0 ° has been selected arbitrarily. These were used to simulate TEM

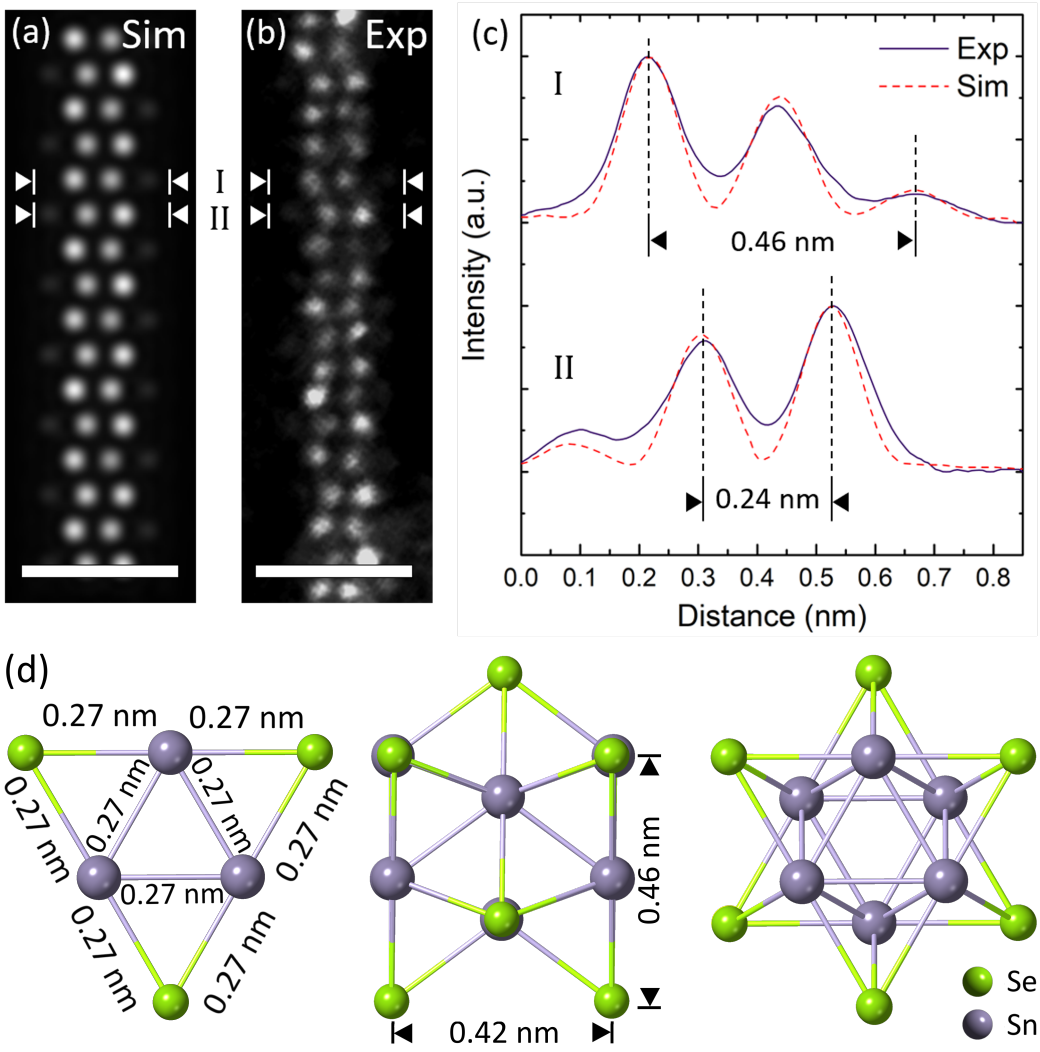


Figure 4.10: Direct comparison of the (a) simulated and (b) experimental ADF-STEM images of tubular nC-SnSe via the corresponding (c) line profile intensities. The experimental line profile intensities are averages across the sum of the equivalent layers. Scale bars are 1 nm.

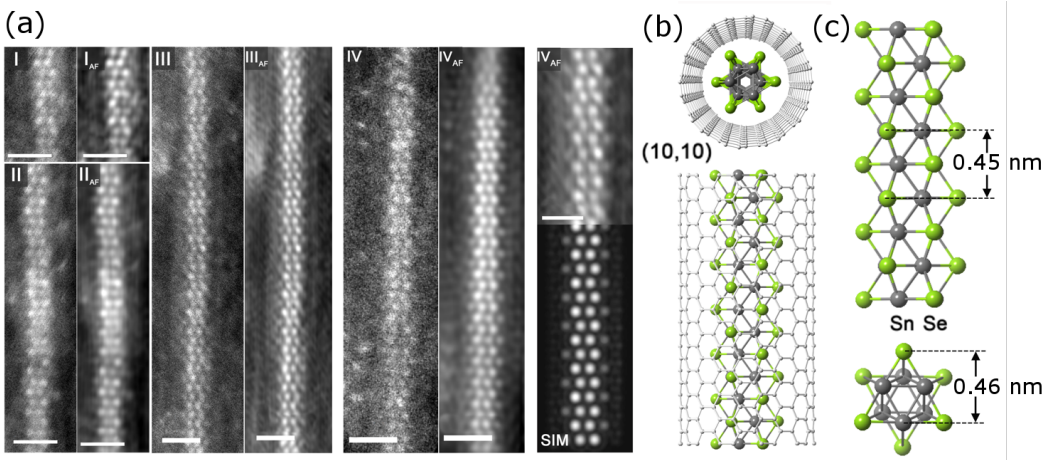


Figure 4.11: Experimental ADF-STEM images of further observations of the novel form of nC-SnSe, alongside the modelled structure. (a) ADF-STEM images of the new form of nC-SnSe, alongside the simulated counterpart (SIM). The simulated image was produced from (b) the model for a corresponding SnSe fragment inside a (10,10) SWCNT. (c) A measurement of the interatomic distances for a model of the fragment. These values correlate well with those measured from the experimental imaging. Scale bars are 1 nm.

and STEM images, as shown in Fig. 4.12 (b-c). The obtained images provided an indication as to why the view at 0 ° and 60 ° is most commonly observed for this structure; the other rotations have considerably lower contrast and less distinct atomic points in both the TEM and STEM imaging. Therefore, it would be significantly more difficult to resolve these structural views in experimental images and recognise them as belonging to the tubular structure, without having seen it at 0 ° or 60 °.

An experimental example of a rotation that the nC-SnSe undergoes is depicted in Fig. 4.13. Whilst this creates challenges in imaging (Fig. 4.12), it offers the valuable opportunity to be able to study the structure from multiple perspectives experimentally, as also reported for the 1:1 MX (M=Mo,W; X=S,Se) monochalcogenide free-standing nanowires [263]. We also note that a new addition to the monochalcogenide family was just reported by Nagata et al., the transition metal telluride MoTe, which is also encapsulated in SWCNTs [264]. Fig. 4.13 corresponds to a ball and stick model of a fragment of the novel SnSe crystalline structure in a tubular SWCNT. Three different views of this structure, corresponding to 30 °, 60 ° and 75 ° rotations around the SWCNT long axis, with respect to a single arbitrary starting view (established in Fig. 4.12), have been modelled (Fig. 4.13 (c)). The expanded rotation set over the range $0\,° - 90\,°$ is presented in Fig. 4.12, which reveals the threefold symmetry of this model, consistent with that reported for 1:1

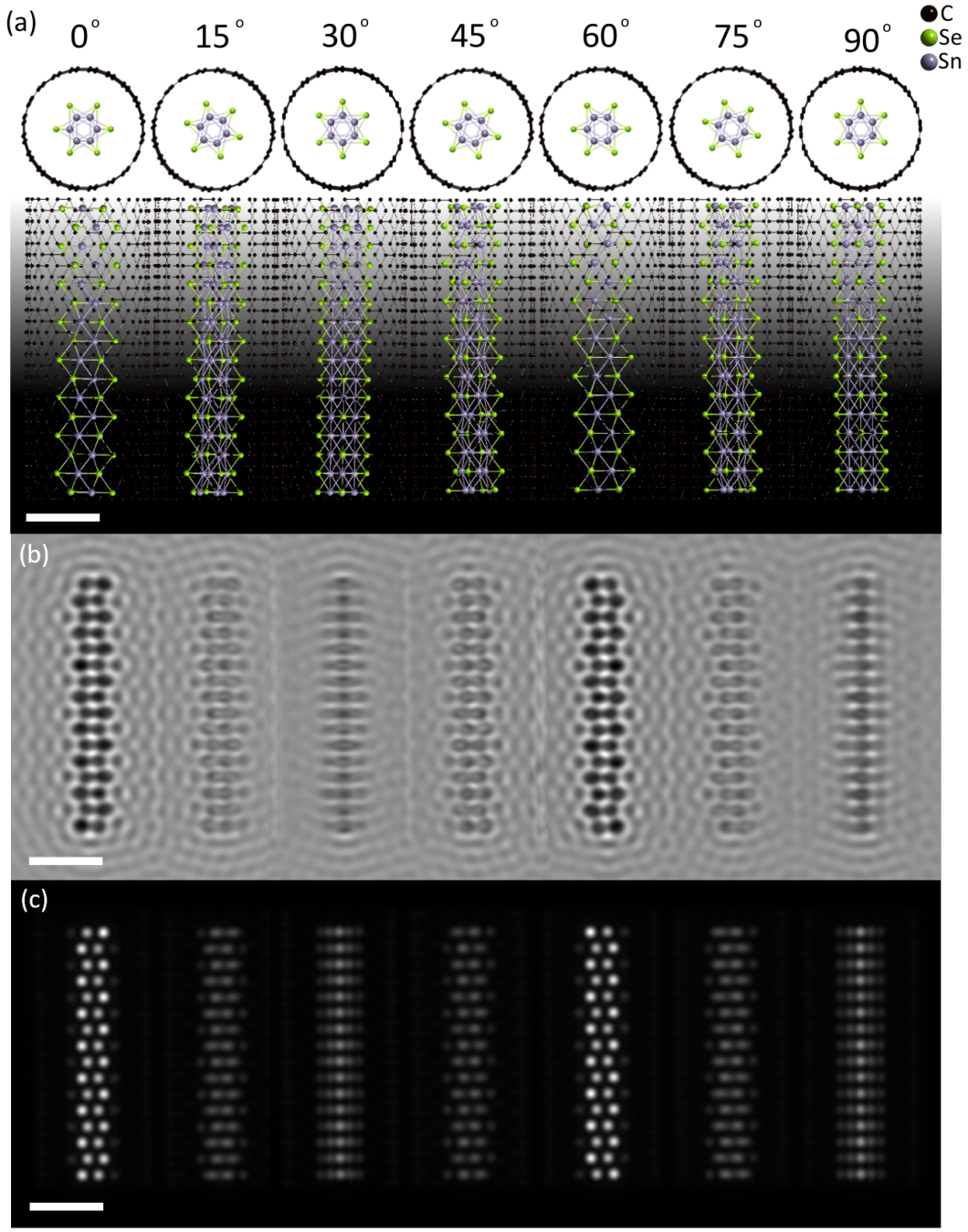


Figure 4.12: The proposed model for the novel tubular nC-SnSe structure inside a (10,10) SWCNT (a) is shown at the rotational intervals of 15 °, from 0 ° to 90 °. These produce observable views of the structure in (S)TEM images. The TEM (b) and ADF-STEM (c) simulations corresponding to the model at these rotations. Scale bars are 1 nm.

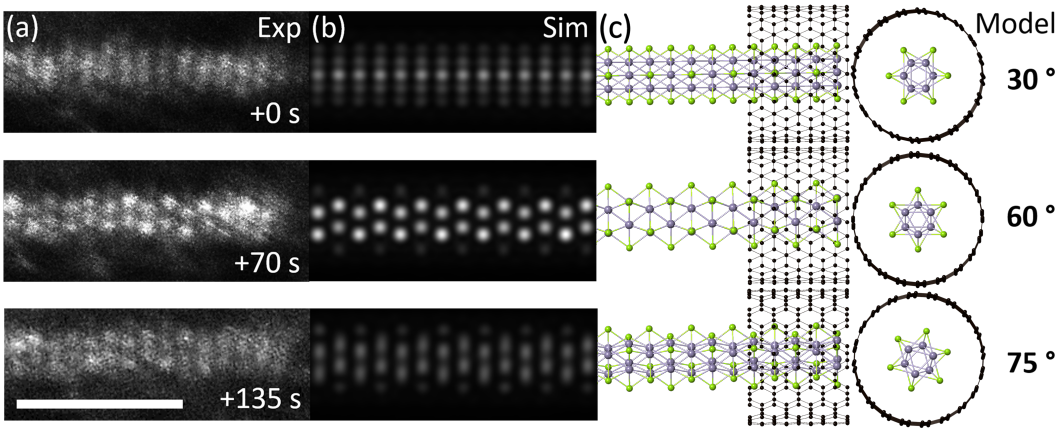


Figure 4.13: Modelling the time-resolved rotation of the new tubular nC-SnSe structure. (a) ADF-STEM images of the tubular structure, taken at the indicated time intervals. These are shown alongside the (b) simulated ADF-STEM images of the corresponding projections of the (c) proposed model. Scale bar is 2 nm.

MX (M=Mo,W; X=S,Se) [265].

The observation that this structure can rotate inside the SWCNT enabled us to view different projections of the structure, which were captured by ADF-STEM images. These *in situ* time sequence experiments - ADF images recorded at different times (Fig. 4.13) - exposed the deformation of the SnSe-filled SWCNTs under the electron beam. The electron irradiation originates the rotation of the crystalline structure inside the SWCNT without destroying it. Three different frames are presented in Fig. 4.13, corresponding to t = 0 s, 70 s and 135 s. These images correspond to the lattice projection of the novel SnSe crystal. Multislice ADF image simulations - built using clTEM [132] - of the model at 30 °, 60 ° and 75 ° (relative to the rotations depicted in Fig. 4.12) are shown next to the experimental images in Fig. 4.13. The comparison between experimental and simulated images confirmed that these confined structures undergo a crystal rotation inside the SWCNT, under sufficient exposure to the electron beam. These results not only demonstrate the good match between the model and experimental results in different projections, but also the comparative stability of this SnSe atomic structure under the electron beam. This is a clear indication of the good mechanical properties of the SnSe comparable to the findings observed in monochalcogenide MX, which can exhibit both torsional and bending behaviour, according to local beam irradiation conditions [263, 265, 266]. However, under prolonged and harsh (high beam current density) electron beam irradiation, the encapsulated SnSe nanowire inside an individualised SnSe@SWCNT - suspended across two bundles - was observed to dissociate into clusters (Fig. 2.15 from Section 2.2.5). Whilst analysis of a bundle of SnSe@SWCNTs provides a more

stable environment for HR-(S)TEM imaging of the structures than an individualised filled SWCNT it was still important that beam intensity and sample exposure were monitored carefully (beam current densities of $\sim 2.0$ pAcm$^{-2}$ for STEM studies) to ensure that accurate structural information was obtained. As mentioned above, this dissociation behaviour is more likely in single, suspended SnSe@SWCNTs as they are more exposed to the electron beam radiation. Bundles of SWCNTs increase the stability of individual constituent SWCNTs due to increased support and energy dissipation across the bundle. Furthermore, each structure reacts differently to exposure to the electron beam. The narrower SnSe structural forms are less stable than others and vibrate more when exposed to the electron beam as evident in the single chain, zig-zag chain and 2 x 1 structures presented in Fig. 4.6(a)-(c) - see also Fig. 2.15 and 4.7. The previously reported 2 x 2 form (Fig. 4.6(d) and 4.8) and the new form (Fig. 4.6(e), 4.13, 4.10, 4.11 and 4.7) are both more robust in the electron beam, but do eventually degrade under either continued electron beam exposure or heightened electron beam dose (beam current density).

The discovery of this new form of confined SnSe offers another dimension in the investigation of this compound as a nC-PCM, in contrast to other types of crystalline fillings. These results also form the basis for studies into further nC-PCMs and, in particular, investigations into the variation of the structure of the encapsulated material as a function of the diameter of the NT, and the effect that this has on *in situ* phase changes. These experiments can then be extended to an analysis of further properties of nC-PCMs, such as conductivity. From previous studies [60, 119], enhanced thermoelectric properties would be anticipated, which is the subject of ongoing investigations in this laboratory, and will be discussed further in Section 6. Indeed, mesoscale SnSe nanotubes (180-400 nm in cross-section) have been formed inside alumina templates [122]. Theoretical studies by Lin and coworkers [123] predict that forming smaller "star-like" SnSe nanotubes at a slightly larger scale than our nanostructures (i.e. with an outer diameter of $\sim$2 nm) considerably enhances their thermoelectric performance. Given that SWCNTs that accommodate the novel SnSe structure span a range of diameters - and therefore chiralities and conformations - it is possible to filter out the confining SWCNTs that are metallic, and to still be left with a substantial volume of semiconducting SWCNTs encapsulating tubular SnSe. Therefore, the margins for investigation into, and application of, the thermo-conductive properties of these samples are large.

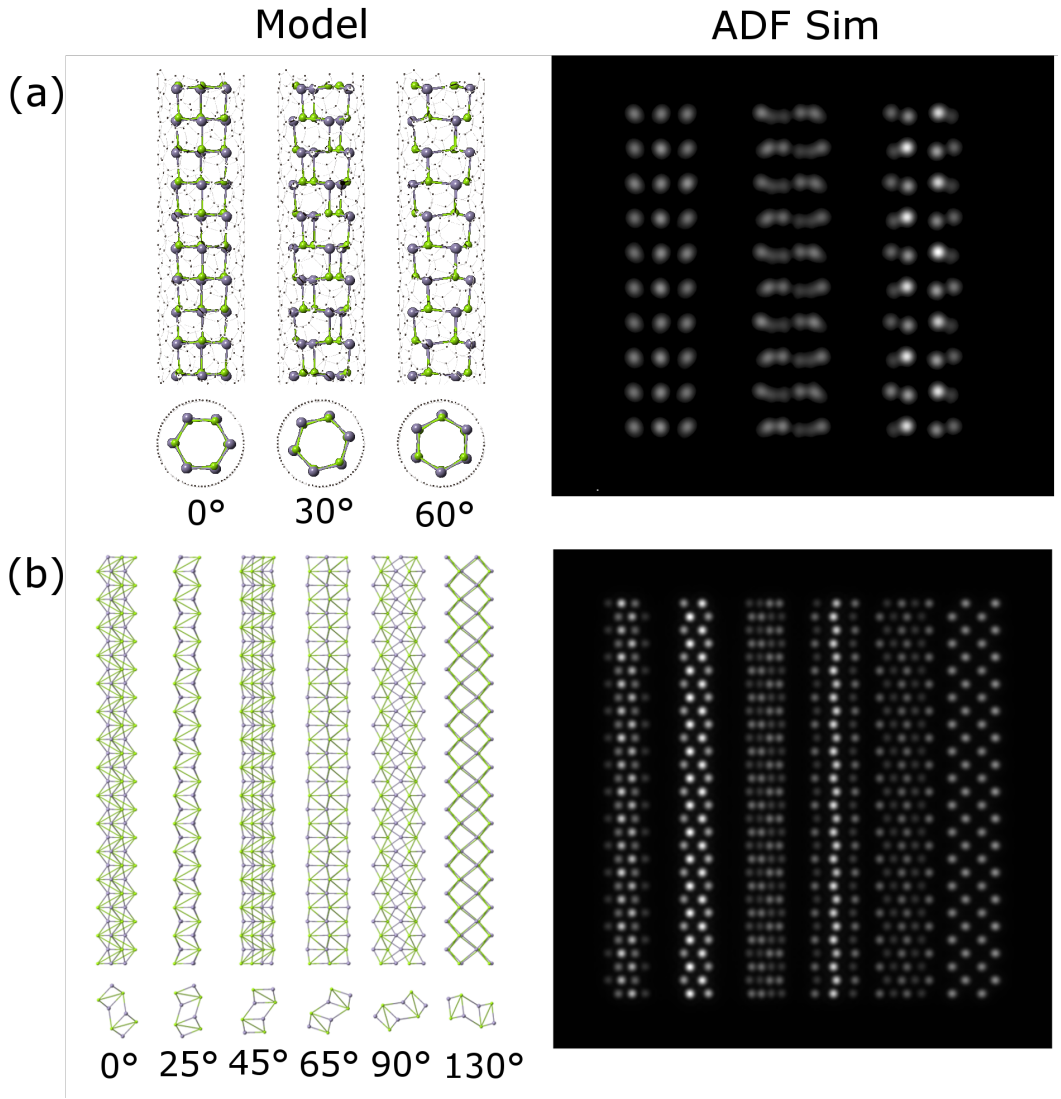


Figure 4.14: Two models for possible stoichiometric nC-SnSe structures, that have not been experimentally observed. (a) A theoretical model built via AIRSS, and using energy minimisation, by P. Medeiros. (b) A model proposed by A. Vasylenko constructed using DFT. [60, 119]

### 4.2.3 Nanoscale Structure Analysis & Image Simulation

Further to the composition of the catalogue of observed structures outlined above, additional structural modelling was carried out in order to try and accurately experimentally and theoretically match the nano-confined forms observed. Since it is a reiterative process involving interatomic distance measurement from HR-TEM images; intensity analysis of ADF-STEM images; building of the models; and simulating the (S)TEM images, there are often many more models developed than structures seen. In the case of the MoS-like structure reported in this research, there were many models that were built before the identified one. These included both theoretical - based on energy minimisation - and experimental structures. An example of a structure identified via AIRSS modelling is shown in Fig. 4.14 (a). It was energetically favourable for the observed diameter range, but did not match the ADF-STEM images when simulated. There was another model built using DFT by A. Vasylenko - shown in Fig. 4.14 (b) - that appeared to line up well with the experimental images. However, although the interatomic distances matched well for some of the projections, the intensities did not. Additionally, some of the simulated ADF-STEM projections for the model structure did not equate to anything seen in the experimental ADF-STEM images, and the overall structure size was deemed too large for the observed diameter range.

## 4.3 SAED

Further to visual inspection of the bulk and SnSe@SWCNT samples at low resolution (Section 4.2.1) and at the low dimensional scale (Section 4.2.2), studying the electron diffraction characteristics provides us with significant additional information about the structural compostion of the samples. Investigations into the room temperature electron diffraction characteristics of the nanocomposites were conducted on samples that had been dispersed onto lacey carbon TEM grids (as outlined in Sections 2.1.5 and 2.2.4). SAED was conducted at 80 kV, and beam current densities (doses) were carefully monitored throughout.

The obtained experimental SADPs (Fig. 4.15 (a-I)) of bundles of SnSe@SWCNT (Fig. 4.15 (a-II)) show clear additional reflections that cannot be attributed to the SWCNTs. These have been indexed with their most likely sources in Fig. 4.15 (a-I), according to measured distances and a comparison with lattice spacings and reflections seen in simulated SADPs (Fig. 4.15 (b-I)) for the model of bulk Pnma SnSe (Fig. 4.15 (b-II)), when viewed in the [010] direction. The diffraction rings of SWCNTs have also been indicated in Fig. 4.15 (a-I) and 4.16, as outlined in Section

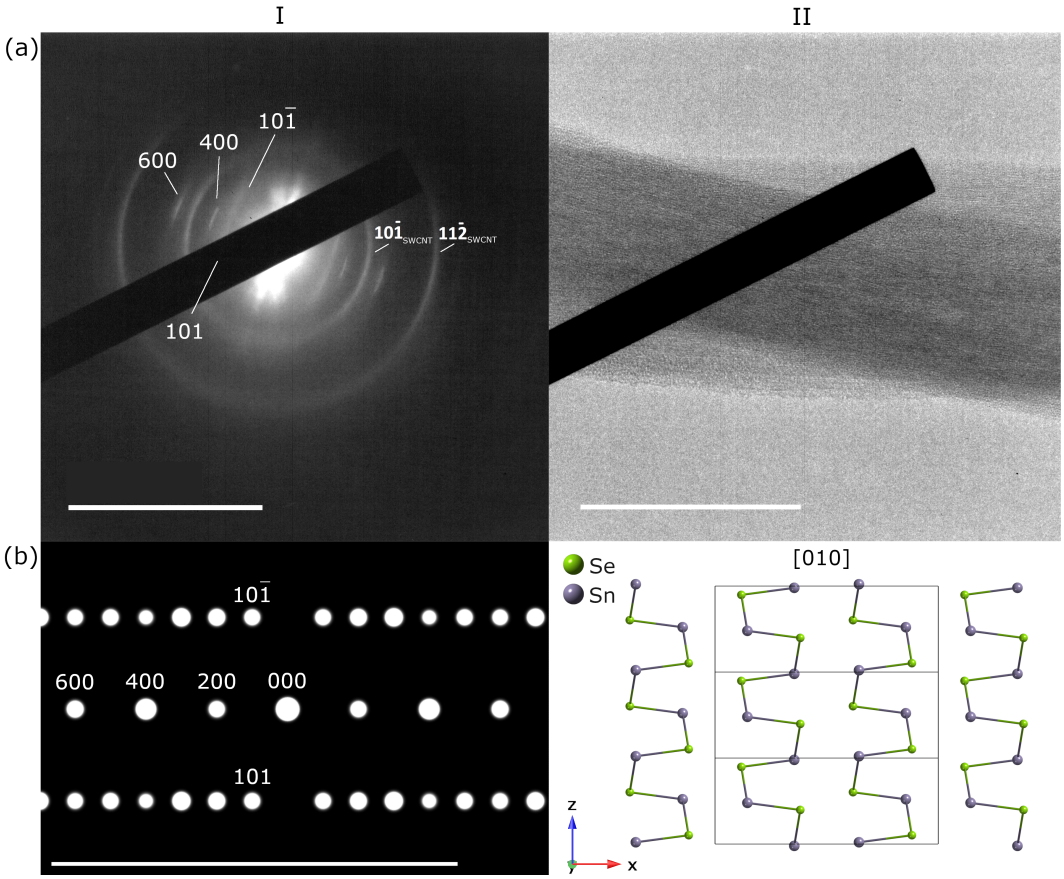


Figure 4.15: (a) Experimental SADP (I) and TEM image (II) of crystalline SnSe@SWCNTs, indexed with SWCNT reflections, and the most likely contributions from the nano-confined SnSe, according to measured distances. (b) Simulated SADP (I) from a model (II) of bulk Pnma SnSe, viewed in the [010] direction. The {200} reflection cannot be discerned in the experimental SADP. Scale bars are 1 $Å^{-1}$ for the SADPs and 50 nm for the TEM image.

2.2.4. These features are consistently present in SADPs of SnSe@SWCNT bundles, indicating that the embedded microstructures are similar and have a common crystalline origin. The result is comparable to the data obtained for nano-confined $Sb_2Te_3$ in Section 3.3.

Furthermore, the nano-confined SnSe has been observed to amorphise under beam irradiation. This amorphisation has been tracked and evidenced by SADPs taken at 80 kV - as shown in Fig. 4.16 (a) - and was observed to occur after ∼240 s of continuous beam irradiation at a current density of 127 $pA{\cdot}cm^{-2}$. If the beam current density is increased to the order of ∼300 $pA{\cdot}cm^{-2}$, then amorphisation occurs in less than 30 s. Beyond this timescale, the encapsulated structures rapidly begin to breakdown and dissociate.

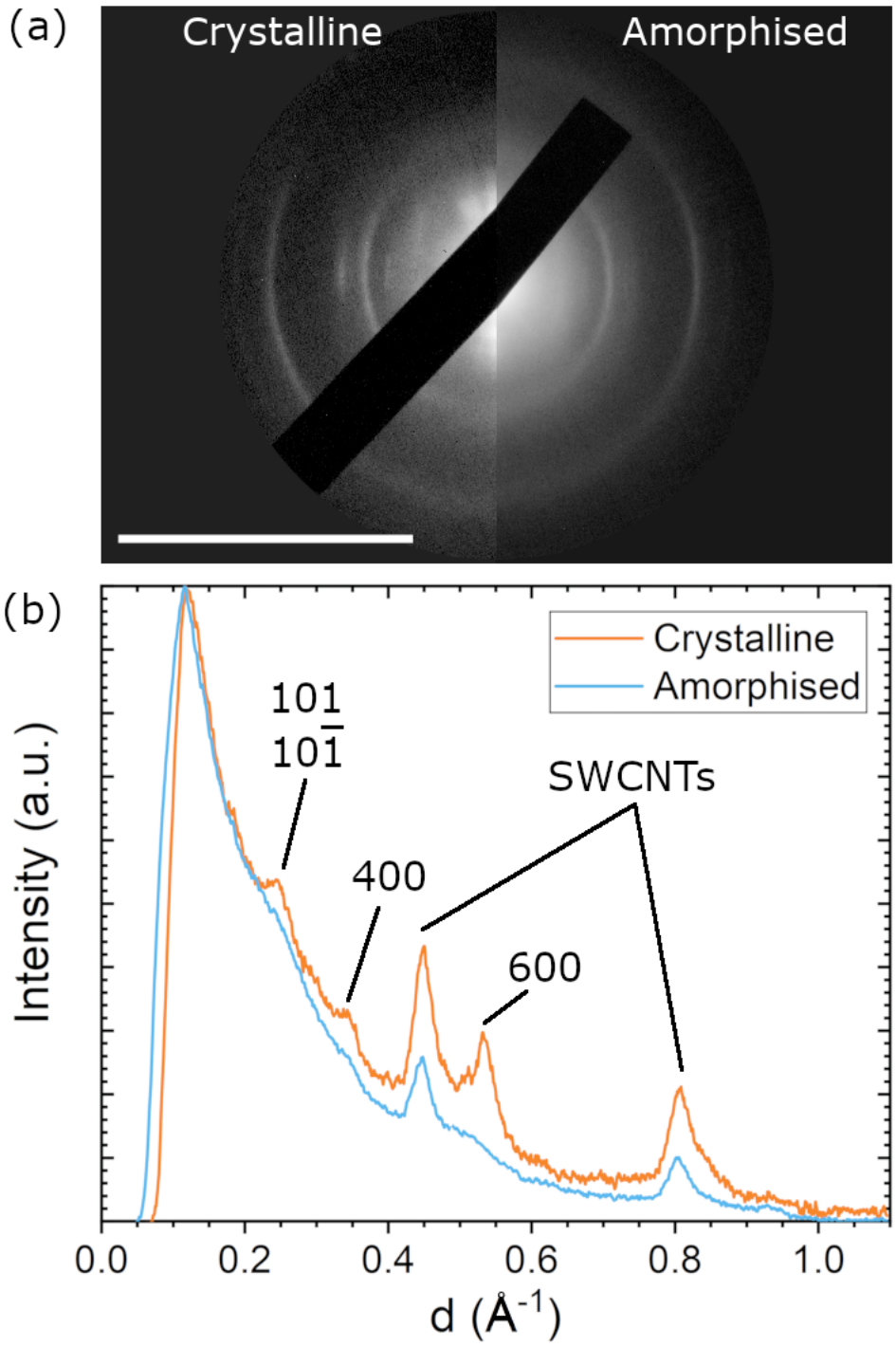


Figure 4.16: (a) Amorphisation of the encapsulated SnSe in the SnSe@SWCNT samples is evidenced by the previously distinct reflections of the SADP blurring into indistinct rings, or fading into the background of the pattern. This can be observed in the blurring, and significant reduction in intensity, of all reflections attributed to the nano-confined SnSe. SADPs obtained at 80 kV. (b) Analysis of the amorphisation of nC-SnSe via radial intensity profiles of SADPs of the crystalline and amorphous phases. Peaks have been indexed as in Fig. 4.15.

A comparison of the radial profiles of the SADPs for crystalline and amorphised nC-SnSe is given in Fig. 4.16 (b), which were obtained using DiffTools plugin for Digital Micrograph (Section 2.2.4). The data was then exported and analysed in OriginPro2019. Amorphisation of the encapsulated SnSe in the SnSe@SWCNT samples is evidenced by the previously distinct reflections in the SADP blurring into indistinct rings, or fading into the background of the pattern. This can be observed in the blurring of all reflections attributed to the nano-confined SnSe in Fig. 4.16 (a) "Amorphised", and the significant reduction in intensity of the corresponding peaks in the amorphised radial profile in Fig. 4.16 (b). This amorphisation has not been observed to be reversible; to date, there has not been any success with inducing the recrystallisation of the nano-confined material.

## 4.4 DSC/TGA

As introduced in Section 4.2.1, the as-supplied bulk SnSe is orthorhombic and belongs to the Pnma space group. As such, it has underlying distorted NaCl structure, which is expected to strongly present in the bulk crystals. SnSe was chosen as a candidate for encapsulation in part due to its fundamentally interesting phase change behaviour. Research into this behaviour and Antoine equations (Section 2.1) of SnSe prior to filling placed it as a good candidate for vapour phase transport, since it melts, and sublimes, congruently from a stoichiometric source material, up to a specific pressure and temperature. Whilst this is theroretically accepted, it is important to verify the quality of the grown nanocomposites. This is especially significant given that the temperature used for growth is >150°C lower than the atmospheric melt temperature of SnSe (Table 4.1). Whilst extensive research into the Antoine equations, amongst others, for SnSe placed this as a suitable temperature for the vacuum pressure used for growth, there are other stoichiometries and phases that have formation temperatures lower than, or closer to, this value, as shown in Table 4.1.

Therefore, whilst EDX and compositional analysis can provide us with a good indication of whether the material is stoichiometric SnSe, it cannot tell us much about the phase properties. By conducting combined DSC and TGA studies on numerous forms of the material, it allowed us to identify characteristic thermal properties of each. More specifically, the data was used to establish key differences in the nC-SnSe, when compared to the bulk, and to expected transitional temperature values (Table 4.1). The results of these measurements were particularly helpful in deter-

mining the point at which the nC-$Sb_2Te_3$ melts, without losing significant mass from the sample. The data provided by the thermal measurements proved valuable for the *ex situ* exfoliation of SnSe@SWCNT bundles. The DSC data in Fig. 4.17 (I) is given in $Wg^{-1}$ to better show heating and cooling curves.

Combined DSC/TGA measurements were conducted under an inert N environment, at 1 atm. As outlined in Table 4.1, the melting temperature of bulk Pnma SnSe is 861°C. Therefore, thermal investigations were carried out up to 900°C, in order to accommodate the full extent of the anticipated transition. Furthermore, as with the structural analysis reported in Section 4.2.1, initial measurements were conducted on bulk SnSe. More specifically, the as-supplied SnSe source powder from Sigma Aldrich (Fig. 4.17 (a)), and bulk remnant samples from two different growth procedures (Fig. 4.17 (b-c)). The full TGA (mass loss) and DSC (heat flow) results for these three samples are given in (Fig. 4.17 (I)), where the arrows indicate the heating and cooling curves. The mass loss experienced by all three samples was ∼8 mg, with starting mass appearing to have little impact upon the rate of, or total, mass loss. Similarly, analysis of the peaks in the heat flow shows them to all appear within the same range. Fig. 4.17 (I) also shows there to be an incongruency in each mass loss curve at the temperature that coincides with these peaks in heat flow. This incongruency is consistent across the three samples. Images of the samples prior to and post-analysis (Fig. 4.17 (II)) show that all three underwent melting, and reformed as a large, polycrystalline mass which was fused to the edge of the DSC pan.

Further investigations into the thermal properties of the bulk SnSe, when repeatededly cycled through 900°C and back to room temperature, revealed consistent behaviour, as shown in Fig. 4.18. The indicative transitional peaks in the DSC data continue to appear within the anticipated ranges in Fig. 4.18, on both the

| Chemical | Melting Temperature (°C) | Boiling Temperature (°C) |
|---|---|---|
| SnSe | 861 | - |
| $SeO_3$ | 118 | - |
| Se | 221 | 685 |
| Sn | 232 | 2602 |
| $SeO_3$ | 340 | 350 |
| $SnSe_2$ | 650 | - |
| SnO | 1080 | 1425 |
| $SnO_2$ | 1630 | - |

Table 4.1: Basic transitional temperatures for SnSe and its constituent elements and oxidation products, ranked by melting temeprature at atmospheric pressure [182].

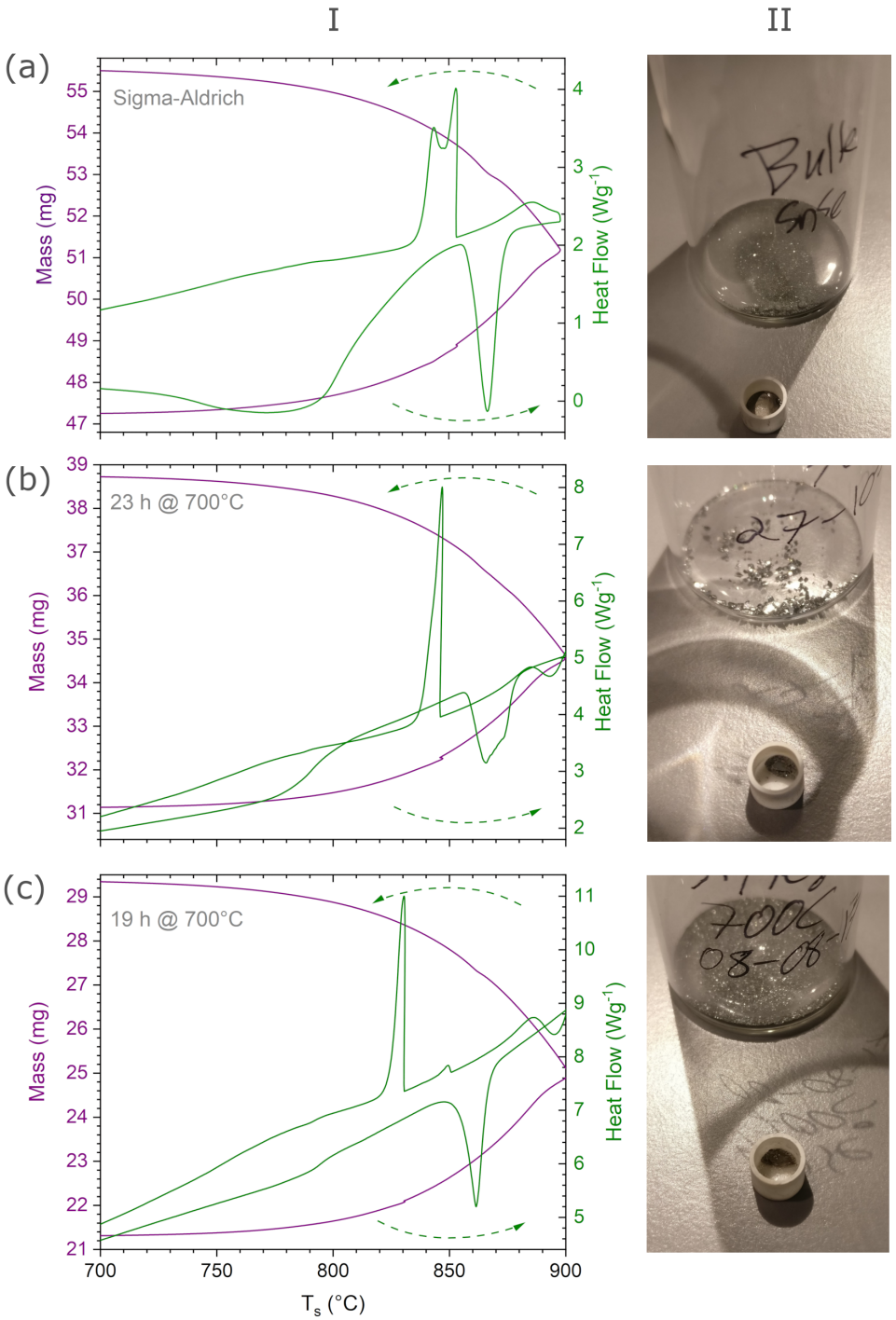


Figure 4.17: Combined DSC/TGA data tracking the heat flow and mass loss characteristics of three forms of bulk SnSe, up to 900°C. The notation 23 h @ 700°C indicates a sample that was grown at 700° with a dwell time of 23 h. The heating and cooling heat flow curves are indicated by the green arrows. The images show the comparative differences in visual appearance between the pre- and post-analysis material.

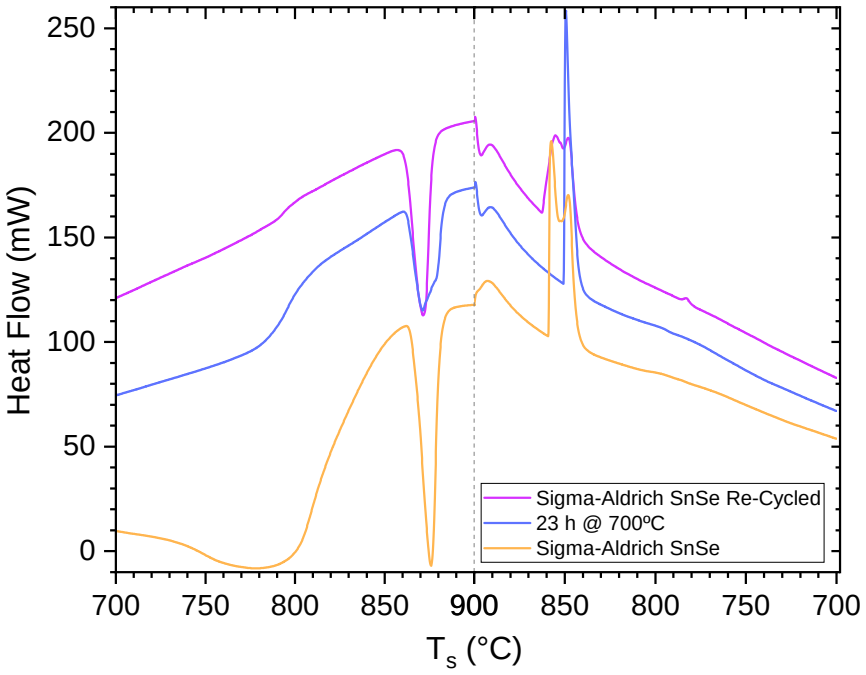


Figure 4.18: Comparison of the heat flow characteristics for different forms of SnSe, when cycled once through 900°C. The notation 23 h @ 700°C indicates a sample that was grown at 700° with a dwell time of 23 h. The peaks in heat flow coincide at the same temperature (±5°C) for the three samples. This shows the resilience of the bulk SnSe to temperature treatment, up to 900°C. The dashed line indicates the transition between the heating and cooling curves.

heating and cooling curves, and line up well with the bulk remnant samples analysed in Fig. 4.17 (b-c) - "23 h @700°C" is given for direct comparison with the source "Sigma Aldrich SnSe" in Fig. 4.18. These results are persistent across all bulk samples and forms. The onset and peak temperatures for the melt transitions for the reported samples are given in Table 4.2. The assessment of the consistency of this behaviour provides a solid grounding for the investigation into nC-SnSe.
The encapsulated sample used for the combined DSC/TGA measurements had been extensively analysed using high resolution (S)TEM and EDX prior to these thermal investigations. Therefore, it was confirmed to have a high filling fraction (as outlined in Section 4.2.1) of stoichiometric SnSe, with no observed external crystalline material. Similarly, the SWCNTs exhibit no transitional properties with temperature, which is extensively documented in Sections 2.5 and 3.4. Therefore, any phase and thermal characteristics exhibited by the SnSe@SWCNT sample are solely from the

| SnSe Sample | Onset Temperature (°C) | Peak Temperature (°C) |
|---|---|---|
| Sigma-Aldrich | 858.7 | 866.5 |
| 23 h @ 700°C | 858.1 | 865.8 |
| 19 h @ 700°C | 854.2 | 861.5 |
| Re-cycled Sigma-Aldrich | 858.4 | 866.8 |

Table 4.2: Onset and peak temperatures for the melt transitions of different forms of SnSe. Values are quoted from direct analysis of the heat flow data plots, using the peak fitting function in the DSC/TGA STARe software.

nC-SnSe.

The mass loss and heat flow characteristics for nC-SnSe, when cycled through 900°C, are given in Fig. 4.19 (a). Arrows have been used to indicated the heat flow heating and cooling curves. The heat flow characteristics are significantly different to that observed in the bulk, as can be seen from the direct comparison given in Fig. 4.19 (b). The melt transition at 860°C, that is present in bulk SnSe - both for bulk remnant material and the source SnSe powder from Sigma Aldrich - is absent for the nC-SnSe. Indeed, there is no clear peak in heat flow which can be attributed to the nC-SnSe having undergone a melt transistion, at the expected temperature or otherwise. However, Fig. 4.19 (a) demonstrates that there is an onset of mass loss from $\sim$ 500°C in the SnSe@SWCNT sample, the rate of which becomes near exponential from $\sim$ 700°C. This indicates that the nC-SnSe is escaping from the sample. This occurs promptly and - as indicated by the plateau that begins to appear at $\sim$ 820°C on the heating curve, and then persists throughout the cooling curve - results in the rapid loss of encapsulated material. Indeed, the lack of continuing mass loss in the higher temperature range on the cooling curve would suggest that the SWCNTs are the only remaining mass in the sample at this point. This was confirmed in (S)TEM imaging of the post-DSC/TGA sample, where the SWCNTs were observed to be devoid of filling material.

Therefore, it would appear that the nC-SnSe does not undergo a melt transition, but rather goes straight from a crystalline state to subliming out of the SWCNTs. Whilst this was unanticipated, it would offer an explanation as to the relative permanence of the amorphous phase state of the encapsulated material reported in Section 4.3. If the nC-SnSe does not undergo a melt transition, then there is no simple way of resetting the system, so that it might reform the crystalline bonds.

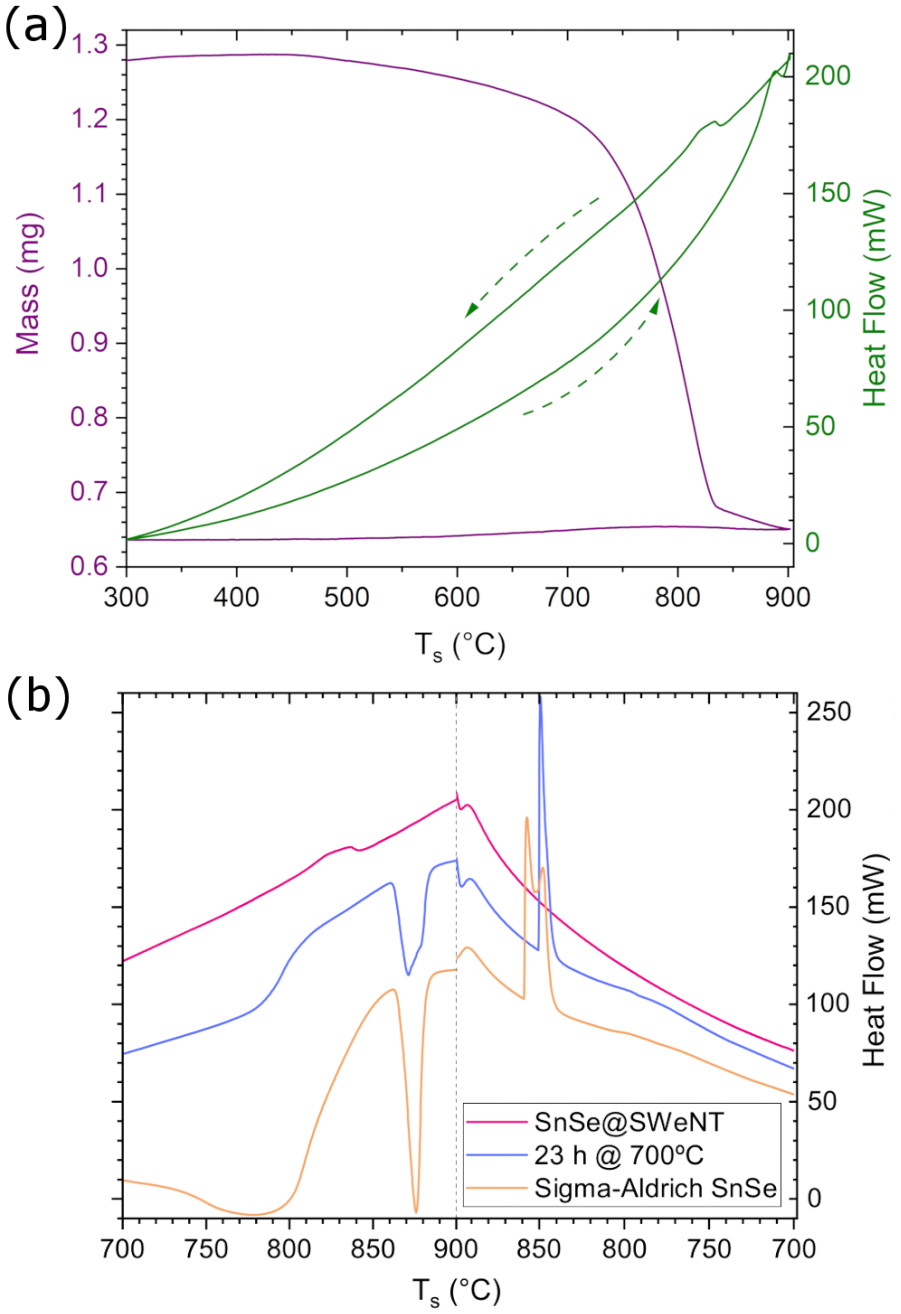


Figure 4.19: The thermal characteristics of nC-SnSe, and a comparison with the heat flow properties of two forms of bulk SnSe, when cycled through 900°C. (a) The heat flow and mass loss characteristics for a representative SnSe@SWCNT sample, cycled once through 900°C. The heating and cooling heat flow curves are indicated by the green arrows. (b) A direct comparison of the heat flow characteristics of shows that the melt transition at 860°C, that is present in bulk SnSe is absent for the nC-SnSe. The notation 23 h @ 700°C indicates a sample that was grown at 700° with a dwell time of 23 h. The dashed line indicates the transition between the heating and cooling curves.

## 4.5 Conclusion

The first section examined the growth and structural characterisation of SnSe@SWCNTs, and how this compares with bulk. A particular focus was made on investigations into the variation of the structure and composition of the encapsulated material as a function of the diameter of the NT. A full catalogue of these observed structures has been compiled, which included an analysis, and modelling, of a newly observed form of nC-SnSe. This cataloguing is complementary to the analysis of the amorphisation of the nC-SnSe, which has been observed in live TEM imaging, but has also been captured and evidenced by time-resolved SAED.

Furthermore, the discovery of this new form of confined SnSe offers another dimension in the investigation of this compound as a nC-PCM, in contrast to other types of crystalline fillings. These results also form the basis for studies into further nC-PCMs and, in particular, investigations into the variation of the structure of the encapsulated material as a function of the diameter of the NT, and the effect that this has on *in situ* phase changes. These experiments can then be extended to an analysis of further properties of nC-PCMs, such as conductivity. From previous studies [60, 119], enhanced thermoelectric properties would be anticipated, which is the subject of ongoing investigations in this laboratory, and will be discussed further in Section 6. Indeed, while mesoscale SnSe nanotubes (180-400 nm in cross-section) have been formed inside alumina templates,[122] theoretical studies by Lin and coworkers predict that forming smaller "star-like" SnSe nanotubes at a slightly larger scale than our nanostructures theoretical studies by Lin and coworkers predict that forming smaller "star-like" SnSe nanotubes at a slightly larger scale than our nanostructures (i.e. with an outer diameter of $\sim$2 nm) considerably enhances their thermoelectric performance. [123]. Given the conformation options afforded by the confining diameter range of the novel SnSe structure, it is possible to filter out the metal SWCNTs and still be left with a substantial volume of the new structure encapsulated inside semiconducting SWCNTs. Therefore, the margins for investigation into, and application of, the thermo-conductive properties of these samples are large.

Further temperature-dependence and compositional analysis of the various forms of SnSe have been conducted, and were facilitated by DSC/TGA. The experiments sought to illustrate the phase and temperature characteristics and the corresponding response of the nC-SnSe, in comparison with the bulk. The apparant rapid and complete sublimation of the nC-SnSe from $\sim$ 700°C also offers an explanation as to the permanence of the beam-induced amorphous state, as evidenced by SAED

analysis of the SnSe@SWCNTs sample.

# Chapter 5

# CNT Growth on $Si_3N_4$ Substrates

## 5.1 Introduction

This chapter outlines some of the ongoing collaborative work with J. Viner & D. Smith (supervisor) from the University of Southampton, which comprised imaging CNTs grown across slits in $Si_3N_4$ substrates using electron microscopy. The course of the collaboration has been from inception to the most recent efforts towards filling the as-grown SWCNTs. Therefore, images evidence and catalogue the process of fine tuning the development of appropriate substrates and growth procedures in order to obtain true SWCNTs from precursors. This work was conducted with a view to the consistent growth of suspende nanocomposites, so that they might be characterised by Raman spectroscopy and Rayleigh scattering, on an individual CNT basis.

## 5.2 Substrates for CNT growth

The characterisation work carried out at Warwick consisted of combined EM and EDX, in order to get a complete visual and compositional picture of the results of different growth procedures. By using both SEM and TEM, we were able to observe the extent and composition of the large scale material growth at the surface and the nanoscale structure and makeup of the grown CNTs. This provided us with information on the efficiency and relative success of different growth mechanisms.
The very first experiments were conducted using silicon nitride thin films as substrates - as shown in Fig. 5.1. These thin films were suspended across holes in silicon nitride wafers. Slits were then etched in the films using Focussed Ion Beam

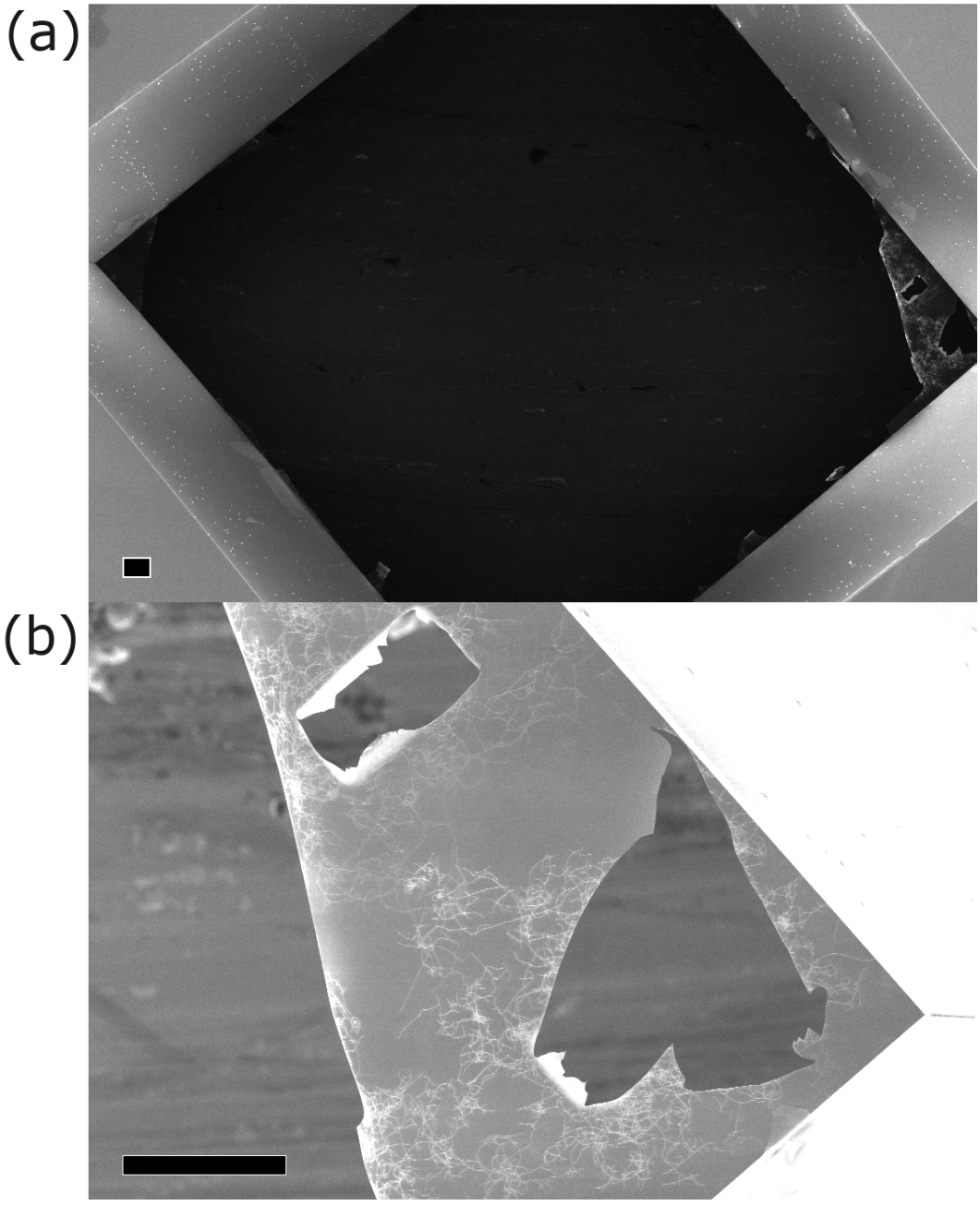


Figure 5.1: SEM images of the result of a growth of CNTs on an etched $Si_3N_4$ window. (a) The slits decreased the integrity of the $Si_3N_4$ window, which often caused the window to rupture during the CNT growth process. (b) The population of grown CNTs can be seen to be confined to the $Si_3N_4$ film in bundled groups, with no traversing of the slits. Scale bars are 20 $\mu$m.

SEM (FIB-SEM). The main issues with these substrates lay in the resilience of the etched films; if the FIB etching did not wholly destroy the film, then the decreased integrity caused by the slits often resulted in the destruction of the film during growth or transit - as depicted in Fig. 5.1 (a). Furthermore, the minimum width of the slits was dictated by the beam size, which typically proved too large for CNTs to traverse (Fig. 5.1 (b)). This resulted in the CNT population being confined solely to the surface of the window, where the window was still intact, as illustrated in Fig. 5.1 (b).

So whilst this method and substrate may be adequate for large scale analysis of the growth efficiency and composition, it is not sufficient for analysing CNTs on an individual scale - particularly for Raman spectroscopy, where spot sizes are conventionally limited to $\sim 0.5$ $\mu$m [267]. Therefore, a new substrate was developed by J. Viner & D. Smith. The $Si_3N_4$ substrates were designed with a focus on growing CNTs across robust and stable cavities: they comprised a $Si_3N_4$ wafer with a narrow slit down the centre (Fig. 5.2). The slit in the $Si_3N_4$ substrate was achieved by partially slicing through the substrate and then etching using KOH. This results in a tapered, triangular prism slit through the $Si_3N_4$. There is a modicum of variation in the slit dimensions at the growth surface, with lengths on the order of $\sim 1$ mm and widths of $\sim (1 - 15)$ $\mu$m- as can be seen in the TEM images in Fig. 5.2.

The SEM images shown in Fig. 5.2 (a) were taken at minimum to low magnification, in order to best show the large ratio of width to length in the slits. As the magnification is increased, the variation in achieved slit widths can be observed. The higher magnification SEM images (Fig. 5.2 (b)) depict slits with widths in the range $(2.5 - 8.0)$ $\mu$m. However, as can be seen in two images in Fig. 5.2 (a), there can be a large variation in lateral dimension of the hole, and some tapering, along the full length. Due to the etching procedure, the slit follows a trapezoidal depth profile, with a minimum at the growth surface and a maximum at the opposite face. The $Si_3N_4$ substrates are approximately 100 mm$^2$, with a depth of $\sim 1$ mm. This is considerably larger and thicker than a standard TEM grid. Therefore, a custom holder attachment was designed for analysis in the TEM, by S. Hindmarsh. This attachment replaced the clip-in head of a conventional single-tilt TEM sample holder, and incorporated a larger recess and cover to accommodate the silicon nitride substrates.

The procedure used for the growth of the CNTs for this work was Chemical Vapour Deposition (CVD) [192, 268]. This involves sputtering the prepared substrate with catalyst nanoparticles - typically a pure metal or alloy containing some combination of Fe, Ni, and Co [26]. The use of a $Si_3N_4$ substrate results in the catalyst particles

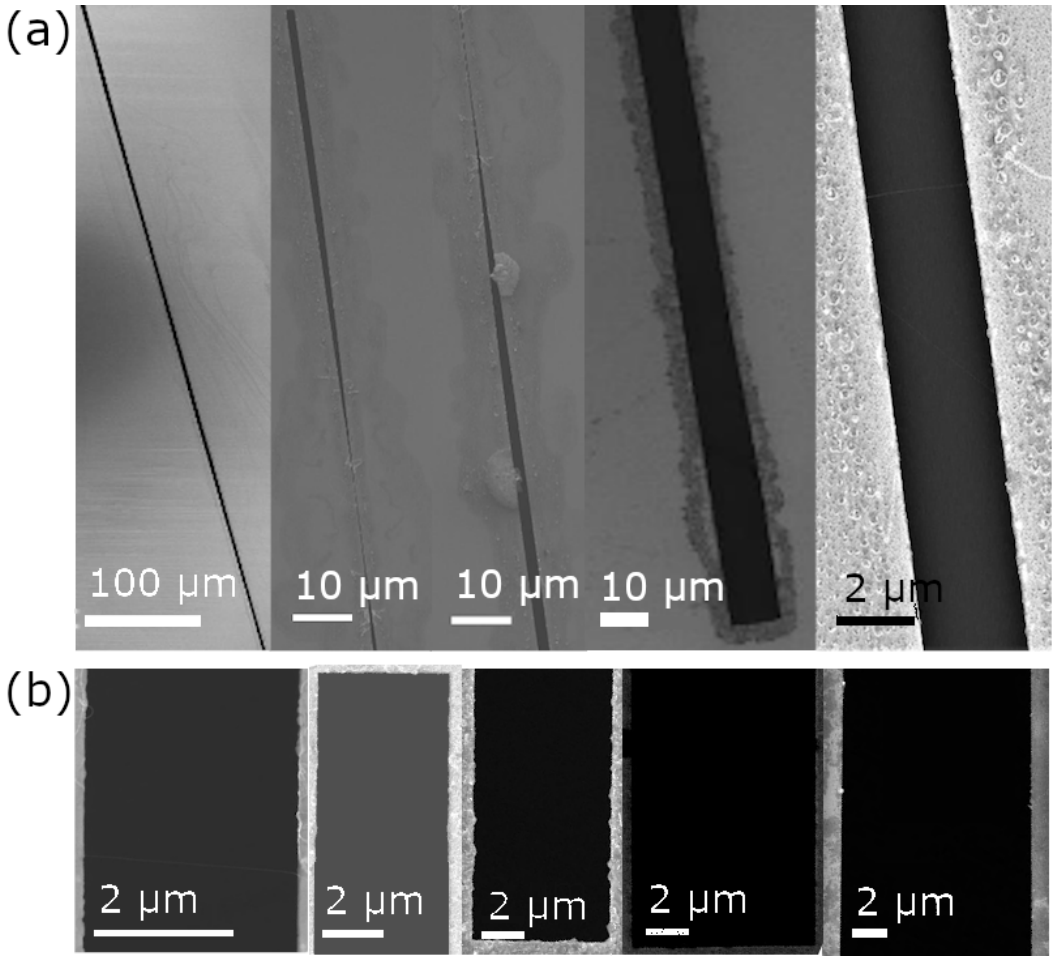


Figure 5.2: SEM images of the prepared samples, post-growth protocol, depicting the slit etched into the $Si_3N_4$ substrate and the surrounding material. (a) Indicative SEM images, taken at minimum to low magnification depicting the ratio of slit length to width. The slits are on the order of $\sim 1$ mm in length at the growth surface. (b) Higher magnification images of the variation in slit width. The etched slits have observed widths in range $\sim (1-15)$ $\mu$m at the growth surface. Images were obtained at 1 kV.

being larger and more dispersed than when $SiO_2$ is used. This is due to the relatively weaker attraction between $Si_3N_4$ and, in this case, Fe [23, 25, 27].
A carbon-containing gas is then passed over at high temperature, typically $(500 - 1100)°C$. The gas used in this case was high pressure ($\sim$1 MPa) CO [20, 269]. The density of the catalyst, the speed at which the gas is travelling as it passed over the substrate, and the temperature are the key factors in controlling the length, diameter, and multiplicity of the grown CNTs [26, 146]. Whilst this is an efficient method for growing high density CNTs at low cost, it can result in a sample that is well-populated by crystalline structures, as well as SWCNTs and MWCNTs. In this work, this is particularly evident in TEM images, where the crystals encroach on the slit in the $Si_3N_4$, as can be seen in Fig. 5.3. However, as illustrated in the tableau of low magnification TEM images - taken and comprised by J. Sloan - in Fig. 5.3, these nanoparticles can be helpful for being able to relocate the point along the slit where a particular CNT has grown, since the catalyst particles can act as visual markers along the otherwise uniform slit walls.

## 5.3 Analysis of CNTs Grown on $Si_3N_4$ Substrates

Many issues were encountered when developing and fine tuning the growth processes: many initial samples were devoid of CNTs (Fig. 5.4 (a)). Those samples where growth had been successful were often populated by defective CNTs (Fig. 5.4 (b)) or saturated with growth material and CNTs (Fig. 5.4 (c)). A fast heating protocol attempted to combat this issue, but resulted in striated deposition and growth patterns (Fig. 5.4 (c) "Fast"), In either scenario, there were often swathes of crystalline formations that comprised a mixture of growth precursors (Fig. 5.4 (d)). Even in later experiments, the slits were occasionally observed to be partially filled with crystalline formations, which comprised a combination of the growth and precursor materials (Fig. 5.4 (d)). This composition was confirmed by SEM imaging and EDX mapping (Fig. 5.5). Such formations cannot be isolated from the individual CNTs, and so greatly interfere with Raman Spectroscopy measurements.

Despite these initial issues, later procedures proved successful in the growth of individualised CNTs. These were able to be visualised via low voltage (1 kV) SEM studies (Fig. 5.4 (d) and 5.6 (a)), which provided a quick method of rudimentarily checking the success of an experiment. However, upon higher resolution analysis in the TEM, many of these turned out to be MWCNTs (Fig. 5.6 (b)) or bundled CNTs (Fig. 5.6 (c)). Therefore, further adjustment of the parameters for growth -

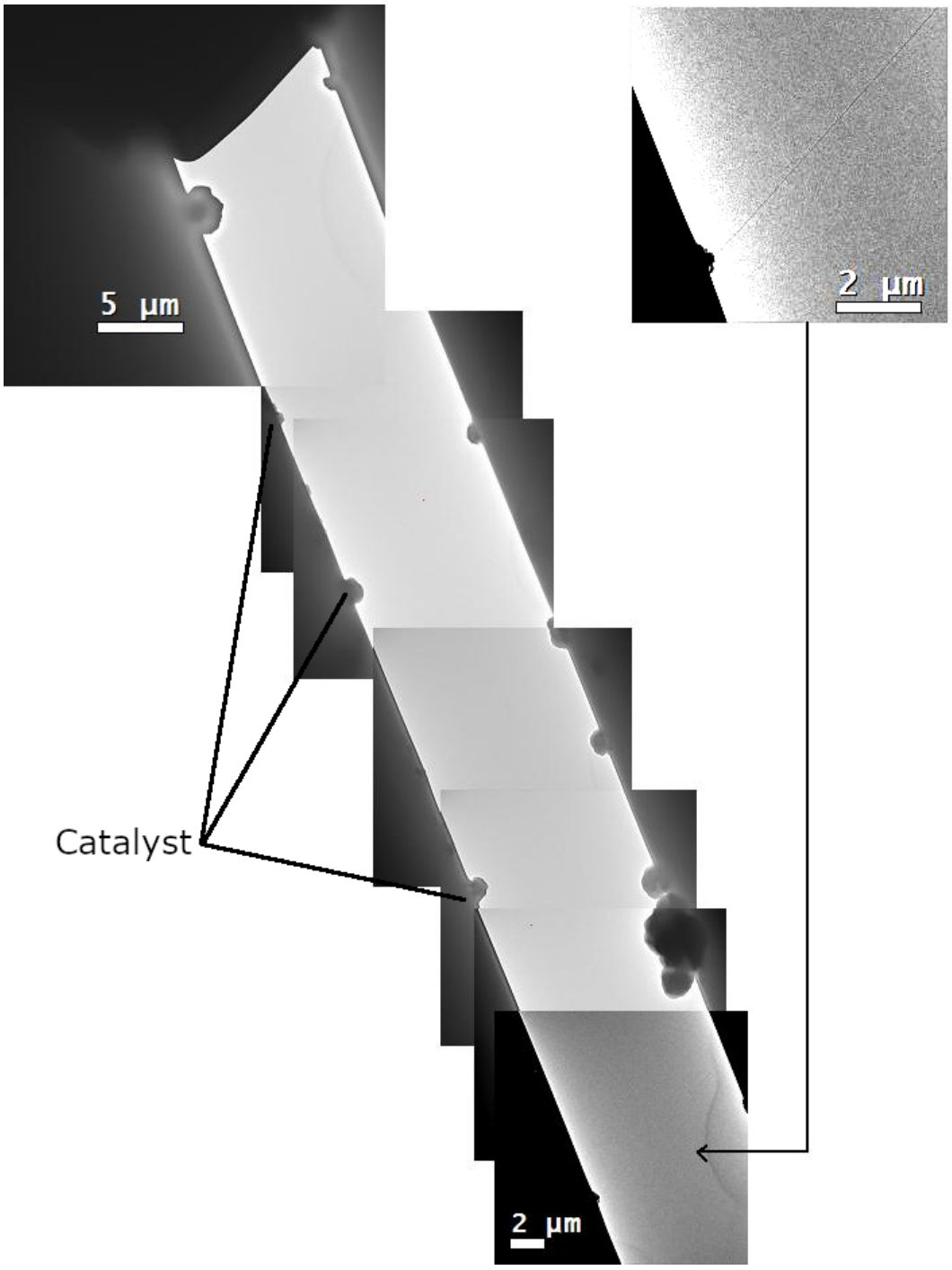


Figure 5.3: Tableau of low magnification TEM images depicting the slit etched into the $Si_3N_4$ substrate, the catalyst particles, and CNT growth. The encroachment of the catalyst particles into the slit provides unique visual markers for position (re)location. Images were obtained at 200 kV by J. Sloan.

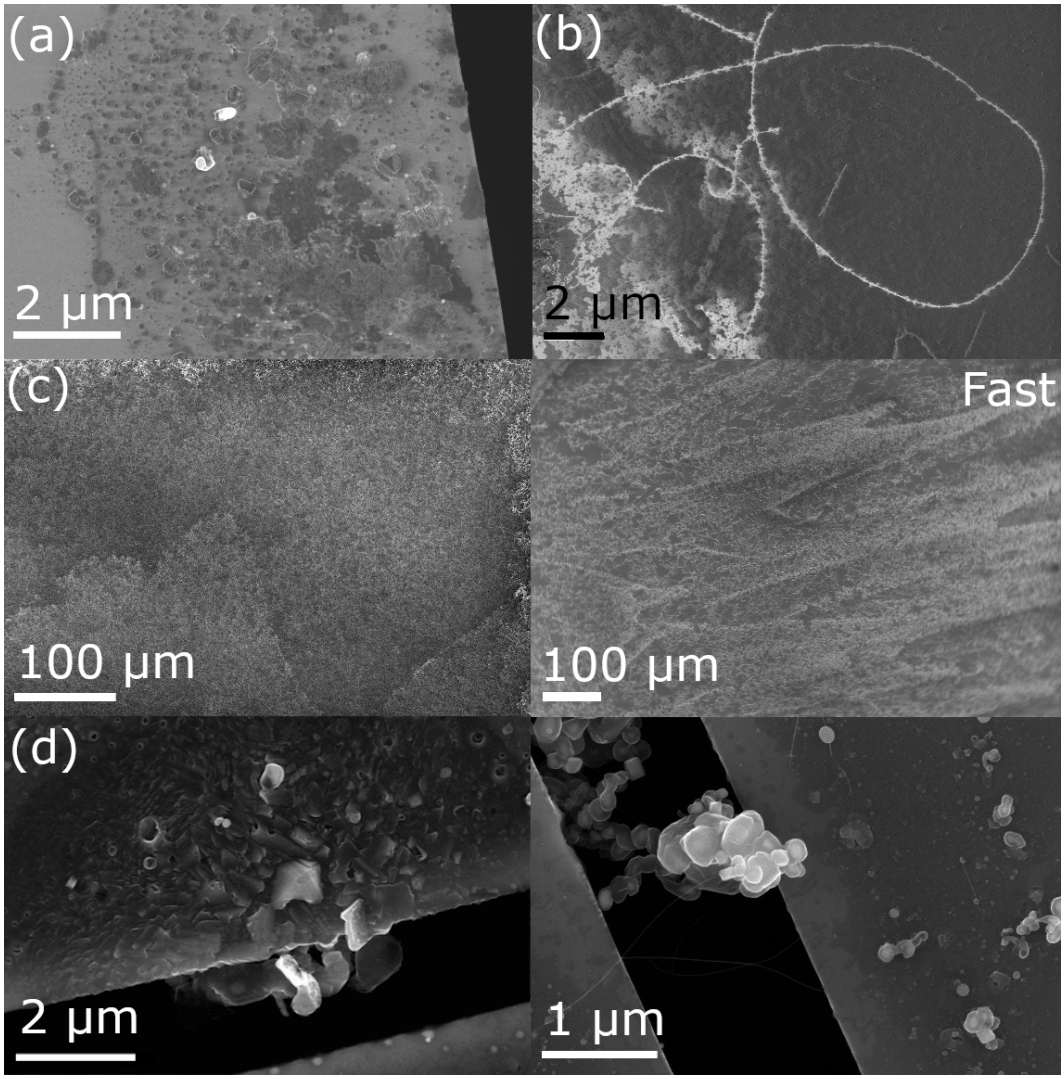


Figure 5.4: SEM images of initial growth attempts of CNTs on $Si_3N_4$ substrates. Many issues were encountered when developing and fine tuning the growth processes. (a) Devoid of CNTs, (b) defective CNTs, (c) samples were saturated with CNTs and growth material, where fast growth protocols created striations across the substrate. (d) Crystalline formations across the substrates, and wedged in the slits themselves. CNTs can be seen to have grown and attached themselves to these crystals.

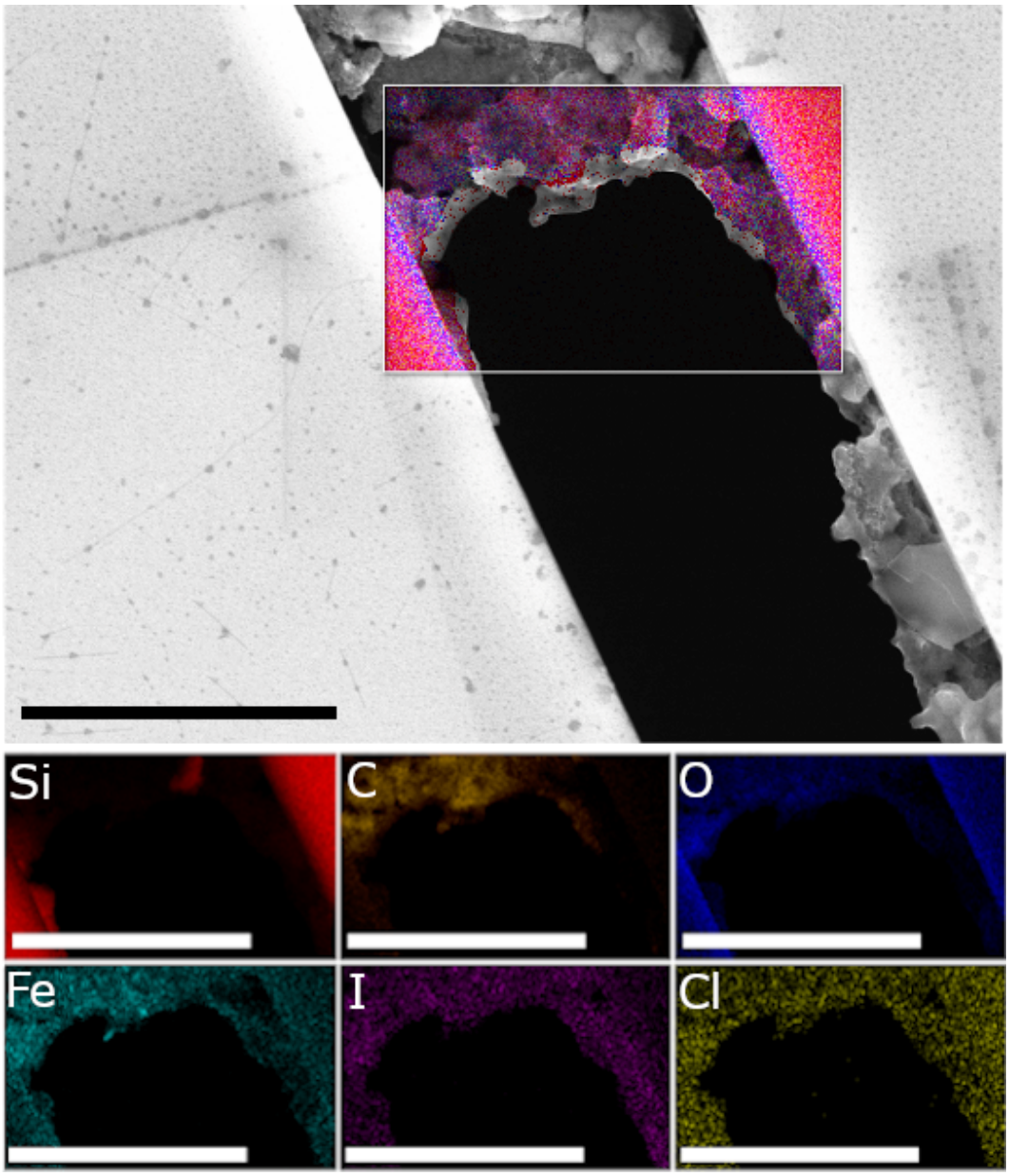


Figure 5.5: Representative SEM image and EDX mapping overlay of crystalline formations in slits in $Si_3N_4$ substrates, and on the samples as a whole, after growth and filling attempt of individualised CNTs. The crystals comprise a mixture of the elemental precursors used in the growth of the CNTs. No CNTs can be discerned in this image. SEM and EDX conducted at 20 kV. Scale bars are 5 $\mu$m.

including the quantity of source material, and growth time and temperature - were conducted. This resulted in the ability to consistently grow true, individualised SWCNTs across slits, with no defects (Fig. 5.6 (d)).

## 5.4 SAED on Single Filled SWCNTs

Ongoing experiments include attempting to fill the grown SWCNTs. This is conducted using similar procedures to those outlined in Section 2.1. The grown CNTs are gently heated at $\sim 400°C$ in air to open the ends of the CNTs, and then filled using VPT. Initial filling experiments utilised iodine, which has highly predictable and well-documented filling results and properties. These early experiments resulted in large quantities of iodine deposition across the sample, as outlined in the EDX mapping in Fig. 5.5 in Section 5.3. However, unlike the samples made by this lab at the University of Warwick, the University of Southampton samples cannot be so readily processed or cleaned. This is due to the fragile nature of the suspended CNTs. The ultimate aim of this work is to have single, suspended filled SWCNTs, that can then be analysed using EM, Raman, Rayleigh, and optical spectroscopy on an individualised basis. Future experiments would like to see the encapsulation of SnSe, due to the promising results outlined in this thesis in Chapter 4.
However, there have recently been significant developments in this branch of experimentation; J. Viner has successfully grown and filled SWCNTs suspended across slits with $Sb_2Te_3$ (Fig. 5.7 (a)). Therefore, this offers us the opportunity to study individualised, and very thin bundles of, filled $Sb_2Te_3$@SWCNTs via TEM and SAED. These same $Sb_2Te_3$@SWCNTs can then be relocated and characterised via Raman, Rayleigh, and optical spectroscopy by J. Viner & D. Smith at the University of Southampton.
We know that these SWCNTs are filled not only from the variable contrast in TEM imaging, but also by the characteristics of their SADPs - as can be seen in Fig. 5.7 (a). What we see is that the samples produced by J. Viner have diffraction characteristics that are near identical to that of the proposed structure for nC-$Sb_2Te_3$ - simulated SADP in Fig 5.7 (b) - and that of the samples grown at Warwick (Fig. 5.7 (c)) - as reported in Chapter 3. This is a significant result, as it shows us that even on a the scale of a few SWCNTs, these reflections - and so this particular structure - are dominant. This is especially true given the sharpness of the reflections attributed to the nC-$Sb_2Te_3$ in Fig. 5.7 (a), as the $\{015\}$ reflections are particularly sensitive to rotation. An indexed SADP from Chapter 3 has been included (Fig. 5.7

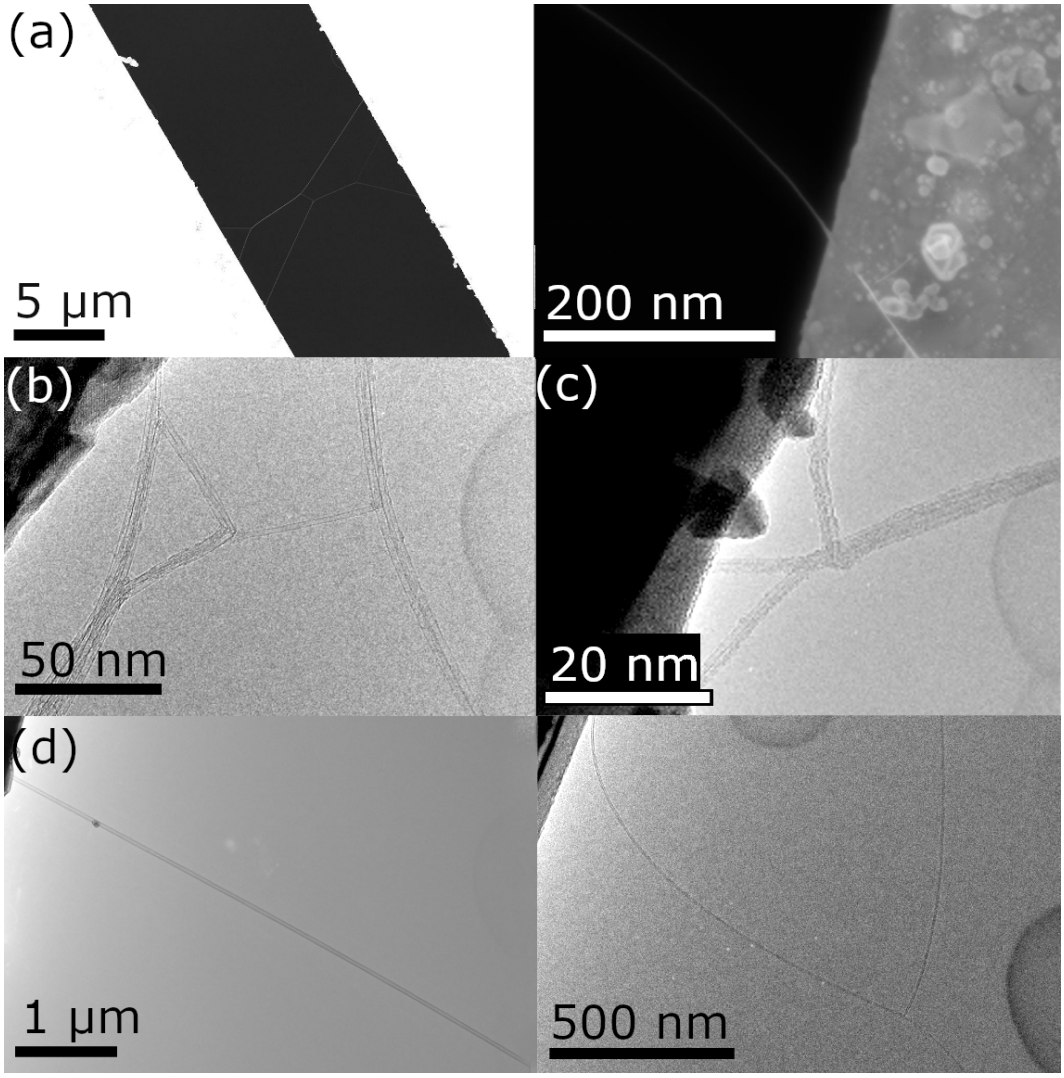


Figure 5.6: SEM and TEM images of CNTs grown across slits in the $Si_3N_4$ substrate. (a) Low voltage SEM imaging (1 kV) allows the CNTs to be clearly visualised. TEM imaging allowed the walls of the CNTs to be clearly discerned, such that (b) MWCNTs, (c) CNT bundles, and (d) true individualised SWCNTs were able to be distinguished from one another. The SWCNTs had measured diameters in the range $\sim (1.7 - 5.9)$ nm.

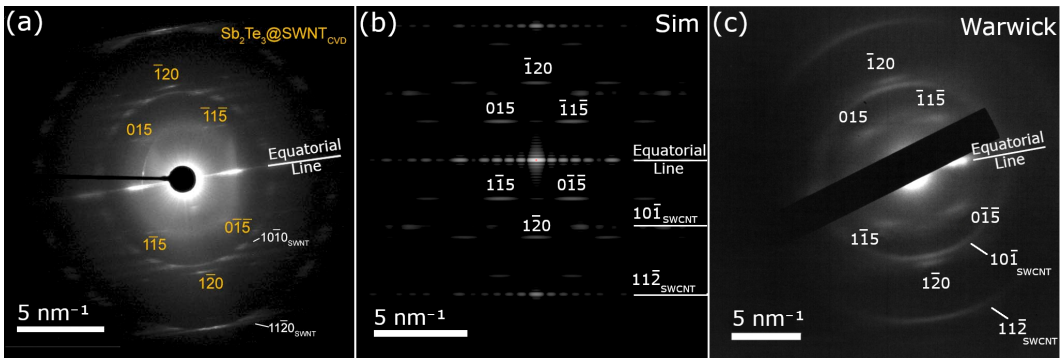


Figure 5.7: Experimental and simulated SADPs of filled SWCNTs. (a) Experimental SADP - taken by J. Sloan - of a few SWCNTs $Sb_2Te_3$@SWCNTs in a thin bundle, suspended across a slit in a $Si_3N_4$ substrate - synthesised by J. Viner under the supervision of D. Smith. (b) Simulated SADP of a single (10,10) SWCNT filled with $Sb_2Te_3$. Simulated in clTEM using a model built in CrystalMaker$^{TM}$. (c) Experimental SADP of a bundle of (∼1000s) $Sb_2Te_3$@SWCNTs. The key reflections for the SWCNTs and $Sb_2Te_3$ have been indexed.

(c)) to show the extent of the effect that increased bundle size has on the blurring of the reflections, both in the case of the SWCNT and the nano-confined crystalline $Sb_2Te_3$. The SADP in Fig. 5.7 (c) was for a bundle with a diameter of $\sim$ 100 nm, which is equivalent to several thousands of SWCNTs.

## 5.5 Conclusion

The work outlined in this chapter detailed the ongoing collaborative work with J. Viner & D. Smith from the University of Southampton, which comprised imaging CNTs grown across slits in $Si_3N_4$ substrates using electron microscopy. The characterisation work carried out at Warwick consisted of combined EM and EDX, in order to get a complete visual and compoistional picture of the results of different growth procedures. By using both SEM and TEM, we were able to observe the extent and composition of the large scale material growth at the surface and the nanoscale structure and makeup of the grown CNTs. This provided us with information on the efficiency and relative success of different growth mechanisms.
Therefore, images evidence and catalogue the process of fine tuning the development of appropriate substrates and growth procedures in order to obtain true SWCNTs from precursors, and then efficiently fill them. This work was conducted with a view to the consistent growth of suspende nanocomposites, so that they might be characterised by Raman spectroscopy and Rayleigh scattering, on an individual CNT basis.

# Chapter 6

# Conclusions and Future Work

Encapsulated materials, particularly on the atomic-level scale addressed in this research, have significant potential in the area of nanotechnology and computing. Given the appropriate confining material, and isolated nano-confined structure with desired properties, then we have a ready-prepared component. This wire could be utilised in memory allocation, photovoltaics, or as a low resistance connector.

As introduced in Section 1.2, there lies considerable interest in the separation of SWCNTs according to their specific conformation (diameter) via ultracentrifugation. These investigations are ongoing, and form part of the research carried out carried out by J.Sloan, M. Burdanova, K. Bal, E. Hu, R. Kashtiban, and J. Lloyd-Hughes as part of ESPRC project EP/R019428/1. Considerable care has to be taken during processing so as to not to damage the SWCNTs, as outlined in Section 2.1. The next step is then to extend this process to filled SWCNTs. However, due to the added variation to the density of the combined structures, it is not as simple as separating by diameter (conformation). Special consideration must also be taken due to the overlap of the observed diameter ranges in which particular structures form.

Further to Section 2.1.3, investigations could be made into encapsulating materials with higher melt temperatures. Such structures could prove even more robust, especially to variable thermal environments, and therefore would entertain a wider range of applications.

Chapter 3 provided evidence for three methods of sample exfoliation and purification from extraneous bulk material, as introduced in Section 2.1.5. In addition, whilst a melt point depression is expected for materials on the nanoscale when compared with their bulk form, we found an unprecedented drop in the melting temperature to repeatedly occur across all nC-$Sb_2Te_3$ forms (Section 3.4). So then, further ex-

perimentation could be conducted on what would happen to the material and its heat flow characteristics if we were to focus on a range around the transition and cycle back and forth across it. This should include analysis, and characterisation, of the XRD behaviour of nC-$Sb_2Te_3$, further to the data and results presented in Section 3.5.

As introduced in Section 3.6, capturing the glassy phase *ex situ* can be achieved via heating to above the melt temperature of the sample, followed by rapid quenching. The sealed ampoule containing the nC-$Sb_2Te_3$ must be wrapped in damp towel for quenching. This is due to the wetting phenomenon causing delayed cooling, if the ampoule alone is dropped straight into liquid Ni. Therefore, future experiments on nC-$Sb_2Te_3$ could include *ex situ* capturing of the glassy phase, photoconductivity and thermoconductivity measurements on thin films, and *in situ* synchotron X-ray studies with R. Walton at the Diamond Light Source. This could then lead to investigations into whether the *ex situ* captured glassy phase can also be recrystallised *ex situ*, for example via laser irradiation. Similarly, would it then be possible for amorphisation via irradiation be achieved *ex situ*, so that a more technologically-applicable phase cycling could be achieved.

Further to this, there lies interest in studying the encapsulation of complementary $Sb_2X_3$ materials, $Sb_2S_3$ and $Sb_2Se_3$, and full characterisation of these forms. The same could also be said for the encapsulation of GeSbTe (GST), due to its impressive fundamental and tunable properties and applications for non-volatile memories and optical modualtors, which has garnered significant interest across disciplines [51, 54, 61, 270].

Thinking about PCMs more generally, investigations into the photocondutivity of thin films of PCMs@SWCNTs could prove technologically important. Preliminary investigations conducted by M. Burdanova indicate a transition from negative photoconductivity in the unfilled SWCNTs, to positive in the processed samples. As outlined in Section 1.3 and Chapter 4, bulk SnSe has established applications as a low-cost photovoltaic, and in memory-switching devices. Therefore, it would be of great interest to see how the nano-confinement of this PCM would impact the photoconductive and photovoltaic properties. Furthermore, is there a thickness dependence for the photoluminescence of the nC-PCMs, as with layered 2D InSe [248, 271].

Such investigations could prove complementary to ones into the bandgap alterations associated with nano-confining materials inside SWCNTs, and the progression of the bandgaps either side of, and across, the phase transition boundaries. Furthermore, would the properties of the nano-confined materials be significantly altered to those

reported here if boron nitride nanotubes were used in the place of SWCNTs. Similarly, there would be a wider range of accessible material for encapsulation and atmospheric temperature investigations, since they are thermally stable in air up to $\sim 950°C$.

# References


[1]X. P. Wang et al., *Phys. Chem. Chem. Phys.* **16**, 10810–15 (2014).

[2]L. Wang and S. Gai, *Contemp. Phys.* **55**, 75–93 (2014).

[3]V. T. Dau et al., *Smart Mater. Struct.* **19**, 075003 (2010).

[4]T. Dinh et al., *Adv. Mater. Interfaces* **5**, 1–9 (2018).

[5]Y. Zhou and L.-D. Zhao, *Adv. Mater.* **29**, 1702676 (2017).

[6]P. H. Jiang et al., *Phys. Chem. Chem. Phys.* **17**, 27558–64 (2015).

[7]P. Chakraborty et al., *Adv. Condens. Matter Phys.* **2018**, 1–29 (2018).

[8]S. Liu et al., *Angew. Chemie - Int. Ed.* **50**, 12050–3 (2011).

[9]W. Shi et al., *Adv. Sci.* **5**, 1700602 (2018).

[10]O. Vigil-Galán et al., *Semicond. Sci. Technol.* **24**, 025025 (2009).

[11]X. Li and H. Zhu, *J. Mater.* **1**, 33–44 (2015).

[12]S. Y. Chew et al., *Carbon N. Y.* **47**, 2976–83 (2009).

[13]D. Wei et al., *J. Mater. Chem.* **21**, 9762–7 (2011).

[14]R. Chau et al., *Nat. Mater.* **6**, 810–12 (2007).

[15]T. D. Steiner, *Semiconductor Nanostructures for Optoelectronic Applications* (Artech House Inc., London, 2004).

[16]K. D. Sattler, *Handbook of Nanophysics: Nanotubes and Nanowires* (CRC Press, 2011).

[17]S. Iijima and T. Ichihashi, *Nature* **363**, 603–5 (1993).

[18]C. Journet et al., *Nature* **388**, 756–8 (1997).

[19]M. Dresselhaus et al., *Carbon N. Y.* **33**, 883–91 (1995).

[20]M. S. Dresselhaus et al., *Top. Appl. Phys.* **80**, 1–9 (2001).

[21]K. Hata, *Science (80-. ).* **306**, 1362–4 (2004).

[22]B. Kitiyanan et al., *Chem. Phys. Lett.* **317**, 497–503 (2000).

[23]C. T. Kingston and B. Simard, *Anal. Lett.* **36**, 3119–45 (2003).

[24]M. V. Kharlamova and D. Eder, "Synthesis and Properties of Single-Walled Carbon Nanotubes Filled with Metal Halogenides and Metallocenes", in *Perspect. carbon nanotub.* (IntechOpen, Dec. 2019).

[25]J. S. Barnard et al., *Nanoscale* **8**, 17262–70 (2016).

[26]S. Reich et al., *Carbon Nanotubes: Basic Concepts and Physical Properties* (Wiley, 2004).

[27]L. Hu et al., *Chem. Rev.* **110**, 5790–844 (2010).

[28]Q. Wang and H. Moriyama, "Carbon Nanotube-Based Thin Films: Synthesis and Properties", in *Carbon nanotub. - synth. characterisation, appl.* (InTechOpen, 2011).

[29]R. F. Egerton et al., *Micron* **35**, 399–409 (2004).

[30]D. B. Williams and C. B. Carter, *Transmission Electron Microscopy* (Springer, New York, 2009).

[31]J. Kong et al., *Phys. World* **17**, 17–8 (2004).

[32]P. Khalid et al., *Int. J. Appl. Eng. Res.* **11**, 148–57 (2016).

[33]J.-k. Qin et al., 1–45 (2020).

[34]A. Eliseev et al., *Nano Lett.* **17**, 805–10 (2017).

[35]A. Bondi, *J. Phys. Chem.* **68**, 441–51 (1964).

[36]Y. Y. Huang and E. M. Terentjev, *Polymers (Basel).* **4**, 275–95 (2012).

[37]R. Saito et al., *Physical Properties of Carbon Nanotubes* (Imperial College Press, July 1998).

[38]S. Friedrichs et al., *Phys. Rev. B - Condens. Matter Mater. Phys.* **64**, 1–8 (2001).

[39]P. Lambin et al., *Phys. Rev. B - Condens. Matter Mater. Phys.* **64**, 1–7 (2001).

[40]V. Jakubsky and A. Perez-Obiol, *Phys. Rev. B* **95**, 245431 (2017).

[41]SWeNT, *SWeNT CG 200 Data Sheet Single Wall Carbon Nanotubes*, tech. rep. (2008).

[42]NanoIntegris, *Technical Data Sheet*, tech. rep. (2013).

[43]S. Toyokuni, *Adv. Drug Deliv. Rev.* **65**, 2098–110 (2013).

[44]N. Kobayashi et al., *J. Occup. Health* **59**, 394–407 (2017).

[45]A. P. Francis and T. Devasena, *Toxicol. Ind. Health* **34**, 200–10 (2018).

[46]Y. Liu et al., *Acc. Chem. Res.* **46**, 702–13 (2013).

[47]W. Qi et al., *Sci. Rep.* **7**, 1–14 (2017).

[48]S. Raoux and M. Wuttig, *Phase Change Materials* (Springer US, Boston, MA, 2009).

[49]S. Raoux et al., *MRS Bull.* **39**, 703–10 (2014).

[50]G.-C. Wang and T.-M. Lu, *RHEED Transmission Mode and Pole Figures* (Springer New York, New York, 2014).

[51]J.-F. Zheng, *Germanium Antimony Telluride Materials and Devices Incorporating the Same*, 2015.

[52]S. Mukhopadhyay et al., *Sci. Rep.* **6**, 25981 (2016).

[53]S. Wei et al., *Phys. Rev. Appl.* **7**, 1–10 (2017).

[54]P. Guo et al., *Appl. Sci.* **9**, 530 (2019).

[55]S. Caravati et al., *Phys. Rev. B - Condens. Matter Mater. Phys.* **81**, 1–8 (2010).

[56]S. Marks et al., *Acta Phys. Pol. A* **131**, 1324–8 (2017).

[57]Y. Chen et al., *Mater. Lett.* **243**, 153–6 (2019).

[58]J. M. Marin et al., *Meas. Sci. Technol.* **14**, 184–9 (2003).

[59]Y. Yin et al., *J. Appl. Phys.* **102**, 064503 (2007).

[60]P. V. Medeiros et al., *ACS Nano* **11**, 6178–85 (2017).

[61]G. P. Kissling et al., *J. Electrochem. Soc.* **165**, D557–67 (2018).

[62]U. Möhring et al., "Textiles for Patient Heat Preservation During Operations", in *Handb. med. text.* (Elsevier, 2011), 434–42.

[63]M. Lanaro et al., *Electrofluidodynamic Technologies for Biomaterials and Medical Devices* (Elsevier, 2018).

[64]S. Coyle and D. Diamond, "Smart Nanotextiles: Materials and Their Application", in *Ref. modul. mater. sci. mater. eng.* (Elsevier, 2016).

[65]B. Pause, "Phase Change Materials and their Application in Coatings and Laminates for Textiles", in *Smart text. coatings laminates* (Elsevier, 2010), 236–50.

[66]R. Meirowitz, "Microencapsulation Technology for Coating and Lamination of Textiles", in *Smart text. coatings laminates* (Elsevier, 2010), 125–54.

[67]C. Ho et al., "Improving Thermal Comfort in Apparel", in *Improv. comf. cloth.* (Elsevier, 2011), 165–81.

[68]M. Mapston and C. Westbrook, "Prefabricated Building Units and Modern Methods of Construction (MMC)", in *Mater. energy effic. therm. comf. build.* (Elsevier, 2010), 427–54.

[69]A. Pisello, "High-Albedo Roof Coatings for Reducing Building Cooling Needs", in *Eco-efficient mater. mitigating build. cool. needs* (Elsevier, 2015), 243–68.

[70]A. Adesina, *Renew. Energy Environ. Sustain.* **4**, 9 (2019).

[71]S. Mondal, *Appl. Therm. Eng.* **28**, 1536–50 (2008).

[72]A. Hasan et al., *Energy Convers. Manag.* **81**, 322–9 (2014).

[73]W. Su et al., *Renew. Sustain. Energy Rev.* **48**, 373–91 (2015).

[74]S. Raoux et al., *Chem. Rev.* **110**, 240–67 (2010).

[75]S. Bhatia, "Solar Thermal Energy", in *Adv. renew. energy syst.* (Elsevier, 2014), 94–143.

[76]M. Farid and A. Sherrif, "Phase Change Materials for Energy Storage and Thermal Comfort in Buildings", in *Mater. energy effic. therm. comf. build.* (Elsevier, 2010), 384–98.

[77]J. Park et al., *Sol. Energy* **105**, 561–74 (2014).

[78]M. Wuttig and N. Yamada, *Nat. Mater.* **6**, 824–32 (2007).

[79]H. Hayat et al., "Emerging Nanoscale Phase-Change Memories: A Summary of Device Scaling Studies", in *Ref. modul. mater. sci. mater. eng.* (Elsevier, 2016).

[80]J. Xu et al., *Electrochem. Solid-State Lett.* **15**, 53–9 (2012).

[81]M. Van Parys, "Smart Textiles Using Microencapsulation Technology", in *Funct. coatings* (Wiley, Weinheim, 2006), 221–58.

[82]C. Zhao and G. Zhang, *Renew. Sustain. Energy Rev.* **15**, 3813–32 (2011).

[83]S. Behzadi and M. Farid, *Appl. Energy* **122**, 11–6 (2014).

[84]N. Pan and G. Sun, *Functional Textiles for Improved Performance, Protection and Health* (Woodhead Publishing, 2011).

[85]B. Boh et al., *J. Microencapsul.* **22**, 715–35 (2005).

[86]W. Shi et al., *Adv. Mater.* **20**, 1892–7 (2008).

[87]S.-W. Jung et al., *J. Nanosci. Nanotechnol.* **11**, 1569–72 (2011).

[88]C. E. Giusca et al., *MRS Proc.* **1251**, 1251–H06–03 (2010).

[89]C. E. Giusca et al., *Nano Lett.* **13**, 4020–7 (2013).

[90]K. Chang and S. S. P. Parkin, *APL Mater.* **7**, 041102 (2019).

[91]L.-D. Zhao et al., *Nature* **508**, 373–7 (2014).

[92]S. Cantor, *Thermochim. Acta* **26**, 39–47 (1978).

[93]K. A. Campbell and C. M. Anderson, *Microelectronics J.* **38**, 52–9 (2007).

[94]T. Wang et al., *Adv. Sci.* **4**, 1600289 (2017).

[95]J. L. F. Da Silva et al., *Phys. Rev. B* **78**, 224111 (2008).

[96]T. Shintani, *eprint arXiv: 1811.09969* (2018).

[97]L. Bolotov et al., *Jpn. J. Appl. Phys.* **55**, 04EK02 (2016).

[98]S. Soeya et al., *Appl. Phys. Lett.* **103**, 053103 (2013).

[99]H. Maier and D. R. Daniel, *J. Electron. Mater.* **6**, 693–704 (1977).

[100]J. G. Yu et al., *J. Cryst. Growth* **54**, 248–52 (1981).

[101]L. G. Khvostantsev et al., *Phys. Status Solidi* **58**, 37–40 (1980).

[102]K. Kokh et al., *Solid State Commun.* **177**, 16–9 (2014).

[103]M. Longo, "Nanowire phase change memory (PCM) technologies: properties and performance", in *Adv. non-volatile mem. storage technol.* (Elsevier, 2014), 231–61.

[104]M. Longo, "Advances in nanowire PCM", in *Adv. non-volatile mem. storage technol.* (Elsevier, 2019), 443–518.

[105]M. A. Caldwell et al., *Nanoscale* **4**, 4382 (2012).

[106]J. S. Lee et al., *J. Am. Chem. Soc.* **130**, 6252–8 (2008).

[107]Z. Song et al., *Sci. China Inf. Sci.* **61**, 081302 (2018).

[108]J. H. Spencer et al., *ACS Nano* **8**, 9044–52 (2014).

[109]Z. Wang et al., *J. Am. Chem. Soc.* **132**, 13840–7 (2010).

[110]S. Sandoval et al., *Inorganica Chim. Acta* **492**, 66–75 (2019).

[111]D. G. Calatayud et al., *ChemistryOpen* **7**, 144–58 (2018).

[112]C. Fu et al., *ACS Nano* **12**, 9775–84 (2018).

[113]A. Chu et al., *Chem. Mater.* **8**, 2751–4 (1996).

[114]R. Carter et al., *Phys. Rev. Lett.* **96**, 1–4 (2006).

[115]V. G. Ivanov et al., *Phys. Rev. B* **98**, 125429 (2018).

[116]T. Fujimori et al., *Nat. Commun.* **4**, (2013).

[117]M. Hart et al., *Angew. Chemie - Int. Ed.* **56**, 8144–8 (2017).

[118]M. Hart et al., *Angew. Chemie Int. Ed.* **57**, 11649–53 (2018).

[119]A. Vasylenko et al., *ACS Nano* **12**, 6023–31 (2018).

[120]A. S. Kumskov et al., *J. Microsc.* **248**, 117–9 (2012).

[121]R. Senga et al., *Nat. Mater.* **13**, 1050–4 (2014).

[122]L. Zhao et al., *Angew. Chemie Int. Ed.* **45**, 311–5 (2006).

[123]C. Lin et al., *Phys. Chem. Chem. Phys.* **19**, 23247–53 (2017).

[124]C. A. Slade et al., *Nano Lett.* **19**, 2979–84 (2019).

[125]J. B. W. Webber et al., *J. Phys. Condens. Matter* **19**, 415117 (2007).

[126]R. Carter et al., *Dalt. Trans.* **43**, 7391–9 (2014).

[127]D. Schebarchov and S. C. Hendy, *Nano Lett.* **8**, 2253–7 (2008).

[128]D. F. Urban and H. Grabert, *Phys. Rev. Lett.* **91**, 256803 (2003).

[129]Y. M. Zuev et al., *Nano Lett.* **10**, 3037–40 (2010).

[130]M. V. Kharlamova et al., *J. Mater. Sci.* **53**, 13018–29 (2018).

[131]S. Brown, "Modelling Nanowires: Crystals Encapsulated in Carbon Nanotubes", PhD thesis (University of Warwick, 2016).

[132]J. J. P. Peters, *clTEM - OpenCL accelerated multislice*, 2020.

[133]D. C. Smith et al., *J. Vis. Exp.* 53434 (2016).

[134]J. H. Spencer et al., *RSC Adv.* **6**, 95387–95 (2016).

[135]M. G. Burdanova et al., *ACS Photonics* **6**, 1058–66 (2019).

[136]M. G. Burdanova et al., *Nano Lett.* **20**, 3560–7 (2020).

[137]O. Koshy et al., "Differential Scanning Calorimetry in Nanoscience and Nanotechnology", in *Therm. rheol. meas. tech. nanomater. charact.* Vol. 121 (Elsevier, 2017) Chap. 5, 109–22.

[138]P. Gill et al., *J. Biomol. Tech.* **21**, 167–93 (2010).

[139]N. Jiang and J. C. Spence, *Ultramicroscopy* **113**, 77–82 (2012).

[140]R. F. Egerton, *Ultramicroscopy* **127**, 100–8 (2013).

[141]J. H. Warner et al., *ACS Nano* **3**, 1557–63 (2009).

[142]R. F. Egerton, *Micron* **119**, 72–87 (2019).

[143]P. Buffat and J.-P. Borel, *Phys. Rev. A* **13**, 2287–98 (1976).

[144]K. V. Agrawal et al., *Nat. Nanotechnol.* **12**, 267–73 (2017).

[145]Q. Liu et al., *Prog. Mater. Sci.* **70**, 1–49 (2015).

[146]A. Eliseev et al., *Carbon N. Y.* **48**, 2708–21 (2010).

[147]F. Schuh, *Chem. Mater.* **26**, 423–34 (2014).

[148]A. Hirata et al., *Nat. Mater.* **10**, 28–33 (2010).

[149]M. V. Kharlamova et al., *J. Spectrosc.* 1–9 (2018).

[150]S. V. Pol et al., *J. Phys. Chem. C* **111**, 13309–14 (2007).

[151]S. Zhao et al., *Nano Res.* **8**, 288–95 (2015).

[152]J. Sloan et al., *Chem. Commun.* **8**, 699–700 (1999).

[153]R. D. Gately and M. in het Panhuis, *Beilstein J. Nanotechnol.* **6**, 508–16 (2015).

[154]P. E. De Jongh and T. M. Eggenhuisen, *Adv. Mater.* **25**, 6672–90 (2013).

[155]A. Marmur, *J. Colloid Interface Sci.* **122**, 209–19 (1988).

[156]A. Marmur, *Adv. Colloid Interface Sci.* **39**, 13–33 (1992).

[157]D. Schebarchov and S. C. Hendy, *Nanoscale* **3**, 134–41 (2011).

[158]Y. Wang et al., *Comput. Fluids* **134**, 190–5 (2016).

[159]S. Palzer et al., *Chem. Eng. Technol.* **26**, 962–6 (2003).

[160]J. K. Holt, *Science (80-. ).* **312**, 1034–7 (2006).

[161]M. Whitby and N. Quirke, *Nat. Nanotechnol.* **2**, 87–94 (2007).

[162]M. Whitby et al., *Nano Lett.* **8**, 2632–7 (2008).

[163]S. Marks, "Characterisation of Encapsulation Grown Nanowires", PhD thesis (Univeristy of Warwick, 2017).

[164]S. Wei et al., *Phys. Rev. Appl.* **7**, 034035 (2016).

[165]V. Piacente et al., *J. Alloys Compd.* **178**, 101–15 (1992).

[166]S. Boone and O. J. Kleppa, *Thermochim. Acta* **197**, 109–21 (1992).

[167]O. Madelung et al., "Antimony telluride (SbTe) crystal structure, chemical bond, lattice parameters (including data for BiSe, BiTe)", in *Non-tetrahedrally bond. elem. bin. compd. i*, Vol. C, 3 (Springer-Verlag, Berlin, 2008), 1–4.

[168]T. L. Anderson and H. B. Krause, *Acta Crystallogr. Sect. B Struct. Crystallogr. Cryst. Chem.* **30**, 1307–10 (1974).

[169]C. L. Yaws and M. A. Satyro, *The Yaws Handbook of Vapor Pressure* (Elsevier, Oxford, 2015).

[170]J. H. Greenberg, *Thermodynamic Basis of Crystal Growth*, Vol. 44, Springer Series in Materials Science (Springer Berlin Heidelberg, Berlin, Heidelberg, 2002).

[171]T. L. Anderson and H. B. Krause, *Acta Crystallogr. Sect. B Struct. Crystallogr. Cryst. Chem.* **30**, 1307–10 (1974).

[172]J. Sloan et al., *J. Am. Chem. Soc.* **124**, 2116–7 (2002).

[173]Y. Feutelais et al., *J. Phase Equilibria* **17**, 40–9 (1996).

[174]V. N. Volodin et al., *Russ. J. Phys. Chem. A* **88**, 2029–34 (2014).

[175]D. R. Stull, *Ind. Eng. Chem.* **39**, 517–50 (1947).

[176]D. R. Stull, *Ind. Eng. Chem.* **39**, 540–50 (1950).

[177]I. Barin, *Thermochemical Data of Pure Substances* (VCH, New York, 1995).

[178]G. Ghosh, *J. Phase Equilibria* **14**, 753–63 (1993).

[179]C. Hirayama et al., *J. Phys. Chem.* **67**, 1039–42 (1963).

[180]R. C. Sharma and Y. A. Chang, *Bull. Alloy Phase Diagrams* **7**, 68–72 (1986).

[181]G. Ustyugov et al., *Izv. Akad. Nauk SSSR- Neorg. Mater.* **5** (1969).

[182]W. M. Haynes, *Handbook of Chemistry and Physics* (CRC Press, 2016).

[183]C. E. Giusca et al., *Nano Lett.* **13**, 4020–7 (2013).

[184]M. Zhu et al., *Nanoscale* **7**, 9935–44 (2015).

[185]M. Brun et al., *Thermochim. Acta* **21**, 59–88 (1977).

[186]C. L. Jackson and G. B. McKenna, *J. Chem. Phys.* **93**, 9002–11 (1990).

[187]J. B. W. Webber, *Prog. Nucl. Magn. Reson. Spectrosc.* **56**, 78–93 (2010).

[188]B.-M. Koo et al., *Macromol. Rapid Commun.* **29**, 498–502 (2008).

[189]J. M. Wynn, "First-Principles Structure Prediction of Extreme Nanowires", PhD thesis (Unviersity of Cambridge, 2018).

[190]S. Banerjee and S. S. Wong, *Nano Lett.* **4**, 1445–50 (2004).

[191]S. Huang and L. Dai, *J. Phys. Chem. B* **106**, 3543–5 (2002).

[192]N. Grobert, *Mater. Today* **10**, 28–35 (2007).

[193]T. W. Ebbesen and T. Takada, *Carbon N. Y.* **33**, 973–8 (1995).

[194]M. P. Petkov, *Microsc. Microanal.* **11**, 1928–9 (2005).

[195]S. Banerjee and S. S. Wong, *J. Phys. Chem. B* **106**, 12144–51 (2002).

[196]R. Brydson, *Aberration-Corrected Analytical Transmission Electron Microscopy* (John Wiley & Sons, Chichester, UK, 2011).

[197]P. J. Goodhew et al., *Electron Microscopy and Analysis* (CRC Press, 2000).

[198]J. C. Vickerman and I. S. Gilmore, *Surface Analysis: The Principal Techniques* (John Wiley & Sons, Chichester, 2009).

[199]M. T. Otten, *J. Electron Microsc. Tech.* **17**, 221–30 (1991).

[200]L. Zarraoa et al., *Sci. Rep.* **9**, 1–11 (2019).

[201]S. D. Findlay et al., *Ultramicroscopy* **110**, 903–23 (2010).

[202]P. W. Hawkes and J. C. H. Spence, *Springer Handbook of Microscopy*, Springer Handbooks (Springer International Publishing, Cham, 2019).

[203]R. Zan et al., "Atomic Structure of Graphene and h-BN Layers and Their Interactions with Metals", in *Adv. graphene sci.* (InTech, July 2013).

[204]J. Ayache et al., *Sample Preparation Handbook for Transmission Electron Microscopy* (Springer, New York, 2010).

[205]R. Erni, *Aberration-Corrected Imaging in Transmission Electron Microscopy* (Imperial College Press, 2010).

[206]S. Ram et al., *Proc. Natl. Acad. Sci.* **103**, 4457–62 (2006).

[207]J. R. Hook and H. Hall, *Solid-State Physics* (Springer Berlin Heidelberg, 2009).

[208]N. Wiberg et al., *Holleman-Wiberg's Inorganic Chemistry* (Elsevier Science, 2001).

[209]J. .-F. Colomer et al., *Phys. Rev. B* **64**, 125425 (2001).

[210]S. Amelinckx et al., *Reports Prog. Phys.* **62**, 1471–524 (1999).

[211]J.-F. Colomer et al., *Eur. Phys. J. B - Condens. Matter* **27**, 111–8 (2002).

[212]J. M. Zuo et al., *Zeitschrift fur Krist.* **222**, 625–33 (2007).

[213]V. Mittal, *Polymer Nanotube Nanocomposites : Synthesis, Properties, and Applications* (Wiley and Sons, 2014).

[214]J.-F. Colomer et al., *Phys. Rev. B* **64**, 125425 (2001).

[215]D. Mitchell and T. Petersen, *Microsc. Res. Tech.* **75**, 153–63 (2012).

[216]D. R. G. Mitchell, *Microsc. Res. Tech.* **71**, 588–93 (2008).

[217]P. A. Buffat, *Philos. Trans. R. Soc. A Math. Phys. Eng. Sci.* **361**, 291–5 (2003).

[218]B. Fultz and J. M. Howe, *Transmission Electron Microscopy and Diffractometry of Materials* (Springer, 2013).

[219]S. T. Skowron et al., *Acc. Chem. Res.* **50**, 1797–1807 (2017).

[220]S. T. Skowron et al., *Micron* **120**, 96–103 (2019).

[221]D. Mattia and Y. Gogotsi, *Microfluid Nanofluid* **5**, 289–305 (2008).

[222]V. G. Dubrovskii et al., *Phys. Rev. B* **79**, 205316 (2009).

[223]J. Gibbs, *The Scientific Papers of J. Willard Gibbs* (Dover Publications, New York, 1961).

[224]D. Narayanaswamy and L. D. Marks, *Zeitschrift fur Phys. D Atoms Mol. Clust.* **26**, 70–2 (1993).

[225]P. M. Ajayan and L. D. Marks, *Phys. Rev. Lett.* **63**, 279–82 (1989).

[226]L. D. Marks, *Reports Prog. Phys.* **57**, 603–49 (1994).

[227]P. M. Ajayan and L. D. Marks, *Phase Transitions* **24-26**, 229–58 (1990).

[228]*International Center for Diffraction Data (ICDD).*

[229]*Inorganic Crystal-Structure Database (ICSD).*

[230]*National Institute of Standards and Technology (NIST) ICSD.*

[231]M. A. Dyson, "Advances in Computational Methods for Transmission Electron Microscopy Simulation and Image Processing", PhD thesis (University of Warwick, 2014).

[232]E. J. Kirkland, *Advanced Computing in Electron Microscopy* (Springer US, 2010).

[233]J. M. Cowley, *Diffraction Physics* (Elsevier Science, 1995).

[234]K. S. Coleman et al., *Chem. Mater.* **19**, 1076–81 (2007).

[235]*Mettler Toledo TGA/DSC Instrumentation.*

[236]E. Prenner and M. Chiu, *J. Pharm. Bioallied Sci.* **3**, 39–59 (2011).

[237]B. D. Cullity, *Elements of X-ray Diffraction*, Addison-Wesley Series in Metallurgy and Materials (Addison-Wesley, 1978).

[238]Z. Ullah et al., *J. Sci. Res.* **5**, 235–44 (2013).

[239]X. Zhao and Y. Ando, *Jpn. J. Appl. Phys.* **37**, 4846–9 (1998).

[240]A. Cao et al., *Chem. Phys. Lett.* **344**, 13–7 (2001).

[241]R. Das et al., *Curr. Nanosci.* **11**, 23–35 (2014).

[242]S. S. Garje et al., *J. Am. Chem. Soc.* **128**, 3120–1 (2006).

[243]Wang et al., *J. Am. Chem. Soc.* **127**, 13792–3 (2005).

[244]Z. Zhang et al., *Appl. Phys. A* **118**, 1043–51 (2015).

[245]A. Eliseev et al., "One-Dimensional Crystals inside Single-Walled Carbon Nanotubes: Growth, Structure and Electronic Properties", in *Electron. prop. carbon nanotub.* (InTech, 2011) Chap. 8, 127–56.

[246]Y. Zheng et al., *Nano Res.* **9**, 3453–62 (2016).

[247]J. A. Alonso et al., *J. Chem. Soc. Dalt. Trans.* **3**, 2225–9 (1985).

[248]N. Balakrishnan et al., *2D Mater.* **5**, 035026 (2018).

[249]G. Ghosh, *J. Phase Equilibria* **15**, 349–60 (1994).

[250]T. C. Harman et al., *J. Phys. Chem. Solids* **2**, 181–90 (1957).

[251]R. H. Asendorf, *J. Chem. Phys.* **27**, 11–6 (1957).

[252]M. Zhu et al., *Nat. Commun.* **5**, 4086 (2014).

[253]V. Biju et al., *J. Mater. Sci.* **43**, 1175–9 (2008).

[254]R. Yogamalar et al., *Solid State Commun.* **149**, 1919–23 (2009).

[255]H. P. Klug and L. E. Alexander, *X-Ray Diffraction Procedures: For Polycrystalline and Amorphous Materials* (Wiley, 1974).

[256]D. Balzar, *J. Res. Natl. Inst. Stand. Technol.* **98**, 321–53 (1993).

[257]L. W. da Silva et al., *J. Appl. Phys.* **97**, 114903 (2005).

[258]N. Hatsuta et al., *J. Alloys Compd.* **685**, 147–52 (2016).

[259]S. Chen et al., *Semicond. Sci. Technol.* **32**, 065003 (2017).

[260]F. Zocchi and V. Piacente, *J. Mater. Sci. Lett.* **14**, 235–7 (1995).

[261]M. Wilson and P. A. Madden, *J. Am. Chem. Soc.* **123**, 2101–2 (2001).

[262]A. L. Koh et al., *Nano Lett.* **16**, 1210–7 (2016).

[263]J. Lin et al., *Nat. Nanotechnol.* **9**, 436–42 (2014).

[264]M. Nagata et al., *Nano Lett.* **19**, 4845–51 (2019).

[265]Y.-C. Lin et al., *Nat. Nanotechnol.* **9**, 391–6 (2014).

[266]P. Koskinen, *Phys. Rev. Appl.* **6**, 1–9 (2016).

[267]G. Li et al., *J. Am. Chem. Soc.* **138**, 40–3 (2016).

[268]P. Finnie et al., *Nanotechnology* **19**, 335202 (2008).

[269]V. Datsyuk et al., *Carbon N. Y.* **46**, 833–40 (2008).

[270]R. Sankar et al., *CrystEngComm* **17**, 3440–5 (2015).

[271]D. A. Bandurin et al., *Nat. Nanotechnol.* **12**, 223–7 (2017).